

Cross Sections for Inner-Shell Ionization by Electron Impact

Xavier Llovet, Cedric J. Powell, Francesc Salvat, and Aleksander Jablonski

Citation: *Journal of Physical and Chemical Reference Data* **43**, 013102 (2014); doi: 10.1063/1.4832851

View online: <https://doi.org/10.1063/1.4832851>

View Table of Contents: <http://aip.scitation.org/toc/jpr/43/1>

Published by the *American Institute of Physics*

Articles you may be interested in

[Atomic radiative and radiationless yields for K and L shells](#)

Journal of Physical and Chemical Reference Data **8**, 307 (1979); 10.1063/1.555594

[Comparison of Electron Elastic-Scattering Cross Sections Calculated from Two Commonly Used Atomic Potentials](#)

Journal of Physical and Chemical Reference Data **33**, 409 (2004); 10.1063/1.1595653

[Use of the Bethe equation for inner-shell ionization by electron impact](#)

Journal of Applied Physics **119**, 184904 (2016); 10.1063/1.4948700

[Natural widths of atomic K and L levels, \$K\alpha\$ X-ray lines and several KLL Auger lines](#)

Journal of Physical and Chemical Reference Data **8**, 329 (1979); 10.1063/1.555595

[Secondary electron emission in the scanning electron microscope](#)

Journal of Applied Physics **54**, R1 (1983); 10.1063/1.332840

[A Review, Bibliography, and Tabulation of K, L, and Higher Atomic Shell X-Ray Fluorescence Yields](#)

Journal of Physical and Chemical Reference Data **23**, 339 (1994); 10.1063/1.555955

Cross Sections for Inner-Shell Ionization by Electron Impact

Xavier Llovet^{a)}

Centres Científics i Tecnològics, Universitat de Barcelona, Lluis Solé i Sabarís 1-3, 08028 Barcelona, Spain

Cedric J. Powell

Materials Measurement Science Division, National Institute of Standards and Technology, Gaithersburg, Maryland 20899-8370, USA

Francesc Salvat

Facultat de Física (ECM and ICC), Universitat de Barcelona, Diagonal 645, 08028 Barcelona, Spain

Aleksander Jablonski

Institute of Physical Chemistry, Polish Academy of Sciences, ul. Kasprzaka 44/52, 01-224 Warsaw, Poland

(Received 7 November 2013; accepted 7 November 2013; published online 16 January 2014)

An analysis is presented of measured and calculated cross sections for inner-shell ionization by electron impact. We describe the essentials of classical and semiclassical models and of quantum approximations for computing ionization cross sections. The emphasis is on the recent formulation of the distorted-wave Born approximation by Bote and Salvat [Phys. Rev. A **77**, 042701 (2008)] that has been used to generate an extensive database of cross sections for the ionization of the K shell and the L and M subshells of all elements from hydrogen to einsteinium ($Z = 1$ to $Z = 99$) by electrons and positrons with kinetic energies up to 1 GeV. We describe a systematic method for evaluating cross sections for emission of x rays and Auger electrons based on atomic transition probabilities from the Evaluated Atomic Data Library of Perkins *et al.* [Lawrence Livermore National Laboratory, UCRL-ID-50400, 1991]. We made an extensive comparison of measured K-shell, L-subshell, and M-subshell ionization cross sections and of $L\alpha$ x-ray production cross sections with the corresponding calculated cross sections. We identified elements for which there were at least three (for K shells) or two (for L and M subshells) mutually consistent sets of cross-section measurements and for which the cross sections varied with energy as expected by theory. The overall average root-mean-square deviation between the measured and calculated cross sections was 10.9% and the overall average deviation was -2.5% . This degree of agreement between measured and calculated ionization and x-ray production cross sections was considered to be very satisfactory given the difficulties of these measurements. © 2014 by the U.S. Secretary of Commerce on behalf of the United States. All rights reserved. [<http://dx.doi.org/10.1063/1.4832851>]

Key words: Auger emission; Bethe asymptotic formula; cross sections; distorted-wave Born approximation (DWBA); electron-impact ionization; relativistic plane wave Born approximation (PWBA); x-ray emission.

CONTENTS

1. Introduction	5	2.2.1. Electron wave functions and the interaction Hamiltonian	10
2. Theoretical Calculations of Ionization Cross Sections	7	2.2.2. Plane-wave Born approximation (PWBA)	11
2.1. Classical and semiclassical approximations	7	2.2.3. Distorted-wave Born approximation	16
2.2. Plane-wave and distorted-wave Born approximations	9	2.2.4. Corrected plane-wave Born approximation	17
		2.3. Applicability of atomic calculations to molecules and solids	17
		3. Analytical Formulae for Inner-Shell Ionization Cross Sections	18
		3.1. The Bethe formula	18
		3.2. Empirical modifications to the Bethe formula	21

^{a)}Electronic mail: xavier@ccit.ub.edu.

© 2014 by the U.S. Secretary of Commerce on behalf of the United States. All rights reserved.

3.3. The Kolbenstvedt formula	23	3. Measurements of L-shell ionization cross sections published up to May 2013.	57
3.4. The Gryzinski formula	23	4. Measurements of M-shell ionization cross sections performed up to May 2013.	68
3.5. Empirical formulae	24	5. Measurements of L-shell x-ray production cross sections performed up to May 2013.	70
3.6. Parameterization of cross sections from the DWBA and PWBA.	25	6. Measurements of M-shell x-ray production cross sections performed up to May 2013.	78
4. X-ray and Auger-Electron Emission	26	7. Selected sets of measured K-shell ionization cross sections that were included in the evaluation of experimental data.	79
4.1. Transition probabilities and emission yields	29	8. Average values of RMS and R for each selected element shown in Table 7, \overline{RMS} and \overline{R} , for K-shell ionization cross sections.	86
4.2. Emission cross sections.	30	9. Selected sets of measured L-shell ionization cross sections that were included in the evaluation of experimental data.	90
4.3. Emission cross sections with data from the Evaluated Atomic Data Library (EADL) ..	31	10. Average values of RMS and R for each selected element, \overline{RMS} and \overline{R} , from the measurements of L-subshell ionization cross sections shown in Table 9.	90
5. Experimental Techniques.	33	11. Selected sets of measured total M-shell ionization cross sections that were included in the evaluation of experimental data.	92
5.1. Ionization cross sections from x-ray measurements	33	12. Average values of RMS and R for each selected element, \overline{RMS} and \overline{R} , using the measurements of M-shell ionization cross sections shown in Table 11.	92
5.1.1. Measurement of x-ray production cross sections.	34	13. Selected sets of measured L-shell x-ray production cross sections included in the evaluation of experimental data.	92
5.1.2. Conversion of the x-ray production cross sections into ionization cross section	35	14. Average values of RMS and R for each selected element, \overline{RMS} and \overline{R} , using the measurements of L-shell x-ray production cross sections shown in Table 13.	94
5.2. Ionization cross sections from Auger-electron measurements	37	15. Summary of $\langle \overline{RMS} \rangle$ and $\langle \overline{R} \rangle$ values found in the evaluation of K-, L-, and M-shell ionization cross sections and of La x-ray production cross sections from the selected sources with superior data.	95
5.3. Ionization cross sections from electron energy-loss spectroscopy measurements ...	40	16. Summary of methods used for the measurement of (a) K-, (b) L-, and (c) M-shell ionization cross sections and for the measurement of (d) La x-ray production cross sections, as listed in Tables 2–5, respectively.	95
5.4. Ionization cross sections from crossed-beam experiments	40	17. Values of RMS and R determined using Eq. (138) with differences of K-shell ionization cross sections calculated using the formulae of Gryzinski, Casnati <i>et al.</i> , Hombourger, and Jakoby <i>et al.</i> from the cross sections obtained with the Bote <i>et al.</i> formulae for the indicated elements.	95
6. Comparison of Measured Cross Sections with DWBA Calculations.	40	18. Values of RMS and R determined using Eq. (138) with differences of L_3 -subshell ionization cross sections calculated using the formulae of Gryzinski, Casnati <i>et al.</i> , Hombourger, and Jakoby <i>et al.</i> from the cross sections obtained with the Bote <i>et al.</i> formulae for the indicated elements.	95
6.1. K-shell ionization cross sections	40		
6.2. L-subshell ionization cross sections	52		
6.3. M-subshell ionization cross sections	56		
6.4. L-shell x-ray production cross sections.	56		
6.5. M-shell x-ray production cross sections ...	60		
7. Evaluation of Measured Cross Sections	60		
7.1. Evaluation criteria.	61		
7.2. K-shell ionization cross sections	64		
7.3. L-subshell ionization cross sections	71		
7.4. M-subshell ionization cross sections	72		
7.5. $L\alpha$ x-ray production cross sections.	74		
7.6. Evaluation summary.	76		
8. Evaluation of Analytical Formulae	84		
8.1. K-shell ionization cross sections	85		
8.2. L_3 -subshell ionization cross sections	85		
8.3. M_5 -subshell ionization cross sections.	86		
8.4. Evaluation summary.	86		
9. Summary.	86		
Acknowledgments	91		
10. Appendix: Calculations of Ionization Cross Sections from the Bote Formulae	91		
11. References.	99		

List of Tables

1. Radiative transitions for the relevant groups in the K, L, and M series.	29
2. Measurements of K-shell ionization cross sections published up to May 2013.	42

19. Values of RMS and R determined using Eq. (138) with differences of M_5 -subshell ionization cross sections calculated using the formulae of Gryzinski, Casnati *et al.*, Hombourger, and Jakoby *et al.* from the cross sections obtained with the Bote *et al.* formulae for the indicated elements. 99
20. Summary of $\langle \overline{RMS} \rangle$ and $\langle \overline{R} \rangle$ values found in the evaluation of the Gryzinski, Casnati *et al.*, Hombourger, and Jakoby *et al.* formulae for K-shell, L_3 -subshell, and M_5 -subshell ionization cross sections. 99

List of Figures

1. The GOS (top) and the TGOS (middle) for ionization of the K shell ($1s_{1/2}$) of the hydrogen atom ($Z = 1$), represented as Bethe three-dimensional surfaces (top and middle) and as color-level diagrams (bottom). 14
2. The GOS (top) and the TGOS (middle) for ionization of the M_3 subshell ($3p_{3/2}$) of the gold atom ($Z = 79$), represented as Bethe three-dimensional surfaces (top and middle) and as color-level diagrams (bottom). 15
3. (Color online) Fano plots for K-shell ionization of N, Fe, Ag, and Au obtained from Eqs. (71) and (72). 20
4. (Color online) Fano plots for the L subshells of Cu and Au obtained from Eqs. (71) and (72). 21
5. (Color online) Fano plots for the K shell and the L_3 -subshell of the indicated elements, with cross sections calculated from the DWBA (Bote *et al.*³¹). 22
6. (Color online) Fano plots for the K shell and the L subshells of Au, with cross sections calculated from the DWBA (Bote *et al.*³¹). 22
7. (Color online) Absolute cross sections for ionization of the K shells of N, Si, Fe, Y, Ag, and Au vs. incident electron energy. 26
8. (Color online) Absolute cross sections for ionization of the L shells of Ag, Xe, Ta, and Bi vs. incident electron energy. 28
9. (Color online) Absolute cross sections for ionization of the M shells of Au and Bi vs. incident electron energy. Solid curves are the results of the DWBA calculations and of the analytical formulae indicated in the legends. 29
10. Elements for which (a) K-shell, (b) L-shell, and (c) M-shell ionization cross sections have been measured. 41
11. (Color online) Absolute K-shell ionization cross sections vs. incident electron energy for H, He, C, N, O, and Ne. 46
12. (Color online) Absolute K-shell ionization cross sections vs. incident electron energy for Na, Mg, Al, Si, S, and Cl. Solid curves are the results of the

- DWBA calculations. Symbols are experimental measurements. Notice the change of abscissa scale.
13. (Color online) Absolute K-shell ionization cross sections vs. incident electron energy for Ar, K, Ca, Sc, Ti, and V. 48
14. (Color online) Absolute K-shell ionization cross sections vs. incident electron energy for Cr, Mn, Fe, Co, Ni, and Cu. 49
15. (Color online) Absolute K-shell ionization cross sections vs. incident electron energy for Zn, Ga, Ge, As, Se, and Br. 50
16. (Color online) Absolute K-shell ionization cross sections vs. incident electron energy for Kr, Rb, Sr, Y, Zr, and Nb. 51
17. (Color online) Absolute K-shell ionization cross sections vs. incident electron energy for Mo, Pd, Ag, Cd, In, and Sn. 52
18. (Color online) Absolute K-shell ionization cross sections vs. incident electron energy for Sb, Te, Xe, Ba, La, and Ce. 53
19. (Color online) Absolute K-shell ionization cross sections vs. incident electron energy for Pr, Nd, Sm, Eu, Gd, and Ho. 54
20. (Color online) Absolute K-shell ionization cross sections vs. incident electron energy for Er, Tm, Yb, Ta, W, and Au. 55
21. (Color online) Absolute K-shell ionization cross sections vs. incident electron energy for Pb, Bi, and U. 56
22. (Color online) Absolute L_1 -subshell ionization cross sections vs. incident electron energy for Cu, Sr, Ag, Sn, Xe, and Sm. 58
23. (Color online) Absolute L_1 -subshell ionization cross sections vs. incident electron energy for Ta, W, Au, Pb, and Bi. 59
24. (Color online) Absolute L_2 -subshell ionization cross sections vs. incident electron energy for Cu, Sr, Ag, Sn, Xe, and Sm. 60
25. (Color online) Absolute L_2 -subshell ionization cross sections vs. incident electron energy for Ta, W, Au, Pb, and Bi. 61
26. (Color online) Absolute L_{23} -subshell ionization cross sections vs. incident electron energy for Si, P, S, Cl, Ar, and Ti. 62
27. (Color online) Absolute L_3 -subshell ionization cross sections vs. incident electron energy for Cu, Sr, Ag, Sn, Xe, and Sm. 63
28. (Color online) Absolute L_3 -subshell ionization cross sections vs. incident electron energy for Ta, W, Au, Pb, and Bi. 64
29. (Color online) Total L-shell ionization cross sections vs. incident electron energy for Cu, Kr, Sr, Nb, Pd, and Ag. 65
30. (Color online) Total L-shell ionization cross sections vs. incident electron energy for In, Sn, Xe, Ba, Sm, and Ho. 66

- | | | | |
|---|----|--|----|
| 31. (Color online) Total L-shell ionization cross sections vs. incident electron energy for Yb, Ta, Pb, Bi, and U..... | 67 | 47. (Color online) Plots of percentage deviations between measured K-shell ionization cross sections and the corresponding cross sections calculated from the Bote <i>et al.</i> predictive formulae as a function of U_K on logarithmic scales: (a) for U_K between 1 and 10, and (b) for U_K between 1 and 2×10^5 | 85 |
| 32. (Color online) Absolute M-shell ionization cross sections vs. incident electron energy for Au, Pb, Bi, and U..... | 68 | 48. (Color online) Plot of percentage deviations between measured K-shell ionization cross sections and the corresponding cross sections calculated from the Bote <i>et al.</i> predictive formulae as a function of U_K for U_K between 1.0 and 1.2.... | 86 |
| 33. (Color online) Absolute M_{45} -subshell ionization cross sections vs. incident electron energy for Br, Kr, and Sn..... | 69 | 49. (Color online) Plots of the average values of RMS and R from Table 8 for each element, \overline{RMS} and \overline{R} , as a function of Z | 87 |
| 34. (Color online) Absolute $L\alpha$, $L\beta$, $L\gamma$, and $L\ell$ x-ray production cross sections vs. incident electron energy for Pb..... | 71 | 50. (Color online) Percentage deviation Δ_i of experimental values of L_3 -subshell and total L-shell ionization cross sections from calculated values using the Bote <i>et al.</i> formulae as a function of electron energy for Ag (L), Sn (L), Xe (L_3), Sm (L), Ta (L), and Pb (L)..... | 88 |
| 35. (Color online) Absolute $L\alpha$ x-ray production cross sections vs. incident electron energy for Ga, Ge, As, In, Sn, and I..... | 72 | 51. (Color online) Percentage deviation Δ_i of experimental values of total L-shell ionization cross sections from calculated values using the Bote <i>et al.</i> formulae as a function of electron energy for Bi and U..... | 89 |
| 36. (Color online) Absolute $L\alpha$ x-ray production cross sections vs. incident electron energy for Ba, Sm, Gd, Dy, Ho, and Er..... | 73 | 52. (Color online) (a) Plots of percentage deviations between measured L-shell ionization cross sections and the corresponding cross sections calculated from the Bote <i>et al.</i> predictive formulae as a function of U_L on logarithmic scales. (b) Plots of percentage deviations between measured L_3 -subshell ionization cross sections ^{204,207} for Xe and the corresponding cross sections calculated from the Bote <i>et al.</i> predictive formulae as a function of U_{L3} on linear scales..... | 89 |
| 37. (Color online) Absolute $L\alpha$ x-ray production cross sections vs. incident electron energy for Tm, Yb, Hf, Ta, W, and Re..... | 74 | 53. (Color online) Plots of the average values of RMS and R from Table 10 for each element, \overline{RMS} and \overline{R} , as a function of Z | 90 |
| 38. (Color online) Absolute $L\alpha$ x-ray production cross sections vs. incident electron energy for Os, Pt, Au, Pb, and Bi..... | 75 | 54. (Color online) Percentage deviation Δ_i of experimental values of M-shell ionization cross sections from calculated values using the Bote <i>et al.</i> formulae, as a function of electron energy for Au, Pb, and Bi..... | 91 |
| 39. (Color online) Absolute total L-shell x-ray production cross sections vs. incident electron energy for Ar, Ag, Sm, Ho, Er, and Tm..... | 76 | 55. (Color online) Plot of percentage deviations between measured M-shell ionization cross sections and the corresponding cross sections calculated from the Bote <i>et al.</i> predictive formulae as a function of U_M on a logarithmic scale..... | 91 |
| 40. (Color online) Absolute total L-shell x-ray production cross sections vs. incident electron energy for Yb, Ta, Au, Pb, and Bi..... | 77 | 56. (Color online) Percentage deviation Δ_i of experimental values of $L\alpha$ x-ray production cross sections from calculated values using the Bote <i>et al.</i> formulae together with relaxation parameters extracted from the EADL as a function of electron energy for Gd, Er, Yb, W, Pt, and Au..... | 93 |
| 41. (Color online) Absolute $M\alpha$ x-ray production cross sections vs. incident electron energy for Au, Pb, and Bi..... | 78 | 57. (Color online) Percentage deviation Δ_i of experimental values of $L\alpha$ x-ray production cross sections from calculated values using the Bote <i>et al.</i> formulae together with relaxation | 93 |
| 42. (Color online) Percentage deviation Δ_i of experimental values of K-shell ionization cross sections from calculated values using the Bote <i>et al.</i> formulae, as a function of electron energy for C, N, O, Ne, Al, and Si..... | 81 | | |
| 43. (Color online) Percentage deviation Δ_i of experimental values of K-shell ionization cross sections from calculated values using the Bote <i>et al.</i> formulae, as a function of electron energy for Ar, Ca, Ti, Cr, Mn, and Fe..... | 82 | | |
| 44. (Color online) Percentage deviation Δ_i of experimental values of K-shell ionization cross sections from calculated values using the Bote <i>et al.</i> formulae, as a function of electron energy for Ni, Cu, Zn, Ga, Ge, and Se..... | 83 | | |
| 45. (Color online) Percentage deviation Δ_i of experimental values of K-shell ionization cross sections from calculated values using the Bote <i>et al.</i> formulae as a function of electron energy for Y, Pd, Ag, Sn, Sb, and Au..... | 84 | | |
| 46. (Color online) Percentage deviation Δ_i of experimental values of K-shell ionization cross sections from calculated values using the Bote <i>et al.</i> formulae, as a function of electron energy for Pb and Bi..... | 85 | | |

- parameters extracted from the EADL as a function of electron energy for Pb and Bi.
58. (Color online) Plot of percentage deviations between measured $L\alpha$ x-ray production cross sections and the corresponding cross sections calculated from the Bote *et al.* predictive formulae for L_3 -subshell ionization together with relaxation parameters extracted from the EADL as a function of U_{L3} on a logarithmic scale. ...
59. (Color online) Plots of the average values of RMS and R from Table 14 for each element, \overline{RMS} and \overline{R} , as a function of Z
60. (Color online) Percentage deviations Δ_i between K-shell ionization cross sections calculated using different analytical formulae (as indicated in the legends) and values calculated from the Bote *et al.* formulae as a function of electron energy for N, Si, Fe, Y, Ag, La, Ho, and Au.
61. (Color online) Percentage deviations Δ_i between L_3 -subshell ionization cross sections calculated using different analytical formulae (as indicated in the legends) and values calculated from the Bote *et al.* formulae as a function of electron energy for Si, Fe, Y, Ag, Xe, Gd, Ta, and Bi.
62. (Color online) Percentage deviations Δ_i between M_5 -subshell ionization cross sections calculated using different analytical formulae (as indicated in the legends) and values calculated from the Bote *et al.* formulae as a function of electron energy for Y, Ag, La, Ho, Au, and Bi.

Notation:

- m_e , electron mass.
 e , absolute value of the electron charge.
 \hbar , reduced Planck's constant, $= h/(2\pi)$.
 c , speed of light in vacuum.
 E , electron kinetic energy.
 \mathbf{p} , electron linear momentum.
 v , velocity of an electron with kinetic energy E .
 β , electron velocity in units of c .
 γ , total energy of the electron in units of the rest energy.
 $\tilde{\alpha}, \tilde{\beta}$, Dirac matrices.
 W , electron energy loss.
 θ , polar scattering angle.
 \mathbf{q} , momentum transfer in units of \hbar .
 Q , recoil energy.
 n, ℓ, j , quantum numbers of a subshell Si .
 $\kappa = (\ell - j)(2j + 1)$, relativistic angular momentum quantum number.
 $P_{nk}(r), Q_{nk}(r)$, large and small radial Dirac wave functions for bound spherical orbitals $\psi_{nk\kappa m}$.
 $P_{Ek}(r), Q_{Ek}(r)$, large and small radial Dirac wave functions for free spherical orbitals $\psi_{Ek\kappa m}$ of (kinetic) energy E .
 σ_i , ionization cross section of subshell Si .
 E_i , binding energy of subshell Si .

$U = E/E_i$, overvoltage of electrons with kinetic energy E for ionization of subshell Si .

$T_i = \langle \mathbf{p}^2/2m_e \rangle_{nlj}$, average kinetic energy of a bound electron in subshell Si .

$Y = T_i/E_i$.

Constants and kinematical quantities:

- 94 $E_h = m_e e^4 / \hbar^2 = 27.2114$ eV, Hartree energy.
 $a_0 = \hbar^2 / (m_e e^2) = 5.29177 \times 10^{-9}$ cm, Bohr radius.
 $\pi e^4 = \pi (a_0 E_h)^2 = 6.5141 \times 10^{-14}$ cm² eV².
 $m_e c^2 = 510.999$ keV, rest energy of the electron.
 $\beta = \frac{v}{c} = \sqrt{\frac{E(E+2m_e c^2)}{(E+m_e c^2)^2}}, \gamma = \frac{1}{\sqrt{1-\beta^2}} = \frac{E+m_e c^2}{m_e c^2}$.

Acronyms and abbreviations:

- 96 AES, Auger electron spectroscopy.
DCS, differential cross section.
DHFS, Dirac-Hartree-Fock-Slater.
DWBA, distorted-wave (first) Born approximation.
EADL, Evaluated Atomic Data Library.¹
EELS, electron energy-loss spectroscopy.
97 EPMA, Electron-probe microanalysis.
GOS, generalized oscillator strength.
OOS, optical oscillator strength.
PWBA, plane-wave (first) Born approximation.
TGOS, transverse generalized oscillator strength.
98

1. Introduction

Cross sections for the removal of atomic inner-shell electrons by electron impact are needed in many branches of physics including atomic physics, plasma physics, radiation physics, materials analysis by electron-probe microanalysis (EPMA), surface analysis by Auger-electron spectroscopy (AES), and thin-film analysis by electron energy-loss spectroscopy (EELS). For example, these cross sections are utilized in Monte Carlo simulations of EPMA and AES measurements, particularly to derive correction factors to account for diminished or enhanced EPMA and AES signal intensities from heterogeneous specimens. Nevertheless, despite more than seven decades of effort by many scientists, there is still inadequate experimental and theoretical knowledge of the dependence of the cross sections for ionization of different inner subshells on atomic number and electron kinetic energy.

Over 35 years ago, Powell² reviewed the available measurements, calculations, and predictive formulae for inner-shell ionization cross sections, and presented an analysis of the data in terms of the Bethe³ equation for the ionization cross section. Subsequent articles provided additional information and updates.^{2,4-7} The present review is intended, in part, to be an update to these earlier papers. In addition, a more extensive comparison is provided here of measured and calculated cross sections to show the extent of agreement in

the data from different sources and the trends with atomic number and electron energy. We also evaluate cross sections from a number of widely used analytical formulae. Of necessity, most of the comparisons are made using cross sections for ionization of the K-shell and L-subshells. These comparisons also illustrate the limitations in the available data, and particularly the need for more extensive (and more accurate) measurements, particularly for subshells other than the K shell.

Until recently, theoretical calculations of cross sections for inner-shell ionization were based either on classical or semi-classical approximations or on the nonrelativistic plane-wave Born approximation (PWBA). Calculations of ionization cross sections for the K shell and L subshells within this approximation have been reviewed by Powell.^{2,5} More recent calculations are those of Batchelor *et al.*,⁸ Luo and Joy,⁹ and Rez.¹⁰ Hippler¹¹ used the PWBA with approximate corrections to account for modification of the projectile wave function by the electrostatic field of the target atom and for the effect of exchange between the projectile and the atomic electrons. This modification of the PWBA has also been used by Khare *et al.*^{12,13}

Scofield¹⁴ described a fully relativistic formulation of the PWBA and gave total cross sections for the K shell and L subshells of selected elements. Approximations based on the PWBA have also been proposed by a number of authors, usually by combining analytical approximate forms of the generalized oscillator strength with phenomenological low-energy corrections. Among the most elaborate of these formulations are the binary-encounter-Bethe model of Kim and Rudd¹⁵ and Kim *et al.*¹⁶ The Weizsäcker-Williams method of virtual quanta^{17,18} used by Kolbenstvedt,^{19,20} Seltzer,²¹ and others can also be regarded as a simplification of the PWBA (see, e.g., Ref. 22).

The PWBA is known to be reliable only for projectiles with kinetic energies well above the ionization threshold. Its limitations at near-threshold energies are mostly caused by (1) the neglect of the distortion of the projectile wave functions by the field of the target atom, and (2) the inadequate treatment of electron exchange which can only be accounted for approximately within the PWBA.¹¹ A more elaborate theoretical framework is provided by the relativistic distorted-wave Born approximation (DWBA) which consistently accounts for the effects of both distortion and exchange.^{23,24} DWBA calculations of ionization cross sections for ions have been reported by various authors.^{23,25–27} Calculations for neutral atoms are more difficult because of the slower convergence of the partial-wave series, and require substantial computer power. Only recently, Segui *et al.*²⁸ and Colgan *et al.*²⁹ have reported semirelativistic DWBA calculations for neutral atoms and electrons with kinetic energies ranging from threshold up to about 10 times the ionization energy. Bote and Salvat³⁰ developed a composite scheme that combines the DWBA with the PWBA to produce cross sections with the reliability of the DWBA for projectile electrons and positrons with energies from the ionization threshold to 1 GeV.

The present review is organized as follows. In Sec. 2 we give a summary of the theoretical models used to calculate cross

sections for the ionization of inner shells, from classical formulae to the quantum PWBA and DWBA. Section 3 is devoted to analytical formulae that have proved useful in applied fields (EPMA, AES, etc.) where knowledge of ionization cross sections is required. We also introduce the parameterized cross sections of Bote *et al.*^{31,32} that have been fitted to the K-, L-, and M-shell ionization cross sections calculated with the Bote and Salvat DWBA method for all elements from hydrogen to einsteinium. In practical work, cross sections for x-ray and Auger-electron emission are frequently needed. These cross sections are also easier to measure than those for inner-shell ionization. In Sec. 4 we consider atomic relaxation and the relationship between ionization cross sections and x-ray and Auger emission cross sections. Experimental techniques employed to determine these cross sections are reviewed in Sec. 5. A systematic comparison of measured K-, L-, and M-shell ionization cross sections with the theoretical cross sections of Bote *et al.* is given in Sec. 6. We present graphical comparisons for the subshells and elements for which experimental data are available, and for electrons with kinetic energies from the ionization threshold to 1 GeV. These comparisons include the energy ranges of interest for EPMA, AES, and EELS. In Sec. 7, the graphical comparisons enable us to identify three or more sets of K-shell ionization cross-section data for particular elements and two or more sets of L- and M-shell ionization cross-section data for various elements that are consistent with each other and with the energy dependences expected from the Bote *et al.* formulae. We also make similar comparisons of measured L-shell x-ray production cross sections with the corresponding cross sections calculated from the DWBA ionization cross sections and needed atomic data (such as fluorescence yields and transition rates), and we are again able to find two or more sets of x-ray production cross sections for particular elements that are consistent with each other and with the energy dependences from the Bote *et al.* formulae. We examine the percentage deviations between the measured cross sections for the identified elements and data sets and the corresponding calculated cross sections, and calculated average root-mean-square percentage deviations and mean percentage deviations. These percentage deviations are judged to be satisfactorily small. In Sec. 8, we compare K-, L-, and M-shell ionization cross sections from the Bote *et al.* formulae for selected elements with cross sections calculated from four widely used analytical formulae, and again quantify the degree of agreement. We present our conclusions in Sec. 9 regarding the reliability of the DWBA cross sections and various analytical formulae for estimating ionization cross sections. Finally, the Appendix gives guidance on calculations of ionization cross sections from the Bote *et al.* formulae.

We use the term “shell” to refer to the set of one-electron orbitals having the same principal quantum number n . Each shell consists of $2n - 1$ “subshells” characterized by the orbital angular momentum and the total angular momentum quantum numbers, ℓ and j , respectively. We recall that the ranges of these quantum numbers are the following: $n = 1, 2, \dots, \ell = 0, 1, 2, \dots, n - 1; j = \ell \pm 1/2$ ($j > 0$). Individual subshells $n\ell j$ will be denoted by using either the familiar spectroscopic notation

($1s_{1/2}, 2s_{1/2}, 2p_{1/2}, 2p_{3/2}, 3s_{1/2}, \dots$) or the x-ray notation ($K, L_1, L_2, L_3, M_1, \dots$).

2. Theoretical Calculations of Ionization Cross Sections

The theory for the ionization of atoms by the impact of charged particles has been a subject of continuous interest since the pioneering work of Thomson in the early 1910s.³³ Reviews have been published by Rudge³⁴ and Powell.² The theoretical description of ionizing collisions is far more difficult than that of collisions causing excitation of the target atom to bound states, because the former involve two free electrons in the final state. In the present article we are concerned with cross sections for the ionization of inner-shell or core electrons by impact of projectile electrons. The theory can be readily adapted to describe ionization by positron impact; the calculations are easier than for electron collisions, because positrons do not experience exchange effects.

We consider collisions of a projectile electron or positron, having kinetic energy E , with a neutral atom of the element of atomic number Z that result in the ionization of an inner subshell $n\ell j$ of the latter. For concreteness, we limit our considerations to the case of closed subshells with $2j + 1$ electrons in equivalent orbitals. Obviously, ionization is possible only when the collision involves an energy transfer W which is larger than the ionization energy E_i of the active subshell.

2.1. Classical and semiclassical approximations

The first theoretical study of the ionization of atoms by electron impact was performed by Thomson³³ using nonrelativistic classical mechanics (see also Ref. 34). Thomson derived the differential cross section (DCS) for collisions of a projectile electron with a target electron assumed to be at rest. Expressed in terms of the energy loss W , the Thomson DCS is

$$\frac{d\sigma^{\text{Th}}}{dW} = \frac{2\pi e^4}{m_e v^2} \frac{1}{W^2}, \quad (1)$$

where $v = (2E/m_e)^{1/2}$ is the velocity of the projectile before the interaction and E is its kinetic energy. In the center-of-mass frame, the Thomson DCS is identical to the familiar Rutherford DCS; the formula (1) results from the transformation from the center-of-mass frame to the laboratory frame, in which the target electron is at rest. When the target electron is bound in an atomic subshell Si , ionizing collisions are only possible for $W > E_i$, where E_i is the binding energy of an electron in the subshell. Consequently, the total cross section for ionization of a closed subshell $n\ell j$ with $2j + 1$ equivalent electrons can be approximated as

$$\sigma_i^{\text{Th}} = (2j + 1) \int_{E_i}^E \frac{d\sigma^{\text{Th}}}{dW} dW. \quad (2)$$

That is,

$$\sigma_i^{\text{Th}} = (2j + 1) \frac{2\pi e^4}{m_e v^2} \frac{1}{E_i} \left(1 - \frac{1}{U}\right), \quad (3)$$

where $U \equiv E/E_i$ is the overvoltage.

Attempting to improve Thomson's theory, Gryzinski,³⁵ and Stabler³⁶ studied collisions with target electrons moving isotropically with kinetic energy T_i . The classical energy-loss DCS for these collisions takes the form³⁷

$$\frac{d\sigma^{\text{CBE}}}{dW} = \frac{2\pi e^4}{m_e v^2} \left(\frac{1}{W^2} + \frac{4T_i}{3W^3} \right) \quad \text{for } W \leq E - T_i, \quad (4a)$$

$$= \frac{2\pi e^4}{m_e v^2} \left(\frac{1}{W^2} + \frac{4(E - W)}{3W^3} \right) \left(\frac{E - W}{T_i} \right)^{1/2} \quad (4b)$$

for $W > E - T_i$.

This result is usually referred to as the classical binary-encounter (CBE) approximation. The corresponding ionization cross section for a subshell $n\ell j$ can be obtained by considering T_i as the average kinetic energy of the atomic electron ($T_i = \langle \mathbf{p}^2/2m_e \rangle_{n\ell j}$) and integrating over the energy-loss interval (E_i, E).

Gryzinski³⁸⁻⁴⁰ went a step further and, to get ionization cross sections with an energy-dependence closer to that predicted by the Bethe theory [see Eq. (52)], assumed that the atomic electron moves with an isotropic velocity distribution given by

$$f(v) = (\bar{v}/v)^3 \exp(-v/\bar{v}), \quad (5)$$

where \bar{v} is the mean velocity of the atomic electron. On averaging over this distribution, he obtained the following formula for the ionization cross section:

$$\sigma_i^{\text{Gr}} = (2j + 1) \frac{2\pi e^4}{m_e v^2} \frac{1}{E_i} \frac{1}{U} \left(\frac{U - 1}{U + 1} \right)^{3/2} \times \left[1 + \frac{2}{3} \left(1 - \frac{1}{2U} \right) \ln(2.7 + \sqrt{U - 1}) \right]. \quad (6)$$

The distribution (5) is not realistic; it was introduced as an *ad hoc* device to obtain a logarithmic term like that in Eq. (52) below. Nevertheless, Eq. (6) provides a real improvement over the Thomson cross section and has been used, combined with a relativistic correction [Eq. (83c)], as a convenient semiempirical formula to obtain fast estimates of ionization cross sections (see Sec. 3.2). The need for such a formula was particularly important before the widespread availability of personal and laboratory computers.

The cross sections from these classical formulae differ significantly from the available experimental data^{2,5} and also from the results of elaborate quantum calculations. To improve the classical theory, relevant features of the quantum treatment must be accounted for. The first of these is the indistinguishability of the colliding electrons, i.e., exchange effects. To include exchange, the Thomson DCS must be replaced by the exact quantum DCS for binary-electron collisions derived by

Mott,⁴¹

$$\frac{d\sigma^{\text{Mott}}}{dW} = \frac{2\pi e^4}{m_e v^2} \left\{ \frac{1}{W^2} + \frac{1}{(E-W)^2} - \frac{1}{W(E-W)} \cos \left(\sqrt{\frac{E_h}{E}} \ln \left[\frac{W}{E-W} \right] \right) \right\}, \quad (7)$$

where $E_h = m_e e^4 / \hbar^2 = 27.2114$ eV is the Hartree energy. Notice that this DCS, as well as the Thomson DCS (1), describes collisions with a target electron initially at rest. The first term on the right-hand side of Eq. (7) accounts for “direct” collisions where the primary electron loses energy W , the second term corresponds to “exchange” collisions in which the projectile loses energy $E - W$, and the last term accounts for the interference between the wave functions of the two electrons. Notice that the kinetic energies of the two electrons after the interaction are $E - W$ and W , for both direct and exchange collisions. The Mott DCS (7) is symmetric under the exchange of W and $E - W$, reflecting the indistinguishability of the electrons.

As discussed by Rudge,³⁴ the Mott formula is inconsistent when applied to ionization because it lacks the expected symmetry under exchange of the final kinetic energies of the two electrons, which are $W - E_i$ and $E - W$. To circumvent this difficulty (i.e., to restore the symmetry under the exchange of electrons in the final state), the energy E of the projectile in expression (7) should be replaced by $E + E_i$. Moreover, to account for the attraction of the projectile electron by the nucleus, we may consider that the projectile electron gains a certain kinetic energy, of the order of the average potential energy of the atomic electron ($= E_i + T_i$), and loses an equivalent amount of potential energy.³⁴ This correction is normally introduced by multiplying the DCS by a so-called “focusing factor” or “acceleration factor” given by

$$B = \frac{E}{E + E_i + T_i}. \quad (8)$$

Note that the effect of this factor is equivalent to replacing the factor $2/(m_e v^2) = 1/E$ on the right-hand side of Eq. (7) by $1/(E + E_i + T_i)$. The focusing factor reduces the ionization cross section, and improves the agreement with experimental data and with more elaborate calculations for projectiles with kinetic energies near and below the energy for the maximum of the ionization cross section vs. energy curve. Finally, in accordance with the classical binary-encounter approximation, Eq. (4), we should include an extra term proportional to T_i [here we assume that $W < E - T_i$] for collisions with energy transfers W and $E + E_i - W$. These considerations lead to a nonrelativistic semiclassical impulse approximation (IA). The corresponding energy-loss DCS is

$$\frac{d\sigma^{\text{IA}}}{dW} = \frac{2\pi e^4}{m_e v^2} B \left\{ \frac{1}{W^2} + \frac{1}{(E + E_i - W)^2} + \frac{4T_i}{3} \left(\frac{1}{W^3} + \frac{1}{(E + E_i - W)^3} \right) - \frac{1}{W(E + E_i - W)} \times \cos \left(\sqrt{\frac{E_h}{2(E + E_i)}} \ln \left[\frac{W}{E + E_i - W} \right] \right) \right\}. \quad (9)$$

As indicated above, the kinetic energies of the two electrons after a direct collision with energy transfer W are $E - W$ and $W - E_i$. The equivalent exchange collision corresponds to the energy transfer $W' = E + E_i - W$; this energy transfer leads to the same final energies, $E - W' = W - E_i$ and $W' - E_i = E - W$. Because the DCS (9) does account for direct and exchange collisions, the ionization cross section is obtained by integrating the DCS over the interval from $W = U_i$ to $W_{\text{max}} = (E + E_i)/2$. Thus, the ionization cross section for a closed subshell $n\ell j$ is

$$\sigma_i^{\text{IA}} = (2j + 1) \int_{U_i}^{(E+E_i)/2} \frac{d\sigma^{\text{IA}}}{dW} dW. \quad (10)$$

If the argument of the cosine in Eq. (9) is assumed to be constant and equal to g , the integral can be evaluated analytically giving

$$\sigma_i^{\text{IA}} = (2j + 1) \frac{2\pi e^4}{m_e v^2} \frac{B}{E_i} \times \left[1 - \frac{1}{U} + \frac{2Y}{3} \left(1 - \frac{1}{U^2} \right) - \frac{\cos g \ln U}{U + 1} \right]. \quad (11)$$

with $Y = T_i/E_i$. Vriens⁴² recommends taking

$$g = \sqrt{\frac{E_h}{2E_i(U + 1)}} \ln U. \quad (12)$$

where E_h is the Hartree energy. The relativistic extension of the impulse approximation (RIA) is obtained by replacing the Mott DCS by the Møller⁴³ DCS

$$\frac{d\sigma^{\text{Møller}}}{dW} = \frac{2\pi e^4}{m_e v^2} \left\{ \frac{1}{W^2} + \frac{1}{(E - W)^2} - \frac{1 - b_0}{W(E - W)} + \frac{b_0}{E^2} \right\}, \quad (13)$$

with

$$b_0 = \left(\frac{E}{E + m_e c^2} \right)^2. \quad (14)$$

The quantity v is the speed of the projectile, which is related to its kinetic energy E through the relativistic relation

$$v = c\beta = c \sqrt{\frac{E(E + 2m_e c^2)}{(E + m_e c^2)^2}}. \quad (15)$$

While the Mott formula is the exact nonrelativistic quantum DCS for binary collisions, the Møller DCS is obtained within the plane-wave Born approximation. Hence, the non-relativistic limit of the Møller DCS (which is obtained by setting $b_0 = 0$) differs slightly from the Mott DCS, Eq. (7). With the same considerations as for the nonrelativistic formulation, we arrive at the following energy-loss DCS,

$$\frac{d\sigma^{\text{RIA}}}{dW} = \frac{2\pi e^4}{m_e v^2} B \left\{ \frac{1}{W^2} + \frac{1}{(E + E_i - W)^2} + \frac{4T_i}{3} \left(\frac{1}{W^3} + \frac{1}{(E + E_i - W)^3} \right) - \frac{1 - b_0}{W(E + E_i - W)} + \frac{b_0}{(E + E_i)^2} \right\}. \quad (16)$$

The ionization cross section for a closed subshell $n\ell j$ is

$$\begin{aligned}\sigma_i^{\text{RIA}} &= (2j + 1) \int_{E_i}^{(E+E_i)/2} \frac{d\sigma^{\text{RIA}}}{dW} dW \\ &= (2j + 1) \frac{2\pi e^4}{m_e v^2} \frac{B}{E_i} \left[1 - \frac{1}{U} + \frac{2Y}{3} \left(1 - \frac{1}{U^2} \right) \right. \\ &\quad \left. - \frac{(1 - b_0) \ln U}{U + 1} + \frac{b_0(U - 1)}{2(U + 1)^2} \right].\end{aligned}\quad (17)$$

The above semiclassical approximations are expected to be appropriate for describing close binary collisions. However, they miss, at least partially, the effect of distant interactions. Seltzer²¹ estimated the contribution from distant interactions using the Weizsäcker-Williams method of virtual quanta, and showed that the sum of contributions from close and distant interactions yields ionization cross sections in reasonable agreement with experimental data (see also Ref. 22). An alternative model has been proposed by Kim and Rudd¹⁵ in which the nonrelativistic energy-loss DCS is expressed as a mixture of the energy-loss DCSs obtained from the impulse approximation and from the dipole approximation. Their DCS was constrained to reproduce the high-energy asymptotic limit given by the Bethe formula, Eq. (52). A relativistic version of this model was formulated by Kim *et al.*^{15,16} (see also Ref. 44). It should be mentioned that the energy-loss DCS for distant interactions requires knowledge of the optical (dipole) oscillator strength or, equivalently, of the cross section for photoelectric absorption. Since these quantities are only available for a limited number of atoms, molecules, and solids, Kim *et al.* approximated the dipole oscillator strength with simple analytical expressions from which they derived closed formulae for the ionization cross section.

These semiclassical models are useful for obtaining quick estimates of ionization cross sections. They have also been used as a guide in the development of semiempirical formulae. However, their accuracy is insufficient for most practical applications: (1) they give appreciable errors for projectiles with near-threshold energies, and (2) models that disregard distant interactions fail to reproduce the correct high-energy behavior obtained from the Bethe theory (to be described in Sec. 3.1). More reliable ionization cross sections can only be obtained from quantum-mechanical calculations of the type described in Sec. 2.2.

2.2. Plane-wave and distorted-wave Born approximations

The first quantum-mechanical calculation of the ionization of atoms by impact of charged particles was performed by Bethe³ in 1932 using the nonrelativistic plane-wave Born approximation (PWBA). In this formulation, as well as in subsequent improvements of the theory, the Coulomb interaction of the projectile with the target atom is considered as a weak perturbation which causes transitions of the atom from

its initial ground state to excited states. The states of the projectile are represented as plane waves, and transition probabilities are evaluated by using first-order perturbation theory. Within the PWBA, the DCS is expressed as the product of purely kinematical factors and the generalized oscillator strength (GOS) that is a function of the energy and the magnitude of the momentum transferred in the collision. An elementary derivation can be found in the textbook by Bethe and Jackiw.⁴⁵ Approximate analytical formulae of the GOSs for K-, L-, and M-shell electrons have been derived using screened hydrogenic wave functions.^{3,46,47} These formulae have been used in approximate calculations, as the basis of semiempirical formulae, and in calculations of the stopping power of charged particles in matter (see, e.g., Refs. 11, 12, 20, 48, and 49). More accurate GOSs for the different electron shells of atoms can be calculated numerically using atomic wave functions obtained from self-consistent Hartree-Fock-Slater calculations. Calculations of this type were reported by McGuire,^{50,51} Manson,⁵² Rez,^{10,53} and others. It should be mentioned that the PWBA does not allow a consistent description of electron exchange because the wave functions of the projectile and of the active target electron are not orthogonal.⁵⁴ Exchange effects can be partially accounted for by means of the Ochkur approximation,^{34,55} as employed, e.g., by Hippler¹¹ and Rez.^{10,53}

The PWBA theory for electron impact was generalized by Bethe⁵⁶ and Møller⁴³ to a relativistic form in which electron wave functions are solutions of the Dirac equation and the interaction is represented by an effective Hamiltonian obtained from elementary quantum electrodynamics. Scofield¹⁴ reported relativistic PWBA calculations for ionization of the K shell and the L subshells from a set of nine elements with atomic numbers covering the interval from $Z = 18$ to $Z = 92$. More recently, Bote and Salvat³⁰ performed systematic calculations of GOSs for K, L, and M subshells of neutral atoms. In these calculations, atomic electrons are described using the Dirac-Hartree-Fock-Slater potential.

A systematic improvement of the PWBA is obtained by considering the distortion of the projectile wave function caused by the atomic potential. The easiest method consists in replacing the projectile plane waves by Dirac distorted plane waves, i.e., by exact solutions of the Dirac equation for an electron in the electrostatic potential of the atom. This replacement yields the so-called distorted-wave Born approximation (DWBA). If the projectile is assumed to “see” the same potential as the active target electron, the wave functions of the projectile and target electrons are orthogonal and the DWBA allows a consistent description of exchange effects. Relativistic DWBA calculations for ionization of neutral atoms by electron impact have been performed by Segui *et al.*²⁸ and Colgan *et al.*²⁹

In this section we briefly present the theoretical models employed to calculate the ionization cross sections from the PWBA and the DWBA. More details can be found in the articles by Segui *et al.*²⁸ and Bote and Salvat.³⁰ All calculations are based on first-order perturbation theory. We consider the interaction of the projectile with the target atom as a weak perturbation which causes transitions of the atom from its ground state to excited states in the continuum spectrum. For

simplicity, we disregard excitations to discrete bound states that are not of interest here. To account for the dominant relativistic effects, all one-electron wave functions are solutions of the Dirac equation.

It is worth pointing out that the models considered here are based on the assumption that the wave functions of the two free electrons in the final state are uncorrelated. That is, after the collision, each free electron does not “feel” the electrostatic field of the other. This assumption is valid for soft collisions of high-energy projectiles (i.e., collisions involving moderate energy transfers), in which the projectile leaves the target atom with a velocity much larger than that of the knocked-on electron. It is also expected to hold for the ionization of inner shells of atoms with intermediate and large atomic numbers because of the dominance of the electrostatic field of the nucleus. Conversely, these models are not expected to be reliable for ionization of light atoms by low-energy projectiles (see, e.g., Refs. 34, 57, and references therein) because the electrostatic field of the emerging knocked-on electron is comparable to the screened field of the nucleus and, therefore, correlation effects related to the “post-collision interaction” between the ionized atom and the two slowly moving electrons become important.⁵⁷ We also note that our atomic model for inner-shell ionization should break down for solid targets and projectile energies close to the ionization threshold because we do not consider the influence of the electronic structure of the solid and screening effects following the production of an inner-shell vacancy. These points are discussed further in Section 2.3. Our evaluation in Section 7 will seek to determine the extent to which the calculated ionization cross sections agree with measured cross sections for atoms, molecules, and solids for a wide range of atomic numbers and for incident energies from close to the ionization threshold to 1 GeV.

2.2.1. Electron wave functions and the interaction Hamiltonian

The states of the target atom are described within a central-field independent-electron approximation, that is, as Slater determinants built with one-electron orbitals ψ_n which are eigenstates of the one-electron Dirac Hamiltonian, $\mathcal{H}_D = \mathcal{K} + V(r)$, where

$$\mathcal{K} = c\tilde{\alpha} \cdot \mathbf{p} + (\tilde{\beta} - 1)m_e c^2, \quad (18)$$

is the Dirac kinetic energy operator; here $\mathbf{p} = -i\hbar\nabla$ is the momentum operator, and $\tilde{\alpha}$ and $\tilde{\beta}$ are the Dirac matrices. We limit our considerations to central potentials $V(r)$ for which the Dirac equation⁵⁸

$$[c\tilde{\alpha} \cdot \mathbf{p} + (\tilde{\beta} - 1)m_e c^2 + V(r)]\psi_n(\mathbf{r}) = E\psi_n(\mathbf{r}), \quad (19)$$

can be solved numerically with relative ease.⁵⁹ Note that the eigenvalue E is the electron energy, exclusive of its rest energy. All of the calculations described below are performed using the base of spherical orbitals. These are solutions of the Dirac equation with well-defined parity and angular momentum, characterized by the quantum numbers ℓ (orbital angular momen-

tum), j (total angular momentum), and m (z -component of the total angular momentum). Spherical orbitals have the form^{58,60}

$$\psi_{E\kappa m}(\mathbf{r}) = \frac{1}{r} \begin{pmatrix} P(r) \Omega_{\kappa,m}(\hat{\mathbf{r}}) \\ iQ(r) \Omega_{-\kappa,m}(\hat{\mathbf{r}}) \end{pmatrix}, \quad (20)$$

where $\Omega_{\kappa,m}(\hat{\mathbf{r}})$ are spherical spinors, and $P(r)$ and $Q(r)$ are the large- and small-component radial functions that satisfy the coupled differential equations

$$\begin{aligned} \frac{dP}{dr} &= -\frac{\kappa}{r} P + \frac{E - V + 2m_e c^2}{c\hbar} Q, \\ \frac{dQ}{dr} &= -\frac{E - V}{c\hbar} P + \frac{\kappa}{r} Q. \end{aligned} \quad (21)$$

To simplify the notation, we use the relativistic angular momentum quantum number

$$\kappa = (\ell - j)(2j + 1), \quad (22)$$

which gives both the total angular momentum j and the parity $(-1)^\ell$ of the Dirac spherical orbital,

$$j = |\kappa| - \frac{1}{2}, \quad \ell = j + \frac{\kappa}{2|\kappa|}. \quad (23)$$

The spherical spinors are eigenfunctions of the total angular momentum in Pauli's theory, and are given by

$$\Omega_{\kappa,m}(\hat{\mathbf{r}}) \equiv \sum_{\mu=\pm 1/2} \langle \ell, 1/2, m - \mu, \mu | j, m \rangle Y_{\ell, m-\mu}(\hat{\mathbf{r}}) \chi_\mu. \quad (24)$$

where the quantities $\langle \ell, 1/2, m - \mu, \mu | j, m \rangle$ are Clebsch-Gordan coefficients, $Y_{\ell m}(\hat{\mathbf{r}})$ are spherical harmonics, and χ_μ are the unit spinors.

In our calculations, the radial Dirac equations were solved to high precision (usually to eight or more significant figures) by using the subroutine package RADIAL.⁵⁹ In the case of bound orbitals ($E < 0$), each discrete energy level is characterized by the principal quantum number n and the angular momentum quantum number κ . Bound orbitals calculated by RADIAL are normalized to unity and, therefore, the calculated orbitals satisfy the orthonormality relation⁵⁸

$$\int \psi_{n'\kappa'm'}^\dagger(\mathbf{r}) \psi_{n\kappa m}(\mathbf{r}) d\mathbf{r} = \delta_{n'n} \delta_{\kappa'\kappa} \delta_{m'm}, \quad (25)$$

where $\delta_{m'm}$ is the Kronecker symbol (equal to 1 if $m' = m$ and equal to 0 otherwise). The radial functions of free spherical waves (with $E > 0$) are normalized in such a way that the large-component radial function asymptotically oscillates with unit amplitude,

$$P(r) \underset{r \rightarrow \infty}{\sim} \sin\left(kr - \ell \frac{\pi}{2} - \eta \ln 2kr + \delta_{E\kappa}\right), \quad (26)$$

where

$$k = (c\hbar)^{-1} \sqrt{E(E + 2m_e c^2)} \quad (27)$$

is the wavenumber, $\eta = Z_\infty e^2 m_e / (\hbar^2 k)$ is the Sommerfeld parameter [the quantity $Z_\infty e^2 \equiv \lim_{r \rightarrow \infty} rV(r)$ represents the

strength of the Coulomb tail of the potential], and $\delta_{E\kappa}$ is a phase shift. Free spherical waves normalized in the form (26) satisfy the orthogonality relation

$$\int \psi_{E'\kappa'm'}^\dagger(\mathbf{r})\psi_{E\kappa m}(\mathbf{r})\mathbf{d}\mathbf{r} = \frac{E}{k} \pi \delta(E' - E) \delta_{\kappa'\kappa} \delta_{m'm}, \quad (28)$$

where $\delta(E' - E)$ is the Dirac δ distribution.

To calculate atomic wave functions, we adopt the self-consistent Dirac-Hartree-Fock-Slater (DHFS) potential of the neutral atom with Latter's tail correction,^{61–63} $V^{\text{DHFS}}(r)$. That is, bound orbitals are solutions of the Dirac equation for the potential $V(r) = V^{\text{DHFS}}(r)$. This choice of potential is motivated by the fact that, for inner subshells with ionization energies larger than about 500 eV, the eigenvalues of the one-electron Dirac equation with the DHFS potential are very close to the experimental subshell ionization energies,^{64,65} as discussed further in the Appendix. Final states of the knocked-on electron are also represented by positive-energy spherical orbitals of the DHFS potential. The advantage of using the same potential for bound and free states is that all orbitals are guaranteed to be mutually orthogonal.

As indicated above, the ionization of the target atom is caused by the interaction of the projectile with the atomic electrons. The effective interaction Hamiltonian $\mathcal{H}_{\text{int}}(0, 1)$ between a charged Dirac particle “0” (the projectile) and a target electron “1” can be expressed in the form (see, e.g., Ref. 66)

$$\begin{aligned} \mathcal{H}_{\text{int}}(0, 1) = & -\frac{Z_0 e^2}{|\mathbf{r}_1 - \mathbf{r}_0|} + \frac{Z_0 e^2}{2\pi^2} \int \mathbf{d}\mathbf{q} \frac{\tilde{\alpha}_0 \cdot \tilde{\alpha} - (\tilde{\alpha}_0 \cdot \hat{\mathbf{q}})(\tilde{\alpha} \cdot \hat{\mathbf{q}})}{q^2 - (W/\hbar c)^2} \\ & \times \exp[i\mathbf{q} \cdot (\mathbf{r}_1 - \mathbf{r}_0)], \end{aligned} \quad (29)$$

where $Z_0 e$ is the charge of the projectile ($Z_0 = -1$ for electrons, $+1$ for positrons), $\tilde{\alpha}_0$ and $\tilde{\alpha}$ are the Dirac matrices, and \mathbf{r}_0 and \mathbf{r} are the position coordinates for the projectile and the target electron, respectively. W is the energy exchanged in the course of the interaction, and $\hat{\mathbf{q}}$ is the unit vector in the direction of \mathbf{q} . The first term on the right-hand side of Eq. (29) is the instantaneous Coulomb interaction. The second term accounts for the exchange of virtual photons in the lowest nonvanishing perturbation order, and is usually referred to as the transverse interaction. Because $c\tilde{\alpha}$ is the velocity operator in Dirac's theory, the contribution from each $\tilde{\alpha}$ factor is of the order of v/c , where v is the speed of the particle. Hence, the effect of the transverse interaction is expected to be appreciable only for projectiles with relativistic speeds.

We consider collisions of a projectile electron or positron with linear momentum $\mathbf{p} = \hbar\mathbf{k}$ and kinetic energy E that lead to ionization of the subshell $n\ell j$ of the target atom. After the collision, the energy and momentum of the projectile are $E' = E - W$ and $\mathbf{p}' = \mathbf{p} - \hbar\mathbf{q}$, where W and $\hbar\mathbf{q}$ are the energy loss and the momentum transfer, respectively. The interaction of the projectile with the target atom is described by the Hamiltonian

$$\mathcal{H}' = Z_0 e \varphi_{\text{nuc}}(r_0) + \sum_{I=1}^Z \mathcal{H}_{\text{int}}(0, I), \quad (30)$$

where $\varphi_{\text{nuc}}(r_0)$ is the electrostatic potential of the nucleus, and the summation runs over the atomic electrons ($I = 1, \dots, Z$). With atomic states represented as single Slater determinants, by virtue of the Slater-Condon rules,⁶⁷ the interaction (30) can only induce transitions of the target atom to excited states that differ from the initial (ground) state by a single orbital. That is, in each ionizing collision an atomic electron jumps from one of the bound orbitals $\psi_{n\kappa m}$ of the active subshell $n\ell j$ to a free orbital $\psi_{E_f \kappa_f m_f}$ with kinetic energy $E_f = W - E_i$. With these assumptions, a first-order-perturbation calculation leads to the same formulae as for the ionization of a single electron bound in the DHFS potential. This one-active-electron approximation is the basis of the usual plane-wave and distorted-wave Born approximations; it is also implicitly assumed in the semiclassical models described in Sec. 2.1.

2.2.2. Plane-wave Born approximation (PWBA)

The PWBA assumes that the initial and final states of the projectile electron can be represented by Dirac plane waves, that is, by solutions of the Dirac equation for a free particle [with $V(r) = 0$],

$$[c\tilde{\alpha} \cdot \mathbf{p} + (\tilde{\beta} - 1)m_e c^2]\phi_{\mathbf{k}m_S}(\mathbf{r}) = \epsilon\phi_{\mathbf{k}m_S}(\mathbf{r}). \quad (31)$$

where m_S is the spin quantum number and $\mathbf{k} = \mathbf{p}/\hbar$ is the wave vector. The plane waves have the form

$$\phi_{\mathbf{k}m_S}(\mathbf{r}) = (2\pi)^{-3/2} \exp(i\mathbf{k} \cdot \mathbf{r}) U_{m_S}, \quad (32)$$

where U_{m_S} is a double spinor whose upper component is the unit spinor χ_{m_S} .

The differential cross section for ionization of a closed subshell $n\ell j$ is obtained by treating the interaction (30) as a perturbation to first order, as described by Bote and Salvat.³⁰ The final state of the active electron is represented by a distorted plane wave, i.e., an exact solution of the Dirac equation for the DHFS potential that asymptotically behaves as a plane wave plus an incoming spherical wave. Distorted waves are expanded in terms of spherical waves so that the differential cross section is given by a series that involves only transition matrix elements of the form

$$T_{fi} = \langle \phi_{\mathbf{k}'m'_S}(\mathbf{r}_0) \psi_{E_f \kappa_f m_f}(\mathbf{r}_1) | \mathcal{H}_{\text{int}}(0, 1) | \phi_{\mathbf{k}m_S}(\mathbf{r}_0) \psi_{n\kappa m}(\mathbf{r}_1) \rangle, \quad (33)$$

where the indexes 0 and 1 denote the projectile electron and the active target electron, respectively. The labels n , κ , m , and E_f , κ_f , m_f identify, respectively, the initial and final orbitals of the active electron, whose kinetic energy after the collision is $E_f = -E_i + W$. The calculation of the matrix elements (33) is relatively easy because integration over the position \mathbf{r}_0 of the projectile can be performed analytically, giving a delta function $\delta(\mathbf{k} - \mathbf{k}' - \mathbf{q})$. This situation implies that the variable \mathbf{q} in the integral (29) can be interpreted as the momentum transfer in units of \hbar .

After appropriate sums and averages over spins and magnetic quantum numbers, and integration over the final direction

of the emerging target electron, the doubly differential cross section (DDCS) becomes a function of the energy loss W and the polar scattering angle θ of the projectile. Following Fano,⁶⁶ we introduce the recoil energy Q , defined by

$$Q(Q + 2m_e c^2) = (c\hbar q)^2 = c^2 \hbar^2 (k^2 + k'^2 - 2kk' \cos \theta), \quad (34)$$

where $\hbar q$ is the momentum transfer. Notice that Q is the kinetic energy of a free electron that moves with momentum $\hbar q$. In the case of binary collisions of the projectile with free electrons at rest, we have $Q = W$ because the energy lost by the projectile is equal to the kinetic energy of the recoiling target electron. The DDCS for ionization of a subshell $n\ell j$ takes a simpler and more convenient form when it is considered as a function of the recoil energy instead of the scattering angle θ . We have,³⁰

$$\begin{aligned} \frac{d\sigma_i^{(PW)}}{dW dQ} &= \frac{2\pi Z_0^2 e^4}{m_e v^2} \left[\frac{2m_e c^2}{WQ(Q + 2m_e c^2)} \right. \\ &\times \left\{ \frac{(2E - W + 2m_e c^2)^2 - Q(Q + 2m_e c^2)}{4(E + m_e c^2)^2} \right\} \frac{df_i(Q, W)}{dW} \\ &+ \frac{2m_e c^2 W}{[Q(Q + 2m_e c^2) - W^2]^2} \\ &\times \left. \left(\beta^2 \sin^2 \theta_r + \left\{ \frac{Q(Q + 2m_e c^2) - W^2}{2(E + m_e c^2)^2} \right\} \right) \frac{dg_i(Q, W)}{dW} \right], \quad (35) \end{aligned}$$

where θ_r is the angle between the vectors \mathbf{p} and \mathbf{q} (the recoil angle) that is given by

$$\begin{aligned} \cos \theta_r &= \frac{p^2 - p'^2 + (\hbar q)^2}{2pq} \\ &= \frac{E(E + 2m_e c^2) - (E - W)(E - W + 2m_e c^2) + Q(Q + 2m_e c^2)}{2\sqrt{E(E + 2m_e c^2)} Q(Q + 2m_e c^2)}. \quad (36) \end{aligned}$$

The functions df_i/dW and dg_i/dW are the longitudinal and transverse generalized oscillator strengths (GOS and TGOS), respectively. They are defined by the following series

$$\begin{aligned} \frac{df_i(Q, W)}{dW} &\equiv \frac{W2(Q + m_e c^2)}{Q(Q + 2m_e c^2)} \frac{k_f}{(W - E_i)\pi} \\ &\times \sum_m \sum_{\kappa_f, m_f} |\langle \psi_{E_f \kappa_f m_f} | \exp(\mathbf{i}\mathbf{q} \cdot \mathbf{r}) | \psi_{n\kappa m} \rangle|^2, \quad (37) \end{aligned}$$

and

$$\begin{aligned} \frac{dg_i(Q, W)}{dW} &\equiv \frac{2(Q + m_e c^2)}{W} \frac{k_f}{(W - E_i)\pi} \\ &\times \sum_m \sum_{\kappa_f, m_f} |\langle \psi_{E_f \kappa_f m_f} | \tilde{\alpha}_x \exp(\mathbf{i}\mathbf{q} \cdot \mathbf{r}) | \psi_{n\kappa m} \rangle|^2, \quad (38) \end{aligned}$$

where m is the magnetic quantum number of the initial orbital of the active electron, and κ_f and m_f are, respectively, the

relativistic angular momentum quantum number and the magnetic quantum number of the final orbital. The quantity k_f is the wavenumber of the active electron after the collision, corresponding to the kinetic energy $E_f = W - E_i$. Because of the spherical symmetry of closed subshells, both the GOS and the TGOS are functions only of the energy loss W and the recoil energy Q , i.e., they depend only on the magnitude q of the momentum transfer.

The angular parts of the integrals in Eqs. (37) and (38) can be evaluated analytically using elementary angular-momentum algebra, and the GOS and TGOS can be expressed as converging infinite series of radial integrals that are suited for numerical evaluation. We have

$$\begin{aligned} \frac{df_i(Q, W)}{dW} &= \frac{W}{Q} \frac{2(Q + m_e c^2)}{Q + 2m_e c^2} \frac{k_f}{(W - E_i)\pi} \\ &\times \sum_{\kappa_f} \sum_{L=0}^{\infty} (2L + 1) \langle \ell_{\frac{1}{2}}^L j | \mathbf{C}^{(L)} | \ell_{\frac{1}{2}}^L j \rangle^2 [R_{E_f \kappa_f; n\kappa}^L(q)]^2, \quad (39) \end{aligned}$$

with the radial integrals

$$R_{E_f \kappa_f; n\kappa}^L(q) = \int_0^{\infty} [P_{E_f \kappa_f}(r) P_{n\kappa}(r) + Q_{E_f \kappa_f}(r) Q_{n\kappa}(r)] j_L(qr) dr, \quad (40)$$

where $P_{n\kappa}(r)$ and $Q_{n\kappa}(r)$ are the large- and small-component radial Dirac functions of the initial orbital, $P_{E_f \kappa_f}(r)$ and $Q_{E_f \kappa_f}(r)$ are the corresponding radial functions of the final orbital, and $j_L(x)$ are spherical Bessel functions. The quantities

$$\langle \ell_{\frac{1}{2}}^L j | \mathbf{C}^{(L)} | \ell_{\frac{1}{2}}^L j \rangle = \frac{1}{2} [1 + (-1)^{L+\ell_f}] \sqrt{2j_f + 1} \langle L j_f 0_{\frac{1}{2}}^L | j_{\frac{1}{2}}^L \rangle \quad (41)$$

are reduced matrix elements of the Racah tensors (see, e.g., Ref. 68). Similarly, the transverse generalized oscillator strength (TGOS), Eq. (38), can be expressed as

$$\begin{aligned} \frac{dg_i(Q, W)}{dW} &= \frac{2(Q + m_e c^2)}{W} \frac{k_f}{(W - E_i)\pi} \\ &\times \sum_{\kappa_f} \sum_{L=0}^{\infty} \frac{2L + 1}{2L(L + 1)} \\ &\times \{ \langle \ell_{\frac{1}{2}}^L j | \mathbf{C}^{(L)} | \ell_{\frac{1}{2}}^L j \rangle^2 [{}^e \mathcal{R}_{E_f \kappa_f; n\kappa}^L(q)]^2 \\ &+ \langle \bar{\ell}_{\frac{1}{2}}^L j | \mathbf{C}^{(L)} | \ell_{\frac{1}{2}}^L j \rangle^2 [{}^m \mathcal{R}_{E_f \kappa_f; n\kappa}^L(q)]^2 \}, \quad (42) \end{aligned}$$

with the radial integrals

$$\begin{aligned} {}^e \mathcal{R}_{E_f \kappa_f; n\kappa}^L(q) &= \frac{L(L + 1)}{2L + 1} \left[-\frac{\kappa_f \kappa}{L} (F_{E_f \kappa_f; n\kappa}^{L-1} + G_{E_f \kappa_f; n\kappa}^{L-1}) \right. \\ &+ (F_{E_f \kappa_f; n\kappa}^{L-1} - G_{E_f \kappa_f; n\kappa}^{L-1}) \\ &+ \frac{\kappa_f - \kappa}{L + 1} (F_{E_f \kappa_f; n\kappa}^{L+1} + G_{E_f \kappa_f; n\kappa}^{L+1}) \\ &\left. + (F_{E_f \kappa_f; n\kappa}^{L+1} - G_{E_f \kappa_f; n\kappa}^{L+1}) \right] \quad (43a) \end{aligned}$$

and

$${}^m\mathcal{R}_{E_f\kappa_f;n\kappa}^L(q) = (\kappa_f + \kappa) (F_{E_f\kappa_f;n\kappa}^L + G_{E_f\kappa_f;n\kappa}^L), \quad (43b)$$

where

$$F_{E_f\kappa_f;n\kappa}^L = \int_0^\infty P_{E_f\kappa_f}(r) Q_{n\kappa}(r) j_L(qr) dr, \quad (44)$$

$$G_{E_f\kappa_f;n\kappa}^L = \int_0^\infty Q_{E_f\kappa_f}(r) P_{n\kappa}(r) j_L(qr) dr.$$

The quantity $\bar{\ell}$ in Eq. (42) is the value of the orbital angular momentum corresponding to $-\kappa$, i.e., $\bar{\ell} = \ell - \kappa/|\kappa|$.

Bote and Salvat³⁰ calculated the GOS and the TGOS for all subshells of neutral atoms from hydrogen ($Z = 1$) to einsteinium ($Z = 99$) in their ground-state configurations. A plot of the GOS as a function of W and Q is known as the Bethe surface. Figures 1 and 2 display the Bethe surfaces for ionization of hydrogen and for ionization of the M_3 subshell of gold. A conspicuous feature of the GOS and the TGOS is the peak that develops over the line $Q = W$ at large W , which is known as the Bethe ridge.⁶⁹ The occurrence of this peak shows that, for energy transfers W much larger than the ionization energy, the target electrons react as if they were free. Note that, for a target electron at rest, the Bethe surface reduces to the delta function $\delta(W - Q)$, i.e., to a zero-width Bethe ridge. The Bethe ridge of inner-shells is quite broad;^b its width is a measure of the momentum distribution of the target electrons.

In the limit $Q \rightarrow 0$, both the GOS and the TGOS reduce to the optical oscillator strength (OOS),

$$\frac{df_i(W)}{dW} \equiv \lim_{Q \rightarrow 0} \frac{df_i(W, Q)}{dW} = \lim_{Q \rightarrow 0} \frac{dg_i(W, Q)}{dW}, \quad (45)$$

which can be expressed as

$$\frac{df_i(W)}{dW} = \frac{W2m_e}{3\hbar^2} \frac{k_f}{(W - E_i)\pi} \times \sum_{\kappa_f} \langle \ell_{\frac{1}{2}} j || \mathbf{C}^{(\lambda)} || \ell_f \frac{1}{2} j_f \rangle^2 [D_{E_f\kappa_f;n\kappa}]^2, \quad (46)$$

where

$$D_{E_f\kappa_f;n\kappa} = \int_0^\infty [P_{E_f\kappa_f}(r) P_{n\kappa}(r) + Q_{E_f\kappa_f}(r) Q_{n\kappa}(r)] r dr. \quad (47)$$

These radial integrals are easier to compute than those in the expressions of the GOS and the TGOS for finite Q . The OOS is proportional to the cross section $\sigma_{\text{ph},i}^{\text{dipole}}$ for the photoelectric absorption of photons of energy W calculated within the dipole approximation,

$$\frac{df_i(W)}{dW} = \frac{m_e c}{2\pi e^2 \hbar} \sigma_{\text{ph},i}^{\text{dipole}}(W). \quad (48)$$

The total cross section for ionization of the active subshell is obtained by integrating the DDCS over the kinematically allowed domain of the Q - W plane. We have

$$\sigma_i^{\text{(PW)}} = \int_{E_i}^E dW \int_{Q_-}^{Q_+} dQ \frac{d\sigma_i^{\text{(PW)}}}{dW dQ}, \quad (49)$$

where Q_- and Q_+ are the lower and upper limits of the allowed interval of recoil energies, respectively. These limits are the roots of Eq. (34) with $\cos \theta = 1$ and -1 , respectively. We have

$$Q_{\pm} = \sqrt{[\sqrt{E(E + 2m_e c^2)} \pm \sqrt{(E - W)(E - W + 2m_e c^2)}]^2 + m_e^2 c^4} - m_e c^2. \quad (50)$$

Cross sections for ionization of the K, L, and M shells of neutral atoms ($Z = 1$ to 99) have been calculated numerically from the GOS and TGOS tables of Bote and Salvat.³⁰ Scofield¹⁴ reported equivalent calculations for ionization of the K shell and the L subshells for a set of nine elements with atomic numbers covering the interval from $Z = 18$ to $Z = 92$. Our results agree closely with Scofield's data. Differences are appreciable only for near-threshold energies and very likely arise from variations in the adopted interpolation methods.

The so-called optical-data models (see, e.g., Ref. 70, and references therein) build approximate GOSs from knowledge of measured or calculated cross sections for the photoelectric effect. The basic assumption is that the equality (48) holds also when $\sigma_{\text{ph},i}^{\text{dipole}}(W)$ is replaced by the actual cross section for photoabsorption,

$$\frac{df_i(W)}{dW} = \frac{m_e c}{2\pi e^2 \hbar} \sigma_{\text{ph},i}(W). \quad (51)$$

An optical-data model combines a "measured" OOS, obtained from photoabsorption cross sections and optical dielectric functions, with an extension algorithm that generates the GOS for arbitrary recoil energies. Thus, cross sections for ionization by charged particles are obtained from information on photon absorption. Optical-model calculations have been described by Fernández-Varea *et al.*⁷⁰ The Weizsäcker-Williams method of virtual quanta,^{17,18} used by Kolbenstvedt^{19,20} (see also Ref. 71) and by Seltzer²¹ to calculate cross sections for inner-shell ionization by electron impact, can also be considered as an optical-data model.²²

Bethe³ obtained an asymptotic analytical formula (valid at sufficiently high energies) for the ionization cross section of hydrogen by nonrelativistic charged projectiles. Fano⁷² derived the relativistic version of the formula that is applicable to ionization of any subshell:

$$\sigma_i^{(B)} \simeq \frac{2\pi Z_0^2 e^4}{m_e v^2} \left\{ M_i^2 \left[\ln \left(\frac{\beta^2}{1 - \beta^2} \right) - \beta^2 \right] + C_i \right\}, \quad (52)$$

where $\beta = v/c$, and

$$M_i^2 = \int_{E_i}^\infty \frac{dW}{W} \frac{df_i(W)}{dW} \quad (53)$$

^bThe Bethe ridges in Figs. 1 and 2 appear fairly narrow because the scales of the W and Q axes are logarithmic.

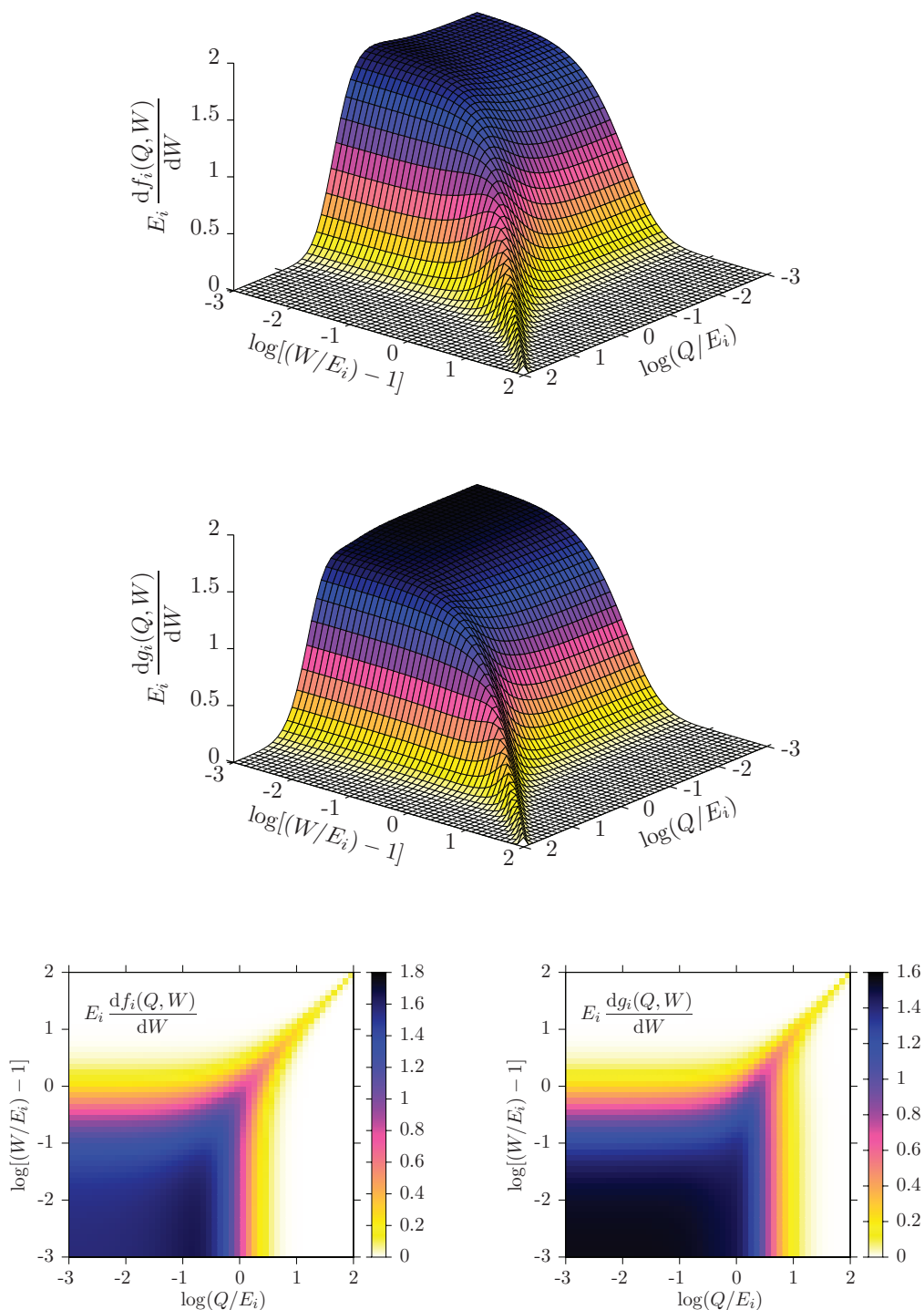


FIG. 1. The GOS (top) and the TGOS (middle) for ionization of the K shell ($1s_{1/2}$) of the hydrogen atom ($Z=1$), represented as Bethe three-dimensional surfaces (top and middle) and as color-level diagrams (bottom). The scales of the Q and W axes are logarithmic (base 10).

is the total dipole-matrix element squared⁶⁹ for ionizing collisions (with $W \geq E_i$) and C_i , another characteristic constant, is given by an integral of the GOS. In fact, the Bethe formula, Eq. (52), gives the leading term of an exact expansion of σ_i in powers of E^{-1} (see, e.g., Ref. 69). That is, for energies sufficiently large, so that the PWBA is adequate, we can write

$$\sigma_i^{(B)} \simeq \frac{2\pi Z_0^2 e^4}{m_e v^2} \left\{ M_i^2 \left[\ln \left(\frac{\beta^2}{1-\beta^2} \right) - \beta^2 \right] + C_i + \frac{\gamma_i}{E} + \frac{\delta_i}{E^2} + \dots \right\}, \quad (54)$$

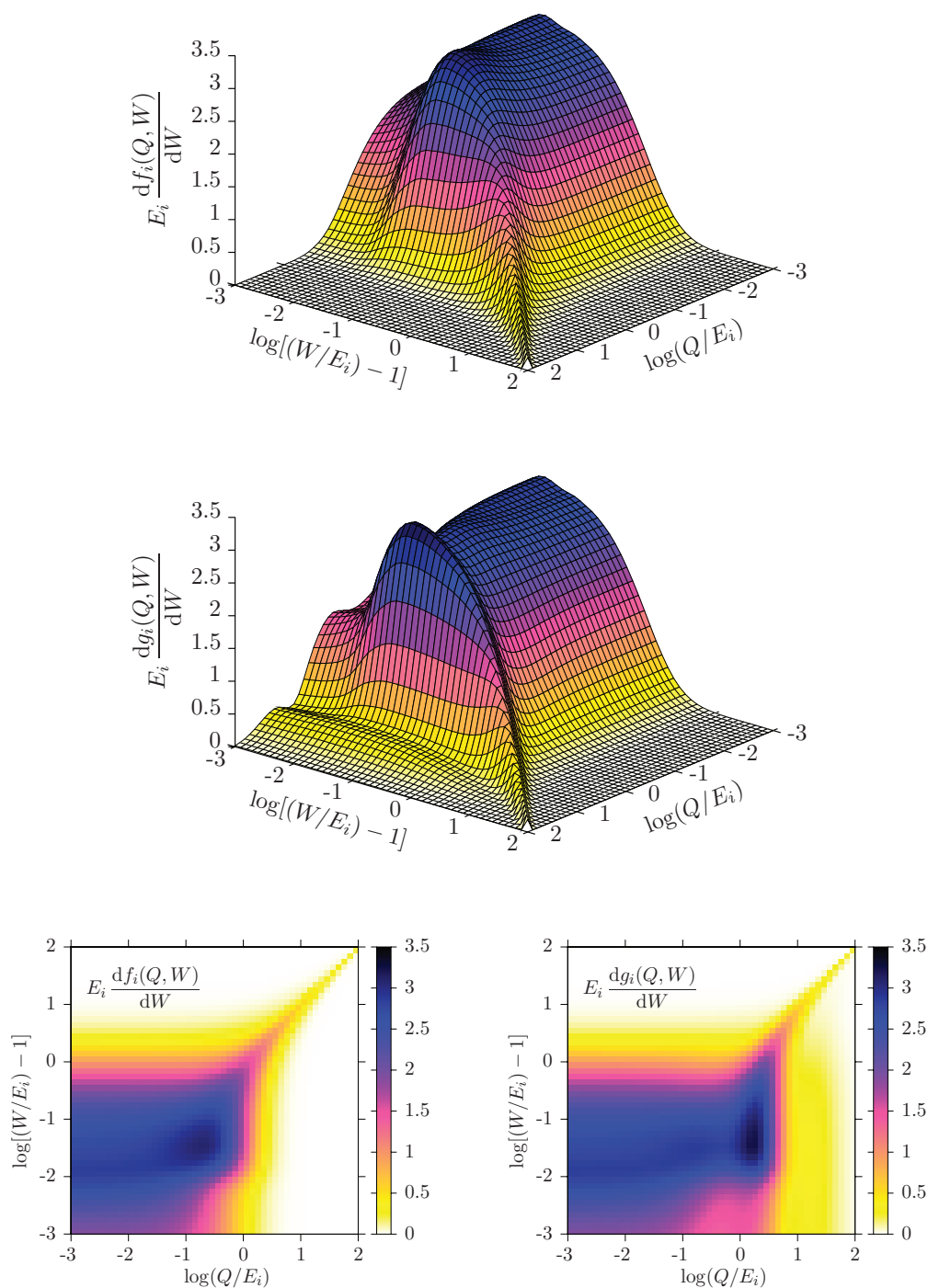


FIG. 2. The GOS (top) and the TGOS (middle) for ionization of the M_3 subshell ($3p_{3/2}$) of the gold atom ($Z = 79$), represented as Bethe three-dimensional surfaces (top and middle) and as color-level diagrams (bottom).

where the terms $\gamma_i/e + \delta_i/E^2 + \dots$ correspond to the so-called shell correction (i.e., the difference between the “exact” cross section obtained from the PWBA and the asymptotic Bethe formula).

As noted by Fano,⁷² a plot of the quantity $\sigma_i \beta^2 (m_e c^2 / 2\pi Z_0^2 e^4)$ as a function of the quantity $\ln[\beta^2 / (1 - \beta^2)] - \beta^2$ is a straight line with slope M_i^2 and ordinate intercept C_i in the energy range where the Bethe formula is valid, as discussed further in Sec. 3.1. This “Fano plot” has been used to assess the validity of the

PWBA at high energies and as a consistency check of experimental data (see, e.g., Refs. 2, 7, and 69). We also note that the nonrelativistic version of Eq. (52) [given as Eq. (68) below] forms the basis of a number of simple semiempirical formulae (see Sec. 3.2).

It is worth mentioning that the PWBA as formulated here disregards electron exchange effects that can be approximately accounted for using Ochkur’s correction.⁵⁵ However, DWBA calculations show that the correction of the total cross section

for exchange effects decreases when the kinetic energy of the projectile increases, becoming practically negligible at the energies where the PWBA is applicable.

2.2.3. Distorted-wave Born approximation

The PWBA yields reliable ionization cross sections for projectile electrons with kinetic energies larger than about 30 times the ionization energy E_i of the active subshell.³⁰ At lower projectile energies, the approximation worsens progressively, partly because the interaction (30) becomes too strong to be described as a first-order perturbation. In principle, one could improve the theory by considering the perturbation \mathcal{H}' to second order. However, the resulting theoretical expressions become too complicated for practical numerical evaluation. A more effective method is provided by the distorted-wave Born approximation (DWBA)²⁸ which consists in removing from the interaction a spherical potential $V_P(r_0)$ that depends only on the coordinates of the projectile. The “unperturbed” states of the projectile are then distorted plane waves of that potential, that is, solutions of the Dirac equation

$$[c\tilde{\alpha}\cdot\mathbf{p} + (\tilde{\beta} - 1)m_e c^2 + V_P(r_0)]\psi_{\mathbf{k}m_S}^{(\pm)}(\mathbf{r}_0) = E\psi_{\mathbf{k}m_S}^{(\pm)}(\mathbf{r}_0), \quad (55)$$

which asymptotically behave as plane waves plus outgoing (+) or incoming (−) spherical waves. The distorted plane waves are expanded in the basis of spherical waves, and radial wave functions are calculated to high precision (usually to eight or nine significant figures) by the RADIAL routines.⁵⁹ Thus, the distorting potential $V_P(r_0)$ is treated exactly. If this potential is selected appropriately, the remaining interaction $\mathcal{H}'' = \mathcal{H}' - V_P(r_0)$ is weaker than \mathcal{H}' , and a first-order perturbation calculation should yield better results.

The DWBA gives an expression of the differential cross section for ionization of a closed subshell that involves transition matrix elements of the form

$$T_{fi}^{(DW)} = \langle \psi_{\mathbf{k}'m'_S}^{(-)}(\mathbf{r}_0) \psi_{E_f \kappa_f m_f}(\mathbf{r}_1) | \mathcal{H}_{\text{int}}(0, 1) | \psi_{\mathbf{k}m_S}^{(+)}(\mathbf{r}_0) \psi_{n\kappa m}(\mathbf{r}_1) \rangle. \quad (56)$$

In the DWBA calculations of Segui *et al.*²⁸ and Bote and Salvat,³⁰ the interaction between the projectile and the active atomic electron was assumed to be purely Coulombian. That is, the effect of the transverse interaction was disregarded, and the operator in Eq. (29) was replaced by

$$\mathcal{H}_{\text{int}}^L(0, 1) = -\frac{Z_0 e^2}{|\mathbf{r}_1 - \mathbf{r}_0|}. \quad (57)$$

This simplification is acceptable for projectiles with velocities much smaller than c . With appropriate sums and averages over spins and magnetic quantum numbers, and integration over the final directions of the projectile and the emerging knocked-on electron, one obtains the following expression for the energy-

loss DCS:³⁰

$$\begin{aligned} \frac{d\sigma_i^{(DW,L)}}{dW} &= \frac{2Z_0^2 e^4}{\hbar v} \frac{(E - W + 2m_e c^2)(W - E_i + 2m_e c^2)}{c^4 \hbar^4 k^2 k' k_f} \\ &\times \frac{E + 2m_e c^2}{E + m_e c^2} \\ &\times \sum_{\kappa_f} \sum_{\kappa_1} \sum_{\kappa_2} \sum_L \frac{1}{2L + 1} (X_{E' \kappa_2; E_f \kappa_f; L}^{E \kappa_1; n \kappa})^2, \end{aligned} \quad (58)$$

where

$$X_{E' \kappa_2; E_f \kappa_f; L}^{E \kappa_1; n \kappa} \equiv \langle \ell_2 \frac{1}{2} j_2 | | \mathbf{C}^{(L)} | | \ell_f \frac{1}{2} j_f \rangle \langle \ell_1 \frac{1}{2} j_1 | | \mathbf{C}^{(L)} | | \ell_2 \frac{1}{2} j_2 \rangle R_{E' \kappa_2; E_f \kappa_f; L}^{E \kappa_1; n \kappa}, \quad (59)$$

and the quantities $R_{E' \kappa_2; E_f \kappa_f; L}^{E \kappa_1; n \kappa}$ are Slater integrals,

$$\begin{aligned} R_{E' \kappa_2; E_f \kappa_f; L}^{E \kappa_1; n \kappa} &= \int \int dr_0 dr \frac{r_{<}^L}{r_{>}^{L+1}} [P_{E \kappa_1}(r_0) P_{E' \kappa_2}(r_0) \\ &+ Q_{E \kappa_1}(r_0) Q_{E' \kappa_2}(r_0)] [P_{n \kappa}(r) P_{E_f \kappa_f}(r) \\ &+ Q_{n \kappa}(r) Q_{E_f \kappa_f}(r)]. \end{aligned} \quad (60)$$

Here κ_1 and κ_2 are angular momentum quantum numbers referring to the initial and final spherical orbitals of the projectile electron, and ℓ_1, j_1 and ℓ_2, j_2 are the corresponding orbital and total angular momentum quantum numbers. The quantities $r_{<}$ and $r_{>}$ are, respectively, the lesser and the greater of the radial distances r_0 and r .

Spherical orbitals of the projectile are calculated with the distorting potential $V_P(r)$ that we can choose freely. With $V_P \equiv 0$ (no distortion), the DWBA reduces to the PWBA. The effectiveness of the DWBA improves when the residual interaction, $\mathcal{H}'' = \mathcal{H}' - V_P(r_0)$, weakens. As discussed by Segui *et al.*,²⁸ a convenient choice is to take $V_P(r) = -Z_0 V^{\text{DHFS}}(r)$. Thus, for projectile positrons ($Z_0 = 1$), the distorting potential equals the DHFS potential with reversed sign. In this case, the total cross section for ionization,

$$\sigma_i^{(DW,L)} = \int_{E_i}^E \frac{d\sigma_i^{(DW,L)}}{dW} dW, \quad (61)$$

is found to agree reasonably with available experimental data.²⁸ For projectile electrons ($Z_0 = -1$), we set $V_P(r) = V^{\text{DHFS}}(r)$, i.e., the distorting potentials for electrons and positrons have opposite signs.

It is worth recalling that the PWBA gives the same cross sections for electrons and positrons because it assumes that the projectile wave functions are not affected by the atomic field. In reality, positrons are less effective for ionization than electrons because they are repelled by the electrostatic field of the atom, while electrons are attracted. The DWBA accounts for this difference in a natural way, and yields cross sections that are larger for electrons than for positrons, the differences being more prominent for near-threshold energies.²⁸

Electrons also differ from positrons in that a projectile electron is indistinguishable from the active target electron and, therefore, the projectile can undergo exchange scattering.

The description of exchange scattering is easy when the initial and final orbitals of the target and the projectile are mutually orthogonal; the problem is much more difficult when orthogonality is not guaranteed (see, e.g., Ref. 54). With the DHFS potential as distorting potential, the orbitals of the projectile and the active target electron are solutions of the same Dirac equation and, consequently, they are orthogonal. We can then account for exchange effects simply by antisymmetrizing the initial and final states in the transition matrix element. The exchange-corrected transition matrix elements read

$$T_{fi}^{(\text{DW,exc})} = \langle \psi_{\mathbf{k}'m'_s}^{(-)}(\mathbf{r}_0) \psi_{E_f \kappa_f m_f}(\mathbf{r}_1) | \mathcal{H}_{\text{int}}(0, 1) | \psi_{\mathbf{k}m_s}^{(+)}(\mathbf{r}_0) \psi_{n\kappa m}(\mathbf{r}_1) \rangle \\ - \langle \psi_{\mathbf{k}'m'_s}^{(-)}(\mathbf{r}_1) \psi_{E_f \kappa_f m_f}(\mathbf{r}_0) | \mathcal{H}_{\text{int}}(0, 1) | \psi_{\mathbf{k}m_s}^{(+)}(\mathbf{r}_0) \psi_{n\kappa m}(\mathbf{r}_1) \rangle. \quad (62)$$

The corresponding energy-loss DCS for electrons, calculated by considering only the longitudinal interaction, is

$$\frac{d\sigma_i^{\text{DW,L,e}}}{dW} = \frac{2e^4}{\hbar v} \frac{(E - W + 2m_e c^2)(W - E_i + 2m_e c^2)}{c^4 \hbar^4 k^2 k' k_f} \frac{E + 2m_e c^2}{E + m_e c^2} \\ \times \sum_{\kappa_1} \sum_{\kappa_2} \sum_{\kappa_f} \left[\sum_L \frac{1}{2L+1} (X_{E' \kappa_2; E_f \kappa_f; L}^{E \kappa_1; n\kappa})^2 \right. \\ \left. + \sum_{L'} \frac{1}{2L'+1} (X_{E_f \kappa_f; E' \kappa_2; L'}^{E \kappa_1; n\kappa})^2 \right. \\ \left. - 2 \sum_L \sum_{L'} (-1)^{L+L'+1} \begin{Bmatrix} j & j_f & L \\ j_1 & j_2 & L' \end{Bmatrix} X_{E' \kappa_2; E_f \kappa_f; L}^{E \kappa_1; n\kappa} X_{E_f \kappa_f; E' \kappa_2; L'}^{E \kappa_1; n\kappa} \right]. \quad (63)$$

where $\{ : : \}$ denote Wigner's 6j symbols.⁷³ The coefficient $X_{E_f \kappa_f; E_2 \kappa_2; L}^{E \kappa_1; n\kappa}$ is obtained from expression (59) by the interchange $E' \kappa_2 \leftrightarrow E_f \kappa_f$ ($E - W \leftrightarrow W - E_i$). The first and second terms in the square brackets correspond to direct and exchange transitions, respectively. The third term results from the interference between the direct and exchange scattered waves. Details on the numerical calculation of the energy-loss DCSs given by Eqs. (58) and (63) can be found in the article of Segui *et al.*²⁸ After the collision, we have two indistinguishable electrons with kinetic energies $E - W$ and $W - E_i$. The maximum energy loss of the "primary" electron (the one with the higher energy) is $W_{\text{max}} = (E + E_i)/2$. Hence, the total cross section for ionization of the closed subshell is

$$\sigma_i^{\text{DW,L,e}} = \int_{E_i}^{(E+E_i)/2} \frac{d\sigma_i^{\text{DW,L,e}}}{dW} dW. \quad (64)$$

2.2.4. Corrected plane-wave Born approximation

Numerical calculations of σ_i based on the semirelativistic DWBA (i.e., with the transverse interaction neglected) are feasible only for projectiles with kinetic energies up to about 25 times the ionization energy of the active shell. This

approximation accounts for the distortion of the projectile wave functions by the field of the atom and, in the case of projectile electrons, also for exchange effects. On the other hand, the relativistic PWBA allows the calculation of ionization cross sections for arbitrary energies, including the effect of the transverse interaction, which is neglected in our DWBA.

In the energy interval where DWBA calculations are feasible, one can compare ionization cross sections obtained from both approximations considering only the longitudinal interaction, Eq. (57). The difference between these cross sections, $\Delta\sigma_i = \sigma_i^{(\text{DW,L})} - \sigma_i^{(\text{PW,L})}$, gives the distortion and exchange corrections to the PWBA. However, this quantity can be evaluated numerically only for projectiles with kinetic energies less than about about $25E_i$. Bote and Salvat³⁰ proposed a "corrected" PWBA, in which the cross section for ionization is obtained as

$$\sigma_i = \begin{cases} \sigma_i^{(\text{PW})} + \Delta\sigma_i & \text{if } E \leq 16E_i, \\ \frac{E}{E + bE_i} \sigma_i^{(\text{PW})} & \text{if } E > 16E_i. \end{cases} \quad (65)$$

The correction $\Delta\sigma_i$ is applied only for energies E less than $16E_i$, where it can be effectively computed, and the scaling parameter b is determined by requiring continuity at $E = 16E_i$. This corrected PWBA has been employed to calculate an extensive database of cross sections for ionization of the K, L, and M subshells of all elements from hydrogen ($Z = 1$) to einsteinium ($Z = 99$) by impact of electrons and positrons with kinetic energies from threshold up to 1 GeV. For energies less than $\sim 30E_i$, the cross section (65) improves the semirelativistic DWBA by including the contribution of the transverse interaction. At higher energies, σ_i smoothly tends to the cross section given by the PWBA which yields reliable results for $E \gtrsim 30E_i$. Hence, the recipe (65) is expected to give results nearly equivalent to those that would be obtained from the DWBA with the full interaction (29). This approach for calculating cross sections for inner-shell ionization by electron impact is believed to be the most reliable method currently available for obtaining these cross sections for any atom.

We will present the analytical formulae of Bote *et al.*³¹ in Sec. 3.6 that are based on Eq. (65). These formulae enable K-, L-, and M-shell ionization cross sections to be readily computed for all atoms from hydrogen to einsteinium. We will evaluate these cross sections in Sec. 7 by making comparisons with measured cross sections for a wide range of atomic numbers and incident electron energies.

2.3. Applicability of atomic calculations to molecules and solids

We have described calculations of inner-shell ionization cross sections for free atoms in this section. While some measurements of these cross sections have been made for free atoms such as the rare gases, many more measurements have been made for diatomic molecules (such as H_2 , N_2 , O_2 , and Cl_2) and elemental solids. We therefore now comment on the

applicability of the atomic calculations to solids and to molecules. X-ray absorption cross sections involving excitation or ionization of inner-shell electrons are very similar for atoms and the corresponding molecules and solids.⁷⁴ However, differences can occur in the threshold energies (as discussed in the Appendix) as well as in the near-edge x-ray absorption fine structure and in the extended x-ray absorption fine structure. Total cross sections for ionization of a particular shell by electron impact involve the integration of the differential cross section (with respect to energy loss) over energy loss. If the incident electron energy is sufficiently high, these differential ionization cross sections correspond closely to the corresponding x-ray absorption cross sections. It is therefore reasonable to expect that total ionization cross sections will be at least approximately similar to those for the corresponding atoms.

Nevertheless, differences between total ionization cross sections for atoms, molecules, and solids are more likely as the incident electron energy becomes closer to the threshold energy for ionization. At near-threshold energies, the final states for ionization of an inner-shell electron from atoms, molecules, and solids will generally be different than for higher incident energies. In addition, there will be different so-called final-state effects in atoms, molecules, and solids. For atoms and molecules, there can be post-collisional ionization effects at near-threshold energies involving Coulomb interactions between the three final particles (an ion and two slow electrons). For solids, the inner-shell vacancy will be at least partially screened by movement of valence electrons. The dynamics of these complex processes in atoms, molecules, and solids are beyond the scope of this review. Instead, we will examine in Sec. 7 the extent to which differences between measured and calculated inner-shell ionization cross sections depend on the overvoltage, U (that is, the ratio of the incident energy to the threshold energy for ionization). Significant increases of these deviations with decreasing U could then indicate differences between measured cross sections for molecules and solids and the corresponding calculated cross sections for atoms and/or the existence of final-state effects that have not been included in the present atomic calculations.

We also note here that ionization of an inner-shell electron by electron impact can lead to excitation and ionization of valence electrons (sometimes referred to as shake-up and shake-off processes, respectively). Subsequent decay of the inner-shell vacancy by emission of x rays or Auger electrons will lead to both “diagram” and “satellite” features in measured x-ray or Auger-electron spectra (as mentioned in Sec. 4). Fortunately, for many cross-section measurements, the diagram and satellite lines may not be resolved. Nevertheless, it is expected that the fraction of x-ray or Auger-electron emission in satellite lines will change for incident energies close to threshold.

3. Analytical Formulae for Inner-Shell Ionization Cross Sections

Because theoretical calculations of cross sections for impact ionization face considerable numerical difficulties, systematic

tabulations of σ_i have become available only in recent years. This lack of reliable theoretical information, combined with the scarcity of available experimental data, has stimulated the proliferation of approximate analytical formulae that were derived from simple theoretical models or high-energy approximations. Simple analytical formulae were also important for estimating ionization cross sections before the widespread availability of laboratory and personal computers. Semiempirical formulae have also been developed from the, always limited, experimental information available. Although many of these formulae have served a useful function (typically soon after they were developed), potential users should be aware that semiempirical formulae may not be valid beyond the range of conditions for which they were initially developed. The apparent success of a particular formula in one application (e.g., for a particular material over a limited range of projectile energies) should not necessarily suggest that the same formula is valid for different materials and conditions.

3.1. The Bethe formula

A simple and useful means of analyzing measured or calculated cross-section data for ionization of a given shell is provided by the Bethe asymptotic formula, Eq. (52). However, it should be borne in mind that the formula is asymptotic, i.e., it gives the first term of an expansion in inverse powers of E of the cross section evaluated within the PWBA. Hence, deviations of experimental data from the Bethe formula do not necessarily imply that the PWBA is not valid.

For practical purposes, it is convenient to express Eq. (52) in the form

$$\sigma_i^{(B)} = \frac{2\pi e^4}{m_e v^2} (2j+1) \frac{b_i}{E_i} \left\{ \left[\ln \left(\frac{\beta^2}{1-\beta^2} \right) - \beta^2 \right] + \ln \left(\frac{c_i m_e c^2}{2E_i} \right) \right\}, \quad (66)$$

where

$$b_i = \frac{E_i M_i^2}{2j+1} \quad \text{and} \quad \ln \left(\frac{c_i m_e c^2}{2E_i} \right) = \frac{C_i}{M_i^2}. \quad (67)$$

The coefficients b_i and c_i are generally referred to as the Bethe parameters and, as indicated above, they are defined as integrals involving the GOS.⁷² Approximate calculations for inner shells using hydrogenic models give values of b_i between 0.2 and 0.6, and the value of c_i was estimated by Bethe to be ~ 4 . Since most of the published analyses using the Bethe formula involved electrons with nonrelativistic energies, it is pertinent to consider the nonrelativistic version of this formula, which is obtained by letting c tend to infinity. Noting that, in the nonrelativistic limit, $m_e v^2/2 = E$ and the expression in square brackets becomes $\ln(2E/m_e c^2)$, we have

$$\sigma_i^{(B,nr)} \simeq \frac{\pi e^4}{E} (2j+1) \frac{b_i}{E_i} \ln \left(\frac{c_i E}{E_i} \right). \quad (68)$$

This formula should not be applied to electrons with energies E higher than about 50 keV.

The Bethe formulae can be used in various ways for analyzing measured or calculated cross-section data for ionization of a given subshell. For such purposes, it is convenient to write the formulae as follows:

$$\sigma_i^{(B)} E_i \beta^2 = \frac{2\pi e^4}{m_e c^2} (2j+1) b_i \left\{ \left[\ln \left(\frac{\beta^2}{1-\beta^2} \right) - \beta^2 \right] + \ln \left(\frac{m_e c^2}{2E_i} \right) + \ln c_i \right\}, \quad (69)$$

and

$$\sigma_i^{(B,mr)} E_i^2 U = \pi e^4 (2j+1) b_i \ln(c_i U) \\ = 6.514 \times 10^{-14} (2j+1) b_i \ln(c_i U) \text{ cm}^2 \text{ eV}^2, \quad (70)$$

where $U = E/E_i$ is the overvoltage.

A valuable form of data analysis is to prepare Fano plots^{2,69,72} in which either $\sigma_i E_i^2 U$ is plotted versus $\ln U$, as suggested by Eq. (70) for the nonrelativistic Bethe formula, or $\sigma_i E_i \beta^2$ is plotted *versus* the quantity

$$X = \left[\ln \left(\frac{\beta^2}{1-\beta^2} \right) - \beta^2 \right] + \ln \left(\frac{m_e c^2}{2E_i} \right), \quad (71)$$

as suggested by Eq. (69) for the relativistic form of the Bethe formula. In the present work, we will present Fano plots displaying the quantity

$$Y_{\text{Fano}} \equiv \frac{\sigma_i E_i^2 U}{\pi e^4 (2j+1)} \frac{m_e c^2 \beta^2}{2E} \quad (72)$$

as a function of X . For sufficiently large overvoltages, where the Bethe formula is valid, the plot is linear, and

$$Y_{\text{Fano}} = b_i \{ \ln c_i + X \}. \quad (73)$$

The Bethe parameter b_i is the slope of the line $Y_{\text{Fano}}(X)$, and the parameter c_i is determined by the ordinate at $X=0$, $Y_{\text{Fano}}(0) = b_i \ln c_i$. In the nonrelativistic limit, $X \sim \ln(E/E_i) = \ln U$ and $m_e c^2 \beta^2 \sim 2E$, and the plot reduces to the familiar nonrelativistic form

$$\frac{\sigma_i E_i^2 U}{\pi e^4 (2j+1)} = b_i \{ \ln c_i + \ln U \}. \quad (74)$$

Figures 3 and 4 display Fano plots for the K shell and the L subshells of selected elements. For convenience, the plots for individual subshells include the energy scale (in keV) showing the correspondence between X and E values. Notice that the E scale is approximately logarithmic only for weakly bound subshells and nonrelativistic energies. The plots combine theoretical results obtained from the DWBA calculations of Bote and Salvat³⁰ and experimental data from different sources (specific references are given in Sec. 6). The Bethe parameters b_i and c_i were determined from a least-squares fit

made to the DWBA cross section in the high-energy region for each element. For comparison, these figures also display plots based on three of the analytical formulae described below for ionization cross sections, namely the Kolbenstvedt formula, Eq. (82) [which is applicable only to the K shell], the Gryzinski formula, Eq. (83), and the Casnati *et al.* formula, Eq. (84). It is seen that Fano plots based on the DWBA ionization cross sections are linear for X greater than about 4 or, equivalently, for overvoltages larger than about 50. That is, the Bethe formula is valid for energies E greater than about 50 times the ionization energy of the active subshell. At lower energies, shell corrections become appreciable, and the plot visibly departs from the asymptotic linear dependences found for $U > 50$.

We also see in Figs. 3 and 4 that the lines based on the Gryzinski formula do not have the same asymptotic slopes as indicated by the lines from the Bethe equation and the DWBA data. Some of the lines based on the Casnati *et al.* equation also depart from the asymptotic Bethe slopes.

The low-energy parts of the plots are displayed in separate diagrams on the right of Figs. 3 and 4. In the range $X \leq 4$, the curvature of the line $Y_{\text{Fano}}(X)$ varies with the atomic number. Indeed, for restricted energy intervals below $X \sim 4$, a linear fit would give an acceptable approximation to each plot; however, the fitted parameters would be different from the Bethe parameters b_i and c_i . It is seen that the slope of the low-energy linear region is greater than that of the asymptotic region. As a result, empirical values of b_i derived from the slope in the low-energy region are greater than would be expected from the corresponding optical oscillator strength.² The empirical values of c_i obtained from the low-energy region are similarly smaller than the corresponding values for the asymptotic region, and may become less than unity. That is, the Bethe formula may yield negative cross sections at near-threshold energies. Such negative cross sections are clearly nonphysical, and have been interpreted by some authors as an indication that the Bethe equation must be incorrect; in fact, it is the use of the Bethe equation in a range where it is not expected to be valid that is incorrect.

A global consistency check is to verify that a value of b_i derived from a Fano plot should agree (within experimental and numerical uncertainties) with the value obtained from integration of the dipole oscillator strength or of photoabsorption data.^{2,5,75} Early studies showed that values of b_K and b_L derived from Fano plots do not vary appreciably (by more than about 10 %) with Z .^{2,76} Figure 5 displays Fano plots based on the DWBA K-shell ionization cross sections of Bote *et al.*^{31,32} for N, Fe, Ag, and Au and on their L_3 -subshell ionization cross sections for Cu, Ag, and Au. In these examples, the parameter b_i (given by the asymptotic slopes of the lines for large values of X) decreases as the atomic number increases. Figure 6 shows similar Fano plots for the K shell and the L subshells of Au. Interestingly, the parameter b_{L_3} is seen to be smaller than b_K . This situation implies that b_i depends on the binding energy in a nontrivial way.

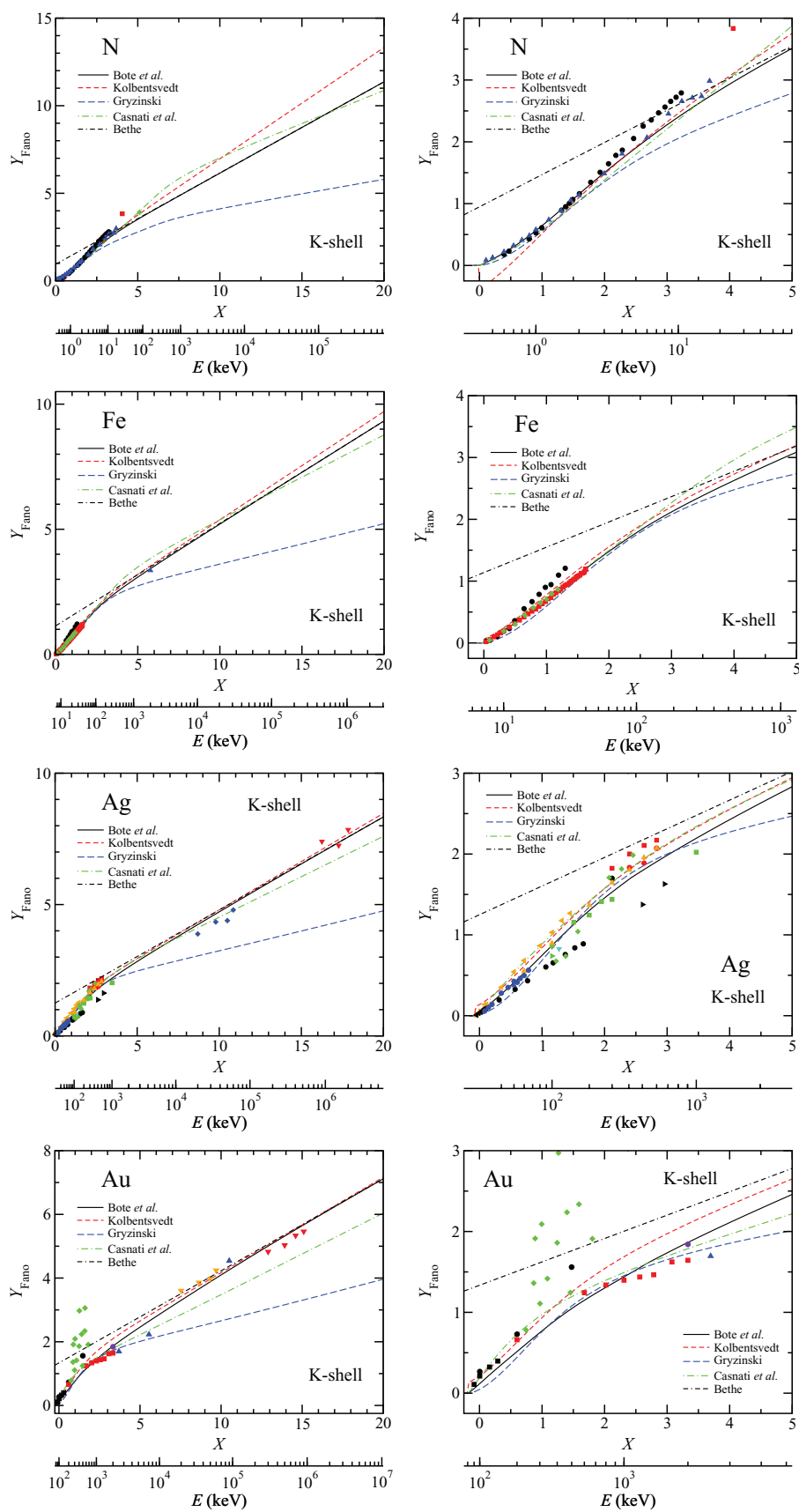


Fig. 3. (Color online) Fano plots for K-shell ionization of N, Fe, Ag, and Au obtained from Eqs. (71) and (72). The solid lines correspond to cross sections calculated from the DWBA (Bote *et al.*) and the dashed lines represent the analytical formulae of Kolbentsvedt [Eq. (82)], Gryzinski [Eq. (83)], and Casnati *et al.* [Eq. (84)]. The dotted-dashed lines are plots based on the Bethe formula [Eq. (69)] with the Bethe parameters b_i and c_i obtained from a fit to the DWBA cross sections in the high-energy region for each element. Symbols are experimental measurements identified in Sec. 6. The figures on the right display the low-energy parts of the plots.

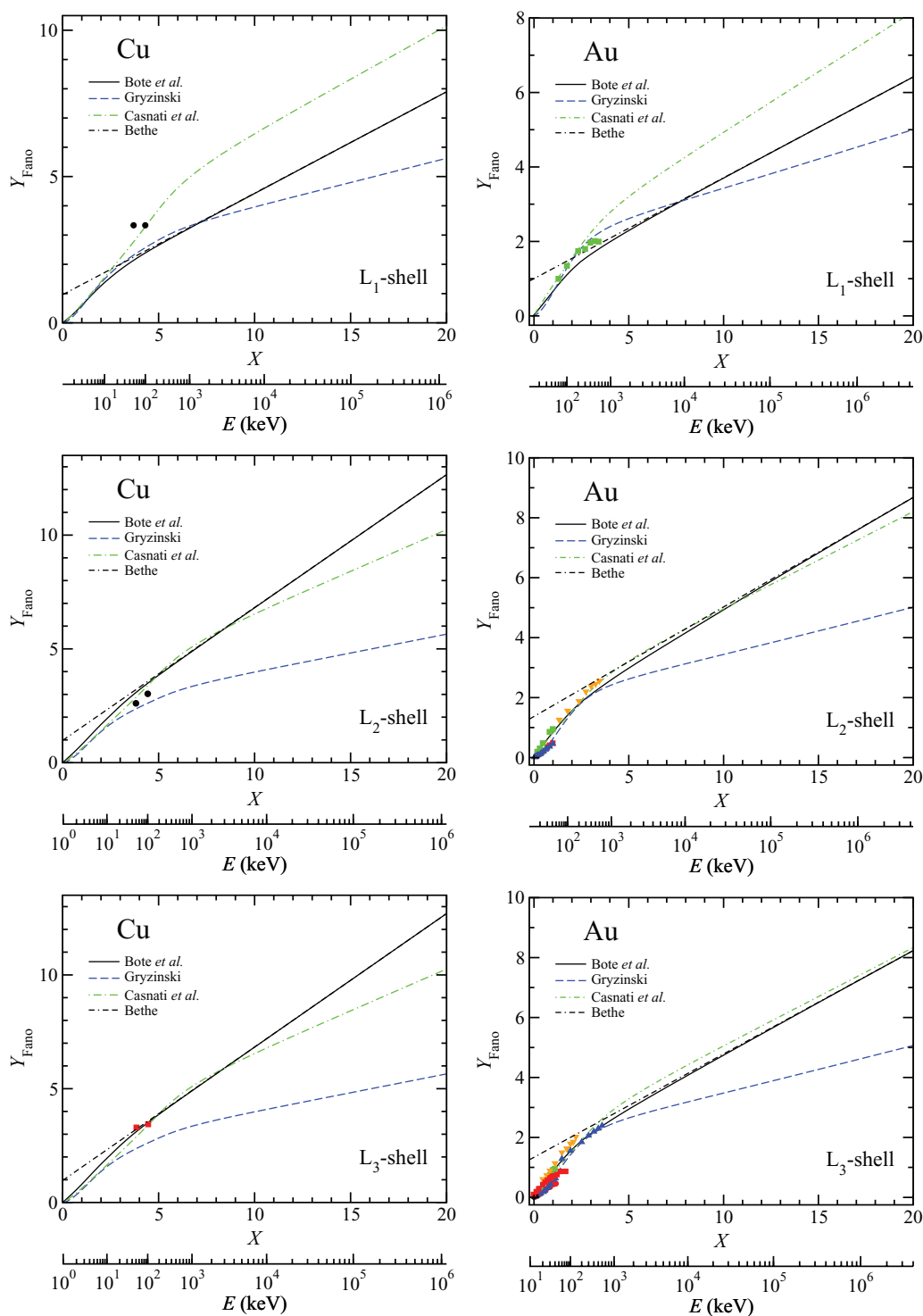


FIG. 4. (Color online) Fano plots for the L subshells of Cu and Au obtained from Eqs. (71) and (72). The solid lines correspond to cross sections calculated from the DWBA (Bote *et al.*) and the dashed lines represent the analytical formulae of Gryzinski [Eq. (83)] and Casnati *et al.* [Eq. (84)]. The dotted-dashed lines represent the Bethe formula [Eq. (69)] with the Bethe parameters b_i and c_i obtained from a fit to the DWBA cross sections in the high-energy region for each element. Symbols are experimental measurements identified in Sec. 6. The figures on the right display the low-energy parts of the plots.

3.2. Empirical modifications to the Bethe formula

Some authors have proposed empirical modifications to the Bethe formula so that it can be used in the near-threshold region ($U < 4$) where the Bethe formula is not valid,

as discussed in the previous paragraphs. Generally, these formulae were developed to describe, at least approximately, the limited body of experimental data and fragmentary theoretical information available at the time of publication.

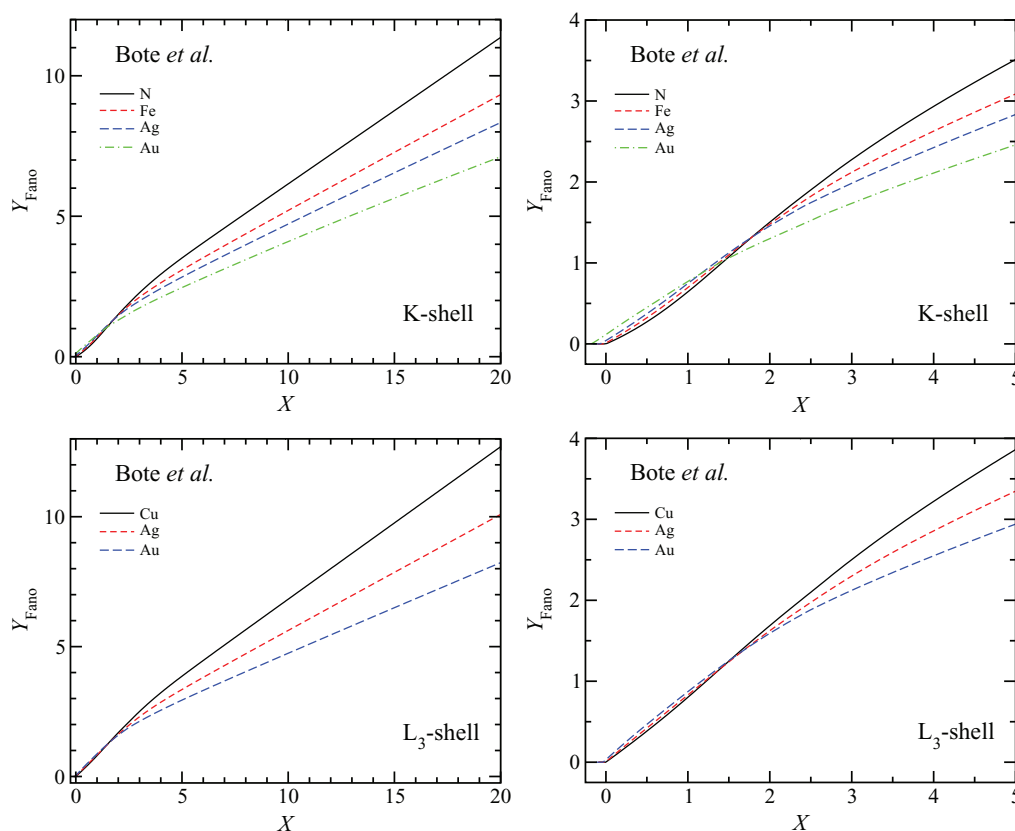


FIG. 5. (Color online) Fano plots for the K shell and the L_3 -subshell of the indicated elements, with cross sections calculated from the DWBA (Bote *et al.*³¹).

The only feature that is common to all of these formulae is that σ_i vanishes at $E = E_i$ ($U = 1$).

The following list describes formulae that were proposed mainly on the basis of empirical evidence. These formulae have been widely used for providing fast estimates of the ionization cross sections in practical applications.

- de la Ripelle⁷⁷ proposed the formula

$$\sigma_i E_i^2 = 6.514 \times 10^{-14} (2j + 1) \frac{\ln(U)}{k_i(U + \chi_i)} \text{ cm}^2 \text{ eV}^2, \quad (75)$$

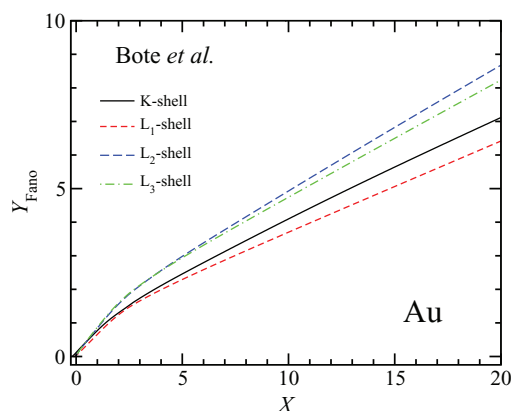


FIG. 6. (Color online) Fano plots for the K shell and the L subshells of Au, with cross sections calculated from the DWBA (Bote *et al.*³¹).

where k_i [equivalent to $1/b_i$ in Eq. (68)] and χ_i are parameters. A fit of measured K-shell cross sections to Eq. (75) gave the values $k_K = 1.18$ and $\chi_K = 1.32$ (de la Ripelle, private communication).

- Worthington and Tomlin⁷⁸ and Fong and Tomlin⁷⁹ used the formula

$$\sigma_i E_i^2 = 6.514 \times 10^{-14} (2j + 1) \frac{b_i}{U} \times \ln\left(\frac{4U}{1.65 + 2.35\exp(1-U)}\right) \text{ cm}^2 \text{ eV}^2, \quad (76)$$

where the argument of the logarithm ensures that σ_i vanishes for $U = 1$ and has the high-energy behavior suggested by the nonrelativistic PWBA. Values of the b_i parameter for the K shell ($b_K = 0.35$) and L subshells ($b_L = 1.05$) were inferred from theoretical calculations.

- Green and Cosslett⁸⁰ proposed a simpler formula for ionization of K shells by assuming that the Bethe parameter c_K was unity and by adjusting the parameter b_K to agree with measurements of σ_K for Ni and Ag for overvoltages near $U = 5$. Their formula reads

$$\sigma_K E_K^2 = 6.514 \times 10^{-14} (2j + 1) \frac{b_K}{U} \ln U \text{ cm}^2 \text{ eV}^2, \quad (77)$$

with $b_K = 0.61$.

- Drawin⁸¹ reviewed existing semiempirical cross-section formulae and proposed the following:

$$\sigma_i E_i^2 = 4.32 \times 10^{-14} (2j+1) f_1 \frac{U-1}{U^2} \times \ln(1.25 f_2 U) \text{ cm}^2 \text{ eV}^2, \quad (78)$$

where the parameters f_1 and f_2 have values in the ranges 0.7–1.3 and 0.8–3.0, respectively, but which are often replaced by unity.

- Hutchins⁸² proposed the following additional modification:

$$\sigma_i E_i^2 = 6.514 \times 10^{-14} (2j+1) \frac{b_i}{U^m} \ln U \text{ cm}^2 \text{ eV}^2, \quad (79)$$

where the parameter m was stated to be between 0.7 and 1.

- Lotz⁸³ proposed the somewhat more involved formula

$$\sigma_i E_i^2 = A_i (2j+1) \frac{\ln U}{U} \{1 - B_i \exp[-C_i(U-1)]\}, \quad (80)$$

where A_i , B_i , and C_i are parameters that Lotz determined from experimental information. For K shells, $A_K = 4.0 \times 10^{-14} \text{ cm}^2 \text{ eV}^2$, $B_K = 0.75$, and $C_K = 0.5$.

- Rudge and Schwartz⁸⁴ proposed a formula with a more flexible form that includes additional terms to account for shell corrections and low-energy departures from the PWBA [see Eq. (54)],

$$\sigma_i E_i^2 = 6.514 \times 10^{-14} (2j+1) \frac{\ln U}{U} \times \left[D_0 + \frac{D_1}{U} + \frac{D_2}{U^2} \right] \text{ cm}^2 \text{ eV}^2, \quad (81)$$

where D_0 , D_1 , and D_2 are parameters characteristic of each atomic subshell that, in principle, should be determined by fitting experimental data or results from theoretical calculations. Rudge and Schwartz determined these parameters for the cases of K shells ($D_0 = 2.799$, $D_1 = -0.218$, $D_2 = 0.047$) and L_1 subshells ($D_0 = 2.168$, $D_1 = 1.147$, $D_2 = -0.212$) from their calculations of σ_K and σ_{L_1} for hydrogenic ions using the nonrelativistic Born-exchange approximation.

3.3. The Kolbenstvedt formula

Kolbenstvedt¹⁹ used the Weizsäcker-Williams method of virtual quanta^{17,18} to derive an analytical formula for calculating K shell ionization cross sections. Close collisions (with large momentum transfers) were considered as binary collisions with free electrons at rest. The effect of distant interactions (with small momentum transfers) was described by considering the electromagnetic field of the projectile to be equivalent to a flux of virtual photons that can ionize the atom by photoelectric absorption. For the case of K-shell ionization, Kolbenstvedt¹⁹ first used a simple approximation to the photoelectric cross section which he later replaced by the nonrelativistic OOS.^{20,71}

The OOS gives a description of distant interactions much closer to the PWBA. The resulting ionization cross section is (see Ref. 20)

$$\sigma_K = \sigma_i^{\text{close}} + \sigma_K^{\text{distant}}, \quad (82a)$$

where

$$\sigma_i^{\text{close}} = \frac{0.99 \times 10^{-24} (T+1)^2}{I T(T+2)} \times \left[1 - \frac{I}{T} \left(1 - \frac{T^2}{2(T+1)^2} + \frac{2T+1}{(T+1)^2} \ln \frac{T}{I} \right) \right] \text{ cm}^2 \quad (82b)$$

is the contribution from close collisions, calculated using Møller's DCS, Eq. (13), and

$$\sigma_i^{\text{distant}} = \frac{0.275 \times 10^{-24} (I_0)^3 (T+1)^2}{I T(T+2)} \left\{ \left[1 - \frac{16}{13} \left(1 - \frac{I}{I_0} \right) \right] \times \left[\ln \left(\frac{2T(T+2)}{I} \right) - \frac{T(T+2)}{(T+1)^2} \right] - \frac{55}{78} - \frac{32}{39} \left(1 - \frac{I}{I_0} \right) \right\} \text{ cm}^2 \quad (82c)$$

is the cross section for distant ionizations, calculated using the nonrelativistic OOS of hydrogenic ions. The quantities

$$I \equiv \frac{E_i}{m_e c^2} \quad \text{and} \quad T \equiv \frac{E}{m_e c^2} \quad (82d)$$

are, respectively, the ionization energy of the active target electron and the kinetic energy of the projectile in units of the electron rest energy. $I_0 = \frac{1}{2} Z^2 E_h / m_e c^2$ is the nonrelativistic binding energy of an electron in the ground state of a hydrogenic ion, also in units of $m_e c^2$. While expression (82b) is applicable to any electron subshell, the expression (82c) is approximately valid only for K shells. Empirical modifications of the Kolbenstvedt formula have been proposed by Uddin *et al.*⁸⁵ and Haque *et al.*⁸⁶

3.4. The Gryzinski formula

The classical model developed by Gryzinski^{38–40} for atomic ionization has been widely used, largely because of its simplicity, analytical convenience, and supposed applicability to all shells. His expression for the cross section for ionization of a subshell is

$$\sigma_i E_i = \pi e^4 (2j+1) g(U) R_{\text{Gr}}, \quad (83a)$$

where $U = E/E_i$,

$$g(U) = \frac{1}{U} \left(\frac{U-1}{U+1} \right)^{3/2} \left[1 + \frac{2}{3} \left(1 - \frac{1}{2U} \right) \ln(2.7 + \sqrt{U-1}) \right], \quad (83b)$$

and R_{Gr} is the relativistic correction factor given by Gryzinski [see Eqs. (59)–(61) in Sec. VII of Ref. 39],

$$R_{\text{Gr}} = \frac{2+I}{2+T} \left(\frac{1+T}{1+I} \right)^2 \left[\frac{(I+T)(2+T)(1+I)^2}{T(2+T)(1+I)^2 + I(2+I)} \right]^{3/2}, \quad (83c)$$

where I and T are, respectively, the ionization energy of the active target electron and the kinetic energy of the projectile in units of the electron rest energy [Eq. (82d)].

The Deutsch and Märk formalism (see Ref. 87, and references therein) is based on a parameterization which is similar, but not identical, to Gryzinski's formula. This formalism, which incorporates parameters characteristic of each electron shell, was later modified by replacing the Gryzinski energy dependence with the correct dependence $\ln(E)/E$ predicted by the Bethe formula.⁸⁸ Haque *et al.*⁸⁹ introduced relativistic corrections by adding a factor similar, but not identical, to R_{Gr} .

3.5. Empirical formulae

Earlier reviews^{2,5,7,90} described the many formulae that have been proposed for predicting inner-shell ionization cross sections. We present here several empirical equations that have been widely used for this purpose or which appear to be useful.

- Casnati *et al.*^{91,92} derived the following empirical formula:

$$\sigma_{\text{K}} E_{\text{K}}^2 = \frac{(a_0 E_{\text{h}})^2}{4} Z_{\text{K}} \left(\frac{2E_{\text{K}}}{E_{\text{h}}} \right)^d \phi \frac{\ln U}{U} R_{\text{Gr}} \quad (84a)$$

where $U = E/E_{\text{K}}$,

$$d = -0.0318 + \frac{0.3160}{U} - \frac{0.1135}{U^2}, \quad (84b)$$

$$\phi = 10.57 \exp\left(-\frac{1.736}{U} + \frac{0.317}{U^2}\right), \quad (84c)$$

and R_{Gr} is the relativistic correction factor derived by Gryzinski, Eq. (83c). Note that $(a_0 E_{\text{h}})^2/4 = e^4/4 = 5.1837 \times 10^{-15} \text{ cm}^2 \text{ eV}^2$. The other factors on the right-hand side of Eq. (84a) are dimensionless and, therefore, the formula is valid in any system of units. Equation (84a) was found to fit K-shell ionization cross-section data to typically better than $\pm 10\%$ over the range $1 \leq U \leq 20$ and $6 \leq Z \leq 79$.

Seah and Gilmore⁹³ compared measured Auger-electron intensities (with primary-electron energies of 5 and 10 keV) for about 60 elemental solids with predictions based on several different analytical formulae for the ionization cross section. From this analysis, Seah and Gilmore recommended the Casnati *et al.* formula for use in AES. Although the Casnati *et al.* formula was derived

from fits to measured K-shell ionization cross sections, it was found useful for other subshells (more details in Sec. 5.2). Furthermore, a recent analysis showed that the Casnati *et al.* formula was better than the Gryzinski formula in calculations of the backscattering factor for AES.⁹⁴ This conclusion was based on comparisons with backscattering factors calculated with ionization cross sections from the analytical formulae of Bote *et al.*³¹ [Eqs. (87) and (88) below].

- Jakoby *et al.*⁹⁵ analyzed about 600 measured K-shell cross sections for elements with $6 \leq Z \leq 92$ and for $E_{\text{K}} \leq E \leq 2$ GeV. Their formula is

$$\sigma_{\text{K}} = a F_1 [F_2 + b F_3 + F_4 (F_5)^c] \text{ cm}^2, \quad (85a)$$

where

$$F_1(Z, \beta) = \frac{2.549 \times 10^{-19} \text{ eV}}{E_{\text{K}} \beta^2}, \quad (85b)$$

$$F_2(\beta) = \ln\left(\frac{\beta^2}{1-\beta^2}\right) - \beta^2, \quad (85c)$$

$$F_3(Z, \beta) = 1 - \beta_0^2/\beta^2, \quad (85d)$$

$$F_4(Z) = \ln(1/\beta_0^2), \quad (85e)$$

$$F_5(Z, \beta) = \beta_0^2/\beta^2, \quad (85f)$$

with

$$\beta^2 = 1 - [1 + (E/m_e c^2)]^{-2}, \quad \beta_0^2 = 1 - [1 + (E_{\text{K}}/m_e c^2)]^{-2} \quad (85g)$$

and

$$a = 5.14 Z^{-0.48}, \quad (85h)$$

$$b = 5.76 - 0.04 Z, \quad (85i)$$

$$c = 0.72 + 0.039 Z - 0.0006 Z^2. \quad (85j)$$

Equation (85a) was found to fit the measured cross sections with a stated accuracy $\pm 13\%$ (which is presumed to be the standard deviation in the fit).

- More recently, Hombourger⁹⁶ derived a formula for K-shell ionization cross sections with a structure analogous to Eq. (84a) and coefficients determined by least-squares fitting of experimental data. Hombourger's formula reads

$$\sigma_{\text{K}} = a_0^2 Z_{\text{K}} \left(\frac{E_{\text{h}}}{2E_{\text{K}}} \right)^{C_U} D_U R_{\text{Gr}} \quad (86a)$$

where

$$C_U = 2.0305 - \frac{0.3160}{U} - \frac{0.1545}{U^2} \quad (86b)$$

and

$$D_U = \left(3.125 - \frac{4.172}{U} + \frac{1.877}{U^2} \right) \frac{\ln U}{U}. \quad (86c)$$

The accuracy of this formula was claimed to be better than 10%.

3.6. Parameterization of cross sections from the DWBA and PWBA

Campos *et al.*⁹⁷ proposed a simple analytical expression for the ionization cross sections of the K shell and L subshells in terms of the atomic number and the overvoltage, with parameters obtained by fitting calculated DWBA results for $U < 10$.

Bote *et al.*^{31,32} have given useful parameterizations of ionization cross sections calculated from the corrected PWBA [Eq. (65)]. Parameter values were obtained from least-squares fitting of a comprehensive numerical database of ionization cross sections for the K shell and L and M subshells of all elements from hydrogen ($Z = 1$) to einsteinium ($Z = 99$) and for the energy range from the ionization threshold to 1 GeV. For overvoltages $U \leq 16$, the cross section is approximated by the following expression:

$$\sigma_i = 4\pi a_0^2 \frac{U-1}{U^2} \left(a_1 + a_2 U + \frac{a_3}{1+U} + \frac{a_4}{(1+U)^3} + \frac{a_5}{(1+U)^5} \right)^2, \quad (87)$$

where a_1, \dots, a_5 are parameters characteristic of each element and electron shell. For $U \geq 16$, the cross section is expressed as

$$\sigma_i = \frac{U}{U+b} \sigma_i^{(\text{PWBA})}, \quad (88a)$$

where b is an energy-independent parameter and $\sigma_i^{(\text{PWBA})}$ is the cross section obtained from the PWBA. The latter is represented as

$$\sigma_i^{(\text{PWBA})} = 4\pi a_0^2 \frac{A_i}{\beta^2} \{ [\ln X^2 - \beta^2] (1 + g_1 X^{-1}) + g_2 + g_3 (1 - \beta^2)^{1/4} + g_4 X^{-1} \}, \quad (88b)$$

where $\beta = v/c$, and

$$X \equiv \frac{p}{m_e c} = \frac{\sqrt{E(E + 2m_e c^2)}}{m_e c^2} \quad (88c)$$

is the momentum of the projectile in units of $m_e c$. The quantity A_i is defined by

$$A_i = \frac{\alpha^4 m_e c^2}{2} \int_{E_i}^{\infty} \frac{1}{W} \frac{df_i(W)}{dW} dW = \frac{\alpha^2}{2} M_j^2, \quad (89)$$

where $df_i(W)/dW$ is the optical oscillator strength of the active subshell, Eq. (45), $\alpha = e^2/\hbar c \sim 1/137$ is the fine-structure constant, and the quantity M_j^2 is the squared

dipole-matrix element for ionization.⁶⁹ The parameters b, A_i, g_1, \dots, g_4 are specific for each element and subshell.

Bote *et al.* provided tables of the parameters a_i, b, A_i , and g_i for K, L, and M shells of all elements ($Z = 1$ to $Z = 99$); a Fortran subroutine which implements these analytical expressions is available in the online version of the Bote *et al.* article. The values from these formulae differ from the cross sections calculated from the corrected PWBA by less than about 1% for $U > 1.3$. For smaller overvoltages, the relative differences are less than about 5%.

An important parameter in Eqs. (87) and (88) is the overvoltage, U , the ratio of the incident electron energy to the binding energy (BE) of the electron for the shell and element of interest. The BEs adopted in the analysis of Bote *et al.* were the negative eigenvalues of the radial Dirac-Hartree-Fock-Slater equations (see, e.g., Ref. 98), because these are consistent with the atomic model underlying the calculations and available for all elements and shells. The Appendix gives information on the magnitudes of differences between these calculated BEs and measured values, and provides recommendations for computing ionization cross sections using appropriate experimental BEs for atoms, molecules, and solids. We have chosen to make use of BEs from Carlson's compilation⁶⁴ since these are measured BEs for commonly occurring elements; calculated BEs are given for other elements. Ionization cross sections calculated with Carlson's BEs may differ from those obtained with the calculated BEs used by Bote *et al.* for U less than about 3 where the cross sections vary relatively rapidly with U .

We now give examples of ionization cross sections calculated from Eqs. (87) and (88) for selected elements and compare these with cross sections obtained from the formulae of Drawin [Eq. (78)], Lotz [Eq. (80)], Kolbenstvedt [Eq. (82)], Gryzinski [Eq. (83)], Casnati *et al.* [Eq. (84)], Jakoby *et al.* [Eq. (85)], and Hombourger [Eq. (86)]. We also show measured ionization cross sections that will be described and presented in Sec. 6. Figure 7 displays K-shell ionization cross sections for N, Si, Fe, Y, Ag, and Au for incident energies from threshold to 1 GeV. The curves labelled DWBA were obtained from Eqs. (87) and (88). It is seen that the DWBA results compare well with experimental data over the whole energy range. Cross sections from the Kolbenstvedt formula generally agree well with the DWBA curves but there are deviations for Y, Ag, and Au at lower energies. Cross sections from the Lotz and Drawin formulae are less than the measured cross sections and the DWBA curves, with the differences becoming more significant with increasing electron energy and atomic number. These differences arise from the fact that the two formulae were fitted to measurements made over 40 years ago for nonrelativistic energies. Distinct differences are seen between the Gryzinski cross sections and the measured values, while the differences for the Casnati *et al.*, Jakoby *et al.*, and Hombourger cross sections are smaller. A more detailed analysis of differences between the DWBA cross sections and the values from the Gryzinski, Casnati *et al.*, Jakoby *et al.*, and Hombourger formulae will be presented in Sec. 8.

Figure 8 contains similar comparisons of total L-shell ionization cross sections for Ag, Xe, Ta, and Bi, and Fig. 9 gives comparisons of total M-shell ionization cross sections

for Au and Bi. We again see failures of the Lotz and Drawin cross sections. More detailed comparisons of results from the other formulae will be given in Sec. 8.

4. X-ray and Auger-Electron Emission

The ionization of an inner shell is followed by the relaxation of the target atom by emission of characteristic x rays and Auger electrons. In applications to electron-probe microanalysis and Auger electron spectroscopy, one is primarily

interested in the cross sections for the emission of characteristic x rays and Auger electrons, respectively. In this section we discuss the relationship between these cross sections and the cross sections for impact ionization described in Secs. 2 and 3.

The primary ionization of an atom by impact of a fast charged particle, produces a vacancy in a certain subshell $Si = (n_i \ell_i j_i)$. We disregard the possibility of collisions producing multiple ionization of the target atom which normally occur with much smaller probabilities. When the

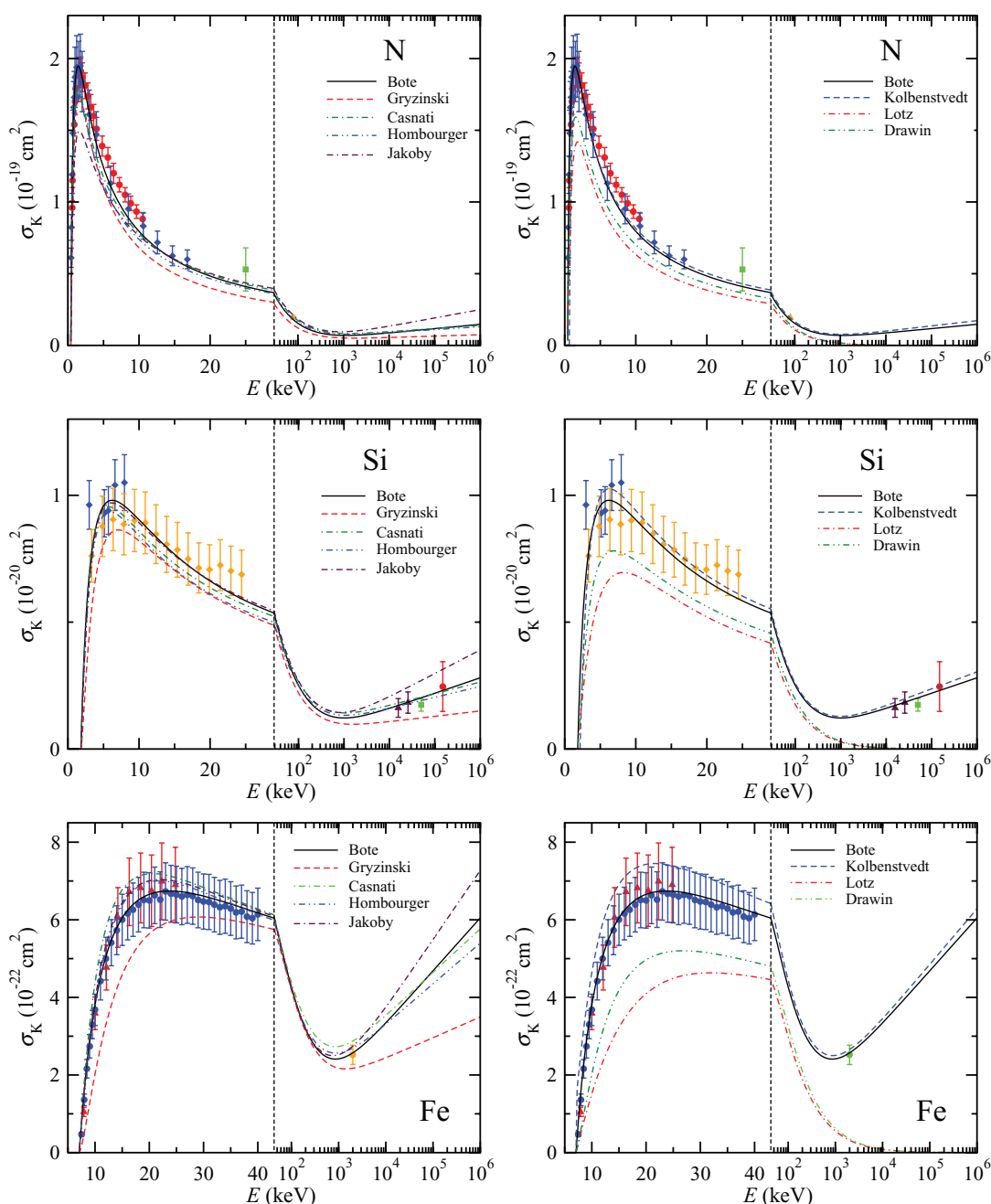


Fig. 7. (Color online) Absolute cross sections for ionization of the K shells of N, Si, Fe, Y, Ag, and Au vs. incident electron energy. The curves are the results of the DWBA calculations (solid lines) and of the analytical formulae indicated in the legends. The symbols represent experimental measurements that are identified in Sec. 6. The error bars are estimates of the one-standard-deviation uncertainties of the measured cross sections provided by the authors. Note the logarithmic scale in the high-energy parts of the horizontal axes.

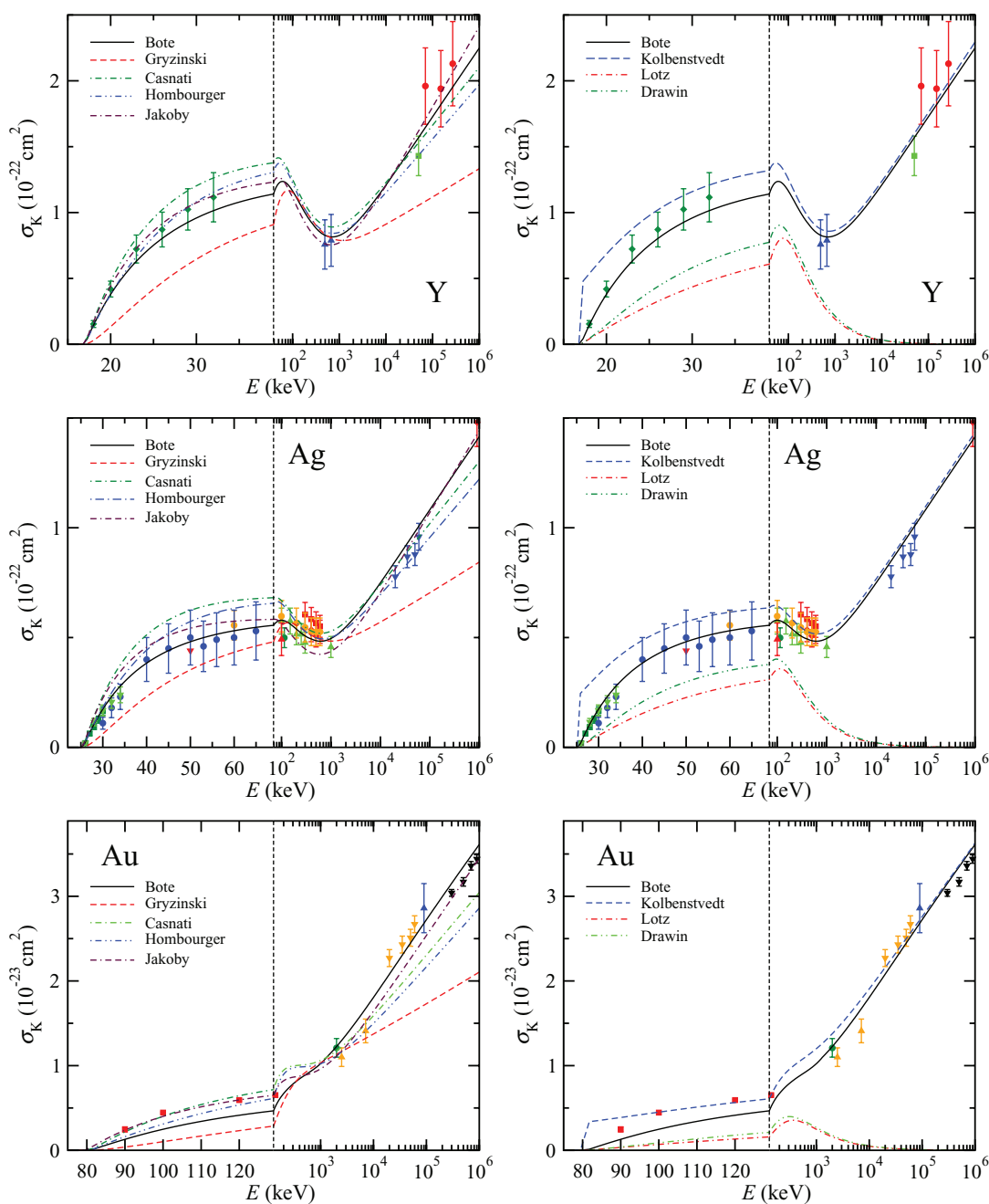


FIG. 7. (Continued.)

primary vacancy is in an inner subshell, the resulting ion is in a highly excited state and it de-excites by migration of the primary vacancy to outer subshells through a cascade of radiative and nonradiative transitions. In a radiative S_0 - S_1 transition, a vacancy in the S_0 subshell migrates to the outer subshell S_1 ($n_1 \geq n_0$) with emission of a characteristic x ray. In a nonradiative S_0 - S_1 - S_2 transition, a vacancy in the S_0 subshell is filled by an electron that falls from the outer S_1 subshell and an electron is ejected from the S_2 subshell; after each nonradiative transition, the residual ion has an additional vacancy. Nonradiative transitions are classified as Auger, Coster-Kronig, and super Coster-Kronig transitions. When the subshells S_1 and S_2 belong to shells different from that of S_0 ($n_0 < n_1$, $n_0 < n_2$), the nonradiative transition is

called an Auger transition. If S_0 and S_1 belong to the same shell ($n_0 = n_1$, $n_2 > n_0$), we have a Coster-Kronig transition. Finally, in super Coster-Kronig transitions, the three active subshells S_0 , S_1 , and S_2 belong to the same shell ($n_1 = n_2 = n_0$).

In the specialized literature, it was customary to represent radiative transitions using Siegbahn's notation in which each transition is designated by the letter code of the shell S_0 that had the initial vacancy followed by a Greek letter and, in some cases, a numeral subscript. Siegbahn's notation is being replaced by the more explicit IUPAC notation adopted here in which the codes of the shells with the initial and final vacancies are written separated by a hyphen.⁹⁹ However, x-ray detectors may not be able to resolve groups of lines that have

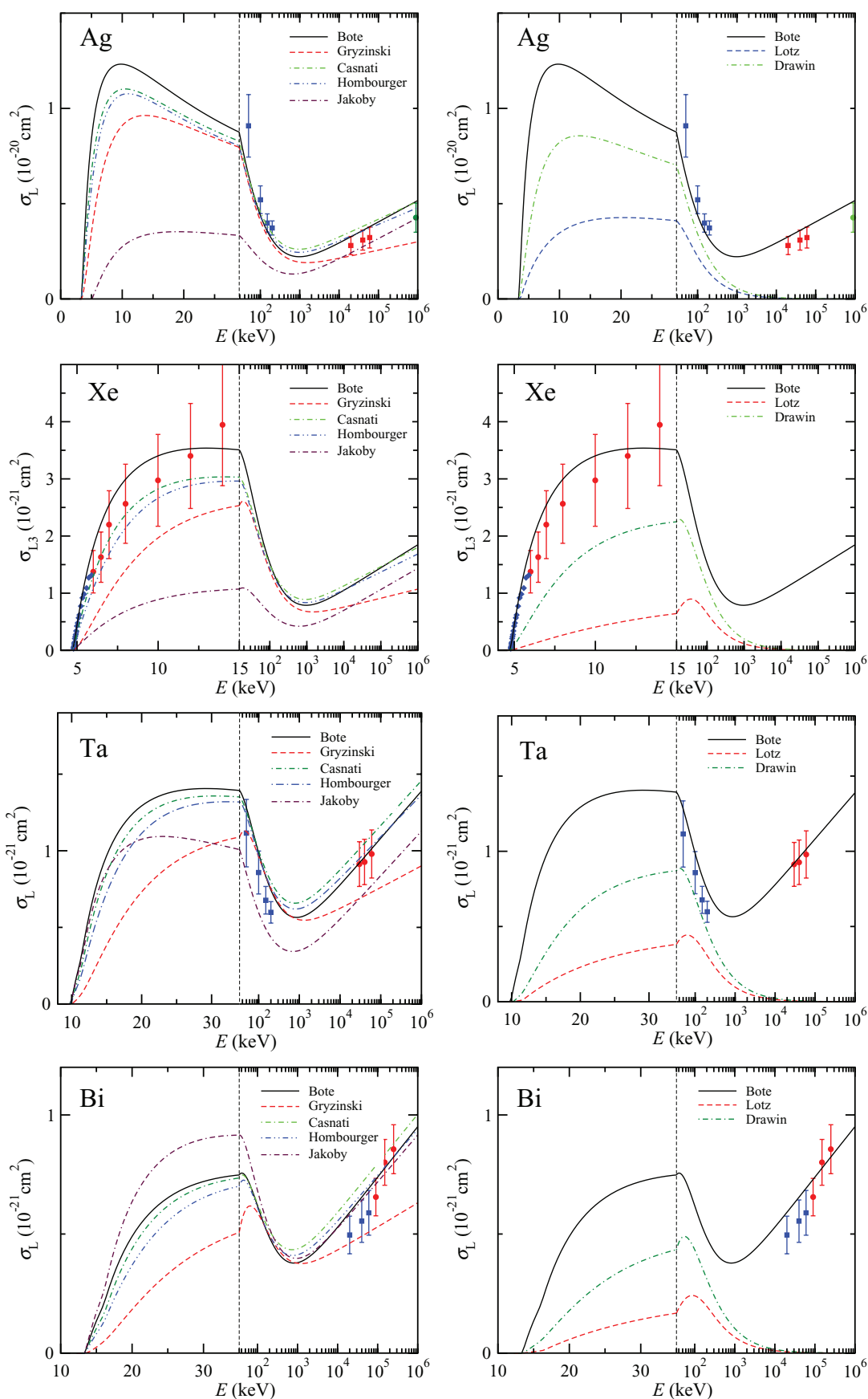


FIG. 8. (Color online) Absolute cross sections for ionization of the L shells of Ag, Xe, Ta, and Bi vs. incident electron energy. Solid curves are the results of the DWBA calculations and of the analytical formulae indicated in the legends. Note the logarithmic scale in the high-energy part of the horizontal axes.

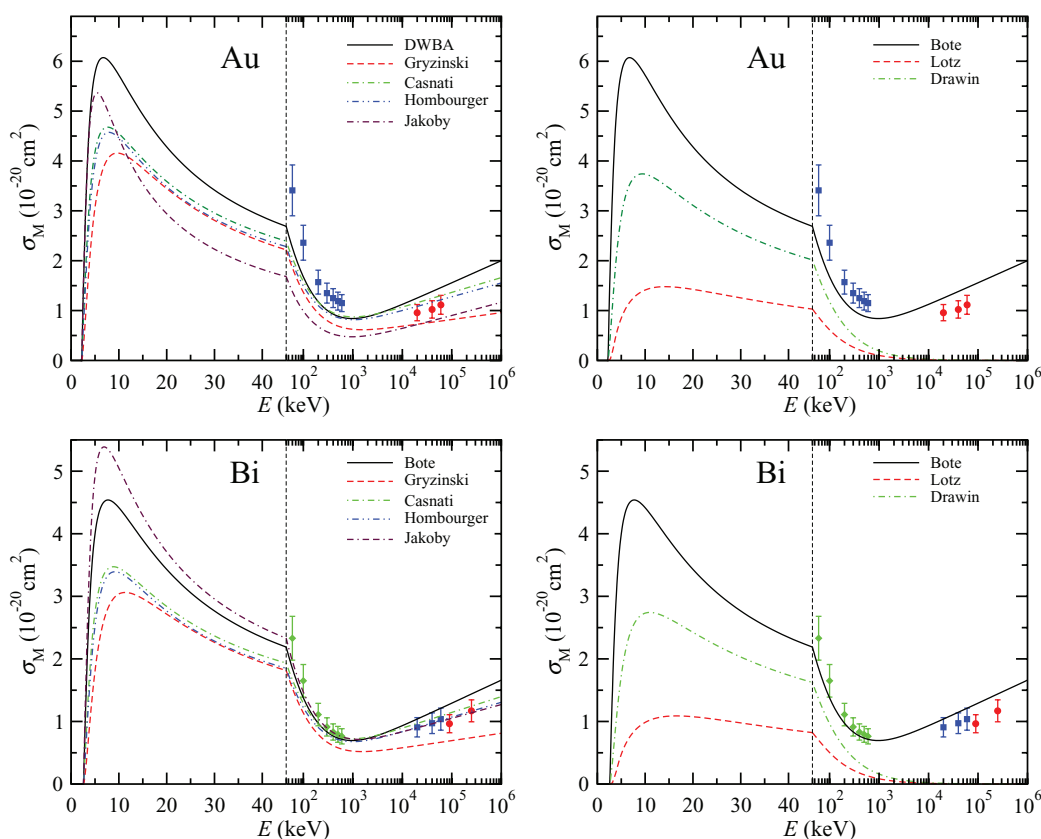


FIG. 9. (Color online) Absolute cross sections for ionization of the M shells of Au and Bi vs. incident electron energy. Solid curves are the results of the DWBA calculations and of the analytical formulae indicated in the legends. Note the logarithmic scale in the high-energy part of the horizontal axes.

similar energies (e.g., the K-L₂ and K-L₃ lines) and, for these unresolved groups, the use of a form like K-L_{2,3} or of Siegbahn's notation (K α) simplifies the text and formulae. The correspondence between Siegbahn's and the IUPAC notations for various K-shell, L-shell, and M-shell lines is given in Table 1.

4.1. Transition probabilities and emission yields

Let τ_{S_0} denote the mean lifetime of an excited state of an atom with a vacancy in the subshell S₀. The reciprocal of this quantity is the probability per unit time of a transition to any lower-energy state. The level width of the initial excited state is $\Gamma_{S_0} = \hbar/\tau_{S_0}$, and can be expressed as the sum of the partial widths $\Gamma_{S_0-S_1}$ and $\Gamma_{S_0-S_1-S_2}$ of all radiative and nonradiative transitions that fill a vacancy in the subshell S₀. The quantity

$$P_{S_0-S_1} \equiv \Gamma_{S_0-S_1}/\Gamma_{S_0} \quad (90)$$

is the probability that a *single vacancy* in subshell S₀ decays through the radiative transition S₀-S₁. Similarly, the probability that the vacancy is filled through the nonradiative transition S₀-S₁-S₂ is

$$P_{S_0-S_1-S_2} \equiv \Gamma_{S_0-S_1-S_2}/\Gamma_{S_0}. \quad (91)$$

TABLE 1. Radiative transitions for the relevant groups in the K, L, and M series. Transitions for the indicated lines are represented using the IUPAC notation (S₀-S₁) and the corresponding Siegbahn notation is indicated in parentheses

Group	Lines	Group	Lines	
K α	K-L ₂ (K α_2)		L ₂ -N ₆ (L ν)	
	K-L ₃ (K α_1)		L ₂ -N ₇ (L ν)	
	K β	K-M ₂ (K β_3)		L ₂ -O ₁ (L γ_8)
		K-M ₃ (K β_1)		L ₂ -O ₄ (L γ_6)
		K-M ₄ (K β_5^I)	L ₃ ℓ	L ₃ -M ₁ (L ℓ)
	K-M ₅ (K β_5^I)	L ₃ t	L ₃ -M ₂ (L t)	
	K-N ₂ (K β_2^I)	L ₃ s	L ₃ -M ₃ (L s)	
	K-N ₃ (K β_2^I)	L ₃ α	L ₃ -M ₄ (L α_2)	
	K-N ₄ (K β_4^I)		L ₃ -M ₅ (L α_1)	
	K-N ₅ (K β_4^I)	L ₃ β	L ₃ -N ₁ (L β_6)	
L ₁ β	L ₁ -M ₂ (L β_4)		L ₃ -N ₄ (L β_{15})	
	L ₁ -M ₃ (L β_3)		L ₃ -N ₅ (L β_2)	
	L ₁ -M ₄ (L β_{10})	L ₃ u	L ₃ -N ₆ (L u)	
	L ₁ -M ₅ (L β_9)		L ₃ -N ₇ (L u)	
	L ₁ γ	L ₁ -N ₂ (L γ_2)	M γ	M ₂ -N ₅ (M γ)
L ₁ -N ₃ (L γ_3)		M β	M ₄ -N ₆ (M β)	
L ₁ -N ₄ (L γ_1)		M ζ	M ₅ -N ₂ (M ζ_2)	
L ₂ η	L ₂ -M ₁ (L η)		M ₅ -N ₃ (M ζ_1)	
L ₂ β	L ₂ -M ₃ (L β_{17})	M α	M ₅ -N ₆ (M α_2)	
	L ₂ -M ₄ (L β_1)		M ₅ -N ₇ (M α_1)	
	L ₂ γ			
	L ₂ -N ₁ (L γ_5)			
	L ₂ -N ₄ (L γ_1)			

Note that

$$\sum_{S1} P_{S0-S1} + \sum_{S1,S2} P_{S0-S1-S2} = 1, \quad (92)$$

where the summations run over all subshells S1 and S2 with ionization energies less than E_{S0} . The radiative (R) and nonradiative (NR) widths are

$$\Gamma_{S0}(R) = \Gamma_{S0} \sum_{S1} P_{S0-S1}, \quad \Gamma_{S0}(NR) = \Gamma_{S0} \sum_{S1,S2} P_{S0-S1-S2}, \quad (93)$$

respectively. The most extensive tabulation of transition probabilities now available is given in the Evaluated Atomic Data Library (EADL) of Perkins *et al.*¹ This tabulation includes transitions of singly-ionized atoms of the elements $Z = 1$ to $Z = 100$ with a single vacancy in the subshells of K, L, M, N, and some O shells. These transition probabilities were initially obtained from calculations using the independent-electron model with the Dirac-Hartree-Fock-Slater potential, and adjusted to reproduce the Z -dependence of the enhanced fluorescence yields that are defined below.

The fluorescence yield ω_{S0} of a state with a vacancy in the subshell S0 is defined as the probability that the vacancy is filled through a radiative transition,

$$\omega_{S0} \equiv \Gamma_{S0}(R)/\Gamma_{S0} = \sum_{S1} P_{S0-S1}. \quad (94)$$

That is, the direct fluorescence yield of a subshell is equal to the average number of photons emitted in the filling of a vacancy in that subshell. Similarly, the nonradiative (or Auger) yield, a_{S0} , of a state with a vacancy in the S0 subshell is defined as

$$a_{S0} \equiv \Gamma_{S0}(NR)/\Gamma_{S0} = \sum_{S1,S2} P_{S0-S1-S2}, \quad (95)$$

and gives the average number of Auger electrons emitted through transitions that fill the original vacancy. Evidently, we have

$$\omega_{S0} + a_{S0} = 1. \quad (96)$$

The Coster-Kronig yield, $f_{S0,1}$, is the probability that a vacancy in the subshell S0 of a singly-ionized atom shifts to a higher subshell S1 of the same shell ($n_1 = n_0$) through a nonradiative transition. That is,

$$f_{S0,1} = \sum_{S2} P_{S0-S1-S2}, \quad (97)$$

where the sum is over subshells S2 above the active shell, with $n_2 > n_0$. A related quantity is the intrashell radiative yield, $f'_{S0,1} \equiv P_{S0-S1}$, which is equal to the probability that the vacancy moves from S0 to S1 ($n_1 = n_0$) through a radiative transition. The sum

$$\eta_{S0,S1} \equiv f_{S0,1} + f'_{S0,1} = P_{S0-S1} + \sum_{S2} P_{S0-S1-S2} \quad (98)$$

is the total probability of intrashell transitions that shift the vacancy from S0 to S1. For a vacancy in a subshell S0, the total

probability of intershell transitions that transfer the vacancy to subshell S1 of an outer shell ($n_1 > n_0$) is

$$\eta_{S0,S1} \equiv P_{S0-S1} + \sum_{S2} P_{S0-S1-S2}. \quad (99)$$

The super Coster-Kronig yield $S_{S0,1}$ is defined as the probability that a vacancy in the subshell S0 of a singly ionized atom shifts to a higher subshell S1 of the same shell ($n_1 = n_0$) through super Coster-Kronig transitions S0-S1-S2, that is,

$$S_{S0,1} = \sum_{S2} P_{S0-S1-S2}, \quad (100)$$

where the summation runs over the subshells S2 of the n_0 shell.

A detailed review on x-ray fluorescence yields, Auger, and Coster-Kronig transition probabilities, including historical aspects, theoretical methods, and experimental techniques was published by Bambynek *et al.*^{100,101} In a widely quoted article, Krause¹⁰² gives tables and graphs of these quantities for the K shell and L subshells obtained from a compilation of available theoretical and experimental information. More recently, Hubbell *et al.*^{103,104} reviewed measurements of K-shell fluorescence yields and of average fluorescence yields of L and M shells.

Note that the above definitions of fluorescence and Auger yields pertain to singly ionized atoms and correspond to the so-called direct yields, i.e., we count only x rays and electrons emitted in radiative and nonradiative transitions that fill the initial vacancy directly. The de-excitation cascade of a parent vacancy in a subshell S0 may produce daughter vacancies in outer subshells of the same shell (e.g., through Coster-Kronig transitions). As the ionization energies of the various subshells of a shell are similar, it may be difficult to distinguish the x rays that originate from the direct filling of the parent vacancy from those emitted in the decay of its daughter vacancies. The *enhanced fluorescence yield* (or *effective fluorescence yield*, in the terminology of Krause) of a shell S0 is defined as the average number of x rays emitted in the filling of a parent vacancy in S0 and of any of its daughter vacancies in other subshells of the same shell. The *total fluorescence yield* of a subshell S0 is the average total number of photons emitted in the course of the complete de-excitation cascade of an initial vacancy in that subshell.

4.2. Emission cross sections

In practical calculations and in Monte Carlo simulations of radiation transport, we need to consider cross sections for the emission of characteristic x rays, σ_{S0-S1} , or Auger electrons, $\sigma_{S0-S1-S2}$, by impact of electrons with kinetic energy E . These cross sections can be measured by counting the number of x rays or Auger electrons emitted from a given transition (i.e., in a given spectral line or a group of lines with similar energies) when primary electrons of energy E impinge normally on a very thin foil of the pure element Z, as described in Sec. 5.1. The probability that an incident electron causes the emission of a characteristic x ray (or an Auger electron) is $\sigma_{S0-S1} \mathcal{N} t$ (or $\sigma_{S0-S1-S2} \mathcal{N} t$ for an Auger electron), where \mathcal{N} is the number of

atoms per unit volume and t is the thickness of the foil. Evidently, to calculate the emission cross sections $\sigma_{S_0-S_1}$ and $\sigma_{S_0-S_1-S_2}$ we need to know the cross section $\sigma_{S_0}(E)$ for ionization of subshell S_0 by the incident radiation. Thus, for x rays and Auger electrons arising from ionizations of the K-shell ($S_0 = K$),

$$\sigma_{K-S_1} = \sigma_K(E) P_{K-S_1}, \quad \sigma_{K-S_1-S_2} = \sigma_K(E) P_{K-S_1-S_2}, \quad (101)$$

where P_{K-S_1} and $P_{K-S_1-S_2}$ are the probabilities for the designated radiative and nonradiative transitions, respectively. For subshells beyond the K shell, the calculation is not trivial because we have to account for the fact that vacancies in a subshell S_0 are produced not only by direct ionization by the incident electrons, but also during the course of the de-excitation cascades of primary vacancies that were generated in deeper subshells. As the de-excitation cascade progresses, the initial vacancy migrates to outer subshells and, in the case of nonradiative transitions, additional vacancies are generated. Multiple vacancies can also be produced by shakeoff in the initial ionization event, preferentially in outer shells (see, e.g., Ref. 105). The presence of multiple vacancies alters both the transition probabilities and the energies of the emitted x rays and Auger electrons; transitions in multivacancy configurations are observable as satellite lines which are shifted (up to a few eV) from the parent (single-vacancy) line. Unfortunately, information on the relaxation of multivacancy states is not generally available.

A common practice in experimental studies of x-ray emission is to express the emission cross sections in terms of partial widths and direct yields that are obtained either from theoretical calculations or from experiments. The ionization cross sections can then be inferred from the observed x-ray intensities. For instance, the emission cross section for the $K\alpha$ group ($K-L_2, K-L_3$),

$$\sigma_{K\alpha} = (P_{K-L_2} + P_{K-L_3}) \sigma_K \quad (102)$$

is normally expressed in the equivalent form

$$\sigma_{K\alpha} = \frac{\Gamma_{K\alpha}}{\Gamma_K(R)} \omega_K \sigma_K, \quad (103)$$

where ω_K is the K-shell fluorescence yield, $\Gamma_{K\alpha}$ is the partial width of the radiative transitions $K-L_{2,3}$, and $\Gamma_K(R)$ is the K-shell radiative width. The partial widths and total radiative widths employed in the literature are normally taken from Scofield's¹⁰⁶⁻¹⁰⁸ tables.

In the case of radiative transitions $Li-S_1$ starting from a vacancy in an L subshell, the initial vacancy Li can be produced not only by direct ionization but also by radiative and nonradiative transitions of a vacancy in the K shell, Coster-Kronig transitions between L subshells and, to a lesser extent, by radiative transitions between L subshells. It is convenient to consider the cross sections for the production of a vacancy in each of the subshells,

$$\sigma_{L_i}^{\text{vac}} = \sigma_{L_i} + \eta_{K-L_i} \sigma_K, \quad (104a)$$

$$\sigma_{L_2}^{\text{vac}} = \sigma_{L_2} + \sigma_{L_1} f_{L_1,2} + \sigma_K(\eta_{K-L_2} + \eta_{K-L_1} f_{L_1,2}), \quad (104b)$$

$$\begin{aligned} \sigma_{L_3}^{\text{vac}} = & \sigma_{L_3} + \sigma_{L_2} f_{L_2,3} + \sigma_{L_1}(f_{L_1,3} + f'_{L_1,3} + f_{L_1,2}f_{L_2,3}) \\ & + \sigma_K[\eta_{K-L_3} + \eta_{K-L_2} f_{L_2,3} \\ & + \eta_{K-L_1}(f_{L_1,3} + f'_{L_1,3} + f_{L_1,2}f_{L_2,3})], \end{aligned} \quad (104c)$$

where η_{K-L_i} is the radiative plus nonradiative yield for transitions of vacancies from the K-shell to the L_i -subshell, $f_{L_1,2}$, $f_{L_1,3}$, and $f_{L_2,3}$ are the Coster-Kronig yields between L-subshells, and $f'_{L_1,3}$ is the intrashell radiative yield for transitions of vacancies from the L_1 subshell to the L_3 subshell. The cross sections for emission of the $L\ell$, $L\alpha$, $L\beta$, and $L\gamma$ x-ray groups are given by (see Table 1)

$$\sigma_{L\ell} = \frac{\Gamma_{L_3\ell}}{\Gamma_{L_3}(R)} \omega_{L_3} \sigma_{L_3}^{\text{vac}}, \quad (105a)$$

$$\sigma_{L\alpha} = \frac{\Gamma_{L_3\alpha}}{\Gamma_{L_3}(R)} \omega_{L_3} \sigma_{L_3}^{\text{vac}}, \quad (105b)$$

$$\sigma_{L\beta} = \frac{\Gamma_{L_3\beta}}{\Gamma_{L_3}(R)} \omega_{L_3} \sigma_{L_3}^{\text{vac}} + \frac{\Gamma_{L_2\beta}}{\Gamma_{L_2}(R)} \omega_{L_2} \sigma_{L_2}^{\text{vac}} + \frac{\Gamma_{L_1\beta}}{\Gamma_{L_1}(R)} \omega_{L_1} \sigma_{L_1}^{\text{vac}}, \quad (105c)$$

$$\sigma_{L\gamma} = \frac{\Gamma_{L_2\gamma}}{\Gamma_{L_2}(R)} \omega_{L_2} \sigma_{L_2}^{\text{vac}} + \frac{\Gamma_{L_1\gamma}}{\Gamma_{L_1}(R)} \omega_{L_1} \sigma_{L_1}^{\text{vac}}, \quad (105d)$$

where ω_{L_i} is the fluorescence yield for the L_i subshell, $\Gamma_{L_i\lambda}$ is the sum of radiative widths of the transitions that belong to the $L_i\lambda$ group, and $\Gamma_{L_i}(R)$ is the total radiative width of the L_i subshell.

In the case of M-shell x rays, the situation is even more complicated, because vacancies can be created by direct ionization, Coster-Kronig and super-Coster-Kronig transitions, and by transitions from vacancies in L_i subshells and the K shell.

4.3. Emission cross sections with data from the Evaluated Atomic Data Library (EADL)

Cross sections for x-ray and Auger emission by electron and positron impact can be calculated in a systematic way by combining our ionization cross sections with needed data from the EADL.¹ As indicated above, it is convenient to introduce first the cross section for the generation of a vacancy in the subshell S_0 of the target atom by incident electrons (or positrons) of energy E that can be expressed as

$$\sigma_{S_0}^{\text{vac}}(E) = \sum_{S_i} \sigma_{S_i}(E) C_{S_i,S_0}, \quad (106)$$

where the summation extends over all subshells S_i with binding energies E_{S_i} larger than that of the considered shell ($E_{S_i} > E_{S_0}$), $\sigma_{S_i}(E)$ is the cross section for ionization of subshell S_i by the incident radiation, and the vacancy-migration coefficient C_{S_i,S_0} is the average number of vacancies induced in subshell S_0 during

the de-excitation cascade of a primary ion with an initial vacancy in subshell S_i . The cross section for emission of characteristic S0-S1 x rays can then be obtained as

$$\sigma_{S0-S1}(E) = \sigma_{S0}^{\text{vac}}(E) P_{S0-S1}. \quad (107)$$

Similarly, the cross section for emission of S0-S1-S2 Auger electrons is given by

$$\sigma_{S0-S1-S2}(E) = \sigma_{S0}^{\text{vac}}(E) P_{S0-S1-S2}. \quad (108)$$

If we disregard the effect of occasional multiple vacancies on the transition probabilities during the de-excitation cascade, the cross sections for the generation of a vacancy in the various subshells can be readily calculated from the EADL transition probabilities. The vacancy-migration coefficients C_{S_i, S_k}^1 resulting from this simplification will be denoted by a superscript “1.” We observe that $C_{S_i, S_i}^1 = 1$, because primary vacancies always count. K-shell vacancies are produced only by direct ionization,

$$\sigma_K^{\text{vac}} = \sigma_K = \sigma_K C_{K,K}^1. \quad (109)$$

Vacancies in the L_1 subshell can be generated either by direct ionization or by migration from the K shell,

$$\sigma_{L_1}^{\text{vac}} = \sigma_K^{\text{vac}} \eta_{K,L_1} + \sigma_{L_1} = \sigma_K C_{K,L_1}^1 + \sigma_{L_1} C_{L_1,L_1}^1, \quad (110)$$

so that $C_{K,L_1}^1 = C_{K,K}^1 \eta_{K,L_1}$ where η_{K,L_1} represents the transition probability for a vacancy in the K shell to move to the L_1 subshell. Similarly,

$$\begin{aligned} \sigma_{L_2}^{\text{vac}} &= \sigma_K^{\text{vac}} \eta_{K,L_2} + \sigma_{L_1}^{\text{vac}} \eta_{L_1,L_2} + \sigma_{L_2} \\ &= \sigma_K C_{K,L_2}^1 + \sigma_{L_1} C_{L_1,L_2}^1 + \sigma_{L_2} C_{L_2,L_2}^1 \end{aligned} \quad (111)$$

with

$$C_{K,L_2}^1 = C_{K,K}^1 \eta_{K,L_2} + C_{K,L_1}^1 \eta_{L_1,L_2}, \quad C_{L_1,L_2}^1 = C_{L_1,L_1}^1 \eta_{L_1,L_2}.$$

Proceeding in this way, we find that the coefficients C_{S_i, S_k} satisfy the following recurrence relation,

$$C_{S_i, S_k}^1 = \sum_{S_a} C_{S_i, S_a}^1 \eta_{S_a, S_k}, \quad (112)$$

where the summation is over all subshells S_a with ionization energies less than or equal to that of the initial subshell and larger than that of the final subshell, i.e., such that $E_{S_k} < E_{S_a} \leq E_{S_i}$.

The coefficients C_{S_i, S_k}^1 obtained in this way are approximate because the transition probabilities in the EADL were obtained by assuming that the atom had a single vacancy in the “initial” S0 shell. Since calculations for multiply-ionized atoms are not generally available, we adopt the following simple method to correct partially for the possible occurrence of multiple vacancies during the de-excitation cascade. We recall that transition probabilities are essentially proportional to the number of vacancies in the initial shell S0 and to the numbers of electrons in the intermediate and final shells, S1 and S2. Hence, the effect of having multiple vacancies can be accounted for approxi-

mately by “re-normalizing” the transition probabilities according to the current occupancies of the active shells. Let v_{S_k} denote the number of vacancies in subshell S_k before the transition; the number of one-electron orbitals in that subshell is $q_{S_k} = 2j_k + 1$. The probabilities of nonradiative and radiative transitions of an ion with multiple vacancies can then be approximated as

$$P_{S0-S1}^{\text{ion}} = P_{S0-S1} v_{S0} \frac{q_{S1} - v_{S1}}{q_{S1}}, \quad (113a)$$

$$P_{S0-S1-S2}^{\text{ion}} = P_{S0-S1-S2} v_{S0} \frac{q_{S1} - v_{S1}}{q_{S1}} \frac{q_{S2} - v_{S2}}{q_{S2}}, \quad (113b)$$

respectively. Of course, in the case of a single vacancy (i.e., $v_{S0} = 1$ and $v_{S1} = v_{S2} = 0$), the probabilities P^{ion} reduce to those in the EADL.

To calculate the vacancy-migration coefficients C_{S_i, S_k} we use the following Monte Carlo method. We assign to each subshell S_k a vacancy counter V_{S_k} that is given the initial value $V_{S_i} = 1$ for the subshell with the primary vacancy and $V_{S_k} = 0$ for all other subshells $k \neq i$. We generate a large number N of random cascades that originate with a single vacancy in subshell S_i and terminate when all vacancies have moved to subshells beyond N1. We then count the total number of vacancies that are generated in each subshell S_k . To simplify the random sampling, the probabilities $P_{S_a-S_b}$ and $P_{S_a-S_b-S_c}$ of radiative and nonradiative transitions are set equal to the values given in the EADL, and modifications caused by the existence of multiple vacancies are accounted for by associating a variable weight w_{S_k} to each subshell S_k . At the beginning of a cascade, the subshell with the “primary” vacancy is assigned a weight $w_{S_i} = 1$, and we set $w_{S_k} = 0$ for all other subshells. At each transition, the weights of the active subshells are modified according to Eq. (113). Thus, for a nonradiative transition $S_a-S_b-S_c$, the weights become^c

$$w_{S_c} \leftarrow w_{S_c} + w_{S_a} \frac{q_{S_b} - v_{S_b}}{q_{S_b}} \frac{q_{S_c} - v_{S_c}}{q_{S_c}}, \quad (114a)$$

$$w_{S_b} \leftarrow w_{S_b} + w_{S_a} \frac{q_{S_b} - v_{S_b}}{q_{S_b}} \frac{q_{S_c} - v_{S_c}}{q_{S_c}}, \quad (114b)$$

$$w_{S_a} \leftarrow w_{S_a} \frac{v_{S_a} - 1}{v_{S_a}}, \quad (114c)$$

and the vacancy counters are modified accordingly,

$$\begin{aligned} V_{S_a} &\leftarrow V_{S_a} + w_{S_a}, \\ V_{S_b} &\leftarrow V_{S_b} + w_{S_b}, \\ V_{S_c} &\leftarrow V_{S_c} + w_{S_c}. \end{aligned} \quad (115)$$

When the decaying ion has vacancies in several different subshells, we assume that those in the innermost subshell migrate first. That is, we give preference to those sequences

^cThe notation $x \leftarrow y$ indicates that the variable x is given the value y of the expression on the right-hand side, i.e., the left arrow has the meaning of the equal sign in Fortran and in other programming languages.

of transitions that fill the innermost open subshell more rapidly. This assumption determines the active subshell Sa of the next transition, and the transition that effectively occurs is sampled randomly from the probabilities $P(Sa - Sb)$ and $P(Sa - Sb - Sc)$. At the end of the simulation run, the sought coefficients are obtained as

$$C_{Si,Sk} = \frac{1}{N} V_{Sk}, \quad (116)$$

where N is the number of simulated de-excitation cascades. For a primary vacancy in a given subshell Si , the Monte Carlo program determines the coefficients $C_{Si,Sk}$ for all the outer subshells Sk (up to the M_5 subshell) in a single run. It is found that the coefficient values obtained from this Monte Carlo counting algorithm differ slightly from the less accurate values $C_{Si,Sk}^1$ given by the recurrence formula (50) that disregards the existence of multiple vacancies. We have generated a table of coefficients $C_{Si,Sk}$ for the K shell, L subshells, and M subshells that is used to calculate vacancy production cross sections from our database of inner-shell ionization cross sections. Note, however, that the transition probabilities P_{S0-S1} and $P_{S0-S1-S2}$ in Eqs. (107) and (108) are taken from the EADL (i.e., neglecting the possible existence of vacancies other than that in the initial S0 subshell).

5. Experimental Techniques

The experimental measurement of the inner-shell ionization cross section by electron impact has been a subject of continuing investigations for many years. Methods for measuring inner-shell ionization cross sections and a description of the difficulties in making these measurements with the accuracy desired for the EPMA, AES, and EELS applications are described in three previous articles.^{2,5,7} For all elements except H and He, the cross sections have been deduced from measurements of x-ray yields, Auger-electron yields or EELS spectra, using gaseous or solid targets. For H and He, the cross sections have been deduced from H^+ and He^+ ion or secondary-electron numbers by crossed-beam methods. We initially make the assumption that the measured cross sections do not depend significantly on physical or chemical state. Thus, as discussed in Section 2.3, no account is taken of differences in the shapes of differential ionization probabilities with respect to excitation energy near innershell ionization thresholds for atoms, molecules, and solids and for elements in different compounds. We will, however, examine in Section 7 whether the calculated cross sections for atoms agree with the measured cross sections for atoms, molecules, and solids for a wide range of incident energies and for a wide range of atomic numbers. Although we consider only elemental targets (i.e., as molecules or solids), we believe that our results should also apply to those elements in compounds.

In this section, we give an overview of the different experimental methods that have been used for the determination of ionization cross sections.

5.1. Ionization cross sections from x-ray measurements

Measurements of x-ray yields emitted from solid or gaseous targets have been used to obtain inner-shell ionization cross sections. The first measurements of this kind were performed by Clark¹⁰⁹ in 1935 and Smick and Kirkpatrick¹¹⁰ in 1945, who determined the K-shell ionization cross sections at 70 keV electron incident energy of Ag and Ni, respectively. Subsequent measurements were performed by Pockman *et al.*¹¹¹ in 1947 for Ni for electron incident energies from 12 to 183 keV.

In the 1960s, Hansen *et al.*¹¹² measured the K-shell ionization cross section of Zr, Sn, W, and Pb from 240 to 1440 keV, and Hansen and Flammersfeld¹¹³ measured the K-shell ionization cross sections of Ag and Sn from 100 to 400 keV and of W, Au, and Pb from 200 to 550 keV. Motz and Placious¹¹⁴ reported measurements of K-shell ionization cross sections for Sn and Au from 50 to 500 keV. Rester and Dance¹¹⁵ extended the measurements of Motz and Placious up to 2 MeV and also measured the ionization cross sections of Ag from 100 keV to 1 MeV. At much lower energy (50 keV), Fischer and Hoffmann¹¹⁶ measured the K-shell ionization cross sections of Al, Mn, Cu, Se, and Ag. Hink and Ziegler¹¹⁷ reported K-shell ionization cross sections of Al for electrons with energies from 3 to 30 keV. The first measurements of L-shell ionization cross sections were performed by Green¹¹⁸ in 1964 and Green and Cosslett¹¹⁹ in 1968; they reported ionization cross sections for the L_2 and L_3 subshells of Au.

In subsequent years, the activity continued and new measurements of K-, L-, and M-shell ionization cross sections were reported in an energy range which extended from a few keV to 2 GeV: Berkner *et al.*,¹²⁰ Middleman *et al.*,⁷¹ Hink and Paschke,¹²¹ Salem and Moreland,¹²² Davis *et al.*,¹²³ Hubner *et al.*,¹²⁴ Scholz *et al.*,¹²⁵ Seif *et al.*,¹²⁶ Langenberg *et al.*,¹²⁷ Jessenberg and Hink,¹²⁸ Park *et al.*,¹²⁹ Schelenk *et al.*,¹³⁰ Ishii *et al.*,¹³¹ Ricz *et al.*,¹³² Berenyi *et al.*,¹³³ Hoffmann *et al.*,¹³⁴ Bonnet *et al.*,¹³⁵ Kamiya *et al.*,¹³⁶ Shima,¹³⁷ Pálinkás and Schlenk,¹³⁸ Kiss *et al.*,¹³⁹ Shima *et al.*,¹⁴⁰ Genz *et al.*,¹⁴¹ Reusch *et al.*,¹⁴² Westbrook and Quarles,¹⁴³ and McDonald and Spicer,¹⁴⁴ Schevelko *et al.*,¹⁴⁵ Singh and Shanker,¹⁴⁶ Schneider,¹⁴⁷ Luo *et al.*,^{148,149} He *et al.*,¹⁵⁰⁻¹⁵² An *et al.*,¹⁵³ Peng *et al.*,¹⁵⁴ and Tang *et al.*^{155,156}

In 2000, Liu *et al.*¹⁵⁷ tabulated experimental K-shell ionization cross sections from papers that were published prior to December 1999. Close inspection of these values revealed that they were still scarce for many elements and that significant discrepancies could be found between results from different authors. These discrepancies were often larger than the claimed experimental uncertainties. The situation for L- and M-shell ionization cross sections was even worse due to the more complex data analysis that is required (Sec. 4.2). Since then, new measurements of K- and L-shell ionization cross sections as well as L- and M-shell x-ray production cross sections have been reported by An *et al.*,¹⁵⁸⁻¹⁶⁰ Campos *et al.*,¹⁶¹ Guo *et al.*,¹⁶² Limandri *et al.*,¹⁶³ Llovet *et al.*,^{164,165} Luo *et al.*,^{166,167} Merlet *et al.*,¹⁶⁸⁻¹⁷¹ Peng

et al.,^{172,173} Tang *et al.*,¹⁷⁴ Zhou *et al.*,^{175–177} Wu *et al.*,^{162,178–188} and Yang *et al.*¹⁸⁹

The determination of the inner-shell ionization cross section σ_i from the x-ray yield N_X can be regarded as a two-step procedure. In the first step, the measured x-ray yield is converted into the cross section σ_X for the production of the considered x-ray line. This conversion depends essentially on the type of sample used. In the second step, the x-ray production cross section is converted into an inner-shell ionization cross section. The second step depends on the considered shell: for K shells, the conversion is straightforward but for L and other shells it becomes more complicated. This complexity arises from the fact that vacancies can now be produced not only by direct impact but also by Coster-Kronig transitions, super-Coster-Kronig transitions, and radiative and nonradiative transitions to inner shells. We discuss these two steps in Sec. 5.1.2.

5.1.1. Measurement of x-ray production cross sections

Measurements of x-ray production cross sections have been performed using electron beams obtained from a wide variety of instruments that range from linear electron accelerators to electron microscopes. The first measurements were carried out using scintillation crystals and proportional counters, and, over the years, these detectors have been replaced by solid-state energy-dispersive detectors such as Si(Li) and germanium detectors, as well as by high-resolution crystal spectrometers.

Different kind of targets have been used for the cross section measurements, namely, self-supporting thin films, thin films deposited on substrates, thick targets, and gases. Most of the measurements have been performed using self-supporting thin films.^{71,109–117,120,121,123–126,128,130,131,133,134,136–144,147,164,165,168,169,171,190} In this case, one generally assumes that electrons penetrate the thin-film samples following a straight-line trajectory without losing energy. This assumption is plausible for very thin films and/or electron beams with relatively high energies. The relationship between N_X and σ_X can be written as

$$\sigma_X = \frac{4\pi}{\mathcal{N} t N_e \epsilon \Delta\Omega} N_X, \quad (117)$$

where N_e is the number of incident electrons, \mathcal{N} is the density of atoms in the target (atoms per unit volume), t is the target thickness, $\Delta\Omega$ is the solid angle of collection, and ϵ is the intrinsic detector efficiency. The factor 4π occurs because the emission of x-rays is assumed to be isotropic.

The determination of the target thickness is generally the most important source of systematic uncertainty when using thin-film targets. This uncertainty can typically range from 10% to 30% depending on the thickness and the method used for thickness determination. Thicknesses can be determined by a number of techniques such as mass weighing (e.g., by a quartz-crystal microbalance), elastic scattering of electrons, Rutherford backscattering spectrometry, variable-voltage electron probe microanalysis, x-ray fluorescence, and x-ray

reflectivity. Other problems associated with the use of thin-film targets are wrinkling, non-uniformity, and, for very thin films, clustering or islanding. To reduce the likelihood of film breakage, the films have often been deposited on self-supporting backing films, generally carbon, aluminum or Mylar. Calibrated radioactive sources are typically used to determine the solid angle as well as the (photopeak) efficiency of the detector. Other methods for determining the absolute efficiency of an x-ray detector include comparisons of experimental x-ray spectra taken on well-characterized materials (generally a low- Z material) with the results of Monte Carlo simulations.¹⁷¹

Electrons undergo elastic scattering and lose energy when passing through a thin-film target. Corrections for longer path lengths due to nonlinear trajectories and for energy loss within the film (“finite” thickness effect) can be performed by replacing the film thickness t in Eq. (117) by the mean track length of transmitted electrons $l_e(E)$ and by replacing the incident electron energy E by $E - \Delta E/2$, where ΔE is the average energy loss of electrons transmitted through the film.¹⁹¹ Notice that the mean track length depends on the incident electron energy. The quantities $l_e(E)$ and ΔE can be obtained from Monte Carlo simulations or transport calculations.¹⁹² Alternatively, cross-section measurements can be performed on films with different thicknesses and an extrapolation made to zero thickness.¹²⁸ If backing films are used, a further correction is required to account for the x-ray enhancement due to the contribution of electrons backscattered from the backing film.¹⁷¹

Relative measurements of inner-shell ionization cross sections have also been reported from x-ray measurements using self-supporting films^{191,193,194} (see also Refs. 195 and 196). The energy-dependence of the x-ray production cross section also provides useful information to test the accuracy of calculations and predictive formulae for ionization cross sections. The advantage of relative measurements is that they do not require knowledge of the target thickness, detector efficiency, and number of incident electrons.

A significant number of recent measurements have been carried out using thin films deposited on thick substrates.^{148–156,158–163,166,167,172–189,197} These targets are much easier to prepare than self-supporting thin films, but there is a contribution to the x-ray yield from ionizations induced by electrons backscattered from the substrate which needs to be taken into account. This contribution may amount to 15% or more for low- Z substrates such as carbon or aluminum.¹⁴⁸ The x-ray production cross section is the difference of the direct and indirect contributions, namely,

$$\sigma_X = \frac{4\pi N_X}{N_e \mathcal{N} t \Delta\Omega \epsilon} - \left[\int_{E_i}^E dE' \sigma_X(E') \int_{-1}^1 d(\cos \theta') \frac{d^2 \eta_b}{dE' d(\cos \theta')} |\cos \theta'|^{-1} \right], \quad (118)$$

where $d^2 \eta_b / dE' d(\cos \theta')$ is the energy distribution of electrons backscattered from the substrate. This quantity has been generally determined from electron transport calculations,

such as the bipartition model¹⁴⁸ or Monte Carlo simulations using general-purpose codes such as EGS4 (Ref. 198) or PENELOPE.¹⁹² The determination of σ_X is now affected by an additional difficulty as this quantity also occurs inside an integral [Eq. (118)], and therefore an iterative procedure is required to obtain σ_X .

Experimental measurement of x-ray production cross sections can also be performed on thick targets.^{181,199–201} These measurements do not require any difficult sample preparation (apart from conventional polishing) but the data analysis is complicated by the effects of multiple scattering and energy loss within the target. As a result, careful consideration of these effects is required. An *et al.*¹⁸¹ assumed that electrons move on straight-line trajectories in the target, and that there is no contribution due to ionizations by bremsstrahlung and by backscattered electrons (with energies larger than 50 eV) to the measured x-ray yield. With these simplifications, the x-ray yield can be written as

$$N_X(E) = \int_{E_i}^E dE' \sigma_X(E') K(E, E'), \quad (119)$$

where

$$K(E, E') = \begin{cases} N_e \mathcal{N} \frac{\Delta\Omega}{4\pi} \epsilon(E_x) \exp\left[\frac{-\mu_x}{\cos\theta_x} \int_{E'}^E \frac{dE''}{S(E'')} \right] / S(E') & \text{if } E' < E \\ 0 & \text{if } E' > E \end{cases}, \quad (120)$$

where $S(E)$ is the stopping power of the material. Due to the mentioned simplifications, the validity of Eq. (120) is limited to low- Z elements and overvoltages $U = E/E_i$ less than ~ 6 .¹⁸¹ Extraction of σ_X from Eq. (120) requires the use of regularization techniques^{200,201} as this equation is ill posed. The effect of surface roughness on cross-section determination from thick targets has been discussed by Tian and An.²⁰²

Finally, cross section measurements have been performed using low-pressure (approx. 0.1 Pa) gas targets, thus minimizing the problems associated with the use of thin-film targets described above.^{134,145,146,203–207} In this case, the conversion from the observed x-ray yield to an ionization cross section is

$$\sigma_X = \frac{4\pi}{\mathcal{N} l N_e \epsilon \Delta\Omega} N_X, \quad (121)$$

where l is the effective length traveled by electrons in the gas. This quantity can be determined to a precision of 2% by means of temperature and pressure measurements.¹³⁴

For any type of target, the x-ray production cross section can also be obtained by normalizing the yield of characteristic x-rays to the yield of simultaneously emitted bremsstrahlung x-rays. This technique was introduced by Hippler²⁰⁴ and subsequently applied by Quarles and Semaan,²⁰⁶ Hippler *et al.*,^{205,207} Shevelko *et al.*,¹⁴⁵ Schneider *et al.*,¹⁴⁷ Singh and Shanker,¹⁴⁶ and Campos *et al.*¹⁶¹ By doing so, knowledge of the target thickness, detector efficiency, and number of incident electrons is not required as

these quantities cancel out in the normalization procedure. The doubly differential cross section (in energy and direction of the emitted photon) for emission of bremsstrahlung photons of energy E can be expressed as (see e.g., Ref. 206)

$$\frac{d^2\sigma_b}{d\Omega dE} = \frac{N_b}{\mathcal{N} t N_e \epsilon \Delta\Omega \Delta E}, \quad (122)$$

where N_b is the number of detected bremsstrahlung photons in an energy interval of width ΔE centered at the energy E . Taking the ratio of the cross section for characteristic x-ray emission, Eq. (118), to that for bremsstrahlung emission, Eq. (122), and assuming that the energy of the characteristic peak E_{ph} is close to the energy E where the bremsstrahlung background is measured, $\epsilon \sim \epsilon(E_{ph})$, we have

$$\sigma_X = 4\pi \frac{N_X}{N_b} \frac{d^2\sigma_b}{d\Omega dE} \Delta E. \quad (123)$$

The main source of systematic uncertainty for this method is associated with the bremsstrahlung cross section. State-of-the-art bremsstrahlung cross sections tabulated by Kissel *et al.*²⁰⁸ are believed to be accurate to about 10% and have been used to determine inner-shell ionization cross sections. In the case of self-supporting films, measurement of bremsstrahlung may be affected by stray radiation, and methods to remove such contributions to the spectral background are required.²⁰⁹

5.1.2. Conversion of the x-ray production cross sections into ionization cross section

The conversion of measured x-ray production cross sections to ionization cross sections depends upon the considered shell and the measured x-ray line.

For K-shells, the ionization cross section σ_K has generally been obtained from the $K\alpha$ x-ray production cross section [see Eq. (103)]. The required fluorescence yields ω_K are available from the compilations of Bambynek,¹⁰⁰ Krause¹⁰² and Hubbell *et al.*,¹⁰³ and the partial and total radiative widths $\Gamma_{K\alpha}$ and $\Gamma_K(R)$ are generally adopted from Scofield.¹⁰⁷ Alternatively, one can use the transition probabilities given in the EADL database of Perkins *et al.*¹ to derive σ_K [(Eq. (102)]. The uncertainties in the adopted relaxation parameters may amount to 10% and they have to be combined with those arising from the experimental determination of the $K\alpha$ x-ray production cross section. The total uncertainty in the measured K-shell ionization cross sections typically ranges from 10% to 20%.

In the case of L-shells, extraction of L-subshell ionization cross sections from measured L x-ray production cross sections is difficult because vacancies in L_i -subshells can be produced not only by direct ionization but also by migration of vacancies from K-shell ionization or from ionization of inner L-subshells. As a result, the x-ray production cross sections $\sigma_{L\ell}$, $\sigma_{L\alpha}$, $\sigma_{L\beta}$, and $\sigma_{L\gamma}$ for the most intense x-ray lines $L\ell$, $L\alpha$, $L\beta$, and $L\gamma$, respectively, are related to the ionization cross sections σ_K and σ_{L_i} through Eqs. (104) and (105). In principle, one could use Eqs. (105b)–(105d) to derive the three subshell ionization cross sections σ_{L_i} . However, x-ray spectra

often consist of a manifold of lines and some of them (e.g., $L\beta$ and $L\gamma$) cannot be sufficiently resolved using conventional solid-state x-ray detectors. Besides, some L lines (e.g., $L\gamma$ or $L\ell$) have very small count rates. As a result, small changes in the measured yields result in large changes in the evaluated cross sections. As pointed out by Cohen,²¹⁰ large differences can exist in the evaluated ionization cross sections depending on the particular choice of conversion equations [Eqs. (105)]. The use of a high-resolution crystal spectrometer allows the derivation of more accurate L subshell ionization cross sections,¹⁴² but this kind of spectrometer has only been used in a few investigations.

The fluorescence yields ω_{L_i} and Coster-Kronig yields $f_{L_i,j}$ required in Eqs. (104) and (105) are available from the compilations of Bambynek *et al.*,¹⁰⁰ Krause,¹⁰² and Campbell.²¹¹ The partial and total radiative widths required in Eq. (105), $\Gamma_{L_i,\lambda}$ and $\Gamma_{L_i}(R)$, respectively, are normally taken from Scofield's tables¹⁰⁷ and Campbell and Wang's compilation.²¹² As in the case of K-shell ionization, the transformation equations can be expressed in terms of the transition probabilities tabulated in the EADL.¹ The choices of both the relaxation parameters and the L lines that can be used to obtain the three subshell ionization cross section σ_{L_i} , may thus lead to large uncertainties in the evaluated cross sections σ_{L_i} . As a result, the estimated one-standard-deviation uncertainties of derived L-subshell ionization cross sections are much larger than those for K-shells, and range typically from 10% to 30%.

Due to the above-mentioned difficulties, there are relatively few reports of L-subshell ionization cross sections.^{118,119,122,123,129,138,140,142,147,199,204,207} Instead, most experimental results have been reported in the form of L-shell x-ray production cross sections.^{71,127,129,132,135,140,161,162,167-169,172,174,179,180,182,183,185-189,197,213}

In this way, the uncertainties in the "relaxation" parameters as well in the choice of L-lines do not contribute to the overall experimental uncertainties. Obviously, to assess the reliability of L-subshell ionization cross-section calculations, the calculated values have to be converted to L-shell x-ray production cross sections using Eqs. (104) and (105). Because of the uncertainties in the relaxation parameters that go into the calculation of x-ray production cross sections, the latter results are now affected by an "uncertainty band" whose width generally ranges from 10% to 30% (see e.g., Fernández-Varea *et al.*²¹⁴). The uncertainty bands (indicating estimated one-standard-deviation limits) are shown as gray shaded areas for the $PbL\alpha$ and $L\beta$ x-ray production cross sections in Fig. 34 that is presented in Sec. 7.2.²¹⁵

In cases where the different L x-ray lines could not be sufficiently resolved, the total L-shell ionization cross section, $\sigma_L = \sum \sigma_{L_i}$, obtained from the total L x-ray production cross section σ_{LX} , has been reported.^{131,134,141,173,206} The relationship between σ_L and σ_{LX} is as follows:

$$\sigma_{LX} = \sigma_L \bar{\omega}_L + \sigma_K \bar{\eta}_{KL}, \quad (124)$$

where $\bar{\omega}_L$ is the average fluorescence yield, defined as¹⁰⁰

$$\bar{\omega}_L = \sum_{i=1}^3 N_{L_i} \nu_{L_i}, \quad (125)$$

where $\sum N_{L_i} = 1$ and N_{L_i} , $i = 1, 2, 3$ are the fractional numbers of initial vacancies in the L_i , $i = 1, 2, 3$, subshells. The ν_{L_i} , $i = 1, 2, 3$, are the effective fluorescence yields

$$\nu_{L1} = \omega_{L1} + f_{L1,2}\omega_2 + (f_{L1,3} + f_{L1,2}f_{L2,3})\omega_3, \quad (126a)$$

$$\nu_{L2} = \omega_{L2} + f_{23}\omega_{L3}, \quad (126b)$$

$$\nu_{L3} = \omega_{L3}, \quad (126c)$$

and $\bar{\eta}_{KL}$ is the average total of L-shell vacancies produced by the decay of a K-shell vacancy. Some studies have simply reported the total L x-ray production cross section σ_{LX} .^{71,132,179}

The analysis of M-shell data is more difficult than that for L- and K-shells because of the multiplicity of processes leading to a vacancy in the active subshell and also because most M-lines cannot be sufficiently resolved using conventional solid-state x-ray detectors. To date, the very few existing studies have limited themselves to reporting the cross section for the production of $M\alpha$ x rays, $\sigma_{M\alpha}$ (e.g., Merlet *et al.*¹⁷¹) that is given by

$$\sigma_{M\alpha} = \frac{\Gamma_{M5\alpha}}{\Gamma_{M5,\text{total}}} \omega_{M5} \sigma_{M5}^{\text{vac}}, \quad (127)$$

where ω_{M5} is the fluorescence yield, and $\Gamma_{M5\alpha}$ and $\Gamma_{M5,\text{total}}$ are the partial and total radiative widths for $M5\alpha$ transitions and for all possible transitions to the $M5$ -shell, respectively, and σ_{M5}^{vac} is the $M5$ -shell vacancy production cross section that can be expressed as

$$\begin{aligned} \sigma_{M5}^{\text{vac}} = & \sigma_{M5} + \sigma_{M4} f_{M4,5} + \sigma_{M3} (S_{M3,5} + S_{M3,4} f_{M4,5}) \\ & + \sigma_{M2} [S_{M2,5} + S_{M2,3} S_{M3,5} + f_{M4,5} (S_{M2,4} \\ & + S_{M2,3} S_{M3,4})] + \sigma_{M1} [S_{M1,5} + S_{M1,2} S_{M2,5} \\ & + S_{M1,3} S_{M3,5} + S_{M1,2} S_{M2,3} S_{M3,5} \\ & + f_{M4,5} (S_{M1,4} + S_{M1,2} S_{M2,4} + S_{M1,3} S_{M3,4} \\ & + S_{M1,2} S_{M2,3} S_{M3,4})] + \sigma_{L3} \eta_{L3M5} \\ & + \sigma_{L2} \eta_{L2M5} + \sigma_{L1} \eta_{L1M5} + \sigma_K \eta_{KM5}, \end{aligned} \quad (128)$$

where σ_{M_i} , σ_{L_i} , and σ_K are the cross sections for the ionization of the M_i , L_i , and K shells, respectively, $f_{M4,5}$ is the Coster-Kronig yield between the $M4$ and $M5$ subshells, $S_{M_j,i}$ are super-Coster-Kronig yields [Eq. (92)] for transitions $M_i - M_j - M_k$, and η_{L1M5} , η_{L2M5} , and η_{L3M5} are the radiative plus nonradiative yields for transitions of vacancies from the L_1 , L_2 , and L_3 subshells to the $M5$ subshell. Notice that the contributions from additional vacancies produced through Coster-Kronig transitions of the type $L_i - L_j - M5$, as well as from transitions to L- and K-shells have been neglected in Eq. (128). Notice also that for elements with $Z \geq 65$, super-Coster-Kronig processes are not allowed.²¹⁶

The relaxation data required in Eq. (128) are available from the theoretical calculations of Bhalla,²¹⁷ McGuire,²¹⁸ and Chen and Crasemann²¹⁹ (see also the tabulations from Chauhan and Puri²²⁰ and Puri²²¹). They can also be extracted from

the EADL.¹ These relaxation parameters are affected by sizeable uncertainties that are generally larger than those for K- and L-shells.

There are also studies that have simply reported the total M-shell ionization cross section σ_M , which was extracted from the total M x-ray production cross section σ_{MX} .^{134,222} The relationship between σ_M and σ_{MX} is as follows:

$$\sigma_{MX} = \sigma_M \bar{\omega}_M + \sigma_L \bar{\eta}_{LM} + \sigma_K \bar{\eta}_{KM}, \quad (129)$$

where $\bar{\omega}_M$ is the mean fluorescence yield¹⁰⁰

$$\bar{\omega}_M = \sum_{i=1}^5 N_{Mi} \nu_{Mi}, \quad (130)$$

and where $\sum N_{Mi} = 1$ and N_{Mi} , $i = 1, 2, 3, 4, 5$, are the fractional numbers of initial vacancies in the M_i , $i = 1, 2, 3, 4, 5$, subshells. The ν_{Mi} , $i = 1, 2, 3, 4, 5$, are the effective fluorescence yields defined as

$$\begin{aligned} \nu_{M1} = & \omega_{M1} + S_{M1,2}\omega_{M2} + (S_{M1,3} + S_{M1,2}S_{M2,3})\omega_{M3} \\ & + (S_{M1,4} + S_{M1,3}S_{M3,4} + S_{M1,2}S_{M2,4} \\ & + S_{M1,2}S_{M2,3}S_{M3,4})\omega_{M4} + (S_{M1,5} + S_{M1,4}f_{M4,5} \\ & + S_{M1,3}S_{M3,5} + S_{M1,2}S_{M2,5} + S_{M1,3}S_{M3,4}f_{M4,5} \\ & + S_{M1,2}S_{M2,4}f_{M4,5} + S_{M1,2}S_{M2,3}S_{M3,5} \\ & + S_{M1,2}S_{M2,3}S_{M3,4}f_{M4,5})\omega_{M5} \end{aligned} \quad (131a)$$

$$\begin{aligned} \nu_{M2} = & \omega_{M2} + S_{M2,3}\omega_{M3} + (S_{M2,4} + S_{M2,3}S_{M3,4})\omega_{M4} \\ & + (S_{M2,5} + S_{M2,4}f_{M4,5} + S_{M2,3}S_{M3,5} \\ & + S_{M2,3}S_{M3,4}f_{M4,5})\omega_{M5} \end{aligned} \quad (131b)$$

$$\nu_{M3} = \omega_{M3} + S_{M3,4}\omega_{M4} + (S_{M3,5} + S_{M3,4}f_{M4,5})\omega_{M5} \quad (131c)$$

$$\nu_{M4} = \omega_{M4} + f_{M4,5}\omega_{M5} \quad (131d)$$

$$\nu_{M5} = \omega_{M5}. \quad (131e)$$

Here $\bar{\eta}_{KM}$ and $\bar{\eta}_{LM}$ are the average total of M-shell vacancies produced by the decay of a K-shell and a L-shell vacancy, respectively.

5.2. Ionization cross sections from Auger-electron measurements

Information on inner-shell ionization cross sections can be obtained from Auger-electron measurements for gases, solids, and atoms or molecules adsorbed on solid surfaces.²²³⁻²³²

Measurements based on Auger-electron spectra are particularly useful for determining ionization cross sections for atoms with inner-shell binding energies less than about 1 keV and for which the fluorescent yields are generally small (less than about 0.01); i.e., the Auger yields or transition probabilities are greater than about 0.99. In these experiments, the Auger yield is typically assumed to be unity. This assumption is reasonable since there are typically much larger sources of uncertainty in the experiments.

Glupe and Mehlhorn^{223,224} measured intensities of KVV Auger electrons from atoms or molecules (C in CH₄, N₂, O₂, and Ne) and reported the corresponding K-shell ionization cross sections. They calibrated the intensity scale of their instrument using calculated and measured differential cross sections for elastic scattering of electrons by He. K-shell cross sections were reported for C at a primary energy of about 1140 eV (at the maximum in the cross section versus energy curve) and for N, O, and Ne for energies from 1.5 times the K-shell binding energy to 10.5 keV (for N and Ne) and to 13 keV (for O). The estimated uncertainty of the cross sections was 5%.

Vrakking and Meyer²²⁷ determined ratios of Auger intensities from molecules containing C and another atom of interest (Si in CH₃SiCl₃, S in C₆H₅SH, and Br in C₆H₅Br); similar ratios were found for molecules containing Cl and another atom of interest (P in PCl₃, Ti in TiCl₄, and Sn in SnCl₄). L₂₃-subshell cross sections (for Si, P, S, Cl, and Ti) and M₄₅-subshell cross sections (for Br and Sn) were then derived using the K-shell cross sections for C measured by Glupe and Mehlhorn. The latter cross sections were considered to be reliable reference values since they were consistent with K-shell cross sections of other low-atomic-number elements. The uncertainties in their cross sections had contributions from the uncertainty in determining intensity ratios (between 3% and 6%), the uncertainty of the C K-shell cross section (estimated to be 2% based on comparisons with other K-shell cross sections for $U_K = 4$), and uncertainties for Coster-Kronig transitions (estimated to be 3% for the L shell and 10% for the M shell). The assumption that Auger electrons were emitted isotropically was estimated to lead to an extra uncertainty in L₂₃-subshell cross sections of less than 3%.

Similar measurements of Auger-electron intensities have been utilized by Hink *et al.*,²²⁸ Yagishita,²²⁹ Platten *et al.*,²³⁰ Suzuki *et al.*,²³¹ and Min *et al.*²³² to determine ionization cross sections. Hink *et al.* measured Auger spectra with an instrument described by Hink, Brunner, and Wolf²³³ and calibrated their Auger-intensity measurements using differential cross sections for elastic scattering of electrons. They determined K-shell ionization cross sections for Ne at electron energies from 871 eV (1 eV above the ionization threshold) to 3 keV with estimated uncertainties of about 5% for excess energies in the ionization >1 keV and of about 10% for an excess energy of 10 eV. Their cross sections agreed satisfactorily with those reported by Glupe and Mehlhorn²²⁴ and Tawara *et al.*²⁰³

In a brief report, Yagishita²²⁹ showed cross sections for ionization of the M₂, M₃, and M₄₅ subshells of Kr with electron energies between 219 eV and 3 keV. The intensity scale of his instrument was calibrated using elastic-scattering cross-section data.

Platten *et al.*²³⁰ determined K-shell ionization cross sections of O, Ne, Si (in SiH₄), and Ar for incident energies between 1.2 and 10 keV. The instrumental intensity scale was calibrated using elastic-scattering cross-section data. The intensities of all KLL Auger lines and satellite Auger lines were summed. The estimated uncertainties of their reported cross sections were 10% for O and Si, 17% for Ne, and 20% for Ar.

Suzuki *et al.*²³¹ reported L₂₃-subshell ionization cross sections for Ar, M₄₅-subshell cross sections for Kr, and

N_{45} -subshell cross sections for Xe at incident energies between about 85 eV and about 1.5 keV. The instrumental intensity scale was calibrated using elastic-scattering cross-section data, and the overall uncertainties of the cross sections were estimated to be about 35%. Similar measurements of N_{45} -subshell cross sections for Xe from the same group were reported by Min *et al.*²³² for incident energies between about 70 eV and 1 keV, and were stated to be of better reliability. The Xe measurements of Suzuki *et al.* and Min *et al.* are interesting in that they show a two-peaked structure in the cross section versus incident energy curve. The N_{45} -subshell ionization cross section rises rapidly with increasing energy to a maximum at about 120 eV (i.e., $U_{N_{45}} \sim 1.7$), then decreases until about 200 eV, and then increases again forming a broad maximum at about 500 eV ($U_{N_{45}} \sim 7.2$). This double-peaked structure has been attributed to a giant resonance and is in qualitative agreement with a calculation by Younger.²³⁴

The dependence of the inner-shell ionization cross section on primary energy has been derived by a number of authors from measurements of the primary-energy dependence of Auger-electron signal intensities from flat surfaces of semi-infinite solids. We first outline a procedure proposed by Gallon²³⁵ and Smith and Gallon.²³⁶ The signal intensity for normal incidence of the primary electron beam, within the common formalism typically used in AES,²³⁷ is expressed by

$$I_A = \frac{\Delta\Omega}{4\pi} TDP_A\lambda_{in}\mathcal{N}RI_0\sigma_{Si}(E_0), \quad (132)$$

where $\Delta\Omega$ is the solid angle subtended by the analyzer, T is the analyzer transmission, D is the detector efficiency, P_A is the probability that a given Auger transition follows the ionization, λ_{in} is the electron inelastic mean free path in the sample material, \mathcal{N} is the atomic density (number of atoms that emit the detected Auger electrons per unit volume), R is the backscattering correction factor, I_0 is the primary beam current, and $\sigma_{Si}(E_0)$ is the cross section for ionization of a particular inner shell at the primary-beam energy E_0 . For simplicity here, we have neglected atomic-relaxation effects such as Coster-Kronig transitions that modify the distribution of inner-shell vacancies following an initial ionization (as described in Sec. 4). The backscattering correction factor R takes into account the additional ionizations due to electrons backscattered from a solid. The following expression is typically used for calculations of this parameter for normal incidence of the primary beam:

$$R = 1 + \frac{2}{\sigma_{Si}(E_0)} \int_{E_i}^{E_0} \frac{d\eta}{dE} \sigma_{Si}(E) dE, \quad (133)$$

where E_i is the ionization energy of a given subshell, and $d\eta/dE$ is the energy distribution of backscattered electrons. This distribution depends on the primary energy and is normalized so that

$$\int_{E_i}^{E_0} \frac{d\eta}{dE} dE = \eta_c, \quad (134)$$

where η_c is the total reflection coefficient for energies between the core-ionization energy and the primary energy. Let us denote

$$C = \frac{\Delta\Omega}{4\pi} TDP_A\lambda_{in}\mathcal{N}. \quad (135)$$

Introducing Eqs. (133) and (135) into Eq. (132), we obtain

$$\frac{I_A}{I_0} = C\sigma_{Si}(E_0) + 2 \int_{E_i}^{E_0} \frac{d\eta}{dE} C\sigma_{Si}(E) dE. \quad (136)$$

Experimentally, we need to determine the Auger-electron signal intensity, I_A , the corresponding primary beam current, I_0 , and the energy distribution of backscattered electrons, $d\eta/dE$. These measurements should be repeated for different primary energies, E_0 . Equation (136) then becomes a so-called Volterra integral equation of the second kind. On solving this equation, we obtain the function $C\sigma_{Si}(E)$. Note that, due to the presence of the constant C , the above method provides the shape of the inner-shell ionization cross section versus energy rather than absolute values of the cross section.

Jablonski and Hartweck²³⁸ proposed a simplification facilitating solution of Eq. (136). The energy distribution of backscattered electrons can be expressed as

$$\frac{d\eta}{dE} = \eta_c(E_0)G(E), \quad (137)$$

where $G(E)$ is the energy distribution of reflected electrons (after normalization to unity). Following Gerlach and DuCharme,²³⁹ one can assume that the energy distribution $G(E)$ is uniform in the relevant energy range. Furthermore, it is assumed that the reflection coefficient $\eta_c(E_0)$ is close to the backscattering coefficient $\eta(E_0)$, the fraction of electrons reflected with energies between 50 eV and E_0 . Values of backscattering coefficients are available in the literature^{240,241} and can be used in calculations. In this way, one avoids the need for measurement of the energy distribution of backscattered electron for different primary energies. On the other hand, the above simplifying assumptions may lead to systematic deviations of the energy dependence of the cross section from the true shape.

The above procedure can be generally used in cases where the backscattering correction factor, R , for a given Auger transition in the solid is unknown. If the energy dependence of the backscattering correction factor for a given material is known, we avoid solution of the integral equation. Assuming different possible shapes for the energy dependence of the ionization cross section, we can calculate relative Auger-signal intensities from Eq. (132). By comparison with the measured energy dependence of the Auger-signal intensities, we can select the shape of the ionization cross section that leads to the best agreement with experiment. In this way, Jablonski *et al.*²⁴² showed that the Casnati *et al.*⁹¹ expression [Eq. (84) of Sec. 3.5] for the cross section for ionization of the gold N_7 subshell was in closer agreement with experiment than the Gryzinski³⁹ expression [Eq. (83) of Sec. 3.4]. Additionally, it was found that the Au N_{67} VV intensity has

substantial contributions from initial ionizations in the N_{45} subshell (by means of the Coster-Kronig $N_{45}N_{67}V$ transition). Consequently, agreement of the experimental yield curve as a function of primary energy is considerably improved when the ionization energy E_i of the N_5 subshell (335.1 eV) is used in the analytical expressions of Casnati *et al.* and Gryzinski.

Gerlach and DuCharme²³⁹ determined K-shell ionization cross sections of C, N, O, and Na from measurements of KVV Auger intensities from saturation coverages of C_2H_4 , N, O, and Na adsorbed at about 100 °C on a W(100) surface. A correction for the effects of backscattered electrons was found to be necessary only for C. The absolute values of the derived cross sections for C had an estimated uncertainty of a factor of 2 due mainly to uncertainty of the C atom density on the surface. K-shell cross sections for N, O, and Na were determined from comparisons of the corresponding Auger intensities with those from carbon, and had estimated uncertainties of a factor of 4 due in part to uncertainties in the adlayer coverages and in part to poorer knowledge of the intrinsic Auger peak shapes and widths. The cross-section measurements were made for primary energies from near the K-shell ionization threshold to about 2 keV (with values of U up to 4.5). In later work, DuCharme and Gerlach²⁴³ used the same approach to determine L_{23} -subshell ionization cross sections for S, Cl, Ti, and Cu. In these experiments, H_2S and CCl_4 were adsorbed to saturation on a W(100) surface while Ti and Cu were evaporated onto the same substrate; for the latter metals, single adlayers were assumed to be present when their Auger intensities were 0.25 of their saturation values. Auger yields were measured from near threshold to values of U up to 6.5. An approximate correction for ionization by backscattered electrons was made for S, Cl, and Ti. The resulting ionization cross sections had an estimated uncertainty of a factor of 3. The shapes of normalized K-shell and L_{23} -subshell cross sections as a function of U were found to be similar to those expected from several calculations.

Goto *et al.*²⁴⁴ analyzed the dependence of the relative intensity of Be KVV Auger electrons as thin films of Be were deposited on a Cu substrate. This Be KVV intensity was plotted as a function of the reflection coefficient for selected primary energies between 200 eV and 2 keV. For primary energies between 800 eV and 2 keV, the plots could be analyzed to determine the backscattering correction factor R for each energy. It was then possible to correct plots of relative Be KVV intensity for the contributions of backscattered electrons and obtain a plot of the relative Be K-shell ionization cross section as a function of primary energy. The shape of this plot was similar to that reported by Smith and Gallon²³⁶ for the K-shell ionization cross section of C. There was also good agreement in the energy dependence of the Be K-shell cross section with that expected from the Gryzinski formula [Eq. (83)] for $U > 7$.

In a later paper, Takeichi and Goto²⁴⁵ derived the shape of the ionization cross section from the primary-energy dependence of the Auger-electron signal intensity. The ionization cross section was calculated from the measured dependence by removing the contribution from backscattered electrons. For

this purpose, the backscattering-factor values calculated by Ichimura and Shimizu²⁴⁶ were used. In this way, the ionization cross section values were obtained for the Cu L_3 subshell (Cu $L_3M_{45}M_{45}$ transition), Cu M_1 subshell (Cu $M_1M_{45}M_{45}$ transition), Ag M_4 subshell (Ag $M_4N_{45}N_{45}$ transition), and Ag M_5 subshell (Ag $M_5N_{45}N_{45}$ transition). The proposed procedure is reliable for sufficiently high primary energies, i.e. energies exceeding 3 keV, since for such energies the backscattering factor values were available.

Batchelor *et al.*²⁴⁷ and Sato *et al.*²⁴⁸ reported relative inner-shell ionization cross sections derived from measured Auger-electron intensities for a number of elemental solids. A backscattering correction to the measured intensities was made from transport calculations of backscattered-electron energy distributions by Batchelor *et al.* and with three proposed formulae by Sato *et al.* Batchelor *et al.* obtained energy dependences of relative cross sections for K-shell ionization of Si, L_3 -subshell ionization of Cu, and M_5 -subshell ionization of Ag and W with incident-electron energies from 3 to 30 keV. Sato *et al.* determined cross-section dependencies on primary energy for K-shell ionization of C, Al, and Si, L-shell ionization of Ti and Cu, and M-shell ionization of Au for values of the overvoltage ratio U between 1.1 and 15. Batchelor *et al.* found satisfactory agreement between the shapes of the plots of measured Auger intensities with those expected from the nonrelativistic Bethe equation [Eq. (71) of Sec. 3.1] for Cu, Ag, and W while better agreement was obtained for Si with cross sections from the Gryzinski formula [Eq. (84) of Sec. 3.4]. Sato *et al.* reported good agreement between the shapes of their relative cross sections and that of the Gryzinski cross section when the backscattering correction was made with the formula proposed by Love *et al.*²⁴⁹

The accuracy of analytical expressions for the ionization cross section can be estimated from comparisons of the measured and calculated Auger-electron signal intensities. For the latter, we need to know the relevant ionization cross sections. Seah and Gilmore²⁵⁰ described a database of absolute Auger spectra originating from K, L, M, and N shells in most elements (74 elements, over 1000 spectra in total). The samples were elemental solids or compounds containing a given element. Two incident electron energies were used: 5 and 10 keV. An important feature of this work was that intensities for several Auger transitions that originated from the ionization of a given shell were added to obtain a total yield for that shell; as a result, there was no need to know the relevant Coster-Kronig transition probabilities that would be required for determination of subshell ionization cross sections. In a later study, Seah and Gilmore⁹³ analyzed the validity, in the common AES formalism (see e.g., Ref. 237), of four popular analytical formulae for the inner-shell ionization cross sections: Gryzinski³⁹ [Eq. (84)], Casnati *et al.*⁹¹ [Eq. (85)], Jakoby *et al.*⁹⁵ [Eq. (86)], and Drawin.^{81,251} To compare the analytical expressions with experiment, Seah and Gilmore calculated ratios of Auger-electron signal intensities for the two primary energies. These intensities were obtained from the common AES formalism [Eq. (132) additionally corrected for elastic scattering of the detected Auger electrons] using each formula in turn for the ionization cross

section. The resulting ratios were compared with the corresponding experimental ratios for the considered elements and Auger transitions. This approach was expected to remove instrumental contributions from the measured intensity ratios. Seah and Gilmore found that the best agreement between the calculated and measured ratios occurred with the Casnati *et al.* formula. They also drew attention to the fact that the Jakoby *et al.* expression only provides cross sections of reasonable accuracy for the K shell. This expression is of limited use for other shells since a calculated cross section may become negative in some cases (e.g., the Zr L shell). In contrast, the Casnati *et al.* expression, although derived from an empirical fit to measured K-shell cross sections, provided reasonable cross sections for K, L, M, and N shells. We stress here that the Seah and Gilmore analysis evaluates the energy dependence of a particular cross-section formula rather than absolute values of the cross sections.

5.3. Ionization cross sections from electron energy-loss spectroscopy measurements

Electron energy-loss spectroscopy is a widely-used analytical technique for thin-film analysis in the electron microscope.²⁵² Electrons transmitted through a selected region of the specimen are energy analyzed, and structure similar to x-ray absorption spectra can be associated with core-electron excitations of particular elements. It is customary to perform quantitative analyses based on measurements of the energy-loss intensity from the core-excitation threshold to a limit of about 20 eV above this threshold (after subtraction of a background associated with inelastic scattering for smaller energy losses). The measured intensities are compared with calculated partial ionization cross sections for limited ranges of energy and momentum transfers in the inner-shell excitation. These partial cross sections have been calculated for typical measurement conditions.²⁵²

In several papers, Gerlach and DuCharme^{239,253–255} reported ionization cross sections from measurements of reflection electron energy-loss spectra of adsorbed atoms or molecules on a W(100) substrate. They reported K-shell ionization cross sections of C, N, O, Na, and Mg, L₁-subshell cross sections of Na, Mg, and S, and L₂₃-subshell cross sections of Mg, S, Cl, and Cu for values of U between 1 and 4. Their data are also partial cross sections in that they measured intensities in the energy-loss spectra only from the core-excitation threshold to an energy of about 3 eV above this threshold. While these partial cross sections had an uncertainty of about a factor of 3 in the absolute values, Gerlach and DuCharme found partial agreement with the energy dependences found from an extension of the Burhop²⁵⁶ theory based on the first Born approximation.

5.4. Ionization cross sections from crossed-beam experiments

For H and He, the cross sections have been deduced from H⁺ and He⁺ ion or secondary-electron numbers by crossed-beam

methods.^{257–267} The first measurements of ionization cross sections using crossed-beam methods were reported by Fite and Brackmann,²⁵⁷ who reported the ionization cross section for atomic H from threshold up to 750 eV.

6. Comparison of Measured Cross Sections with DWBA Calculations

In Secs. 6.1–6.5, we compare measured K-, L-, and M-shell ionization cross sections available in the literature with the results of the DWBA calculations of Bote *et al.*^{31,32} All elements for which K-, L-, or M-shell ionization cross sections have been measured are summarized in Fig. 10. In the case of L and M shells, we also include measured L-shell and M-shell x-ray production cross sections. Our comparisons of measured and calculated ionization cross sections were made as a function of incident electron energy, from near the threshold energy for ionization of a given shell or subshell to 10 keV for H, 100 keV for He, 1 MeV for C, N, O, and Ne, and 1 GeV for all other elements. We also made comparisons of measured $L\alpha$ x-ray production cross sections with corresponding values calculated from the L₃-subshell ionization cross sections of Bote *et al.*^{31,32} and needed atomic data from the EADL, as described in Secs. 4.2 and 4.3. The latter comparisons were made for incident energies near the threshold for ionization to 1 GeV. As explained in Section 2.3, we include measurements made on gaseous and solid samples.

The DWBA cross sections were calculated from the convenient analytical formulae, Eqs. (87) and (88), of Bote *et al.*,³¹ that were obtained from fits to the cross sections from the DWBA for electron energies up to 16 times the threshold energy for inner-shell ionization and the PWBA for higher energies, as described in Sec. 2. These formulae are functions of the overvoltage U , the ratio of the incident electron energy to the ionization energy or binding energy for the shell or subshell of interest. As described in the Appendix, it was convenient for us to compute U using the binding energies for each shell or subshell from the tabulation of Carlson.⁶⁴

6.1. K-shell ionization cross sections

Table 2 lists all measurements of K-shell ionization cross sections that have been reported in the literature up to May 2013. Information on the incident electron energy range, method and target used, simplified reference (as shown in Figs. 11–41), and the full reference is also given. Methods include measurements with x-ray yields (X), Auger yields (A), EELS spectra (E), ion number (I), and secondary electron number (SE). Targets used include self-supporting thin films (T), thin films on substrates (TS), thick substrates (S), and gases (G).

We see from Table 2 that measurements of x-ray yields have been utilized for most of the K-shell cross-section measurements. Of these measurements, self-supporting thin films were the most commonly used targets, with smaller numbers of measurements being made with thin films on substrates, gases,

K - shells																						
H																		He				
Li	Be																B	C	N	O	F	Ne
Na	Mg																Al	Si	P	S	Cl	Ar
K	Ca	Sc	Ti	V	Cr	Mn	Fe	Co	Ni	Cu	Zn	Ga	Ge	As	Se	Br	Kr					
Rb	Sr	Y	Zr	Nb	Mo	Tc	Ru	Rh	Pd	Ag	Cd	In	Sn	Sb	Te	I	Xe					
Cs	Ba	La	Hf	Ta	W	Re	Os	Ir	Pt	Au	Hg	Tl	Pb	Bi	Po	At	Rn					
Fr	Ra	Ac																				
			Ce	Pr	Nd	Pm	Sm	Eu	Gd	Tb	Dy	Ho	Er	Tm	Yb	Lu						
			Th	Pa	U	Np	Pu	Am	Cm	Bk	Cf	Es										

(a)

L - shells																						
H																		He				
Li	Be																B	C	N	O	F	Ne
Na	Mg																Al	Si	P	S	Cl	Ar
K	Ca	Sc	Ti	V	Cr	Mn	Fe	Co	Ni	Cu	Zn	Ga	Ge	As	Se	Br	Kr					
Rb	Sr	Y	Zr	Nb	Mo	Tc	Ru	Rh	Pd	Ag	Cd	In	Sn	Sb	Te	I	Xe					
Cs	Ba	La	Hf	Ta	W	Re	Os	Ir	Pt	Au	Hg	Tl	Pb	Bi	Po	At	Rn					
Fr	Ra	Ac																				
			Ce	Pr	Nd	Pm	Sm	Eu	Gd	Tb	Dy	Ho	Er	Tm	Yb	Lu						
			Th	Pa	U	Np	Pu	Am	Cm	Bk	Cf	Es										

(b)

M - shells																						
H																		He				
Li	Be																B	C	N	O	F	Ne
Na	Mg																Al	Si	P	S	Cl	Ar
K	Ca	Sc	Ti	V	Cr	Mn	Fe	Co	Ni	Cu	Zn	Ga	Ge	As	Se	Br	Kr					
Rb	Sr	Y	Zr	Nb	Mo	Tc	Ru	Rh	Pd	Ag	Cd	In	Sn	Sb	Te	I	Xe					
Cs	Ba	La	Hf	Ta	W	Re	Os	Ir	Pt	Au	Hg	Tl	Pb	Bi	Po	At	Rn					
Fr	Ra	Ac																				
			Ce	Pr	Nd	Pm	Sm	Eu	Gd	Tb	Dy	Ho	Er	Tm	Yb	Lu						
			Th	Pa	U	Np	Pu	Am	Cm	Bk	Cf	Es										

(c)

FIG. 10. Elements for which (a) K-shell, (b) L-shell, and (c) M-shell ionization cross sections have been measured.

and thick substrates. Smaller numbers of K-shell cross sections have been determined from Auger yields with gas targets and from EELS spectra with thin-film specimens. The check marks in Table 2 indicate “superior” cross-section measurements for a given paper, as judged by the mutual consistency of sets of measurements made for a given element from different groups that we will describe in Sec. 7.1.

The graphs in Figs. 11–21 compare theoretical K-shell ionization cross sections obtained from the DWBA for electron energies up to 16 times the threshold energy for inner-shell ionization and the PWBA for higher energies, as described in Sec. 2, with measured cross sections. These comparisons were made for 63 elements from H to U using the experimental results available in the literature up to May 2013. Error bars represent the experimental uncertainties (generally one-standard-deviation limits) estimated by the authors.

In 2000, Liu *et al.*¹⁵⁷ tabulated experimental cross sections for K-shell ionization from papers that were published prior to December 1999. For these measurements, we have used the numerical values listed in the Liu *et al.* tabulation rather than the original values. Notice that in the Liu *et al.* tabulation, the

K-shell ionization cross sections obtained from x-ray and Auger measurements were reevaluated using fluorescence yields given by Bambynek *et al.*¹⁰⁰ and Hubbell *et al.*¹⁰³

We have included all of the numerical values available in the literature and digitized graphs when the experimental data were not numerically available (if the quality of figures allowed). In some cases, we have found that the same element was measured several times by the same group over the years, with no explanation as to what improvement was achieved. Although one would expect the latest measurements to be the most accurate, we have decided to include all the experimental information available without making any *a priori* judgment.

Figure 11 shows comparisons of the DWBA predictions for the K-shells of H, He, C, N, O, and Ne with experimental data. With the exception of the experimental data of Shah *et al.*²⁵⁹ for H and of Hink and Paschke¹²¹ and Colliex and Jouffrey²⁶⁸ for C, the rest of the measurement sets for each element show a remarkable agreement with each other. We note that most of these measurements were made using gas targets. The K-shell ionization cross sections for these elements can thus be regarded as being well known from experiment. For H and

TABLE 2. Measurements of K-shell ionization cross sections published up to May 2013. Information on the incident electron energy range, method and target used, simplified reference [as shown in Figs. 11–21], and the full reference is given. Methods include measurements with x-ray yields (X), Auger yields (A), EELS spectra (E), ion number (I), and secondary electron number (SE). Targets used include self-supporting thin films (T), thin films on substrates (TS), thick substrates (S), and gases (G). The check marks designate particular sets of measurements with superior data from the evaluation of experimental data (see Sec. 7)

Element	Shell	Energy (keV)	Method, target	Superior data	Key	Reference
H	K	0.0146 to 4	I,G	–	Sh87	Shah <i>et al.</i> ²⁵⁹
H	K	0.025 to 0.25	SE,G	–	Sh92	Shyn <i>et al.</i> ²⁶⁰
He	K	0.025 to 1	I,G	–	Ra65	Rapp <i>et al.</i> ²⁶¹
He	K	0.5 to 1.6	I,G	–	Sc66	Schramm <i>et al.</i> ²⁶²
He	K	0.025 to 0.18	I,G	–	St80	Stephan <i>et al.</i> ²⁶³
He	K	0.026 to 0.75	I,G	–	Mo84	Montague <i>et al.</i> ²⁶⁴
He	K	0.02 to 0.2	I,G	–	We87a	Wentzel ²⁶⁵
He	K	0.0266 to 1	I,G	–	Sh88	Shah <i>et al.</i> ²⁶⁶
He	K	0.0225 to 1	I,G	–	Re02	Rejoub <i>et al.</i> ²⁶⁷
C	K	0.426 to 4.8	A,G	✓	Gl67	Glupe and Mehlhorn ²²³
C	K	2 to 30	X,T	–	Hi71	Hink and Paschke ¹²¹
C	K	75	E,T	–	Co72	Colliex and Jouffrey ²⁶⁸
C	K	25	E,T	✓	Is72	Isaacson <i>et al.</i> ²⁶⁹
C	K	0.29 to 16.8	X,G	✓	Ta73	Tawara <i>et al.</i> ²⁰³
C	K	80	E,T	✓	Eg75	Egerton ²⁷⁰
C	K	80	E,T	✓	Ru79	Rossouw and Whelan ²⁷¹
C	K	2.5 to 25	X,TS	✓	Li12	Limandri <i>et al.</i> ¹⁶³
N	K	0.6 to 10.5	A,G	✓	Gl71	Glupe and Mehlhorn ²²⁴
N	K	25	E,T	✓	Is72	Isaacson <i>et al.</i> ²⁶⁹
N	K	0.45 to 16.8	X,G	✓	Ta73	Tawara <i>et al.</i> ²⁰³
N	K	80	E,T	✓	Ro79	Rossouw and Whelan ²⁷¹
O	K	1 to 13	A,G	✓	Gl71	Glupe and Mehlhorn ²²⁴
O	K	25	E,T	✓	Is72	Isaacson <i>et al.</i> ²⁶⁹
O	K	1 to 16.8	X,G	✓	Ta73	Tawara <i>et al.</i> ²⁰³
O	K	1.24 to 3.11	A,G	✓	Pl85	Platten <i>et al.</i> ²³⁰
O	K	2.5 to 25	X,TS	–	Li12	Limandri <i>et al.</i> ¹⁶³
Ne	K	1.31 to 10.4	A,G	✓	Gl71	Glupe and Mehlhorn ²²⁴
Ne	K	0.95 to 14.6	X,G	✓	Ta73	Tawara <i>et al.</i> ²⁰³
Ne	K	1.26 to 5.04	A,G	✓	Pl85	Platten <i>et al.</i> ²³⁰
Ne	K	0.9 to 4.37	A,G	✓	Hi81	Hink <i>et al.</i> ²²⁸
Na	K	7.0×10^4 to 2.3×10^5	X,T	–	Ka80	Kamiya <i>et al.</i> ¹³⁶
Mg	K	5.0×10^4	X,T	–	Ho79	Hoffmann <i>et al.</i> ¹³⁴
Mg	K	7.0×10^4 to 2.3×10^5	X,T	–	Ka80	Kamiya <i>et al.</i> ¹³⁶
Mg	K	1.0×10^4 to 2×10^4	X,T	–	Mc88	McDonald and Spicer ¹⁴⁴
Al	K	2.5 to 29.7	X,T	✓	Hi69	Hink and Ziegler ¹¹⁷
Al	K	1.5×10^5	X,T	✓	Is77	Ishii <i>et al.</i> ¹³¹
Al	K	5×10^4	X,T	✓	Ho79	Hoffmann <i>et al.</i> ¹³⁴
Al	K	80	E,T	✓	Ro79	Rossouw and Whelan ²⁷¹
Al	K	7.0×10^4 to 2.3×10^5	X,T	✓	Ka80	Kamiya <i>et al.</i> ¹³⁶
Al	K	1.0×10^2	X,T	–	We87b	Westbrook and Quarles ¹⁴³
Al	K	1.0×10^4 to 2×10^4	X,T	–	Mc88	McDonald and Spicer ¹⁴⁴
Al	K	2.5 to 20	X,TS	✓	Li12	Limandri <i>et al.</i> ¹⁶³
Si	K	1.5×10^5	X,T	✓	Is77	Ishii <i>et al.</i> ¹³¹
Si	K	5×10^4	X,T	✓	Ho79	Hoffmann <i>et al.</i> ¹³⁴
Si	K	2.99 to 7.9	A,G	✓	Pl85	Platten <i>et al.</i> ²³⁰
Si	K	1.6×10^4 to 2.6×10^4	X,T	✓	Sh94	Shchagin <i>et al.</i> ²⁷²
Si	K	3.3 to 24.4	X,S	✓	Zh09	Zhu <i>et al.</i> ²⁰¹
Si	K	2.5 to 20	X,TS	✓	Li12	Limandri <i>et al.</i> ¹⁶³
S	K	7.0 to 30.0	X,TS	–	Wu10a	Wu <i>et al.</i> ¹⁸⁴
Cl	K	2.7×10^5	X,T	–	Is77	Ishii <i>et al.</i> ¹³¹
Cl	K	7×10^4 to 2.3×10^5	X,T	–	Ka80	Kamiya <i>et al.</i> ¹³⁶
Cl	K	6 to 30	X,TS	–	Wu11	Wu <i>et al.</i> ¹⁸⁷
Ar	K	5 to 18.9	X,G	✓	Ta73	Tawara <i>et al.</i> ²⁰³
Ar	K	2×10^4 to 6×10^4	X,G	✓	Ho79	Hoffmann <i>et al.</i> ¹³⁴
Ar	K	4.19 to 10.3	X,G	✓	Qu82	Quarles and Semaan ²⁰⁶
Ar	K	3.37 to 12.0	X,G	✓	Hi82	Hippler <i>et al.</i> ²⁰⁵
Ar	K	3.2 to 4.2	X,G	✓	Hi83	Hippler <i>et al.</i> ²⁰⁷
Ar	K	3.64 to 9.74	A,G	✓	Pl85	Platten <i>et al.</i> ²³⁰
Ar	K	10 to 24	X,G	✓	Si03	Singh and Shanker ¹⁴⁶
K	K	3.75 to 45	X,G	–	Sh91	Shevelko <i>et al.</i> ¹⁴⁵
K	K	10 to 30	X,TS	–	Wu12	Wu <i>et al.</i> ¹⁸⁸

TABLE 2. Measurements of K-shell ionization cross sections published up to May 2013. Information on the incident electron energy range, method and target used, simplified reference [as shown in Figs. 11–21], and the full reference is given. Methods include measurements with x-ray yields (X), Auger yields (A), EELS spectra (E), ion number (I), and secondary electron number (SE). Targets used include self-supporting thin films (T), thin films on substrates (TS), thick substrates (S), and gases (G). The check marks designate particular sets of measurements with superior data from the evaluation of experimental data (see Sec. 7)—Continued

Element	Shell	Energy (keV)	Method, target	Superior data	Key	Reference
Ca	K	7×10^4 to 2.7×10^5	X,T	✓	Is77	Ishii <i>et al.</i> ¹³¹
Ca	K	2×10^4 to 6×10^4	X,T	✓	Ho79	Hoffmann <i>et al.</i> ¹³⁴
Ca	K	4.5 to 45	X,G	✓	Sh91	Shevelko <i>et al.</i> ¹⁴⁵
Ca	K	7 to 30	X,TS	✓	Wu10a	Wu <i>et al.</i> ¹⁸⁴
Sc	K	4.8 to 45.0	X,TS	–	An00	An <i>et al.</i> ¹⁵⁸
Ti	K	5.9 to 50	X,T	✓	Je75	Jessenberg and Hink ¹²⁸
Ti	K	1.0×10^2	X,T	–	We87b	Westbrook and Quarles ¹⁴³
Ti	K	5.5 to 29.0	X,TS	–	He97	He <i>et al.</i> ¹⁵²
Ti	K	5.6 to 25.9	X,TS	✓	An03	An <i>et al.</i> ¹⁶⁰
Ti	K	6 to 25	X,TS	✓	Li12	Limandri <i>et al.</i> ¹⁶³
V	K	2×10^3	X,T	–	Sc72	Scholz <i>et al.</i> ¹²⁵
V	K	5.9 to 45.0	X,TS	–	An00	An <i>et al.</i> ¹⁵⁸
Cr	K	2×10^3	X,T	✓	Sc72	Scholz <i>et al.</i> ¹²⁵
Cr	K	2×10^4 to 6×10^4	X,T	✓	Ho79	Hoffmann <i>et al.</i> ¹³⁴
Cr	K	6 to 25	X,TS	✓	Lu96	Luo <i>et al.</i> ¹⁴⁸
Cr	K	6 to 25	X,TS	–	He97	He <i>et al.</i> ¹⁵²
Cr	K	6.5 to 40.0	X,T	✓	Li00	Llovet <i>et al.</i> ¹⁶⁴
Cr	K	6.9 to 26.6	X,TS	✓	An03	An <i>et al.</i> ¹⁶⁰
Mn	K	50	X,T	✓	Fi67	Fischer and Hoffmann ¹¹⁶
Mn	K	2×10^3	X,T	✓	Sc72	Scholz <i>et al.</i> ¹²⁵
Mn	K	5×10^4	X,T	✓	Ho79	Hoffmann <i>et al.</i> ¹³⁴
Mn	K	6.7 to 20.0	X,T	✓	Sh80	Shima ¹³⁷
Mn	K	3.5 to 25.9	X,TS	✓	Lu97	Lu <i>et al.</i> ¹⁴⁹
Mn	K	6.9 to 25.1	X,TS	✓	Ta99b	Tang <i>et al.</i> ¹⁵⁶
Mn	K	7.0 to 40.0	X,T	✓	Li02	Llovet <i>et al.</i> ¹⁶⁵
Fe	K	2×10^3	X,T	✓	Sc72	Scholz <i>et al.</i> ¹²⁵
Fe	K	7.5 to 28.0	X,TS	–	He96a	He <i>et al.</i> ¹⁵⁰
Fe	K	7.9 to 24.8	X,TS	✓	Lu97	Luo <i>et al.</i> ¹⁴⁹
Fe	K	7.5 to 40.0	X,T	✓	Li02	Llovet <i>et al.</i> ¹⁶⁵
Co	K	2×10^3	X,T	–	Sc72	Scholz <i>et al.</i> ¹²⁵
Co	K	8.5 to 24.9	X,TS	–	An96	An <i>et al.</i> ¹⁵³
Ni	K	70	X,T	✓	Sm45	Smick and Kirkpatrick ¹¹⁰
Ni	K	1.5×10^1 to 1.8×10^2	X,T	–	Po47	Pockman <i>et al.</i> ¹¹¹
Ni	K	4.9×10^2 to 6.7×10^2	X,T	–	Se74	Seif <i>et al.</i> ¹²⁶
Ni	K	8.9 to 49.7	X,T	✓	Je75	Jessenberg and Hink ¹²⁸
Ni	K	2×10^4 to 6×10^4	X,T	✓	Ho79	Hoffmann <i>et al.</i> ¹³⁴
Ni	K	9×10^5 to 2×10^6	X,T	✓	Ge82	Genz <i>et al.</i> ¹⁴¹
Ni	K	9.0 to 34.0	X,TS	✓	Lu96	Luo <i>et al.</i> ¹⁴⁸
Ni	K	9.0 to 46.0	X,TS	–	He97	He <i>et al.</i> ¹⁵²
Ni	K	9.0 to 40.0	X,T	✓	Li00	Llovet <i>et al.</i> ¹⁶⁴
Ni	K	9.0 to 46.0	X,S	✓	An06	An <i>et al.</i> ¹⁸¹
Cu	K	50	X,T	✓	Fi67	Fischer and Hoffmann ¹¹⁶
Cu	K	1.5×10^5 to 9×10^5	X,T	✓	Mi70	Middleman <i>et al.</i> ⁷¹
Cu	K	25 to 135	X,T	–	Da72	Davis <i>et al.</i> ¹²³
Cu	K	81 to 152	X,T	✓	Hu72	Hubner <i>et al.</i> ¹²⁴
Cu	K	2×10^3	X,T	✓	Sc72	Scholz <i>et al.</i> ¹²⁵
Cu	K	1.5×10^5	X,T	✓	Is77	Ishii <i>et al.</i> ¹³¹
Cu	K	3×10^2 to 6×10^2	X,T	✓	Be78	Berenyi <i>et al.</i> ¹³³
Cu	K	4×10^4	X,T	✓	Ho79	Hoffmann <i>et al.</i> ¹³⁴
Cu	K	9.27 to 25.0	X,T	✓	Sh80	Shima ¹³⁷
Cu	K	9.12 to 25.0	X,T	✓	Sh81	Shima <i>et al.</i> ¹⁴⁰
Cu	K	9×10^5 to 2×10^6	X,T	–	Ge82	Genz <i>et al.</i> ¹⁴¹
Cu	K	1.0×10^2	X,T	–	We87b	Westbrook and Quarles ¹⁴³
Cu	K	9.4 to 25.9	X,TS	✓	An96	An <i>et al.</i> ¹⁵³
Cu	K	9.0 to 28.0	X,TS	✓	He97	He <i>et al.</i> ¹⁵²
Cu	K	9.5 to 40.0	X,T	✓	Li00	Llovet <i>et al.</i> ¹⁶⁴
Cu	K	10.0 to 26.0	X,TS	✓	Zh01c	Zhou <i>et al.</i> ¹⁷⁷
Zn	K	2×10^3	X,T	✓	Sc72	Scholz <i>et al.</i> ¹²⁵
Zn	K	1.5×10^5	X,T	✓	Is77	Ishii <i>et al.</i> ¹³¹
Zn	K	10.3 to 25.7	X,TS	✓	Ta99a	Tang <i>et al.</i> ¹⁵⁵

TABLE 2. Measurements of K-shell ionization cross sections published up to May 2013. Information on the incident electron energy range, method and target used, simplified reference [as shown in Figs. 11–21], and the full reference is given. Methods include measurements with x-ray yields (X), Auger yields (A), EELS spectra (E), ion number (I), and secondary electron number (SE). Targets used include self-supporting thin films (T), thin films on substrates (TS), thick substrates (S), and gases (G). The check marks designate particular sets of measurements with superior data from the evaluation of experimental data (see Sec. 7)—Continued

Element	Shell	Energy (keV)	Method, target	Superior data	Key	Reference
Zn	K	11.0 to 30.0	X,TS	✓	Wu10a	Wu <i>et al.</i> ¹⁸⁴
Ga	K	12.0 to 26.0	X,TS	✓	Zh01c	Zhou <i>et al.</i> ¹⁷⁷
Ga	K	12.0 to 28.0	X,TS	✓	Zh02	Zhou <i>et al.</i> ²⁷³
Ga	K	10.5 to 39.0	X,T	✓	Me06	Merlet <i>et al.</i> ^{169,170}
Ge	K	2×10 ⁴ to 6×10 ⁴	X,T	✓	Ho79	Hoffmann <i>et al.</i> ¹³⁴
Ge	K	11.2 to 25.0	X,T	✓	Sh81	Shima <i>et al.</i> ¹⁴⁰
Ge	K	11.5 to 40.0	X,TS	✓	Ta02a	Tang <i>et al.</i> ¹⁹⁷
Ge	K	12.0 to 26.0	X,TS	✓	Zh02	Zhou <i>et al.</i> ²⁷³
Ge	K	11.6 to 40.6	X,T	✓	Me04	Merlet <i>et al.</i> ¹⁶⁸
As	K	2×10 ³	X,T	–	Sc72	Scholz <i>et al.</i> ¹²⁵
As	K	12.0 to 39.0	X,T	–	Me06	Merlet <i>et al.</i> ^{169,170}
Se	K	50	X,T	–	Fi67	Fischer and Hoffmann ¹¹⁶
Se	K	2×10 ³	X,T	✓	Sc72	Scholz <i>et al.</i> ¹²⁵
Se	K	7×10 ⁴ to 1.5×10 ⁵	X,T	✓	Is77	Ishii <i>et al.</i> ¹³¹
Se	K	3×10 ² to 6×10 ²	X,T	✓	Be78	Barenyi <i>et al.</i> ¹³³
Se	K	6×10 ¹ to 6×10 ²	X,T	✓	Ki81	Kiss <i>et al.</i> ¹³⁹
Se	K	13 to 40	X,TS	✓	Lu01	Luo <i>et al.</i> ¹⁶⁶
Br	K	2×10 ³	X,T	–	Sc72	Scholz <i>et al.</i> ¹²⁵
Kr	K	2×10 ⁴ to 6×10 ⁴	X,G	–	Ho79	Hoffmann <i>et al.</i> ¹³⁴
Rb	K	2×10 ³	X,T	–	Sc72	Scholz <i>et al.</i> ¹²⁵
Rb	K	16 to 45	X,G	–	Sh91	Shevelko <i>et al.</i> ¹⁴⁵
Sr	K	2×10 ³	X,T	–	Sc72	Scholz <i>et al.</i> ¹²⁵
Sr	K	17 to 45	X,G	–	Sh91	Shevelko <i>et al.</i> ¹⁴⁵
Sr	K	1.5×10 ⁵ to 9×10 ⁵	X,T	–	Mi70	Middleman <i>et al.</i> ⁷¹
Y	K	4.9×10 ² to 6.7×10 ²	X,T	✓	Se74	Seif <i>et al.</i> ¹²⁶
Y	K	7×10 ⁴ to 2.7×10 ⁵	X,T	✓	Is77	Ishii <i>et al.</i> ¹³¹
Y	K	5.0×10 ⁴	X,T	✓	Ho79	Hoffmann <i>et al.</i> ¹³⁴
Y	K	18 to 32	X,TS	✓	Lu01	Luo <i>et al.</i> ¹⁶⁶
Zr	K	2.4×10 ² to 1.4×10 ³	X,T	–	Ha64	Hansen <i>et al.</i> ¹¹²
Zr	K	1.0×10 ²	X,T	–	We87b	Westbrook <i>et al.</i> ¹⁴³
Zr	K	18.0 to 34.0	X,TS	–	Zh02	Zhou <i>et al.</i> ²⁷³
Nb	K	20.0 to 34.0	X,TS	–	Pe98	Peng <i>et al.</i> ¹⁵⁴
Mo	K	1.5×10 ⁵ to 9×10 ⁵	X,T	–	Mi70	Middleman <i>et al.</i> ⁷¹
Mo	K	9×10 ⁴ to 2.7×10 ⁵	X,T	–	Is77	Ishii <i>et al.</i> ¹³¹
Mo	K	21.0 to 40.0	X,TS	–	He <i>et al.</i> ¹⁵¹	He <i>et al.</i> ¹⁵¹
Pd	K	2.5×10 ³ to 7.1×10 ⁵	X,T	✓	Be70	Berkner <i>et al.</i> ¹²⁰
Pd	K	9×10 ⁴ to 2.5×10 ⁵	X,T	✓	Is77	Ishii <i>et al.</i> ¹³¹
Pd	K	3×10 ² to 6×10 ²	X,T	✓	Ri77	Ricz <i>et al.</i> ¹⁹⁰
Ag	K	30.5 to 300	X,T	–	Cl35	Clark <i>et al.</i> ¹⁰⁹
Ag	K	1.1×10 ² to 4.3×10 ²	X,T	–	Ha66	Hansen and Flammersfeld ¹¹³
Ag	K	3×10 ² to 1×10 ³	X,T	✓	Re66	Rester and Dance ¹¹⁵
Ag	K	50	X,T	✓	Fi67	Fischer and Hoffmann ¹¹⁶
Ag	K	30 to 140	X,T	–	Da72	Davis <i>et al.</i> ¹²³
Ag	K	1.14×10 ²	X,T	✓	Hu72	Hubner <i>et al.</i> ¹²⁴
Ag	K	4.9×10 ² to 6.7×10 ²	X,T	✓	Se74	Seif <i>et al.</i> ¹²⁶
Ag	K	5×10 ² to 6×10 ²	X,T	✓	Sc76	Schlenk <i>et al.</i> ¹³⁰
Ag	K	3×10 ² to 6×10 ²	X,T	✓	Ri77	Ricz <i>et al.</i> ¹⁹⁰
Ag	K	2×10 ⁴ to 6×10 ⁴	X,T	✓	Ho79	Hoffmann <i>et al.</i> ¹³⁴
Ag	K	6×10 ¹ to 6×10 ²	X,T	✓	Ki81	Kiss <i>et al.</i> ¹³⁹
Ag	K	26 to 30	X,T	✓	Sh81	Shima <i>et al.</i> ¹⁴⁰
Ag	K	9×10 ⁵ to 2×10 ⁶	X,T	✓	Ge82	Genz <i>et al.</i> ¹⁴¹
Ag	K	1.0×10 ²	X,T	✓	We87b	Westbrook and Quarles ¹⁴³
Ag	K	30 to 65	X,T	✓	Sc93	Schneider <i>et al.</i> ¹⁴⁷
Ag	K	26.0 to 34.0	X,TS	✓	Zh01b	Zhou <i>et al.</i> ¹⁷⁶
Cd	K	2×10 ³	X,T	–	Sc72	Scholz <i>et al.</i> ¹²⁵
In	K	7×10 ⁵ to 9×10 ⁵	X,T	–	Mi70	Middleman <i>et al.</i> ⁷¹
In	K	2×10 ³	X,T	–	Sc72	Scholz <i>et al.</i> ¹²⁵
In	K	1.5×10 ⁵	X,T	–	Is77	Ishii <i>et al.</i> ¹³¹
In	K	3×10 ² to 6×10 ²	X,T	–	Ri77	Ricz <i>et al.</i> ¹⁹⁰
Sn	K	50	X,T	✓	Fi67	Fischer and Hoffmann ¹¹⁶
Sn	K	2.4×10 ² to 1.4×10 ³	X,T	–	Ha64	Hansen <i>et al.</i> ¹¹²

TABLE 2. Measurements of K-shell ionization cross sections published up to May 2013. Information on the incident electron energy range, method and target used, simplified reference [as shown in Figs. 11–21], and the full reference is given. Methods include measurements with x-ray yields (X), Auger yields (A), EELS spectra (E), ion number (I), and secondary electron number (SE). Targets used include self-supporting thin films (T), thin films on substrates (TS), thick substrates (S), and gases (G). The check marks designate particular sets of measurements with superior data from the evaluation of experimental data (see Sec. 7)—Continued

Element	Shell	Energy (keV)	Method, target	Superior data	Key	Reference
Sn	K	2×10^2 to 2×10^3	X,T	–	Re66	Rester and Dance ¹¹⁵
Sn	K	1.0×10^2 to 4.1×10^2	X,T	–	Ha66	Hansen and Flammersfeld ¹¹³
Sn	K	2×10^3	X,T	✓	Sc72	Scholz <i>et al.</i> ¹²⁵
Sn	K	3×10^2 to 6×10^2	X,T	–	Ri77	Ricz <i>et al.</i> ¹⁹⁰
Sn	K	1.5×10^5	X,T	✓	Is77	Ishii <i>et al.</i> ¹³¹
Sn	K	2.0×10^4 to 5.0×10^4	X,T	✓	Ho79	Hoffmann <i>et al.</i> ¹³⁴
Sb	K	2×10^3	X,T	✓	Sc72	Scholz <i>et al.</i> ¹²⁵
Sb	K	1.0×10^2	X,T	✓	We87b	Westbrook and Quarles ¹⁴³
Sb	K	1×10^1 to 6×10^2	X,T	✓	Ki81	Kiss <i>et al.</i> ¹³⁹
Te	K	2×10^3	X,T	–	Sc72	Scholz <i>et al.</i> ¹²⁵
Xe	K	2×10^4 to 6×10^3	X,G	–	Sc72	Scholz <i>et al.</i> ¹²⁵
Ba	K	2×10^3	X,T	–	Sc72	Scholz <i>et al.</i> ¹²⁵
Ba	K	7×10^4 to 2.7×10^5	X,T	–	Is77	Ishii <i>et al.</i> ¹³¹
Ba	K	1.0×10^2	X,T	–	We87b	Westbrook and Quarles ¹⁴³
La	K	2×10^3	X,T	–	Sc72	Scholz <i>et al.</i> ¹²⁵
La	K	1.0×10^2	X,T	–	We87b	Westbrook and Quarles ¹⁴³
Ce	K	2×10^3	X,T	–	Sc72	Scholz <i>et al.</i> ¹²⁵
Pr	K	2×10^3	X,T	–	Sc72	Scholz <i>et al.</i> ¹²⁵
Pr	K	1.0×10^2	X,T	–	We87b	Westbrook and Quarles ¹⁴³
Nd	K	2×10^3	X,T	–	Sc72	Scholz <i>et al.</i> ¹²⁵
Sm	K	2×10^3	X,T	–	Sc72	Scholz <i>et al.</i> ¹²⁵
Sm	K	9×10^4	X,T	–	Is77	Ishii <i>et al.</i> ¹³¹
Eu	K	2×10^3	X,T	–	Sc72	Scholz <i>et al.</i> ¹²⁵
Gd	K	2×10^3	X,T	–	Sc72	Scholz <i>et al.</i> ¹²⁵
Ho	K	2×10^4 to 5×10^3	X,T	–	Sc72	Scholz <i>et al.</i> ¹²⁵
Ho	K	9×10^4	X,T	–	Is77	Ishii <i>et al.</i> ¹³¹
Er	K	2×10^3	X,T	–	Sc72	Scholz <i>et al.</i> ¹²⁵
Tm	K	3×10^5 to 9×10^5	X,T	–	Mi70	Middleman <i>et al.</i> ⁷¹
Yb	K	2×10^3	X,T	–	Sc72	Scholz <i>et al.</i> ¹²⁵
Yb	K	4.9×10^2 to 2.0×10^3	X,T	–	Se74	Seif <i>et al.</i> ¹²⁶
Ta	K	3×10^5 to 5×10^5	X,T	–	Mi70	Middleman <i>et al.</i> ⁷¹
Ta	K	4.9×10^2 to 6.7×10^2	X,T	–	Se74	Seif <i>et al.</i> ¹²⁶
W	K	2.4×10^2 to 1.4×10^3	X,T	–	Ha64	Hansen <i>et al.</i> ¹¹²
W	K	2.1×10^2 to 5.5×10^2	X,T	–	Ha66	Hansen and Flammersfeld ¹¹³
Au	K	1.0×10^2 to 5.0×10^2	X,T	–	Mo64	Motz and Placious <i>et al.</i> ¹¹⁴
Au	K	2.3×10^2 to 5.6×10^2	X,T	–	Ha66	Hansen and Flammersfeld ¹¹³
Au	K	2×10^2 to 2×10^3	X,T	✓	Re66	Rester and Dance ¹¹⁵
Au	K	2.5×10^3 to 7.1×10^3	X,T	✓	Be70	Berkner <i>et al.</i> ¹²⁰
Au	K	3.0×10^5 to 9.0×10^5	X,T	✓	Mi70	Middleman <i>et al.</i> ⁷¹
Au	K	2×10^3	X,T	✓	Sc72	Scholz <i>et al.</i> ¹²⁵
Au	K	9×10^1 to 1.4×10^2	X,T	✓	Da72	Davis <i>et al.</i> ¹²³
Au	K	4.9×10^2 to 6.7×10^2	X,T	–	Se74	Seif <i>et al.</i> ¹²⁶
Au	K	9×10^4	X,T	✓	Is77	Ishii <i>et al.</i> ¹³¹
Au	K	2.0×10^4 to 6.0×10^4	X,T	✓	Ho79	Hoffmann <i>et al.</i> ¹³⁴
Au	K	1.0×10^2	X,T	–	We87b	Westbrook and Quarles ¹⁴³
Pb	K	2.4×10^2 to 1.4×10^3	X,T	–	Ha64	Hansen <i>et al.</i> ¹¹²
Pb	K	2.6×10^2 to 5.6×10^2	X,T	–	Ha66	Hansen and Flammersfeld ¹¹³
Pb	K	2×10^3	X,T	✓	Sc72	Scholz <i>et al.</i> ¹²⁵
Pb	K	4.9×10^2 to 6.7×10^2	X,T	✓	Se74	Seif <i>et al.</i> ¹²⁶
Pb	K	9×10^4	X,T	✓	Is77	Ishii <i>et al.</i> ¹³¹
Pb	K	5.0×10^4	X,T	✓	Ho79	Hoffmann <i>et al.</i> ¹³⁴
Bi	K	3.0×10^5 to 9.0×10^5	X,T	✓	Mi70	Middleman <i>et al.</i> ⁷¹
Bi	K	2×10^3	X,T	✓	Sc72	Scholz <i>et al.</i> ¹²⁵
Bi	K	9.0×10^4	X,T	✓	Is77	Ishii <i>et al.</i> ¹³¹
Bi	K	3.5×10^4 to 6.0×10^4	X,T	✓	Ho79	Hoffmann <i>et al.</i> ¹³⁴
U	K	9.01×10^4	X,T	–	Is77	Ishii <i>et al.</i> ¹³¹

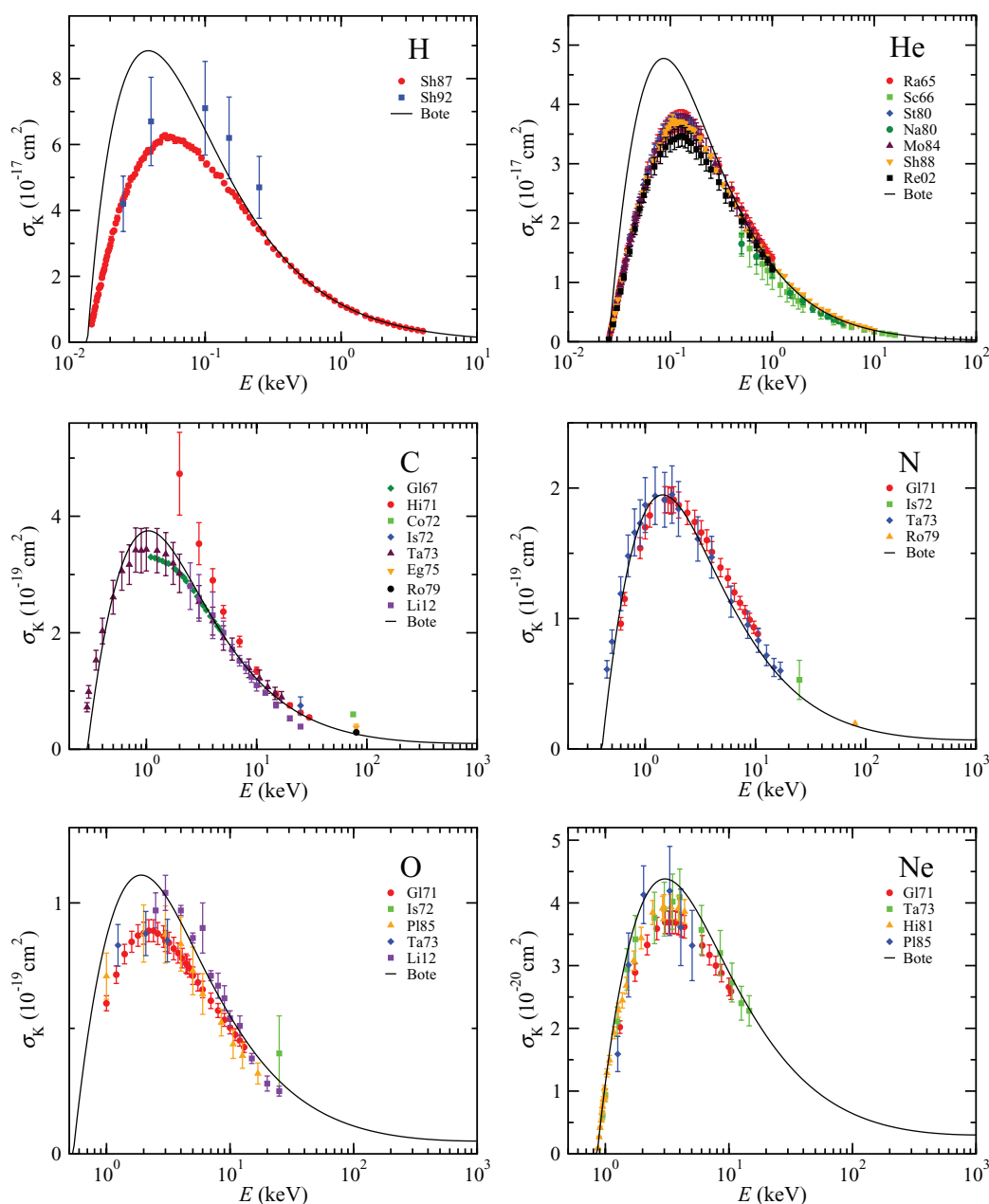


FIG. 11. (Color online) Absolute K-shell ionization cross sections vs. incident electron energy for H, He, C, N, O, and Ne. Solid curves are the results of the DWBA calculations. The symbols show measured cross sections, with the legend indicating the key references identified in Table 2.

He, the predictions of the DWBA overestimate the experimental measurements in the region of the maximum by between 20% and 30%. This result is not surprising since for such small atomic numbers the electrostatic field of the emerging target electron is comparable to the screened field of the nucleus and, consequently, the central-field approximation, implicit in the DWBA, is not appropriate (see Sec. 2.2). A similar tendency is observed for O and Ne, although the discrepancies between calculations and experiment are not as large as for H and He. For C and N, the DWBA cross sections are in very good agreement with the experimental data (not considering the data sets of Shah *et al.*²⁵⁹ for H and of Hink and Paschke¹²¹ and Colliex and Jouffrey²⁶⁸ for C).

Figure 12 displays the experimentally determined K-shell ionization cross sections for Na, Mg, Al, Si, S, and Cl, in comparison with the DWBA predictions. For Na, Mg, and Cl, there are experimental data sets only at high energies; while good agreement between measured and calculated cross sections are found at high energies for Na and Cl (as well as for Si and some Mg and Al data), some measured cross sections for Mg and Al are less than half of the DWBA values. Nearer the ionization threshold, the available experimental data are in satisfactory agreement with the DWBA calculations for Si and Al. For S, the DWBA calculations overestimate the single set of measurements by 15%. We note that the latter experimental data were obtained using ZnS films.

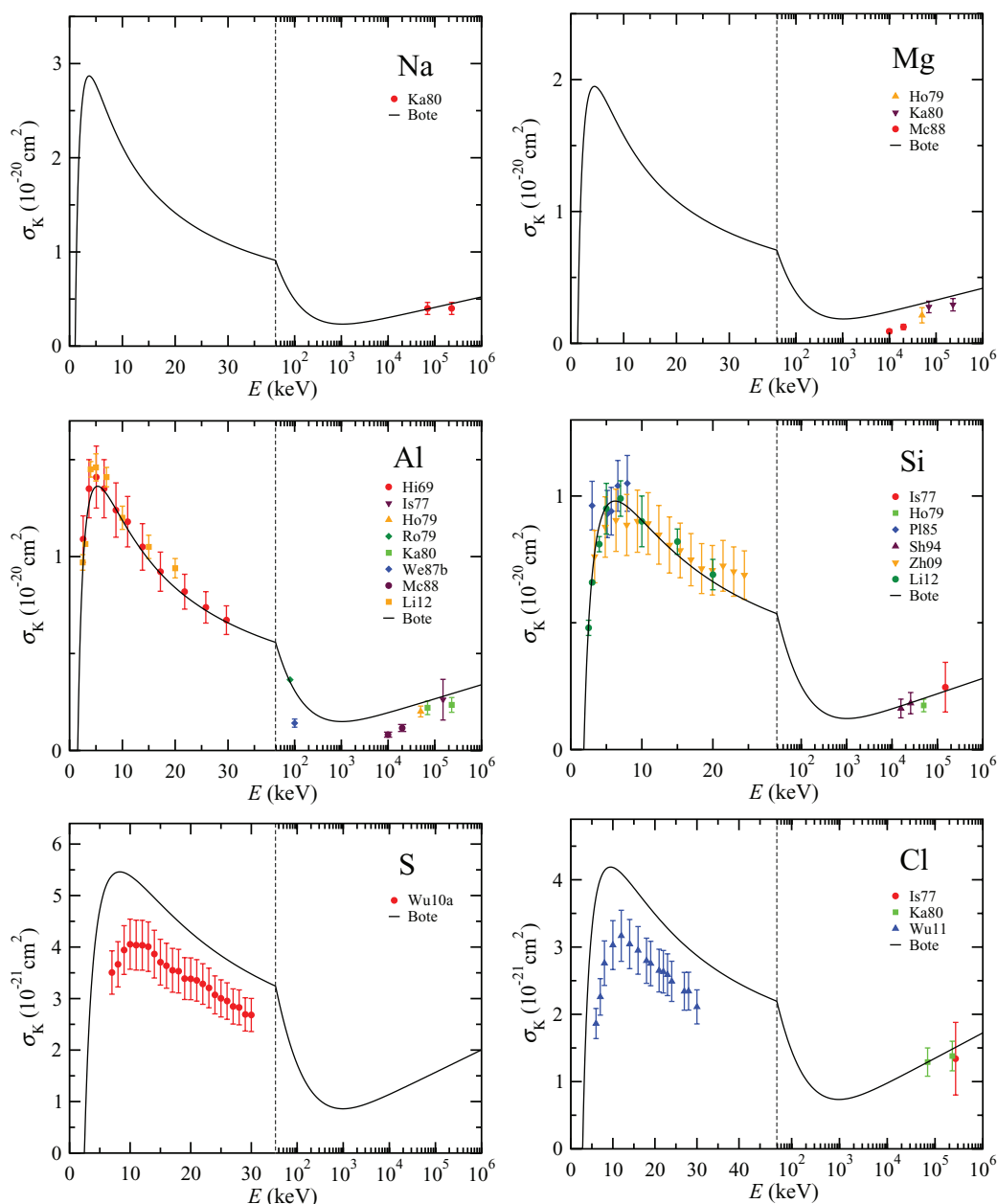


FIG. 12. (Color online) Absolute K-shell ionization cross sections vs. incident electron energy for Na, Mg, Al, Si, S, and Cl. Solid curves are the results of the DWBA calculations. Symbols are experimental measurements. Notice the change of abscissa scale.

For Ar, K, Ca, and Sc (Fig. 13), in comparison with experimental data, the DWBA calculations overestimate the cross sections near the ionization threshold by up to 10% but, in general, there is reasonable agreement as far as the cross-section shapes are concerned. As mentioned earlier, the measurement of the shape of the cross-section curves (i.e., the relative cross sections) is only affected by relative uncertainties which generally are much lower than the total uncertainties displayed by the error bars (which include estimates of possible systematic uncertainties). For Ar and Ca, the experimental data for each element agree well with each other, whereas for K and Sc only one set of experimental data is available in the literature. While there are systematic deviations of some of the measured cross sections for Ca from the Bote curve over a small range of energies

(from about 5 to 15 keV), the magnitudes of these deviations are comparable to those found for other data sets which we will assess as “superior data” in Sec. 7.2. The agreement among the various experimental data sets is not as good for Ti, with the measurements of He *et al.*¹⁵² lying clearly below the other measurements. The DWBA calculations agree reasonably well with the measurements of Jessenberg *et al.*¹²⁸ In the case of V, the predictions of the DWBA represent well the experimental measurements within the stated experimental errors, both at low and high energies.

Figure 14 shows the experimental data available for Cr, Mn, Fe, Co, Ni, and Cu in comparison with the DWBA calculations. Except for Co, the number of experimental data sets available is relatively large. For Cr, Fe, and Ni, some of the

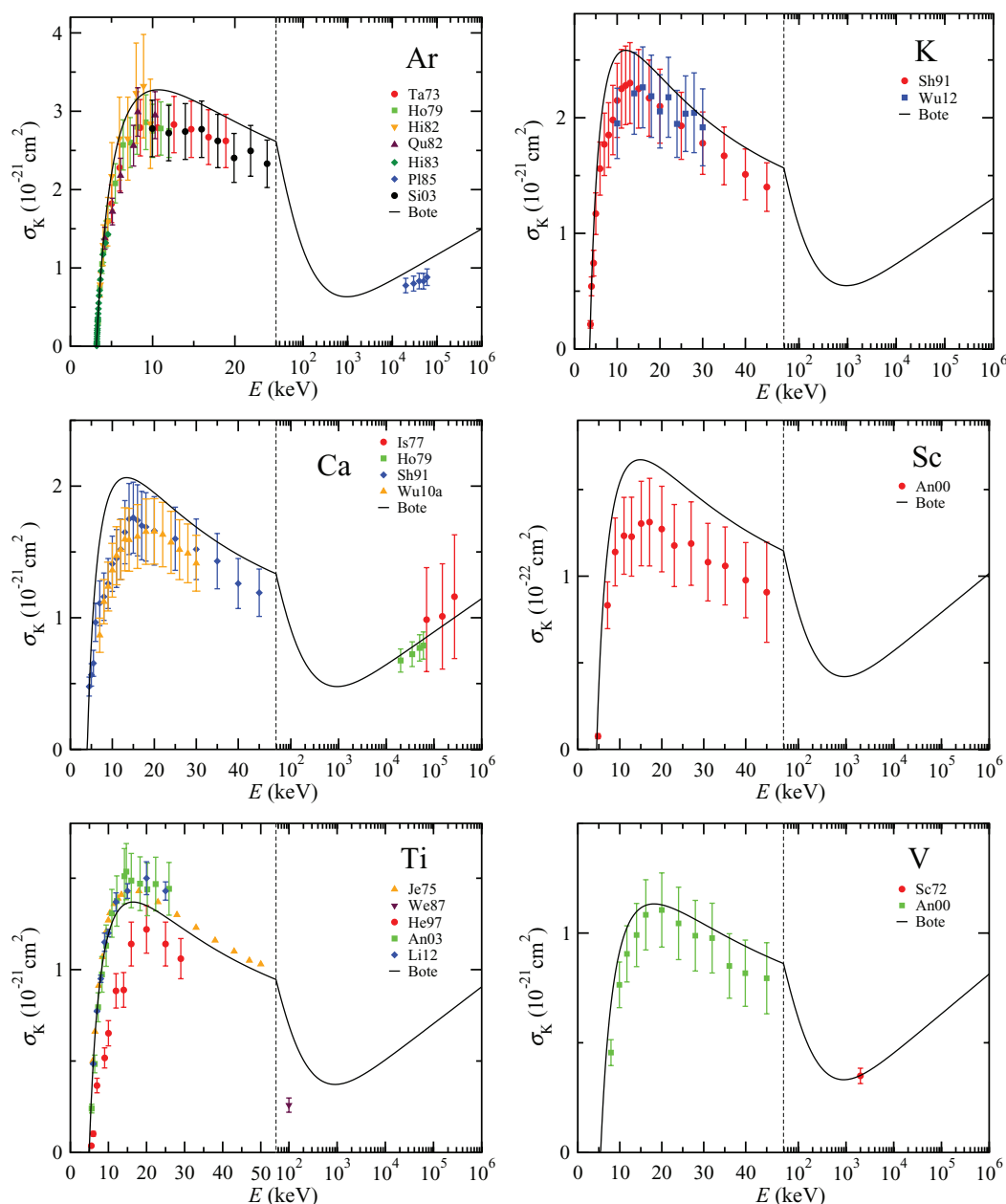


FIG. 13. (Color online) Absolute K-shell ionization cross sections vs. incident electron energy for Ar, K, Ca, Sc, Ti, and V. Solid curves are the results of the DWBA calculations. Symbols are experimental measurements. Note the change of abscissa scale.

experimental data sets available are in marked disagreement with the rest of measurements that agree well with each other. For Cr, the experimental data of He *et al.*¹⁵² lie below the other measurements by as much as 30%; for Fe, the measurements of He *et al.*¹⁵⁰ lie above (by 30%) the other available measurements; for Ni, the experimental data of He *et al.*¹⁵² lie below (by up to 40%) the other measurements; and for Cu, the measurements of Llovet *et al.*¹⁶⁵ and Davis *et al.*¹²³ are systematically above (by 10% and 40%, respectively) the other measurements. With the exceptions mentioned, the available experimental data for Cr, Co, Fe, and Cu are in good agreement with the DWBA predictions, both at low and high energies. For Mn, the predictions of the DWBA agree reasonably well with the experimental data within the quoted

uncertainties, although the spread of the experimental data is much larger.

Figure 15 shows the experimentally determined K-shell ionization cross sections for Zn, Ga, Ge, As, Se, and Br in comparison with the DWBA calculations. With the exception of the experimental data of Tang *et al.*¹⁷⁴ for Ge, the remaining experimental data for each element are in agreement with each other within the quoted error bars of $\pm 10\%$. For all of these elements, the experimental data are well described by the predictions of the DWBA, both in shape and magnitude. We note the excellent agreement between the DWBA and the experimental data of Merlet *et al.*¹⁶⁹ for Ga. For Br, only one single data point at 200 keV is available, and this is consistent with the DWBA.

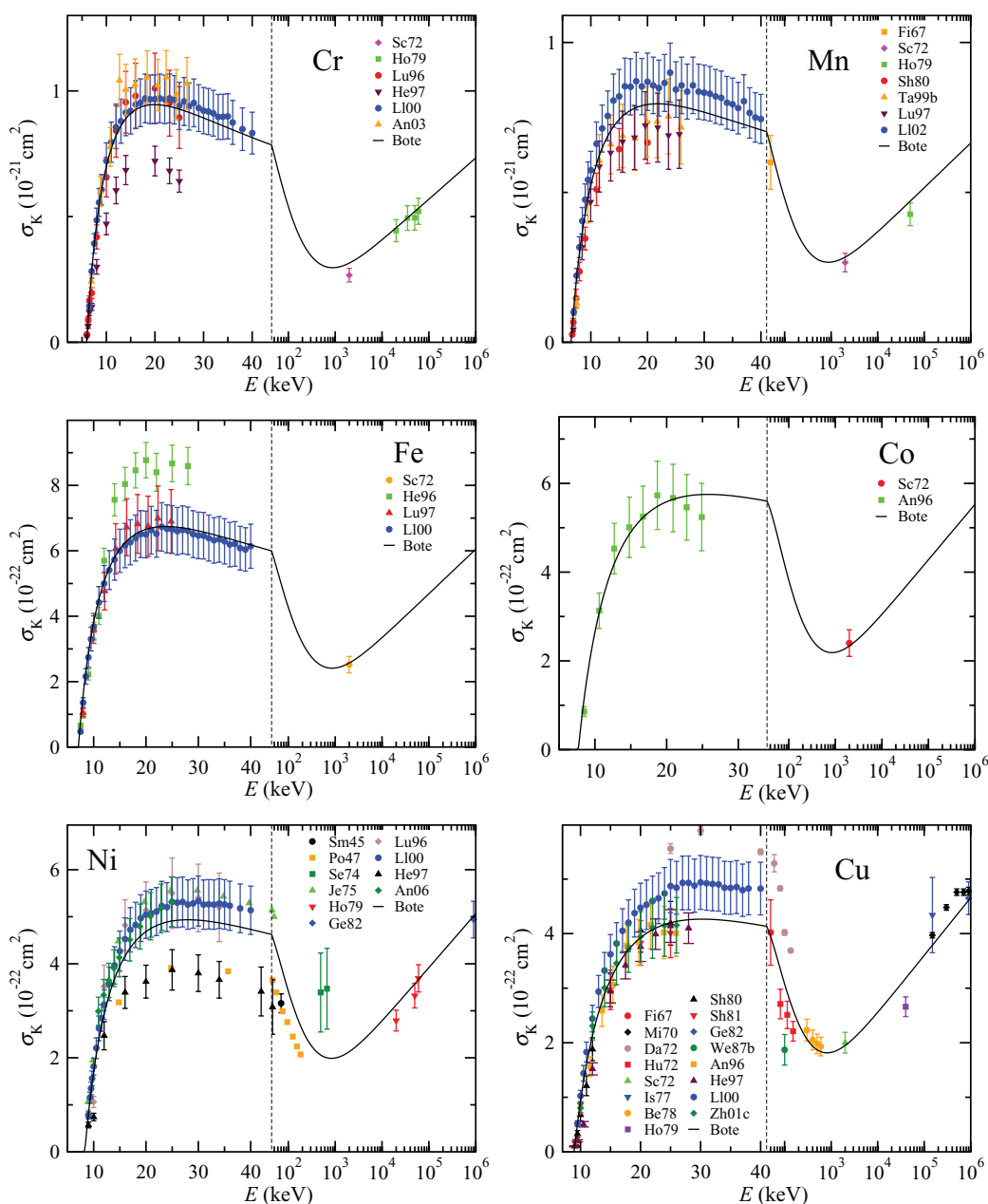


FIG. 14. (Color online) Absolute K-shell ionization cross sections vs. incident electron energy for Cr, Mn, Fe, Co, Ni, and Cu. Solid curves are the results of the DWBA calculations. Symbols are experimental measurements.

We show comparisons of the measured K-shell ionization cross sections for Kr, Rb, Sr, Y, Zr, and Nb in Fig. 16. Good agreement is found between the experimental data available for Y and the predictions of the DWBA over a wide range of incident electron energies. In contrast, the DWBA seems to overestimate the experimental measurements available for Kr, Rb, Sr, Zr, and Nb, although the differences become smaller when the incident electron energy approaches the ionization threshold. Indeed, for the mentioned elements, the predictions of the DWBA seem to increase faster with energy than the experimental data of Shevelko *et al.*¹⁴⁵ (for Rb and Sr), Zhou *et al.*²⁷³ (for Zr), and Peng *et al.*¹⁵⁴ (for Nb).

Similar comparisons are made in Fig. 17 for Mo, Pd, Ag, Cd, Sn, and In. The DWBA calculations are lower than the measurements of He *et al.*¹⁵¹ for Mo at low energies. In contrast, they are in relatively good agreement with the experimental data at high energies. For Pd, the DWBA calculations are also in good agreement with the available measurements at high energy within the quoted errors bars, but near ~ 100 keV, the DWBA calculations lie 10% above the measurements of Ricz *et al.*¹⁹⁰

K-shell ionization cross sections of Ag have been measured by a large number of groups (Fig. 17). For this element, there is good consistency among the various sets of experimental data and good agreement between the predictions of the DWBA

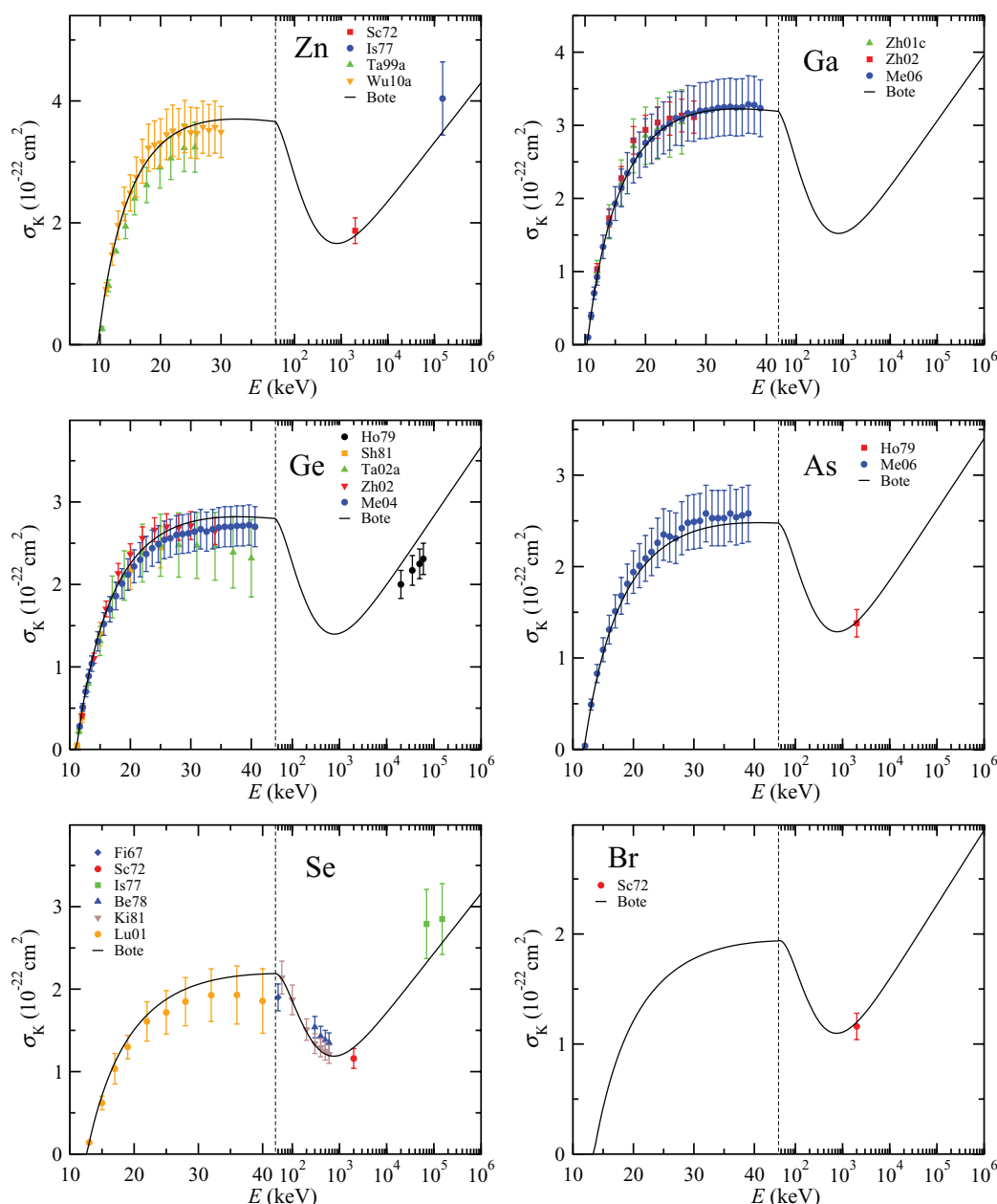


FIG. 15. (Color online) Absolute K-shell ionization cross sections vs. incident electron energy for Zn, Ga, Ge, As, Se, and Br. Solid curves are the results of the DWBA calculations. Symbols are experimental measurements.

and the measured cross sections over a very large range of incident electron energies. In contrast, only one experimental datum is available for Cd, which is slightly overestimated by the present calculations.

There are substantial discrepancies between the experimental data available for Sn in the energy range between 100 and 1000 keV, not only as regards the magnitude of the cross section but also with respect to its shape. The experimental data of Hansen *et al.*¹¹² and Hansen and Flammersfeld¹¹³ are probably affected by systematic uncertainties larger than those quoted by the authors. A similar situation is found for the W, Au, and Pb measurements by the same authors (see below). The agreement between the DWBA cross sections and the other experimental data for Sn is good. For In, the

predictions of the DWBA lie between the different sets of measurements.

Figure 18 compares the experimental K-shell ionization cross sections for Sb, Te, Xe, Ba, La, and Ce with the DWBA calculations. For these elements, no experimental data are available at low energies. For Sb, excellent agreement is observed between the available set of measurements and the predictions of the DWBA which appears to describe very well the cross-section inflection observed at around 200 keV. The situation is less favorable for Xe and Ce, for which the DWBA calculations appear to overestimate the few measured values. For Ba and La, the DWBA results agree with the measurements of Westbrook and Quarles,¹⁴³ but are in disagreement with those of Scholz *et al.*¹²⁵ and Ishii *et al.*¹³¹

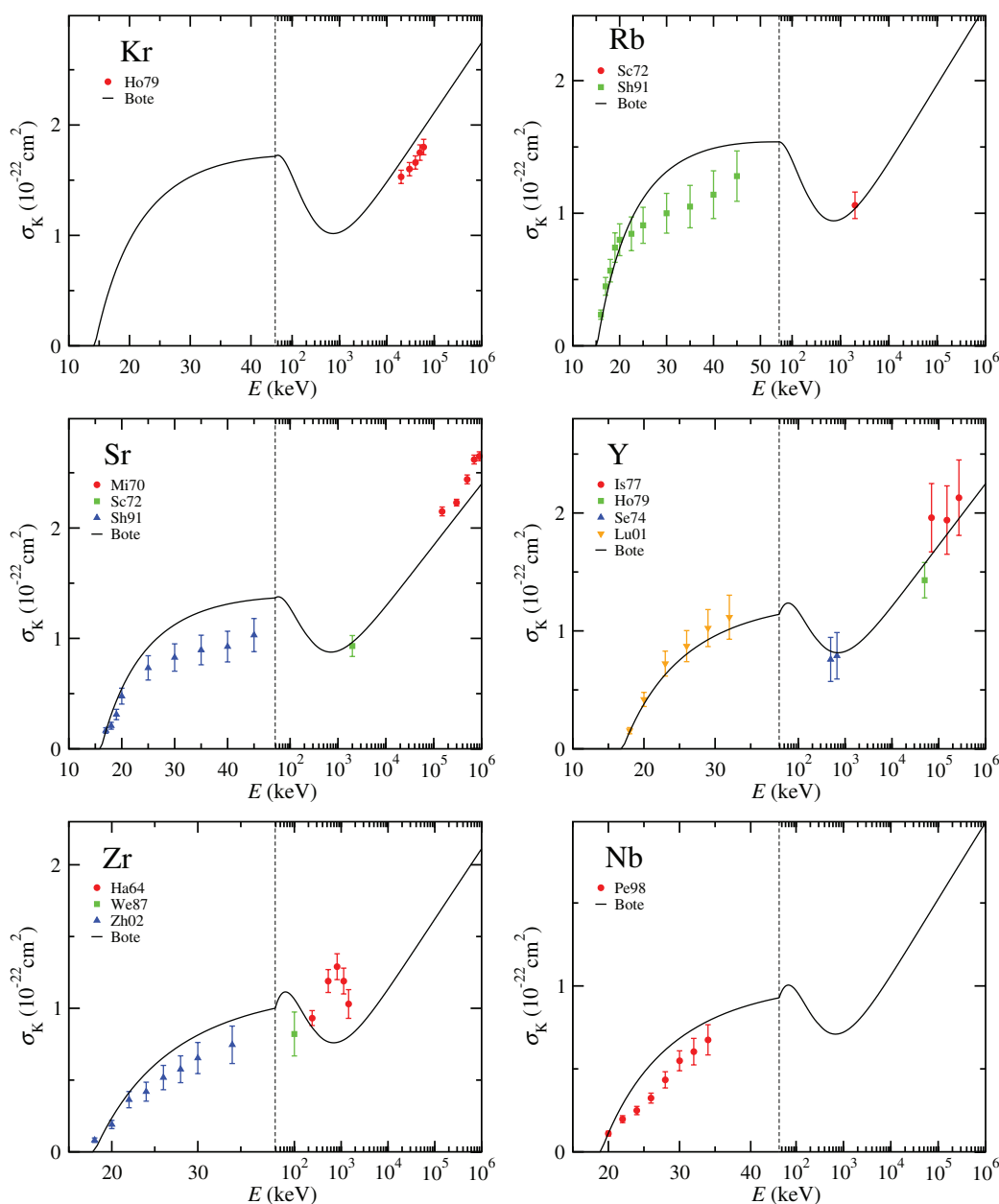


FIG. 16. (Color online) Absolute K-shell ionization cross sections vs. incident electron energy for Kr, Rb, Sr, Y, Zr, and Nb. Solid curves are the results of the DWBA calculations. Symbols are experimental measurements.

For Pr, Nd, Sm, Eu, Gd, and Ho (Fig. 19), there are relatively few measurements, and all of them are at high energies. The predictions of the DWBA are nevertheless in relatively good agreement with the existing sets of experimental cross sections. A similar satisfactory situation is found for Er, Tm, Yb, Ta, W, and Au in Fig. 20 for which, with the exception of Au, there are few measurements. As mentioned earlier, the measurements of Hansen *et al.*¹¹² and Hansen and Flammersfeld¹¹³ for W and Au show a large scatter. Fortunately, there are numerous cross-section measurements for Au, and the high-energy values are in good agreement with the predictions of the DWBA. At lower energies, the DWBA calculations lie above the experimental data of Westbrook and Quarles¹⁴³ and below the experimental data of Davis *et al.*¹²³ and Motz and

Placious.¹¹⁴ We note that the latter measurements are the only K-shell cross-section measurements available for an element with $Z > 47$ near the ionization threshold.

Figure 21 shows similar comparisons for Pb, Bi, and U. For Pb, the experimental data of Hansen *et al.*¹¹² and Hansen and Flammersfeld¹¹³ exhibit a large spread, like that found for Sn, W, and Au cross sections from the same authors. Most of the remaining experimental data are consistent with the DWBA results at high energies (Fig. 14). For Bi, however, the measurements of Middleman *et al.*⁷¹ at ultra-relativistic energies are larger than the DWBA calculations by about 10%. The only data point available for U agrees within the experimental uncertainties with the DWBA cross sections.

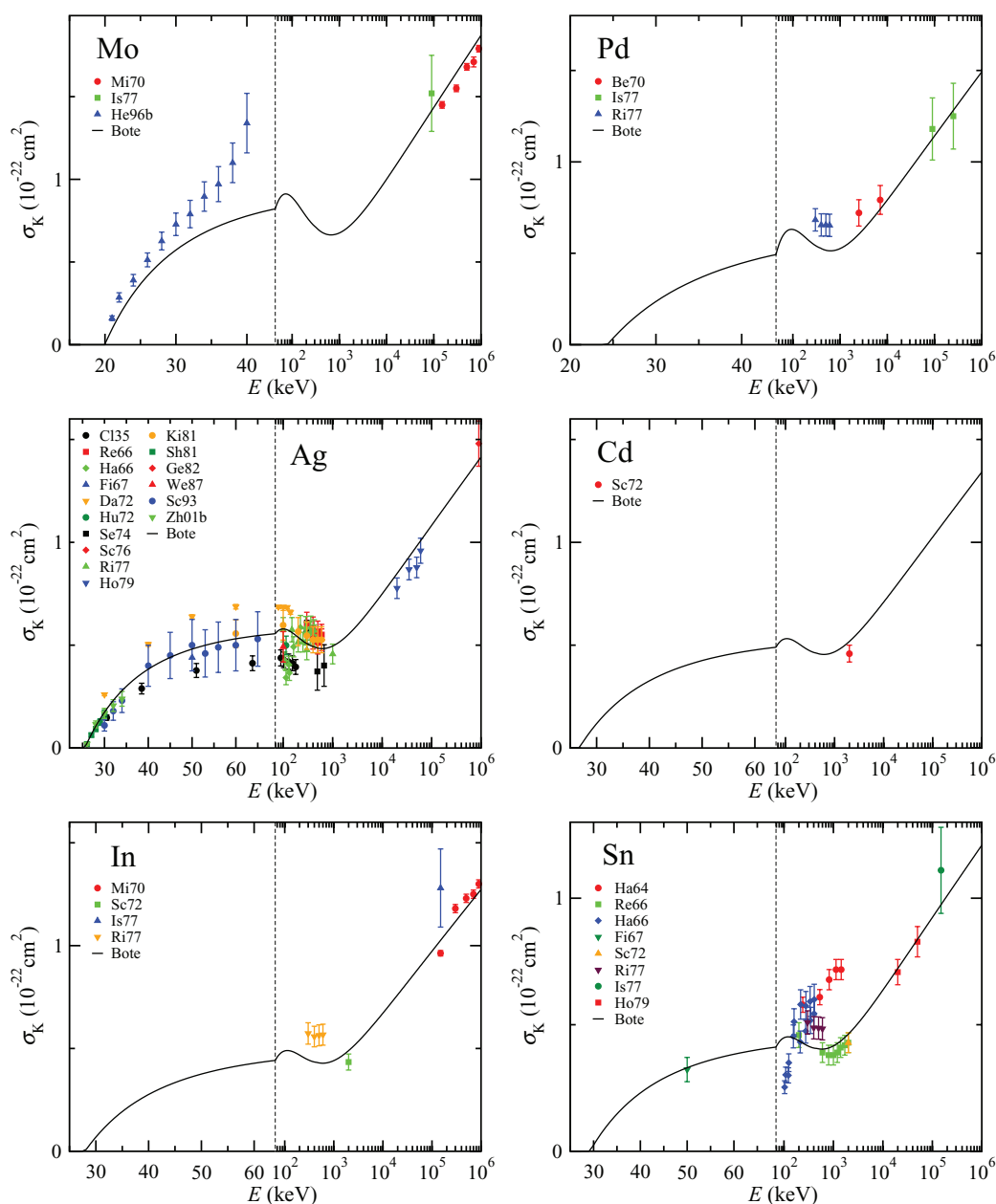


FIG. 17. (Color online) Absolute K-shell ionization cross sections vs. incident electron energy for Mo, Pd, Ag, Cd, In, and Sn. Solid curves are the results of the DWBA calculations. Symbols are experimental measurements.

6.2. L-subshell ionization cross sections

Table 3 lists all measurements of L-shell ionization cross sections that have been reported in the literature up to May 2013. Information on the measured shell, incident electron energy range, method and target used, simplified reference (as shown in Figs. 22–31), and the full reference is also given. Methods include measurements with x-ray yields (X) and Auger yields (A). Targets used include self-supporting thin films (T), thin films on substrates (TS), thick substrates (S), and gases (G).

As for Table 2, we see that measurements of x-ray yields have been utilized for most of the L-shell cross-section measurements. Self-supporting thin films were again the most

commonly used targets, with smaller numbers of measurements being made with thick substrates, gases, and thin films on substrates. Some L-shell cross sections were determined from Auger yields with gas targets but there were no such measurements from EELS spectra. The check marks in Table 3 indicate “superior” cross-section measurements for a given paper, as judged by the mutual consistency of sets of measurements made for a given element from different groups that we will describe in Sec. 7.1.

The plots in Figs. 22–31 show comparisons of measured L-subshell ionization cross sections and total L-shell ionization cross sections with corresponding calculated cross sections. As for the calculated K-shell ionization cross sections in Figs. 11–21,

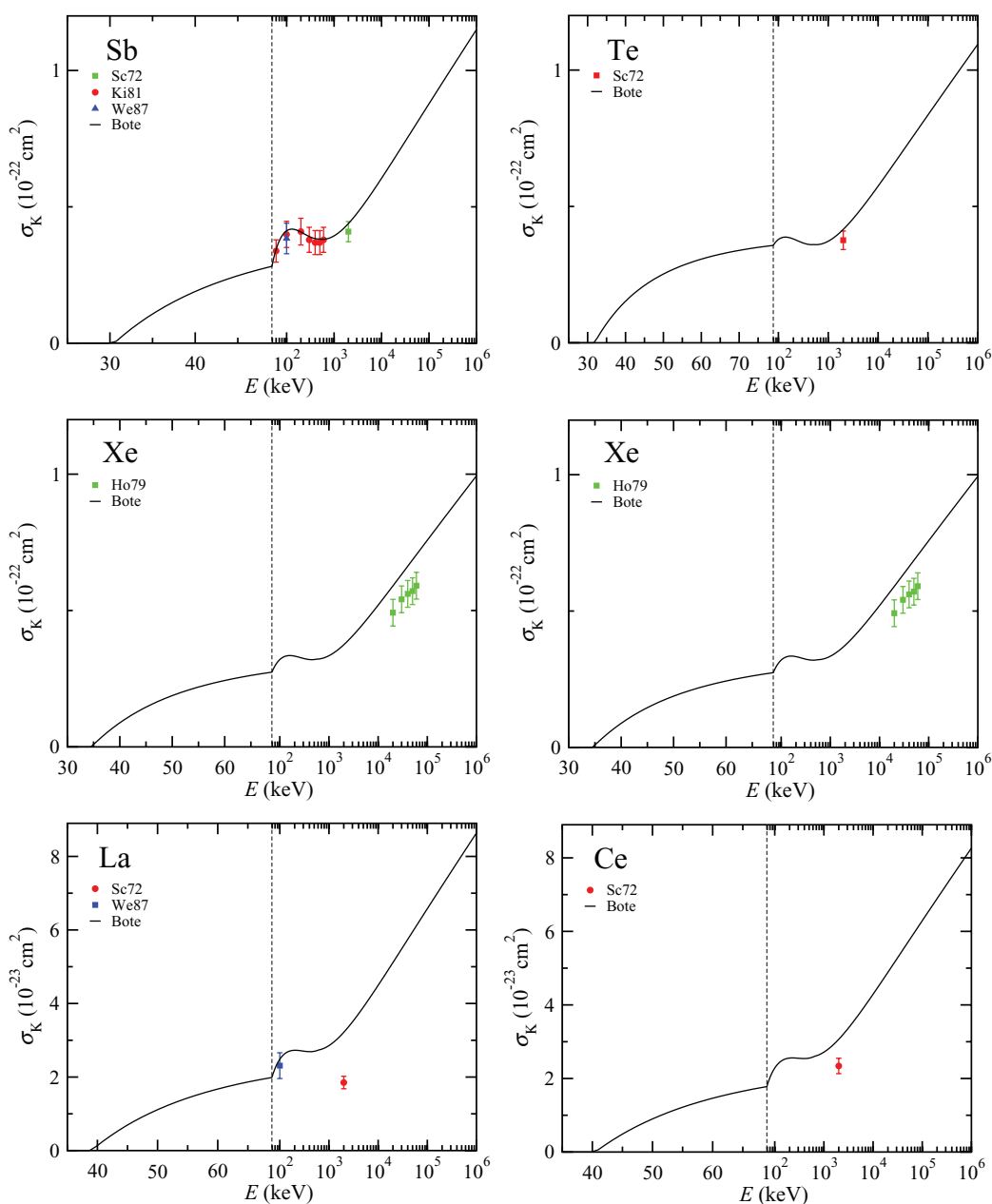


Fig. 18. (Color online) Absolute K-shell ionization cross sections vs. incident electron energy for Sb, Te, Xe, Ba, La, and Ce. Solid curves are the results of the DWBA calculations. Symbols are experimental measurements.

the solid lines in Figs. 22–31 show cross sections from the Bote *et al.* analytical formulae,³¹ Eqs. (87) and (88), that were obtained from fits to the cross sections from the DWBA for electron energies up to 16 times the threshold energy for inner-shell ionization and the PWBA for higher energies, as described in Sec. 2. These formulae are functions of the overvoltage U , the ratio of the incident electron energy to the ionization energy or binding energy for the shell or subshell of interest. As described in the Appendix, it was convenient for us to make use of the binding energies for each shell or subshell from the tabulation of Carlson.⁶⁴ The comparisons in Figs. 22–31 were made for 26 elements (from Si to U, as listed in Table 3).

In contrast to K-shells, no compilation of experimental cross-section data for L shells has been published so far. There

are much fewer measurements of ionization cross sections for L shells than for K shells.

Figure 22 shows measured cross sections for L_1 -subshell ionization cross sections for Cu, Sr, Ag, Sn, Xe, and Sm, and Fig. 23 shows similar cross sections for Ta, W, Au, Pb, and Bi. For each element, only a single source of data is available. In most cases, the measured cross sections follow the trends with energy expected from the solid curves although the energy dependences of the measurements for Ag, Ta, and W show deviations. The magnitudes of the measured cross sections for Sr, Sn, Xe, Au, Pb, and Bi generally agree satisfactorily with the predicted values (i.e., within or close to the indicated error bars) but there are systematic differences for Cu and Sm.

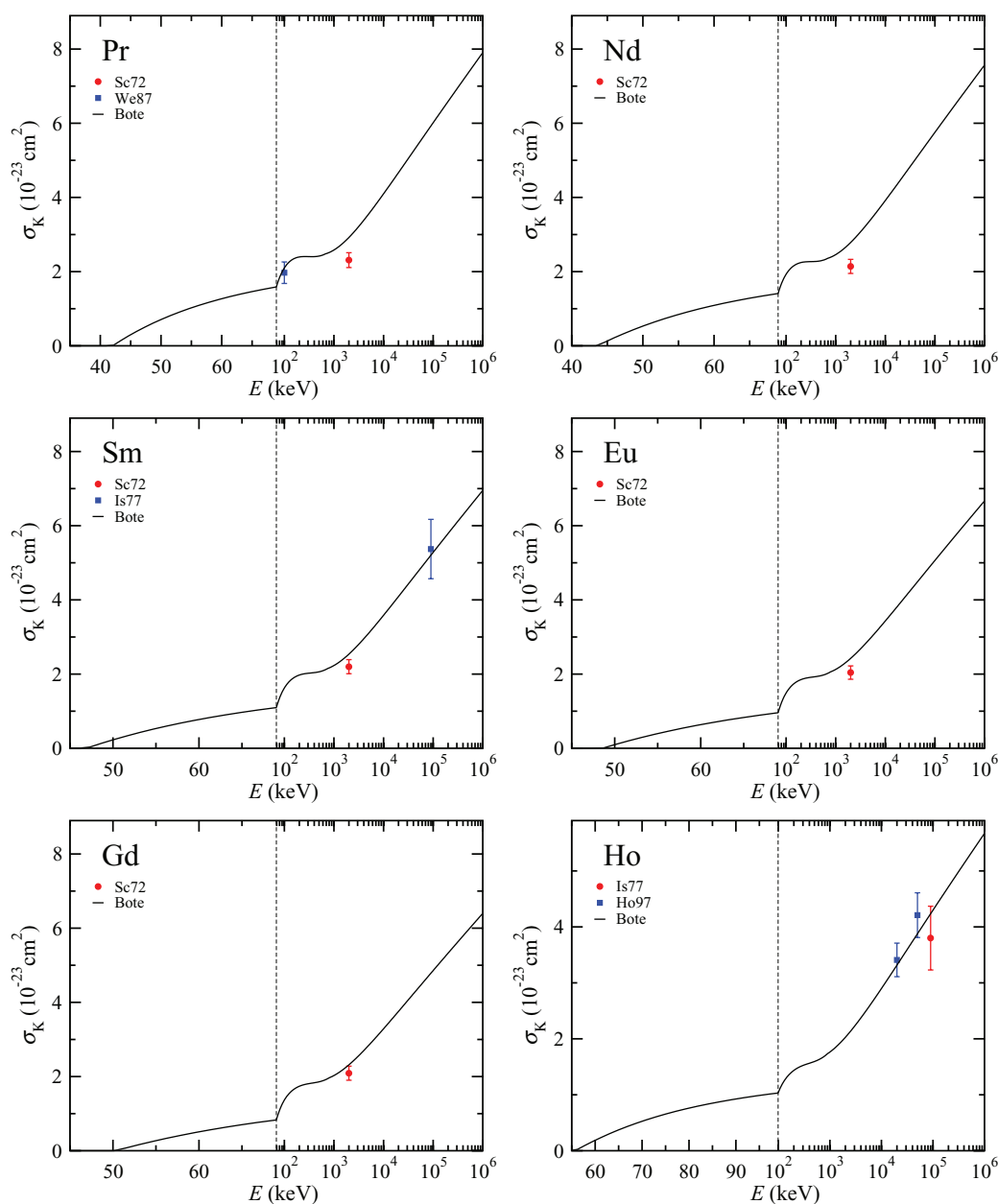


FIG. 19. (Color online) Absolute K-shell ionization cross sections vs. incident electron energy for Pr, Nd, Sm, Eu, Gd, and Ho. Solid curves are the results of the DWBA calculations. Symbols are experimental measurements.

Figures 24 and 25 show measured L_2 -subshell ionization cross sections for the same 11 elements shown in Figs. 22 and 23, and similar comparisons with the calculated cross sections. For Au, there are four sets of measured cross sections available, of which there are two sets that agree reasonably with the solid line [Gr68 (Ref. 119) and Pa80a (Ref. 138)] and two sets [Gr64 (Ref. 118) and Sa71 (Ref. 122)], consistent with each other, that do not. The newer paper of Green and Cosslett¹¹⁹ presumably contains more accurate cross sections than the earlier report of Green.¹¹⁸ Most of the measured L_1 - and L_2 -subshell cross sections for Cu, Sr, Ag, Sn, Ta, Pb, and Bi in Figs. 22 and 23 agree with or are close to the corresponding solid lines but there are deviations for Xe, Sm, Au, and W. We note that the cross sections of Pálinkás and

Schlenk¹³⁸ for Au, Pb, and Bi are generally consistent with the calculated Bote *et al.* cross sections as well as with the Au data of Green and Cosslett,¹¹⁹ thereby suggesting that the latter measurements are more reliable than the earlier results of Green.¹¹⁸

Figure 26 shows comparisons of measured and calculated L_{23} -subshell ionization cross sections for 6 elements (Si, P, S, Cl, Ar, and Ti) while Figs. 27 and 28 have similar comparisons of calculated cross sections for L_3 -subshell ionization with measured cross sections for 11 elements [Cu, Sr, Ag, Sn, Xe, Sm (Fig. 27), Ta, W, Au, Pb, and Bi (Fig. 28)]. For most of these elements, only single sets of measured cross sections are available, and there are substantive disagreements between calculated and measured cross sections for Ti and W.

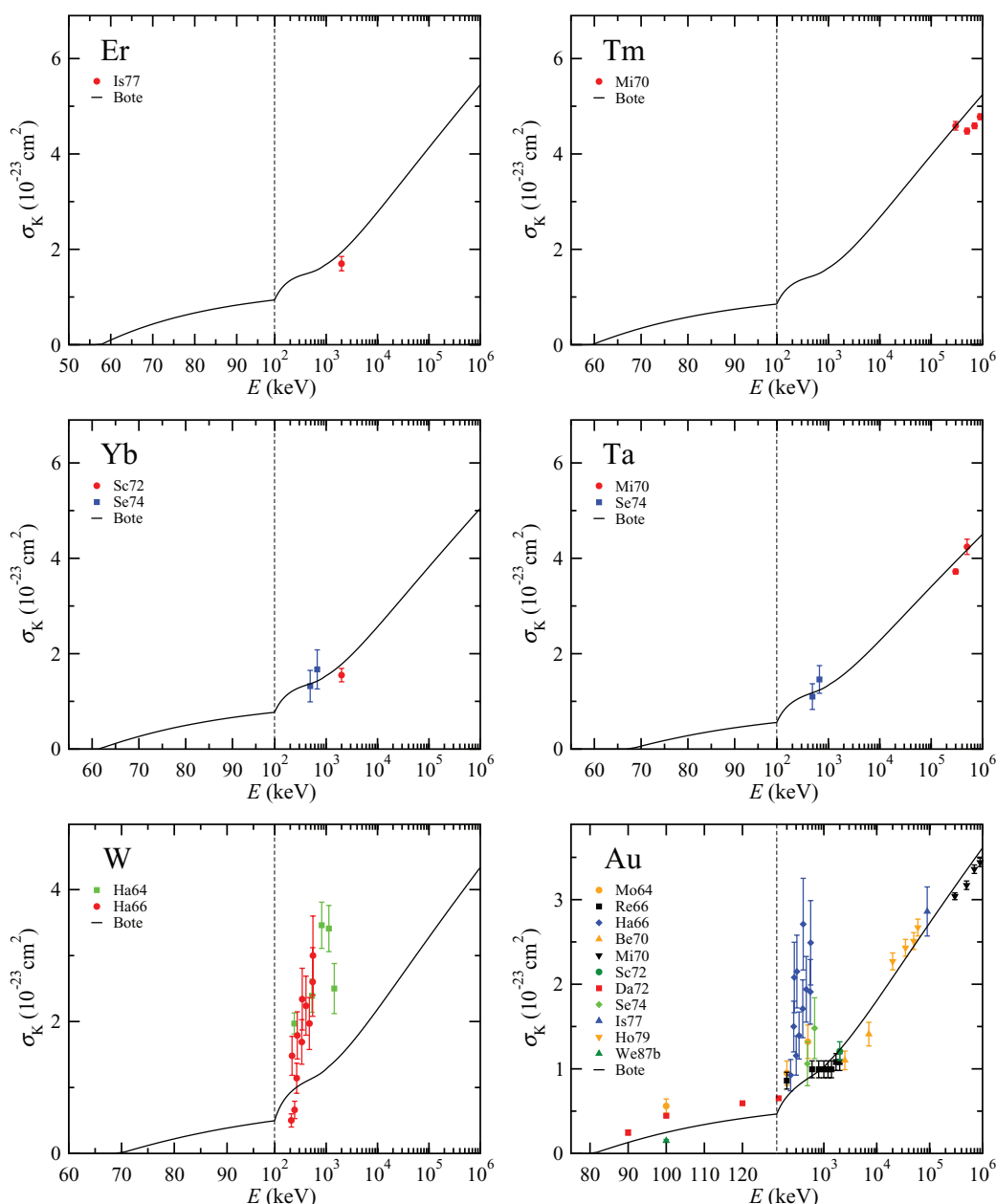


FIG. 20. (Color online) Absolute K-shell ionization cross sections vs. incident electron energy for Er, Tm, Yb, Ta, W, and Au. Solid curves are the results of the DWBA calculations. Symbols are experimental measurements.

Satisfactory agreement is found, however, for Si, P, S, Cl, Cu, Sr, Ag, Sn, Xe, Pb, and Bi. For Sm and Ta, the measurements of Reusch *et al.*¹⁴² exceed the calculated cross sections by up to three times the estimated uncertainties.

Three sets of measurements are available for Ar that show similar energy dependences but only the measurements of Suzuki *et al.*²³¹ agree in magnitude (partially) with the calculated cross sections. For Xe, there are two sets of measurements in nonoverlapping energy ranges^{204,207} that agree well with the solid curve.

There are seven sets of measured cross sections for Au, but only those from Green and Cosslett¹¹⁹ and Pálinkás and Schlenk¹³⁸ show satisfactory consistency with the predicted

cross sections. A similar result was found for the Au L_2 -subshell cross sections of these authors in Fig. 25.

Total L-shell ionization cross sections are shown in Figs. 29–31 for 17 elements [Cu, Kr, Sr, Nb, Pd, Ag (Fig. 29), In, Sn, Xe, Ba, Sm, Ho (Fig. 30), Yb, Ta, Pb, Bi, and U (Fig. 31)]. Three sets of measured cross sections are available for Ag and Sn, and these agree reasonably with the corresponding calculated cross sections in Figs. 29 (Ag) and 30 (Sn). For Sm, Ta, Pb, Bi, and U, there are two sets of measurements for each element, and these agree moderately with the predicted cross sections. There is good agreement between the measured and calculated cross sections for Cu, Sr, Pd, Ba, Ho, and Yb, but there are deviations for Kr, Nb, In, and Xe.

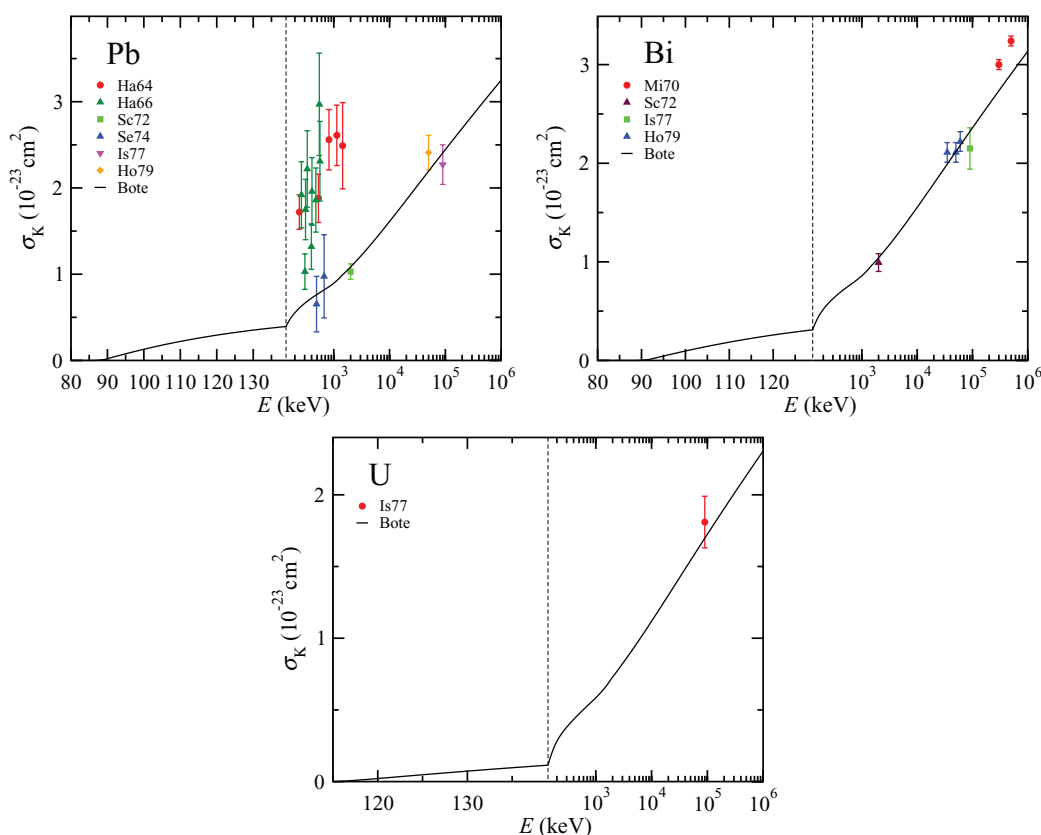


FIG. 21. (Color online) Absolute K-shell ionization cross sections vs. incident electron energy for Pb, Bi, and U. Solid curves are the results of the DWBA calculations. Symbols are experimental measurements.

6.3. M-subshell ionization cross sections

Table 4 lists the measurements of M-shell ionization cross sections reported in the literature up to May 2013. Information on the measured shell, incident electron energy range, method and target used, simplified reference (as shown in the figures), and the full reference is also given. Methods include measurements with x-ray yields (X), Auger yields (A), and EELS spectra (E). Targets used include self-supporting thin films (T) and gases (G).

As for Tables 2 and 3, we see that measurements of x-ray yields were utilized for most of the L-shell cross-section measurements, and self-supporting thin films were again the most commonly used targets. Some L-shell cross sections were determined from Auger yields with gas targets. The check marks in Table 3 indicate “superior” cross-section measurements for a given paper, as judged by the mutual consistency of sets of measurements made for a given element from different groups that we will describe in Sec. 7.1.

We show comparisons of measured total M-shell ionization cross sections in Fig. 32 and measured $M_{4,5}$ -subshell ionization cross sections in Fig. 33 with corresponding calculated cross sections. As for the similar comparisons in the preceding subsections, the solid lines in Figs. 32 and 33 are cross sections from the Bote *et al.* analytical formulae,³¹ Eqs. (87) and (88), that were obtained from fits to the cross sections from the DWBA for electron energies up to 16 times the threshold energy for inner-shell ionization and the PWBA

for higher energies, as described in Sec. 2. These formulae are a function of the overvoltage U , the ratio of the incident electron energy to the ionization energy or binding energy for the shell or subshell of interest. As described in the Appendix, it was convenient for us to make use of the binding energies for each shell or subshell from the tabulation of Carlson.⁶⁴ The comparisons in Figs. 32 and 33 were made for the seven elements listed in Table 4.

Total M-shell ionization cross sections are shown in Fig. 32 for four elements (Au, Bi, Pb, and U). Three sets of measurements are available for Bi and Pb, and these agree moderately well with the calculated cross sections although there are some deviations. Of the two sets of measured cross sections for Au, one set (Pa80b) is systematically larger than the calculated cross sections while the other set (Ho79) is systematically smaller. For U, there is satisfactory agreement of the measured cross sections with the calculated data.

$M_{4,5}$ -subshell cross sections measured for Br and Sn by Vrakking and Meyer²²⁷ and for Kr by Suzuki *et al.*²³¹ are shown in Fig. 33. These cross sections resulted from Auger-yield measurements in gases and are systematically smaller than the calculated cross sections.

6.4. L-shell x-ray production cross sections

Table 5 lists the measurements of L-shell x-ray production cross sections reported in the literature up to May 2013.

TABLE 3. Measurements of L-shell ionization cross sections published up to May 2013. Information on the measured shell(s), incident electron energy range, method and target used, simplified reference (as shown in Figs. 22–31), and the full reference is also given. Methods include measurements with x-ray yields (X), Auger yields (A), and EELS spectra (E). Targets used include self-supporting thin films (T), thin films on substrates (TS), thick substrates (S), and gases (G). The check marks designate particular sets of measurements with superior data from the evaluation of experimental data (see Sec. 7)

Element	Shell	Energy (keV)	Method, target	Superior data	Key	Reference
Si	L ₂₃	0.432	A,G	–	Vr74	Vracking and Meyer ²²⁷
P	L ₂₃	0.26 to 23.0	A,G	–	Vr74	Vracking and Meyer ²²⁷
S	L ₂₃	0.33 to 2.6	A,G	–	Vr74	Vracking and Meyer ²²⁷
Cl	L ₂₃	0.61 to 2.54	A,G	–	Vr74	Vracking and Meyer ²²⁷
Ar	L ₂₃	0.3 to 7.0	A,G	–	Cr70	Christofzik ²²⁵
Ar	L ₂₃	0.3 to 3.0	A,G	–	Og73	Ogurtsov ²²⁶
Ar	L ₂₃	0.2 to 1.48	A,G	–	Su90	Suzuki <i>et al.</i> ²³¹
Ti	L ₂₃	1.87	A,G	–	Vr74	Vracking and Meyer ²²⁷
Cu	L ₁ ,L ₂ ,L ₃ ,L	50 to 100	X,T	–	Re86	Reusch <i>et al.</i> ¹⁴²
Kr	L	3.7 to 7.1	X,G	–	Qu82	Quarles and Semaan ²⁰⁶
Sr	L ₁ ,L ₂ ,L ₃ ,L	50 to 200	X,T	–	Re86	Reusch <i>et al.</i> ¹⁴²
Nb	L	3.0 to 40.0	X,TS	–	Pe01b	Peng <i>et al.</i> ¹⁷³
Pd	L	9×10^4 to 2.50×10^4	X,T	–	Is77	Ishii <i>et al.</i> ¹³¹
Ag	L	2.0×10^4 to 6.0×10^4	X,T	✓	Ho79	Hoffmann <i>et al.</i> ¹³⁴
Ag	L	9×10^5 to 2×10^6	X,T	✓	Ge82	Genz <i>et al.</i> ¹⁴¹
Ag	L ₁ ,L ₂ ,L ₃ ,L	50 to 150	X,T	✓	Re86	Reusch <i>et al.</i> ¹⁴²
In	L	1.5×10^4	X,T	–	Is77	Ishii <i>et al.</i> ¹³¹
Sn	L	1.5×10^4	X,T	✓	Is77	Ishii <i>et al.</i> ¹³¹
Sn	L	2.0×10^4 to 6.0×10^4	X,T	✓	Ho79	Hoffmann <i>et al.</i> ¹³⁴
Sn	L ₁ ,L ₂ ,L ₃ ,L	200	X,T	✓	Re86	Reusch <i>et al.</i> ¹⁴²
Xe	L ₁ ,L ₂ ,L ₃	6.0 to 14.0	X,G	✓	Hi81	Hippler <i>et al.</i> ²⁰⁴
Xe	L	6.1 to 10.3	X,G	–	Qu82	Quarles and Semaan ²⁰⁶
Xe	L ₃	6.0 to 14.0	X,G	✓	Hi83	Hippler <i>et al.</i> ²⁰⁷
Ba	L	9.0×10^4 to 2.5×10^5	X,T	–	Is77	Ishii <i>et al.</i> ¹³¹
Sm	L	3.0×10^4 to 6.0×10^4	X,T	✓	Ho79	Hoffmann <i>et al.</i> ¹³⁴
Sm	L ₁ ,L ₂ ,L ₃ ,L	50 to 150	X,T	✓	Re86	Reusch <i>et al.</i> ¹⁴²
Ho	L	9×10^4	X,T	–	Is77	Ishii <i>et al.</i> ¹³¹
Yb	L	3.0×10^4 to 6.0×10^4	X,T	–	Ho79	Hoffmann <i>et al.</i> ¹³⁴
Ta	L	3.0×10^4 to 6.0×10^4	X,T	✓	Ho79	Hoffmann <i>et al.</i> ¹³⁴
Ta	L ₁ ,L ₂ ,L ₃ ,L	50 to 150	X,T	✓	Re86	Reusch <i>et al.</i> ¹⁴²
W	L ₁ ,L ₂ ,L ₃	11 to 40	X,S	–	Ch79	Chang ¹⁹⁹
Au	L ₂ ,L ₃	13.6 to 41.7	X,S	–	Gr64	Green ¹¹⁸
Au	L ₂ ,L ₃	14.9 to 41.2	X,S	–	Gr68	Green and Cosslett ¹¹⁹
Au	L ₂ ,L ₃	13.6 to 41.2	X,S	–	Sa71	Salem and Moreland ¹²²
Au	L ₃	20 to 140	X,T	–	Da72	Davis <i>et al.</i> ¹²³
Au	L	1.5×10^5	X,T	–	Is77	Ishii <i>et al.</i> ¹³¹
Au	L	2.0×10^4 to 6.0×10^4	X,T	–	Ho79	Hoffmann <i>et al.</i> ¹³⁴
Au	L ₁ ,L ₂ ,L ₃	60 to 600	X,T	–	Pa80a	Pálinkás and Schlenk ¹³⁸
Au	L	9×10^5 to 2×10^6	X,T	–	Ge82	Genz <i>et al.</i> ¹⁴¹
Au	L ₃	12.26 to 13.60	X,T	–	Sh81	Shima <i>et al.</i> ¹⁴⁰
Au	L ₃	12.0 to 75.0	X,T	–	Sc93	Schneider <i>et al.</i> ¹⁴⁷
Pb	L	9.0×10^4 to 1.5×10^5	X,T	✓	Is77	Ishii <i>et al.</i> ¹³¹
Pb	L	2.0×10^4 to 6.0×10^4	X,T	✓	Ho79	Hoffmann <i>et al.</i> ¹³⁴
Pb	L ₁ ,L ₂ ,L ₃	60 to 600	X,T	–	Pa80a	Pálinkás and Schlenk ¹³⁸
Bi	L	9.0×10^4 to 1.5×10^5	X,T	✓	Is77	Ishii <i>et al.</i> ¹³¹
Bi	L	2.0×10^4 to 6.0×10^4	X,T	✓	Ho79	Hoffmann <i>et al.</i> ¹³⁴
Bi	L ₁ ,L ₂ ,L ₃	60 to 600	X,T	–	Pa80a	Pálinkás and Schlenk ¹³⁸
U	L	9.0×10^4	X,T	✓	Is77	Ishii <i>et al.</i> ¹³¹
U	L	2.0×10^4 to 6.0×10^4	X,T	✓	Ho79	Hoffmann <i>et al.</i> ¹³⁴

Information on the measured line [notice that the line LX is defined by Eq. (124)], incident electron energy range, target used, the simplified reference (as shown in Figs. 34–38), and the full reference is also given. Targets used include self-supporting thin films (T), thin films on substrates (T), and gases (G).

As for Tables 2–4, we see that most measurements were made with self-supporting thin films and thin films on substrates as

targets. Two sets of cross sections were determined with gas targets. The check marks in Table 5 indicate “superior” cross-section measurements for a given paper, as judged by the mutual consistency of sets of measurements made for a given element from different groups that we will describe in Sec. 7.1.

Since the *La* line is stronger than the other x-ray lines shown in Table 1, the resulting x-ray production cross sections should be of better accuracy than those for the other

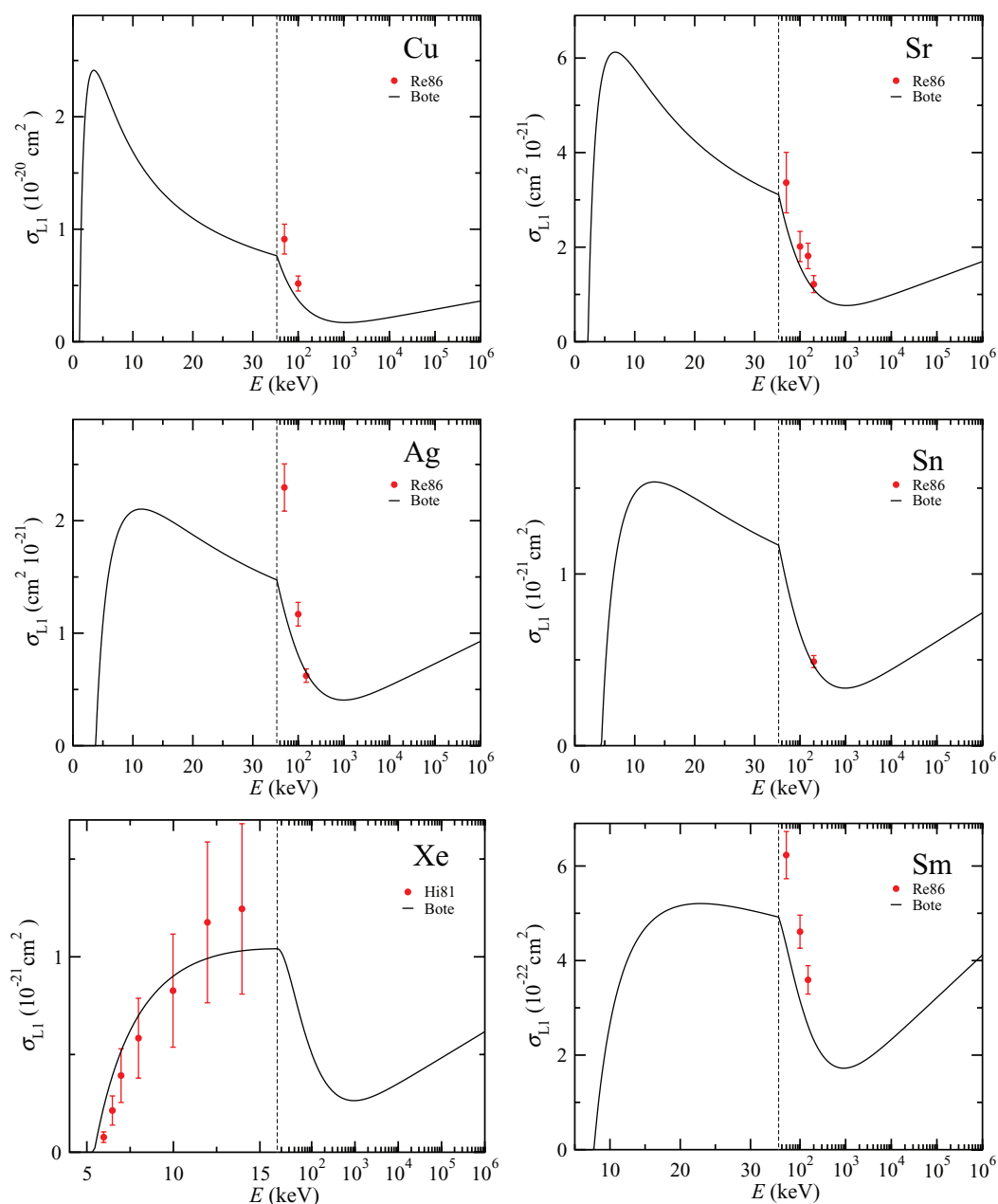


FIG. 22. (Color online) Absolute L_1 -subshell ionization cross sections vs. incident electron energy for Cu, Sr, Ag, Sn, Xe, and Sm. Solid curves are the results of the DWBA calculations. Symbols are experimental measurements.

lines. Figure 34 shows the $L\alpha$, $L\beta$, $L\gamma$, and $L\ell$ x-ray production cross sections for Pb. We see that the $L\alpha$ cross section is approximately double the $L\beta$ cross section, and that these cross sections are about an order of magnitude larger than the $L\gamma$ and $L\ell$ cross sections. We will therefore only make comparisons of $L\alpha$ and total L-shell x-ray production cross sections, the latter denoted by LX in Table 5 and Figs. 39 and 40. The gray shaded areas in Fig. 34 indicate the estimated one-standard-deviation uncertainties in the calculated $L\alpha$ and $L\beta$ x-ray production cross sections arising from the uncertainties of parameters needed in Eq. (105) from the EADL.¹ We see that the resulting uncertainties in the $L\alpha$ and $L\beta$ x-ray production cross sections range from about 10% to 20%.

Figures 35–38 show $L\alpha$ x-ray production cross sections for 23 elements (Ga, Ge, As, In, Sn, I (Fig. 35), Ba, Sm, Gd, Dy, Ho, Er (Fig. 36), Tm, Yb, Hf, Ta, W, Re (Fig. 37), Os, Pt, Au, Pb, and Bi (Fig. 38)). The solid lines are calculated cross sections obtained by combining calculated L_3 -subshell ionization cross sections from the Bote *et al.* formulae [Eqs. (87) and (88)] with transition probabilities extracted from the EADL database,¹ as described in Secs. 4.2 and 4.3 [Eq. (105)].

Five sets of measured cross sections are available for Au, and these cross sections agree well with the calculated cross sections in Fig. 38. For Pb and Bi, there are four sets of measurements for each element, and these agree satisfactorily with the calculated values (although the measured values of

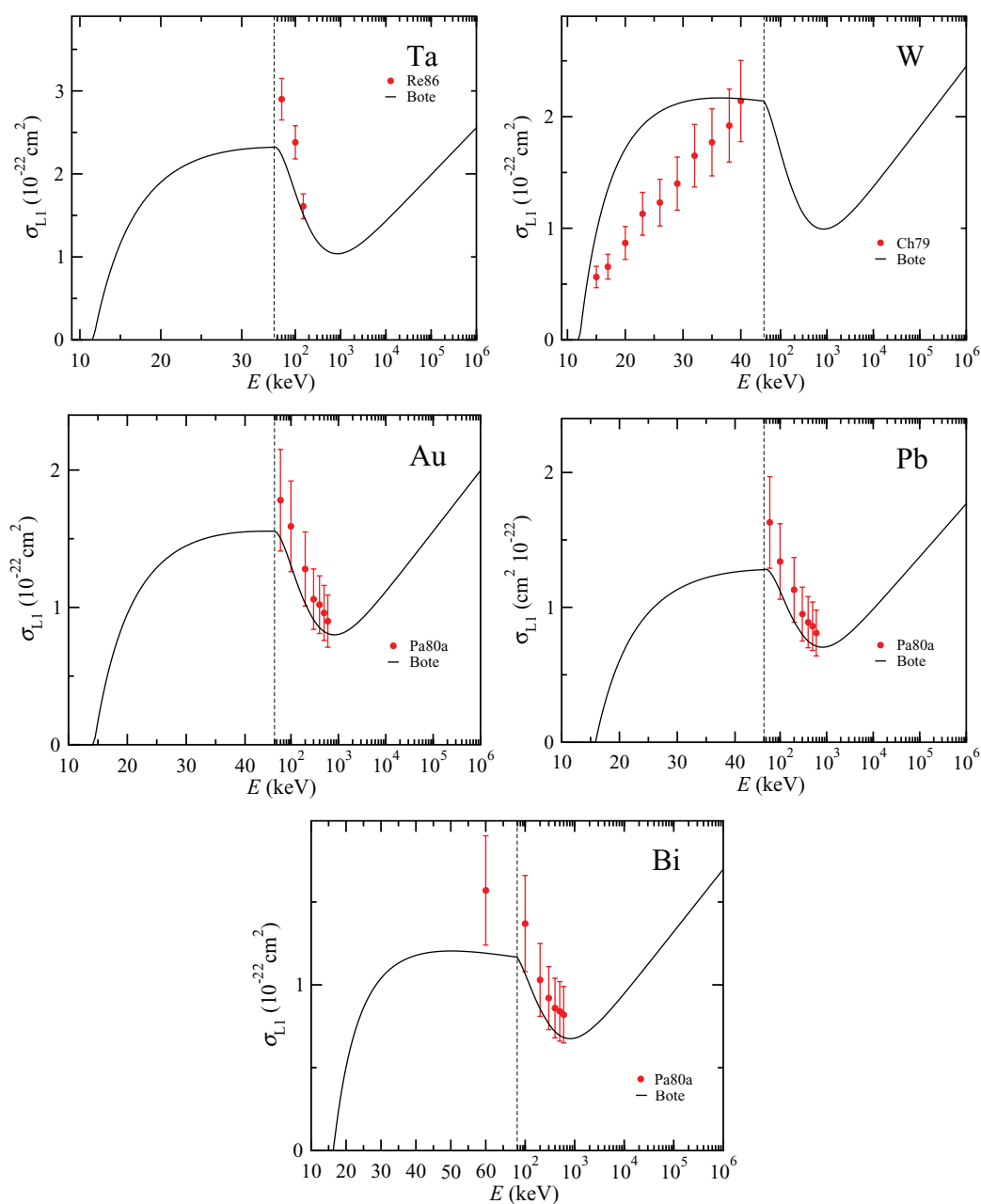


FIG. 23. (Color online) Absolute L_1 -subshell ionization cross sections vs. incident electron energy for Ta, W, Au, Pb, and Bi. Solid curves are the results of the DWBA calculations. Symbols are experimental measurements.

Wu *et al.*¹⁸³ for Pb lie marginally but systematically below the solid line). There are also four sets of measured cross sections for W in Fig. 37 but most of these values lie systematically below the predicted cross sections. For Sm, there are three sets of measured cross sections in Fig. 36, of which the data of Park *et al.*¹²⁹ are appreciably smaller than the predicted cross sections while those of Ricz *et al.*¹³² and Gou *et al.*¹⁶² are slightly less than the calculated values.

There are two sets of measured cross sections for Gd, Ho, and Er in Fig. 36, for Yb, Hf, and Re in Fig. 37, and for Pt in Fig. 38. The measured cross sections agree satisfactorily with the solid lines for Er, Yb, and Pt, and partially for Gd and Ho. There are inconsistencies in the measurements and disagree-

ments with the predicted cross sections for Ho, Hf, and Re. Single sets of measured cross sections are available for Ga, Ge, As, In, Sn, and I in Fig. 35, for Ba and Dy in Fig. 36, for Tm and Ta in Fig. 37, and for Os in Fig. 38. Of these measurements, only those for As, In, Sn, Ba, Gd, Dy, and Ta agree partially with the calculated cross sections.

Total L-shell x-ray production cross sections are shown for 11 elements in Figs. 39 and 40 (for Ar, Ag, Sm, Ho, Er, and Tm in Fig. 39, and for Yb, Ta, Au, Pb, and Bi in Fig. 40). There are two sets of measured cross sections for Ar in Fig. 39, but these values are substantially less than the calculated cross sections. There are also two sets of measured cross sections for Au in Fig. 40, and these are generally consistent with the calculated cross sections

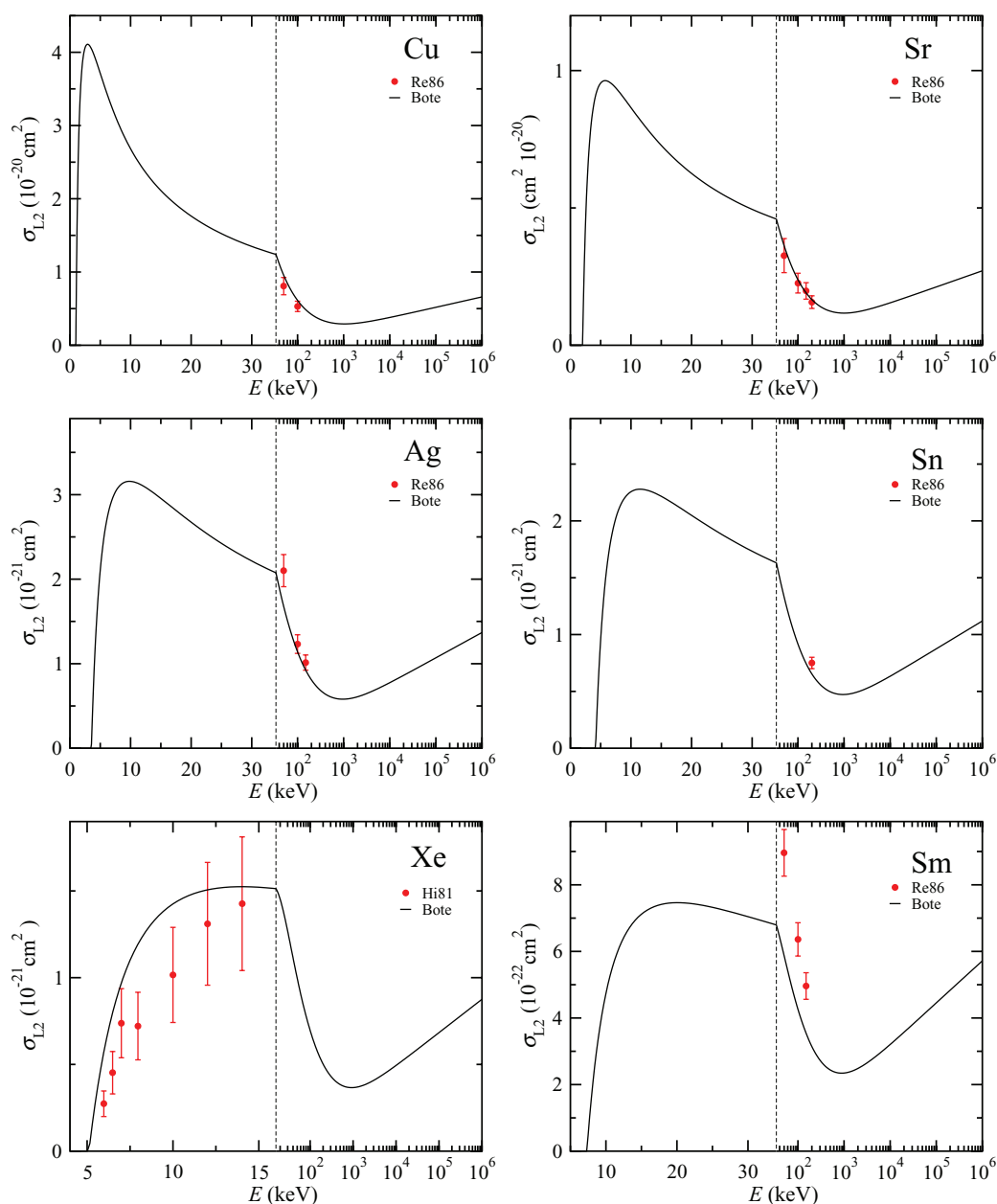


FIG. 24. (Color online) Absolute L_2 -subshell ionization cross sections vs. incident electron energy for Cu, Sr, Ag, Sn, Xe, and Sm. Solid curves are the results of the DWBA calculations. Symbols are experimental measurements.

although the measurements of Middleman *et al.*⁷¹ lie slightly below the solid line. There is general agreement of the measured and calculated cross sections for Sm, Ho, and Er in Fig. 39, and for Yb, Pb, and Bi in Fig. 40. Disagreements of the measured cross sections with the calculated cross sections occur for Ag and Tm in Fig. 39 and for Ta in Fig. 40.

6.5. M-shell x-ray production cross sections

Table 6 lists the measurements of M-shell x-ray production cross sections reported in the literature up to May 2013. Information is given on the measured line, incident electron energy range, target used, the simplified reference (as shown in Fig. 41), and the full reference. Targets used were self-supporting thin films (T).

Figure 41 shows measured $M\alpha$ x-ray production cross sections for Au, Pb, and Bi. The solid lines correspond to cross sections calculated from the M_5 -subshell ionization cross sections from the Bote *et al.* formulae [Eqs. (87) and (88)] with fluorescence yields, radiative widths, and transition probabilities from the EADL database,¹ as described in Secs. 4.2 and 4.3. The experimental cross sections agree well with the corresponding calculated values.

7. Evaluation of Measured Cross Sections

In this Section we evaluate the experimental measurements of K-, L-, and M-shell ionization cross sections and the cross sections for L-shell x-ray production that are available in

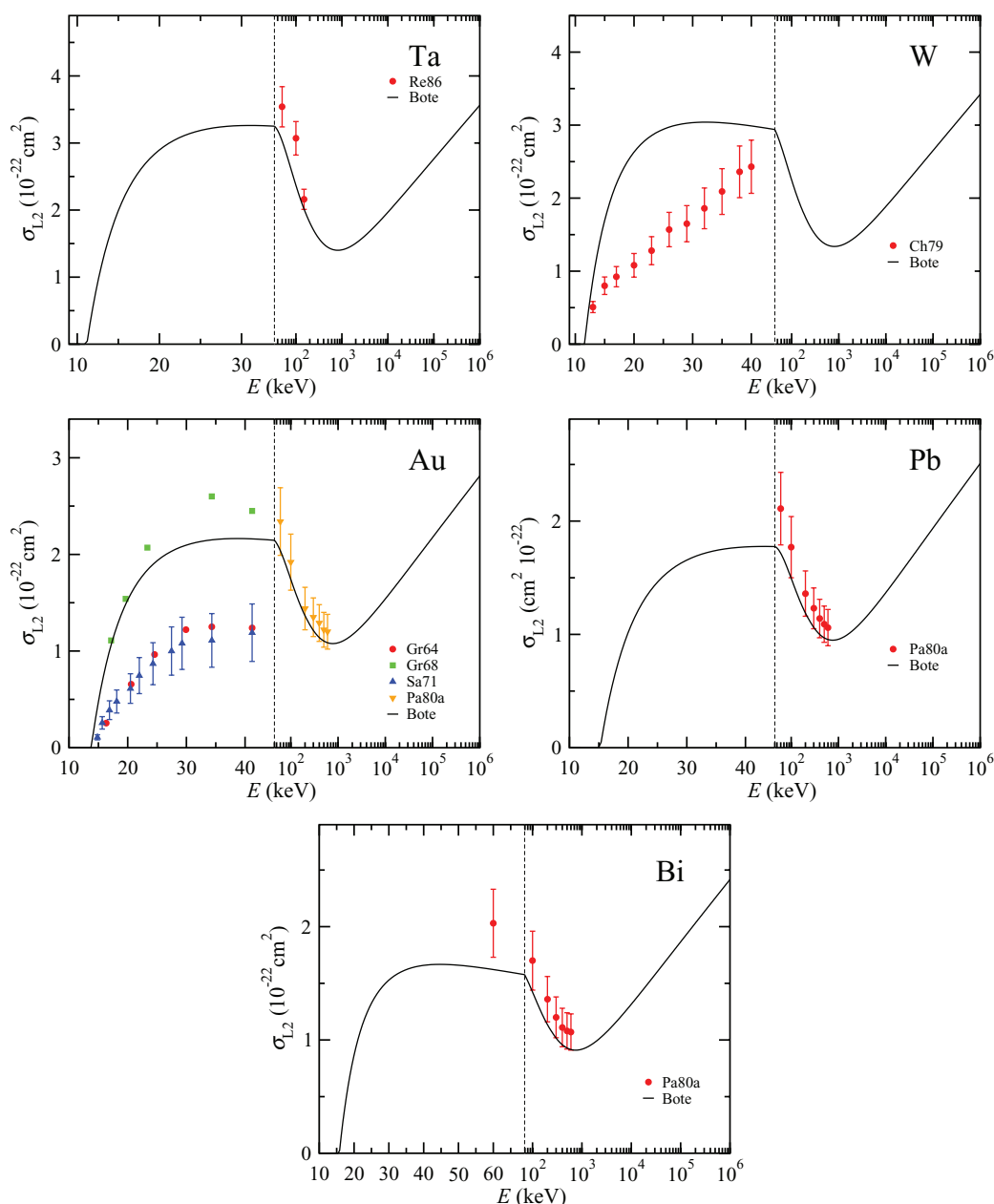


FIG. 25. (Color online) Absolute L_2 -subshell ionization cross sections vs. incident electron energy for Ta, W, Au, Pb, and Bi. Solid curves are the results of the DWBA calculations. Symbols are experimental measurements.

the literature using the criteria described in Subsection 7.1. We then assess the techniques used for the cross-section measurements. Our evaluation is based on comparisons of the calculated atomic cross sections of Bote *et al.*^{31,32} with the corresponding measured cross sections for atoms, molecules, and solids that were presented in Section 6. As pointed out in Section 5, we initially assume that the calculated cross sections should be useful for molecules and solids (for the reasons discussed in Section 2.3) but check this assumption for a wide range of atomic numbers and incident energies.

7.1. Evaluation criteria

Inspection of the measured cross sections presented in Sec. 6 reveals that they are scarce for many elements and, when they

are available, significant discrepancies can be found among data from different authors. These discrepancies are often larger than the claimed experimental uncertainties (for example, see the plot for O in Fig. 11). On the other hand, there are six sets of K-shell cross-section data for Si shown in Fig. 12 that, with the aid of the calculated cross sections, show clear consistency of the data sets for incident energies less than 25 keV with those for energies between 15 and 150 MeV. Similarly, we see that the Al cross sections measured at low energies in Fig. 12 are consistent with the calculated cross sections and with three sets of cross sections measured at high energies but not with two other data sets.^{143,144}

Our selection of data sets for detailed evaluation was, of necessity, qualitative since some data sets were sparse and/or well-separated in energy. Nevertheless, our criteria were

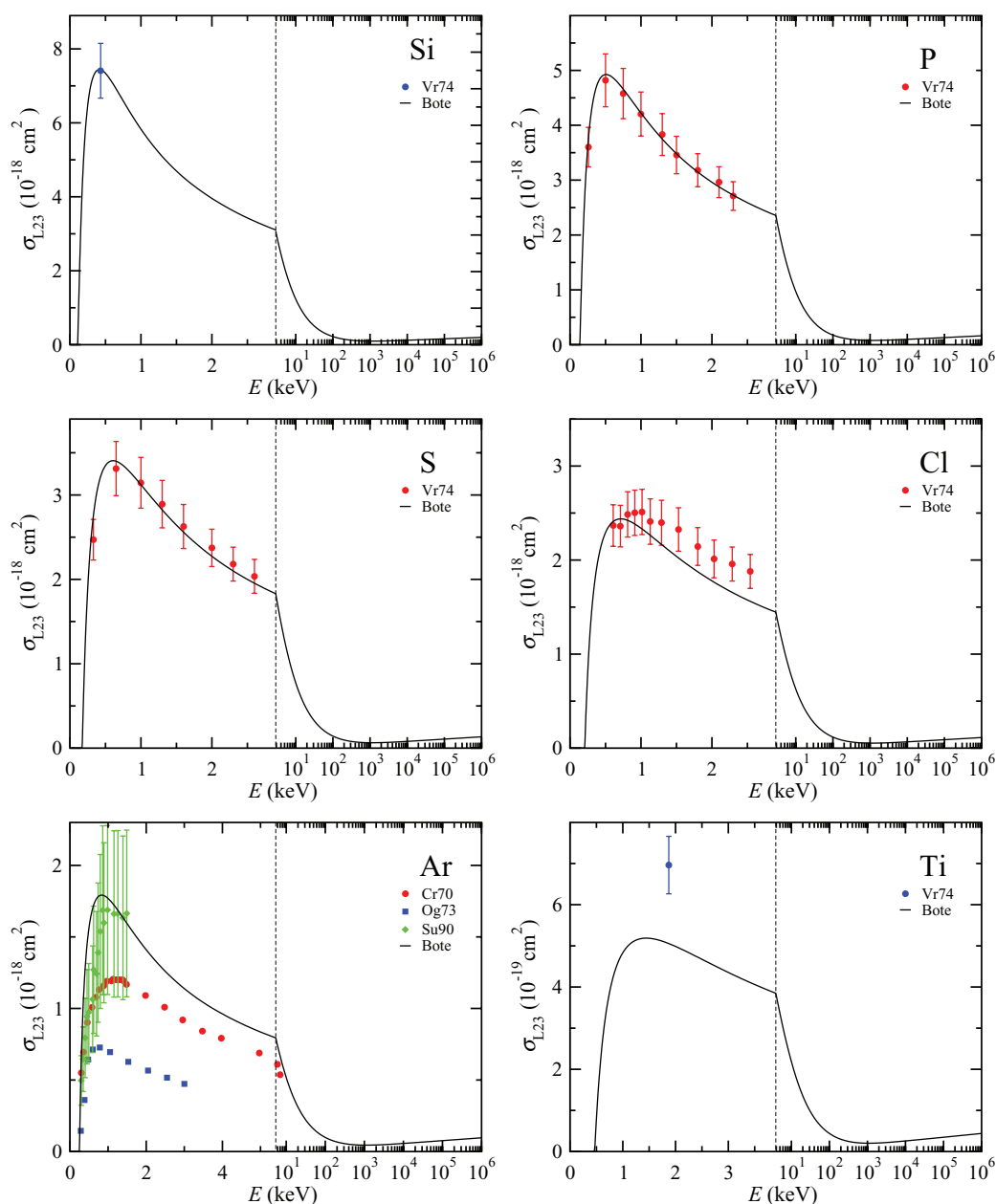


FIG. 26. (Color online) Absolute L_{23} -subshell ionization cross sections vs. incident electron energy for Si, P, S, Cl, Ar, and Ti. Solid curves are the results of the DWBA calculations. Symbols are experimental measurements.

sufficient to identify independent data sets that showed satisfactory consistency with themselves and with theory for further analysis. Since there are more cross-section measurements available for K-shell ionization than for L- and M-shell ionization, we considered that a minimum of three sets of independent measurements would be reasonable for K-shell data while two sets of independent measurements would have to suffice for L- and M-shell data. The sets of data identified in this way are designated by check marks in Tables 2–5 to indicate that these are sources of what we term “superior” data. We could then make a more quantitative evaluation of the selected sets of cross sections by calculating the root-mean-square percentage deviation, RMS , and the mean percentage deviation, R , of the measured cross sections for each selected element from the corre-

sponding DWBA cross sections of Bote *et al.* shown in Figs. 11–41.

The RMS and R parameters are defined as follows:

$$RMS = \sqrt{\frac{1}{n} \sum_{i=1}^n (\Delta_i)^2}, \quad (138a)$$

$$R = \frac{1}{n} \sum_{i=1}^n (\Delta_i), \quad (138b)$$

where n is the number of data points, and

$$\Delta_i = \frac{\sigma_{\text{meas},i} - \sigma_{\text{Bote}}}{\sigma_{\text{Bote}}} \times 100, \quad (138c)$$

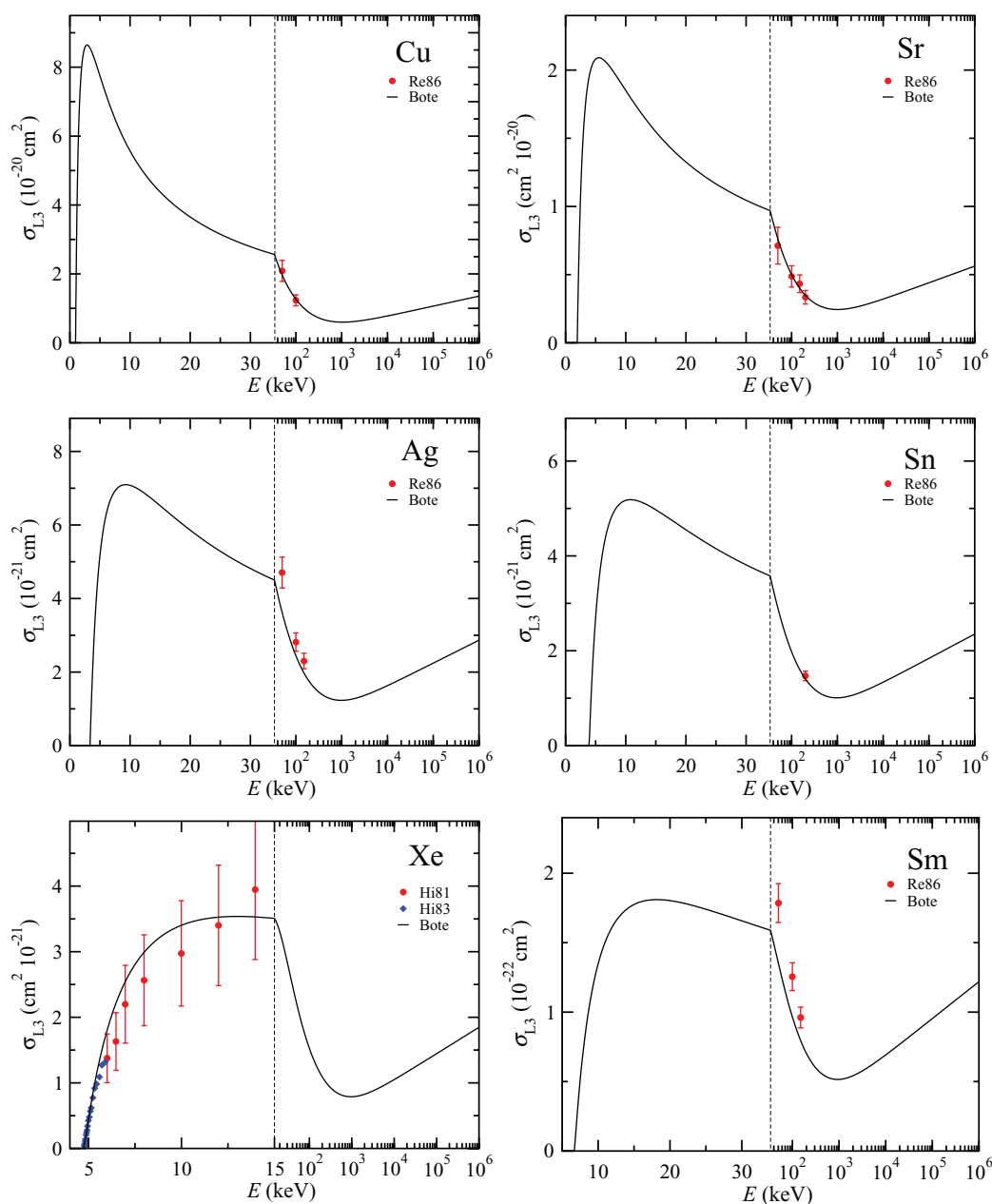


FIG. 27. (Color online) Absolute L_3 -subshell ionization cross sections vs. incident electron energy for Cu, Sr, Ag, Sn, Xe, and Sm. Solid curves are the results of the DWBA calculations. Symbols are experimental measurements.

where $\sigma_{\text{meas},i}$ is a measured cross section in a selected data set for a given element and σ_{Bote} is the corresponding calculated cross section using the DWBA method of Bote *et al.*

Average values of RMS and R for a group of N_j cross-section measurements for a given element j are denoted as \overline{RMS}_j and \overline{R}_j , respectively. Weighted average values of \overline{RMS}_j and \overline{R}_j for a group of M elements, denoted as $\langle RMS \rangle$ and $\langle \overline{R} \rangle$, respectively, are calculated as

$$\langle RMS \rangle = \frac{\sum_{j=1}^M \overline{RMS}_j \times N_j}{\sum_{j=1}^M N_j}, \quad (139a)$$

$$\langle \overline{R} \rangle = \frac{\sum_{j=1}^M \overline{R}_j \times N_j}{\sum_{j=1}^M N_j}. \quad (139b)$$

Our method for evaluating measured cross sections is a test of the hypothesis that the calculated cross sections provide a reliable description of the measured cross sections (i.e., in magnitude as a function both of energy and atomic number). We will therefore later examine the individual percentage deviations between measured cross sections in the selected data sets and the corresponding calculated values to determine whether these deviations depend significantly on the overvoltage ratio, U , and Z . We

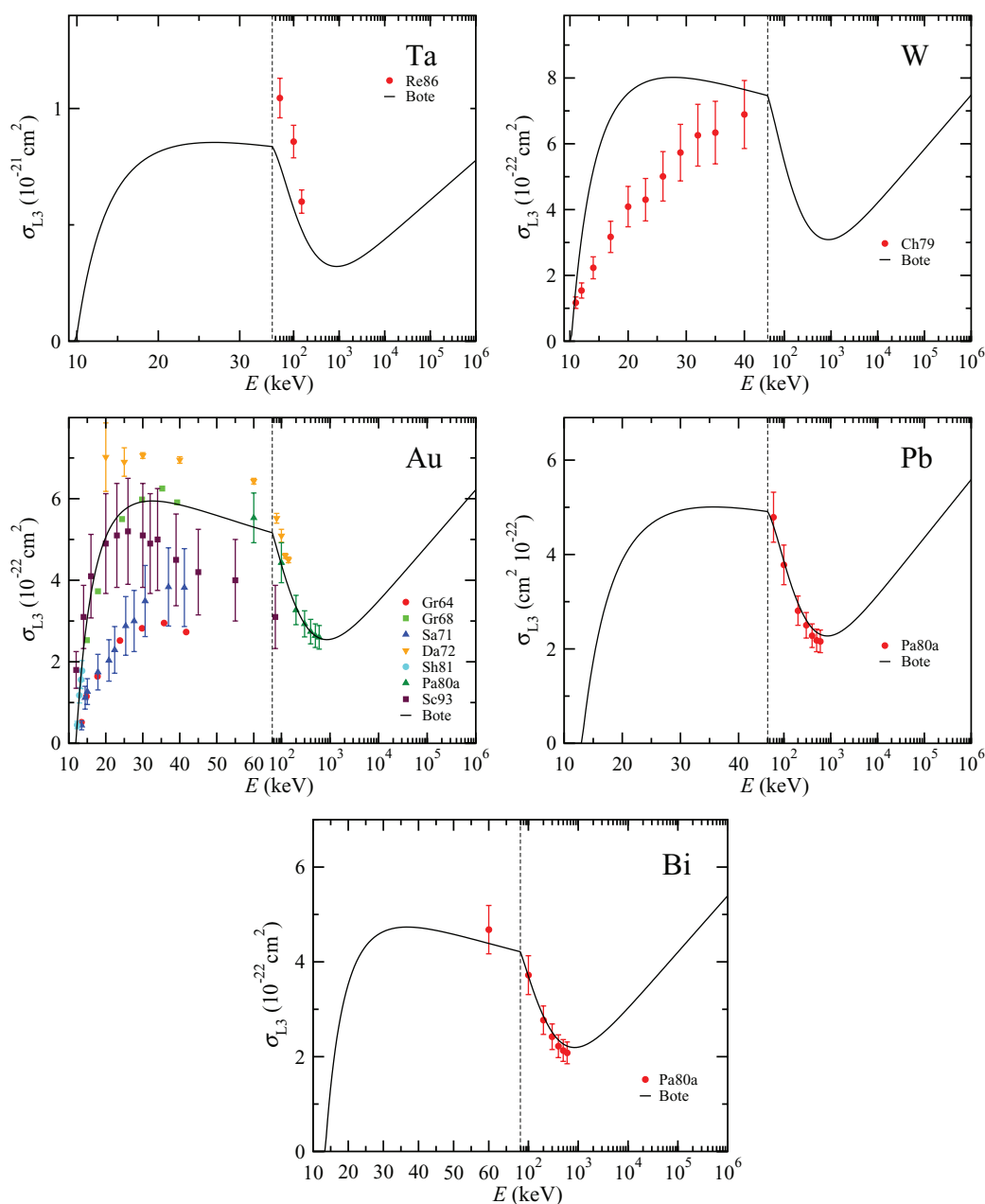


FIG. 28. (Color online) Absolute L_3 -subshell ionization cross sections vs. incident electron L_3 energy for Ta, W, Au, Pb, and Bi. Solid curves are the results of the DWBA calculations. Symbols are experimental measurements.

also need to establish that values of $\langle \bar{R} \rangle$ are small compared to $\langle \overline{RMS} \rangle$.

7.2. K-shell ionization cross sections

We used the evaluation criteria described in Sec. 7.1 to identify the 26 elements shown in Table 7 for which there were three or more sets of measured K-shell ionization cross sections that we considered to have a satisfactory degree of consistency with each other and which showed dependences on electron energy that were judged consistent with that expected from the Bote *et al.* analytical formulae³¹ described in Sec. 3.6. The comparison plots shown in Figs. 11–21 helped us to identify elements that met these criteria. This approach

seemed reasonable since we have utilized the illustrative Fano plots in Fig. 3 to show that the Bote *et al.* formulae were asymptotically consistent with the Bethe formula for inner-shell ionization [Eqs. (52), (66), and (68)]. Figure 3 also indicated that some sets of measured cross sections were consistent with the trends with energy expected from the Bote *et al.* formulae while other sets of data were not.

For 14 of the elements in Figs. 11–21 (N, Ne, Si, Ar, Mn, Zn, Ga, Ge, Se, Y, Pd, Ag, Sb, and Bi), there were clearly multiple sets of measurements that were considered sufficiently consistent with each other and with cross sections from the Bote formulae. This high degree of consistency between measured and calculated cross sections gave us initial confidence that the Bote formulae could be a useful guide for other elements over a

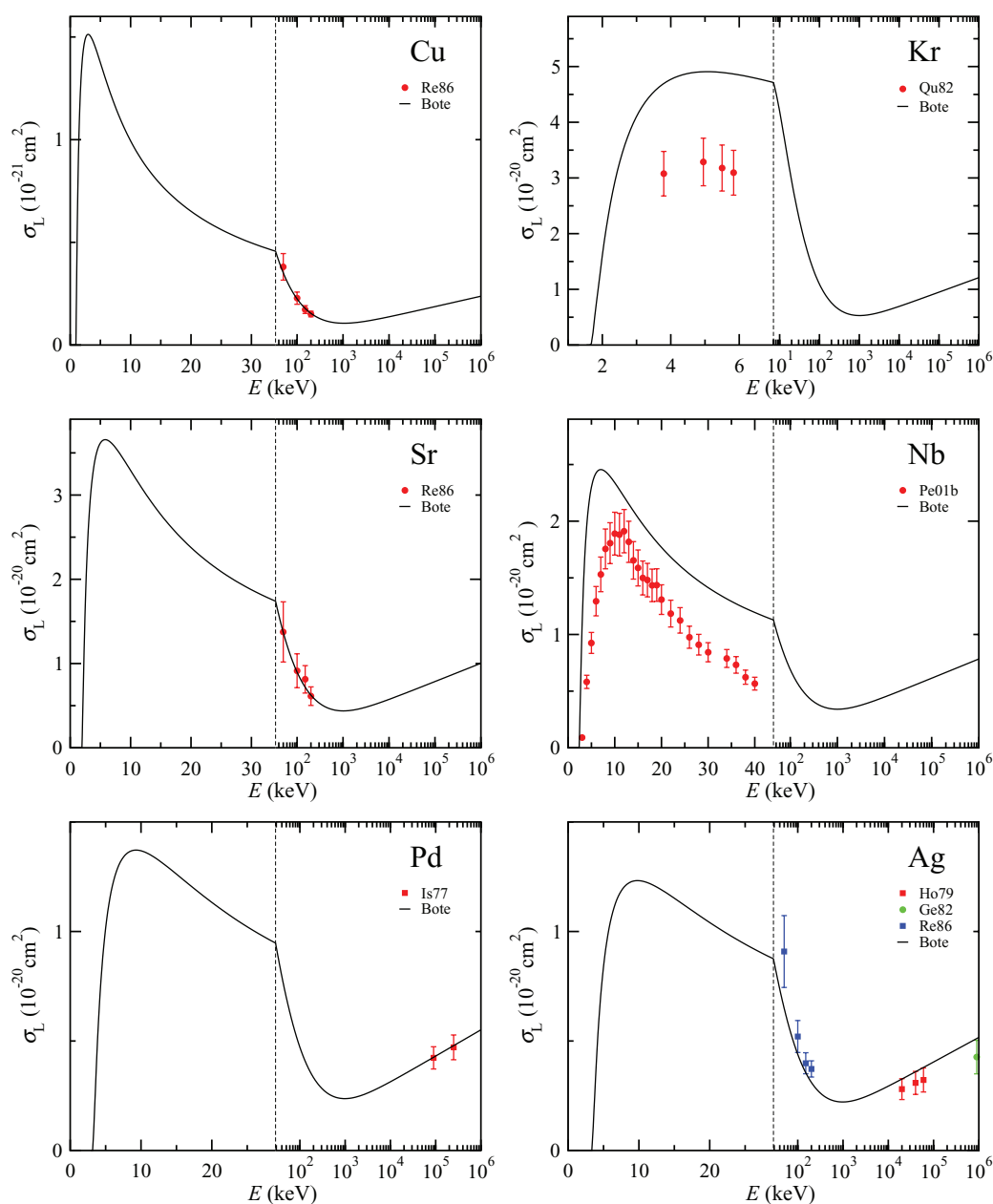


FIG. 29. (Color online) Total L-shell ionization cross sections vs. incident electron energy for Cu, Kr, Sr, Nb, Pd, and Ag. Solid curves are the results of the DWBA calculations. Symbols are experimental measurements.

wide range of Z . For 11 elements (C, Al, Cr, Fe, Ni, Cu, Sn, Au, and Pb), we could identify three or more sets of measured cross sections that showed good consistency with each other and with the Bote energy dependence. In addition, we identified one or more sets of other cross-section measurements for certain elements that showed clear systematic differences with respect to those measurements that were judged to be mutually consistent. For example, we excluded the measurements of Hink and Paschke¹²¹ and of Colliex and Jouffrey²⁶⁸ for C (Fig. 11), and the cross sections of Hansen *et al.*^{112,113} for Sn, W, Au, and Pb which showed erratic dependences on electron energy (Figs. 17, 20, and 21). We have tentatively included Ca in our comparisons since there were four sets of measurements

that showed a high degree of consistency with the Bote energy dependence except for energies between about 5 and 15 keV. For two elements (He and O), there were many sets of measured cross sections that were consistent with each other but which were generally smaller than those expected from the Bote formulae for energies less than 400 eV for He or 1 keV for O (Fig. 11); the data for these elements will be discussed below. These considerations were considered sufficient as a first step in identifying elements that showed generally consistent sets of measured cross sections for further examination.

We now show plots in Figs. 42–46 of percentage deviations of measured cross sections from the calculated Bote cross sections, Δ_i from Eq. (138c), as a function of electron energy

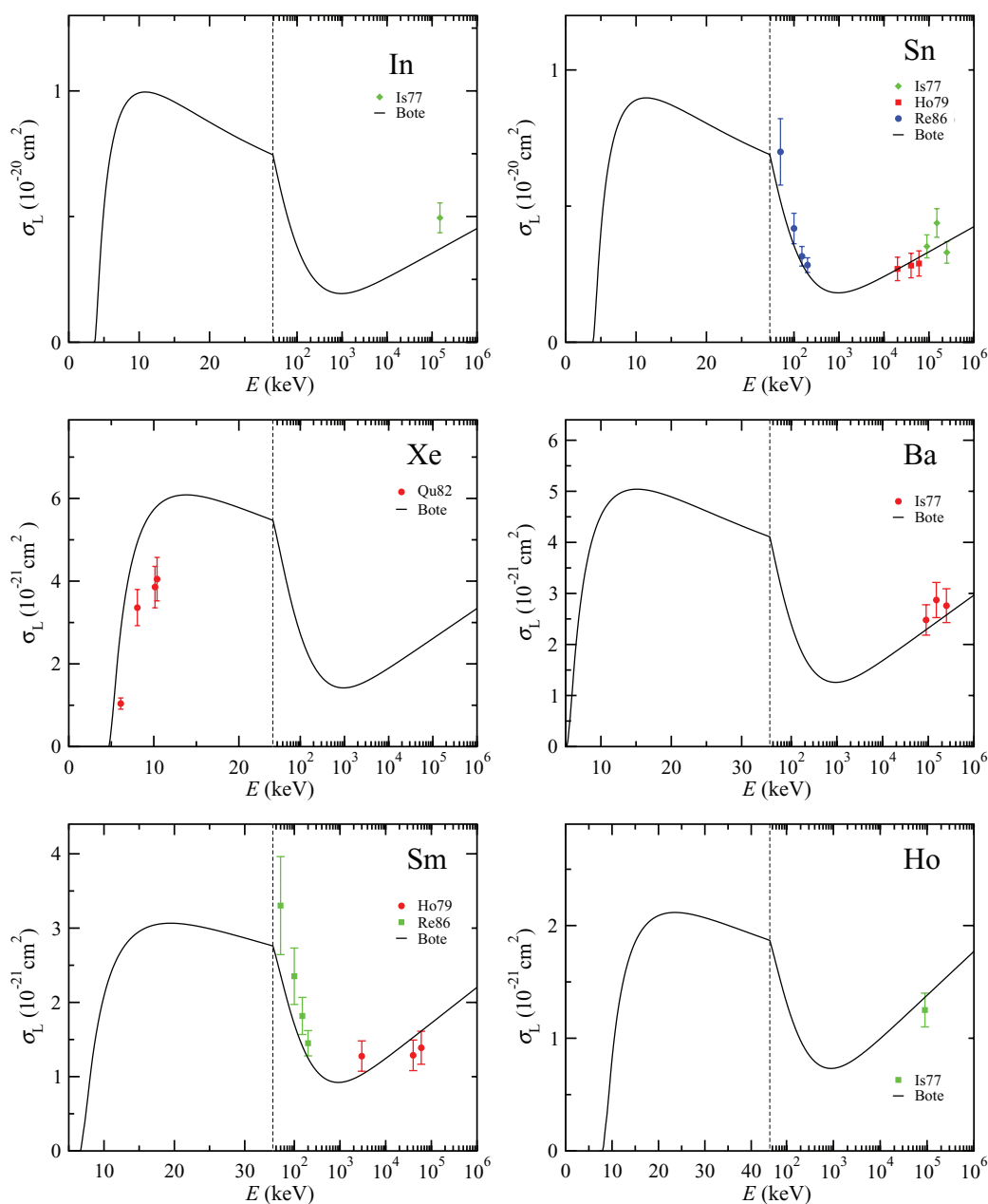


Fig. 30. (Color online) Total L-shell ionization cross sections vs. incident electron energy for In, Sn, Xe, Ba, Sm, and Ho. Solid curves are the results of the DWBA calculations. Symbols are experimental measurements.

for our selected elements. The latter cross sections were evaluated from Eqs. (87) and (88) using K-shell binding energies from the Carlson compilation,⁶⁴ as described in the Appendix. Table 7 identifies the references of papers containing the measured cross sections for the selected elements as well as the simplified or key references that identify the sets of data in Figs. 42–46. We point out that we have chosen the same ordinate scale in Figs. 42–46 (–50% to 50%) so that variations in the magnitudes of Δ_i for different elements can be readily compared (since the K-shell cross sections in Figs. 11–21 vary by over six orders of magnitude).

We see different trends of the Δ_i plots as a function of energy in Figs. 42–46. For some elements (e.g., C, N, O, Ne, Si, Ca, and Zn), there are individual sets of data that show Δ_i increas-

ing with increasing energy, although the difference data for C from Limandri *et al.*¹⁶³ decrease at higher energies. There are other sets of data (e.g., for He, Mn, Ni, Cu, Zn, Ga, Ge, and Pd) where Δ_i decreases with increasing energy. There are also many sets of data (e.g., for N, Al, Ar, Ti, Cr, Mn, Fe, Ni, Cu, Ga, Ge, Se, Y, and Ag) where Δ_i does not vary appreciably with energy. In other cases there are local minima in some sets of data (e.g., for C, N, Ne, Si, Ca, and Sn) and local maxima (e.g., for O, Ne, Mn, Fe, Zn, and Ge). We do not have explanations for these varying systematic trends in the difference plots other than to point out that they likely result from some local systematic effects in the experiments.

We have chosen not to include He in our evaluation because of the systematic differences between the many

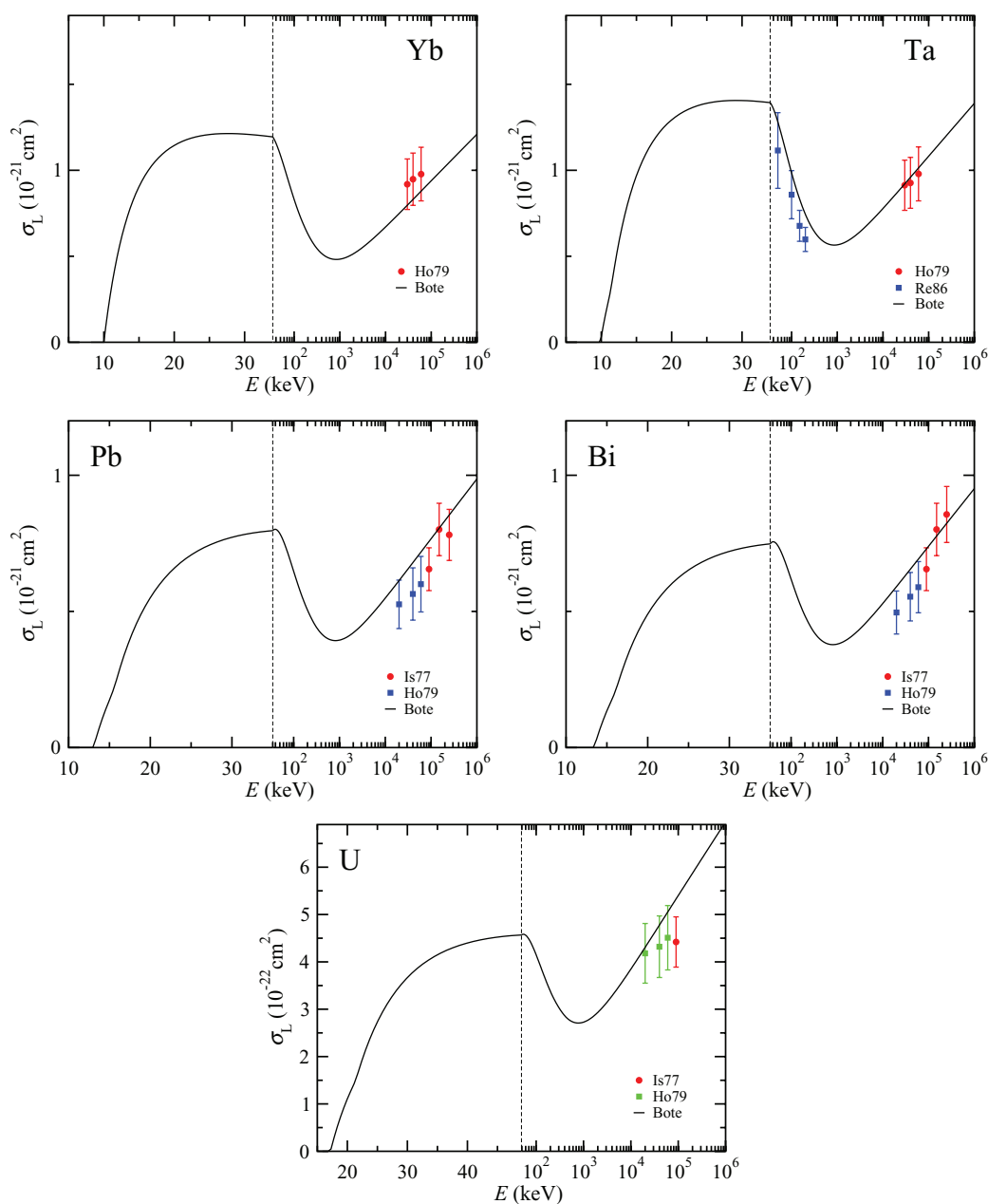


Fig. 31. (Color online) Total L-shell ionization cross sections vs. incident electron energy for Yb, Ta, Pb, Bi, and U. Solid curves are the results of the DWBA calculations. Symbols are experimental measurements.

cross-section measurements in Fig. 11 and the cross sections from the Bote *et al.* formulae for energies less than about 400 eV. As indicated in Sec. 2.2, the DWBA is not expected to be accurate for light elements because it neglects the post-collision interaction between the projectile and the emerging knocked-on electron that is of the same magnitude as the interaction with the nucleus. Similar differences are seen for H in Fig. 11. There is generally good agreement between many of the sets of measured cross sections for C, N, and Ne in Fig. 11 and the corresponding calculated cross sections of Bote *et al.* For O, however, many of the measured cross sections in Fig. 11 are smaller than the corresponding calculated cross sections although the recent measurements of

Limandri *et al.*¹⁶³ agree well with the calculated cross sections.

We now evaluate the distributions in Figs. 42–46 of the percentage deviations of measured K-shell ionization cross sections from the corresponding cross sections calculated from the Bote *et al.* formulae. Figure 47 shows plots of these distributions as a function of U_K , the ratio of the incident energy to the K-shell binding energy. For this purpose, we have again made use of Carlson's⁶⁴ compilation of elemental BEs. Figure 47 indicates that most of the percentage deviations are roughly independent of U_K although we point out some large deviations near the ionization threshold (particularly for $U_K < 1.1$) to be discussed shortly. We also point out that the

TABLE 4. Measurements of M-shell ionization cross sections performed up to May 2013. Information on the measured shell(s), incident electron energy range, method and target used, simplified reference (as shown in Figs. 32 and 33), and the full reference is also given. Methods include measurements with x-ray yields (X) and Auger yields (A). Targets used include self-supporting thin films (T) and gases (G). The check marks designate particular sets of measurements with superior data from the evaluation of experimental data (see Sec. 7)

Element	Shell	Energy (keV)	Method, target	Superior data	Key	Reference
Br	M _{4,5}	0.314	A,G	–	Vr74	Vracking and Meyer ²²⁷
Kr	M _{4,5}	0.12 to 1.48	A,G	–	Su90	Suzuki <i>et al.</i> ²³¹
Sn	M _{4,5}	1.9	A,G	–	Vr74	Vracking and Meyer ²²⁷
Au	M	2×10 ⁴ to 6×10 ⁴	X,T	✓	Ho79	Hoffmann <i>et al.</i> ¹³⁴
Au	M	60 to 600	X,T	✓	Pa80b	Pálinkás and Schlenk ²²²
Pb	M	9×10 ⁴ to 2.5×10 ⁵	X,T	✓	Is77	Ishii <i>et al.</i> ¹³¹
Pb	M	2×10 ⁴ to 6×10 ⁴	X,T	✓	Ho79	Hoffmann <i>et al.</i> ¹³⁴
Pb	M	60 to 600	X,T	✓	Pa80b	Pálinkás and Schlenk ²²²
Bi	M	9×10 ⁴ to 2.5×10 ⁵	X,T	✓	Is77	Ishii <i>et al.</i> ¹³¹
Bi	M	2×10 ⁴ to 6×10 ⁴	X,T	✓	Ho79	Hoffmann <i>et al.</i> ¹³⁴
Bi	M	60 to 600	X,T	✓	Pa80b	Pálinkás and Schlenk ²²²
U	M	2×10 ⁴ to 6×10 ⁴	X,T	–	Ho79	Hoffmann <i>et al.</i> ¹³⁴

percentage deviations in Fig. 47 scatter roughly uniformly about zero over a wide range of U_K .

Figure 47 excludes one particularly large percentage deviation, that of 1474% for C from the work of Tawara *et al.*²⁰³ at a nominal energy of 2 eV above the ionization threshold. We believe that this and some other large percentage deviations at near-threshold energies in Fig. 47(a) with absolute deviations larger than 40% are probably due to uncertainty of the incident-

electron energy scale and/or to uncertainty of the Carlson BE. As pointed out in the Appendix, BE uncertainties of about 2 eV are not uncommon due to inadequacies in the calibrations of instrumental BE scales, to the presence of surface oxides or impurities, and to uncertainties of work functions utilized in the conversion of BEs referenced to the vacuum level (as appropriate for atoms and molecules, and the choice for the Carlson compilation) or to the Fermi level (as appropriate for solids). We also point out that

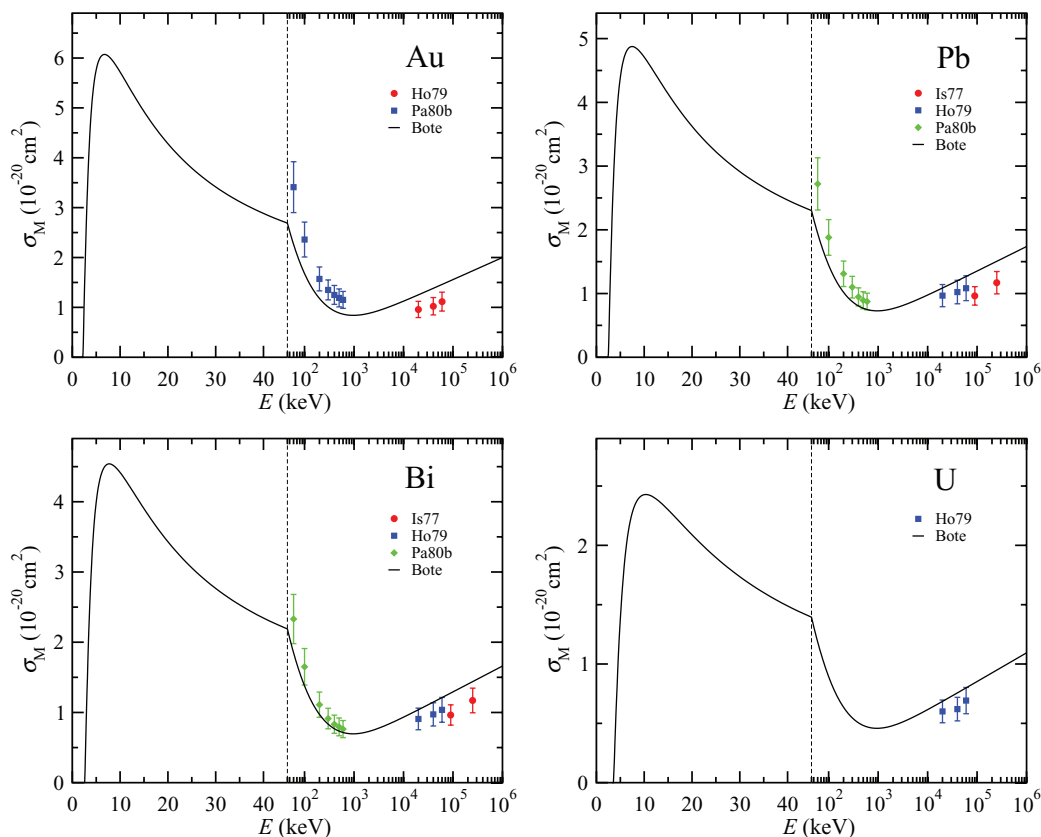


FIG. 32. (Color online) Absolute M-shell ionization cross sections vs. incident electron energy for Au, Pb, Bi, and U. Solid curves are the results of the DWBA calculations. Symbols are experimental measurements.

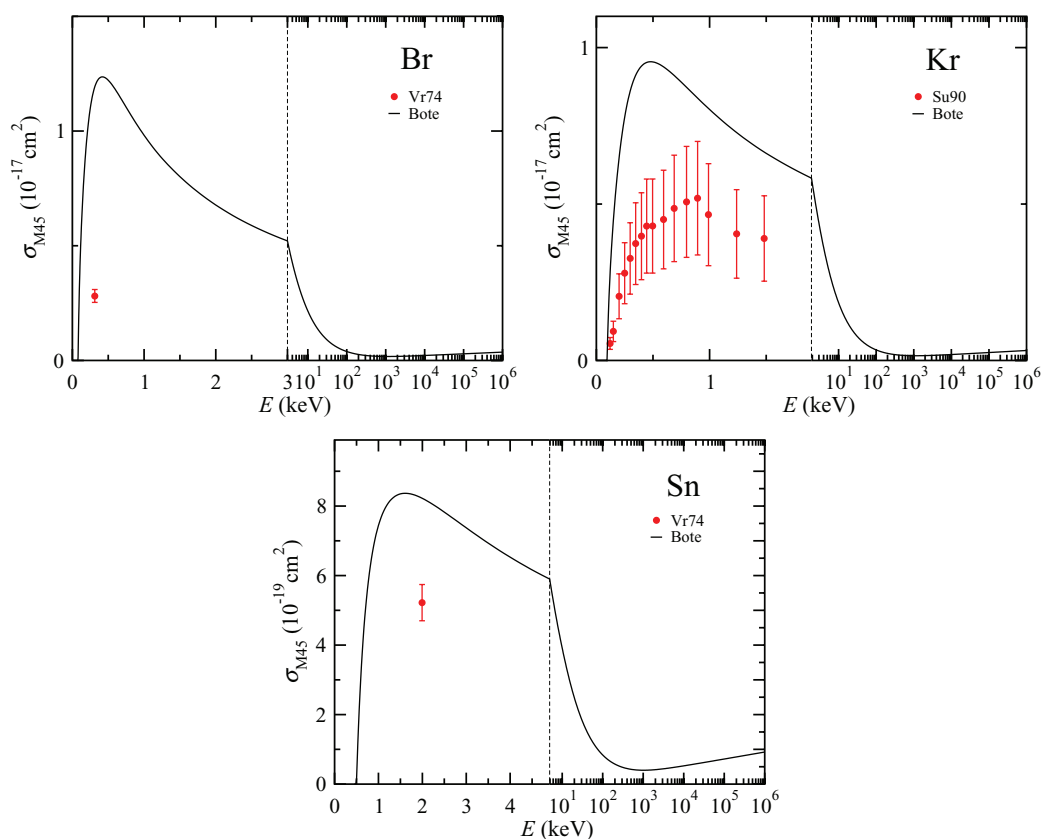


FIG. 33. (Color online) Absolute M_{45} -subshell ionization cross sections vs. incident electron energy for Br, Kr, and Sn. Solid curves are the results of the DWBA calculations. Symbols are experimental measurements.

the near-threshold cross-section measurements, particularly those with $U_K < 2$, would be expected to have larger uncertainties than those for larger U_K values because the cross sections are varying relatively rapidly with U_K and small uncertainties in the incident-energy scale or the BE can lead to larger uncertainties in the U_K values than for larger values of U_K . We also note that the detected signals at energies close to threshold are smaller than at higher energies.

Figure 48 shows the percentage deviations from Fig. 47 as a function of U_K on a linear scale for $U_K < 1.2$. In addition to the large deviations discussed previously, we see a systematic variation of the negative deviations for $U_K < 1.02$. These deviations come from the near-threshold cross-section measurements of Hippler *et al.*²⁰⁷ for Ar. Their cross-section measurements were consistent with the theory of Wannier.²⁷⁴ There is also consistency between the absolute Hippler *et al.* cross-section measurements and the relative cross-section measurements of Gräf and Hink²⁷⁵ for incident energies between 10 and 100 eV above the Ar K-shell ionization threshold of about 3.203 keV.⁶⁴

We conclude from the plots in Figs. 47 and 48 that the calculated Bote *et al.* cross sections for K-shell ionization agree satisfactorily with the self-consistent sets of measured K-shell cross section for overvoltage ratios between 1.02 and 2×10^5 . We note that the excess energy in the ionization should also be larger than about 50 eV (Refs. 207 and 275) when using the Bote *et al.* formulae.

Table 7 lists the root mean square deviation, RMS , and the mean percentage deviation, R , of the measured K-shell ionization cross sections from the corresponding Bote *et al.* cross sections for each data set that were calculated from Eq. (138). In these calculations, we have excluded deviations in Figs. 47 and 48 for $U_K < 1.02$.

Average values of RMS and R , \overline{RMS} and \overline{R} , were calculated for each of the 26 evaluated elements and are shown in Table 8. Figure 49 shows plots of these values versus Z . We see that the \overline{RMS} values are roughly independent of Z although the values for $Z < 20$ may be slightly larger than those for larger values of Z . The \overline{R} values do not appear to vary systematically with Z . We therefore conclude that the Bote *et al.* predictive formulae are satisfactory for elements from at least carbon to bismuth.

We note here that the Bote *et al.* formulae are also consistent with the many measurements of ionization cross sections for He in Fig. 11 for incident energies greater than about 400 eV (i.e., $U_K > 16$). Similarly, the measured ionization cross sections of Shah *et al.*²⁵⁹ for H in Fig. 11 are consistent with the Bote *et al.* values for incident energies greater than about 200 eV (i.e., $U_K > 15$). We therefore infer that the Bote *et al.* formulae should also provide reliable K-shell ionization cross sections for Li, Be, and B at incident energies for which U_K is greater than about 16.

The weighted average values of \overline{RMS} and \overline{R} from Eq. (139) are 10.3% and -1.8% , respectively. The former

TABLE 5. Measurements of L-shell x-ray production cross sections performed up to May 2013. Information on the measured line, incident electron energy range, target used, simplified reference (as shown in Figs. 34–38), and the full reference is also given. Targets used include self-supporting thin films (T), thin films on substrates (TS), and gases (G). The check marks designate particular sets of measurements with superior data from the evaluation of experimental data (see Sec. 7)

Element	Line	Energy (keV)	Target	Superior data	Key	Reference
Ar	LX	0.25 to 14.7	G	–	La75	Langenberg <i>et al.</i> ¹²⁷
Ar	LX	0.3 to 3.0	G	–	Bo79	Bonnet <i>et al.</i> ¹³⁵
Ga	La,Lβ ₁	1.5 to 39.0	T	–	Me06	Merlet <i>et al.</i> ^{169,170}
Ge	La	1.6 to 40.6	T	–	Me06	Merlet <i>et al.</i> ¹⁶⁸
As	La,Lβ ₁	1.5 to 39.0	T	–	Me06	Merlet <i>et al.</i> ^{169,170}
Ag	LX	5.0 to 25.0	TS	–	Wu04	Wu <i>et al.</i> ¹⁷⁹
In	La,Lβ	5.5 to 21.6	TS	–	Ta02b	Tang <i>et al.</i> ¹⁷⁴
Sn	La,Lβ	5.3 to 25.1	TS	–	Ta02a,b	Tang <i>et al.</i> ^{174,197}
I	La	10 to 30	TS	–	Wu12	Wu <i>et al.</i> ¹⁸⁸
Ba	La,Lβ	7 to 30	TS	–	Wu11	Wu <i>et al.</i> ¹⁸⁷
Sm	La,Lβ,Lγ	1.39 × 10 ³	T	–	Pa75	Park <i>et al.</i> ¹²⁹
Sm	La,Lβ,Lγ,Lℓ,LX	300 to 600	T	–	Ri78	Ricz <i>et al.</i> ¹³²
Sm	La,Lβ,Lγ	8.0 to 35	TS	–	Go05	Gou <i>et al.</i> ¹⁶²
Gd	La,Lβ,Lγ	1.39 × 10 ³	T	✓	Pa75	Park <i>et al.</i> ¹²⁹
Gd	La,Lβ	9.0 to 36	TS	✓	Wu10b	Wu <i>et al.</i> ¹⁸⁵
Dy	La,Lβ,Lγ	8.5 to 35	TS	–	Go05	Gou <i>et al.</i> ¹⁶²
Ho	La,Lβ,Lγ,Lℓ,LX	300 to 600	T	–	Ri78	Ricz <i>et al.</i> ¹³²
Ho	LX	9.0 to 36	TS	–	Wu06	Wu <i>et al.</i> ¹⁸²
Er	La,Lβ,Lγ	1.39 × 10 ³	T	✓	Pa75	Park <i>et al.</i> ¹²⁹
Er	La,Lβ,Lγ,Lℓ,LX	300 to 600	T	✓	Ri78	Ricz <i>et al.</i> ¹³²
Tm	LX	3 × 10 ⁵ to 9 × 10 ⁵	T	–	Mi70	Middleman <i>et al.</i> ⁷¹
Tm	La,Lβ,Lγ	10.0 to 37	TS	–	Wu05	Wu <i>et al.</i> ¹⁸⁰
Yb	La,Lβ,Lγ	1.39 × 10 ³	T	✓	Pa75	Park <i>et al.</i> ¹²⁹
Yb	La,Lβ,Lγ, LX	300 to 600	T	✓	Sc77	Schlenk <i>et al.</i> ²¹³
Hf	La,Lβ,Lγ	10.0 to 33.0	TS	–	Lu02	Luo <i>et al.</i> ¹⁶⁷
Hf	La,Lβ,Lγ	10 to 36	TS	–	Ya04	Yang <i>et al.</i> ¹⁸⁹
Ta	La,Lβ,Lγ	10.0 to 36.0	TS	–	Wu05	Wu <i>et al.</i> ¹⁸⁰
W	La,Lβ,Lγ	10.8 to 36.0	TS	–	Pe01a	Peng <i>et al.</i> ¹⁷²
W	La	12.0 to 30.0	TS	✓	Ca02	Campos <i>et al.</i> ¹⁶¹
W	La,Lβ,Lγ	11.0 to 34.0	TS	✓	Ya04	Yang <i>et al.</i> ¹⁸⁹
W	La,Lβ	13.0 to 40.0	TS	✓	Wu10b	Wu <i>et al.</i> ¹⁸⁵
Re	La,Lβ,Lγ	1.39 × 10 ³	T	–	Pa75	Park <i>et al.</i> ¹²⁹
Re	La,Lβ,Lγ	11.1 to 40	TS	–	Ta02b	Tang <i>et al.</i> ¹⁷⁴
Os	La,Lβ,Lγ	12.0 to 36	TS	–	Wu06	Wu <i>et al.</i> ¹⁸²
Pt	La	12.0 to 30.0	TS	✓	Ca02	Campos <i>et al.</i> ¹⁶¹
Pt	La,Lβ,Lγ	1.39 × 10 ³	T	✓	Pa75	Park <i>et al.</i> ¹²⁹
Au	LX	3 × 10 ⁴ to 9 × 10 ⁴	T	–	Mi70	Middleman <i>et al.</i> ⁷¹
Au	La,Lβ,Lγ,Lℓ,LX	300 to 600	T	✓	Sc77	Schlenk <i>et al.</i> ²¹³
Au	La,Lβ,Lγ	60 to 600	T	✓	Pa80a	Pálinkás and Schlenk ¹³⁸
Au	La,Lβ,Lγ	12.0 to 25.0	T	✓	Sh81	Shima <i>et al.</i> ¹⁴⁰
Au	La	12.0 to 30.0	TS	✓	Ca02	Campos <i>et al.</i> ¹⁶¹
Au	La,Lβ	14.0 to 25.0	TS	✓	Wu04	Wu <i>et al.</i> ¹⁷⁹
Pb	La,Lβ,Lγ	1.39 × 10 ³	T	✓	Pa75	Park <i>et al.</i> ¹²⁹
Pb	La,Lβ,Lγ,Lℓ,LX	300 to 600	T	✓	Sc77	Schlenk <i>et al.</i> ²¹³
Pb	La,Lβ,Lγ	60 to 600	T	✓	Pa80a	Pálinkás and Schlenk ¹³⁸
Pb	La,Lβ	16.0 to 40.0	TS	✓	Wu07	Wu <i>et al.</i> ¹⁸³
Pb	La,Lβ	13.0 to 36.0	T	✓	Mo13	Moy <i>et al.</i> ²¹⁵
Bi	LX	3 × 10 ⁴ to 9 × 10 ⁴	T	–	Mi70	Middleman <i>et al.</i> ⁷¹
Bi	La,Lβ,Lγ	1.39 × 10 ³	T	✓	Pa75	Park <i>et al.</i> ¹²⁹
Bi	La,Lβ,Lγ,Lℓ	300 to 600	T	✓	Ri78	Ricz <i>et al.</i> ¹³²
Bi	La,Lβ,Lγ	60 to 600	T	✓	Pa80a	Pálinkás and Schlenk ¹³⁸
Bi	La,Lβ	17.0 to 40.0	TS	✓	Wu10c	Wu <i>et al.</i> ¹⁸⁶

value indicates the degree of agreement between the measured K-shell ionization cross sections from the selected data sets for the 26 elements and the corresponding calculated cross sections from the Bote *et al.* formulae for overvoltage ratios between 1.02 and 2×10^5 and for

atomic numbers between 6 and 83. The latter value is much smaller than the former value, indicating that the calculated K-shell ionization cross sections are not systematically smaller or larger than the measured cross sections in the selected data sets.

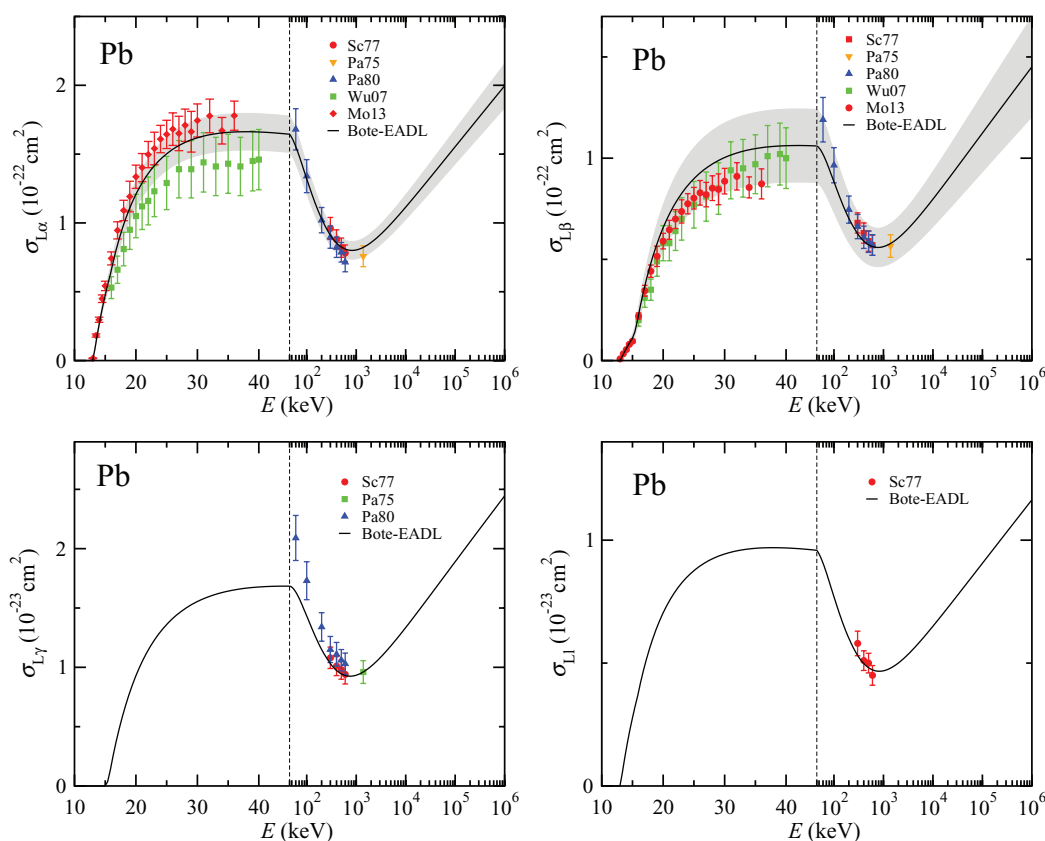


FIG. 34. (Color online) Absolute $L\alpha$, $L\beta$, $L\gamma$, and $L\ell$ x-ray production cross sections vs. incident electron energy for Pb. Solid curves are the results of the DWBA calculations of the relevant ionization cross section combined with data from the EADL database. Symbols are experimental measurements. The gray shaded areas indicate the estimated one-standard-deviation uncertainty bands of the Bote *et al.* calculations that arise from uncertainties in the adopted EADL parameters.

7.3. L-subshell ionization cross sections

We proceed in a similar way to evaluate the measured L-shell cross sections. There are, of course, fewer measurements of L-shell cross sections than for K-shell cross sections, and we have therefore chosen to find a minimum of two sets of L-shell ionization cross-section measurements that were consistent with each other in Figs. 26–28 for L_{23} - or L_3 -subshell cross sections and in Figs. 29–31 for total L-shell cross sections. In making these assessments, we were also guided by the energy dependences expected from the Bote *et al.* cross sections. We were able to identify only one element (Xe) for which there were two sets of consistent L_3 -subshell cross-section measurements (Fig. 27) and seven elements (Ag, Sn, Sm, Ta, Pb, Bi, and U) for which there were two or more sets of consistent measurements of total L-shell cross sections. Table 9 shows the data sets we have identified.

Figures 50 and 51 show plots of the percentage deviations from Eq. (138c) of the measured cross sections from the corresponding cross sections calculated from the Bote *et al.* formulae. The latter calculations were made with Eqs. (87) and (88) and the Carlson BEs, as described in the Appendix. We have also chosen the same ordinate scale in Figs. 50 and 51 as the corresponding plots of the deviations for K-shell cross sections as a function of electron energy in Figs. 42–46.

We proceed as before and plot the percentage deviations for total L-shell ionization cross sections in Figs. 50 and 51 (i.e., for Ag, Sn, Sm, Ta, Pb, Bi, and U). The percentage deviations for all of these elements are plotted as a function of U_L in Fig. 52(a). The latter plot is qualitatively similar to Fig. 47, and the deviations again scatter roughly uniformly about zero over a wide range of U_L , in this case from 5 to about 6×10^5 .

The weighted average values $\langle \overline{RMS} \rangle$ and $\langle \overline{R} \rangle$ from Eq. (139) are 15.0% and -3.1% , respectively. The Bote *et al.* predictive formulae for L-shell ionization cross sections are thus satisfactory for a wide range of Z , from Ag to U, and for overvoltage ratios from 1.02 to 6×10^5 .

Figure 52(b) is a plot of the percentage differences between measured Xe L_3 -subshell cross sections and the predicted cross sections from the Bote *et al.* predictive formulae as a function of U_{L3} on a linear scale. These percentage differences are based on the measurements of Hippler *et al.*^{204,205} As for differences for the Ar K-shell cross-section measurements shown in Fig. 48, there are large negative near-threshold deviations for $U_{L3} < 1.02$ that are consistent with the Wannier theory.²⁷⁴

Table 9 lists the root-mean-square deviation, RMS , and the mean percentage deviation, R , of the measured L-shell cross sections from the corresponding Bote *et al.* cross sections

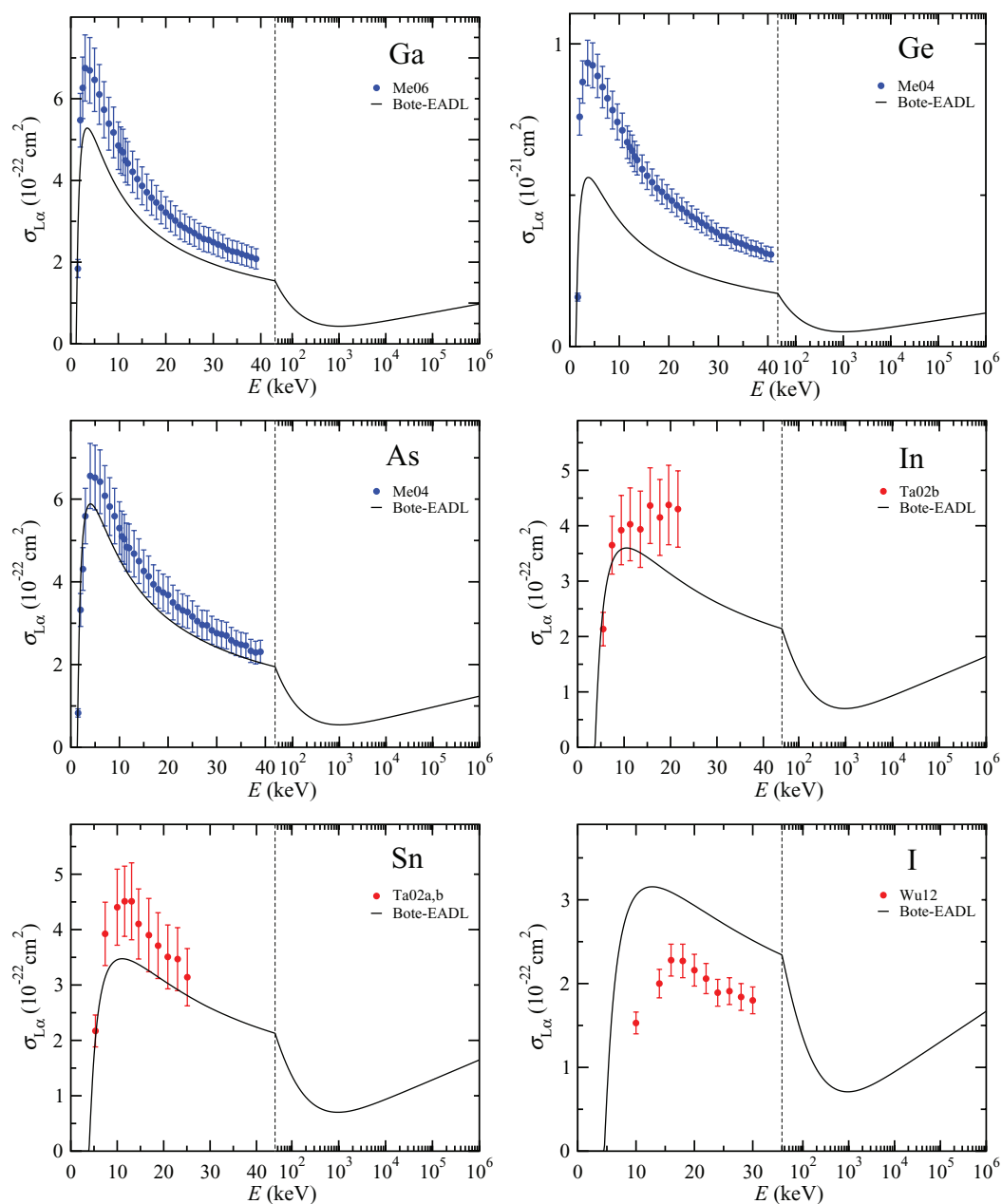


FIG. 35. (Color online) Absolute $L\alpha$ x-ray production cross sections vs. incident electron energy for Ga, Ge, As, In, Sn, and I. Solid curves are the results of the DWBA calculations of the L_3 -subshell ionization cross section combined with data from the EADL database. Symbols are experimental measurements.

for each data set that were calculated from Eq. (138). In these calculations, we excluded the deviations in Fig. 52 for $U_{L3} < 1.02$. Average values of RMS and R , \overline{RMS} and \overline{R} , for the eight elements are shown in Table 10.

Figure 53 shows plots of \overline{RMS} and \overline{R} as a function of Z . Although these parameters do not appear to vary significantly with Z , the \overline{RMS} values do decrease slightly with increasing Z , as for the corresponding plot for K-shell ionization cross sections shown in Fig. 49.

The weighted average values of RMS and R , \overline{RMS} and \overline{R} , from Eq. (139) are 15.0% and -3.1% , respectively. These values are larger than the corresponding values for K-shell ionization (10.3% and -1.9%) because of the additional

uncertainties involved in determining L-shell ionization cross sections, as discussed in Secs. 4.2, 4.3, and 5.1.2, and as illustrated in Fig. 34. Nevertheless, the Bote *et al.* predictive formulae for L-shell ionization are believed to be satisfactory for a wide range of Z , from Ag to U, and for overvoltages from 1.02 to 6×10^5 .

7.4. M-subshell ionization cross sections

We examined Fig. 32 and found three elements (Au, Pb, and Bi) that each had two or more sets of measurements of total M-shell ionization cross sections. These sets of measurements were consistent with each other and/or with the energy

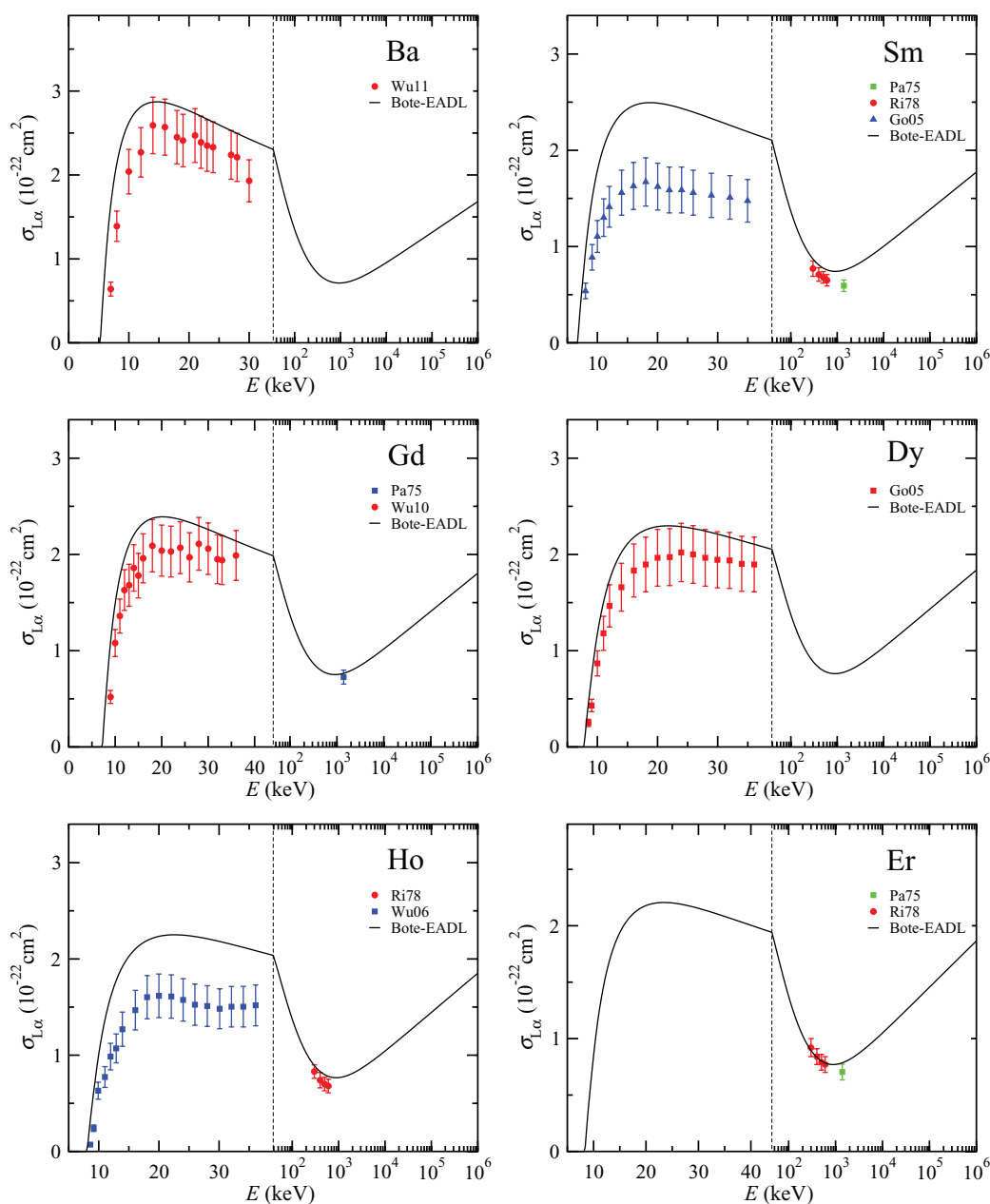


FIG. 36. (Color online) Absolute $L\alpha$ x-ray production cross sections vs. incident electron energy for Ba, Sm, Gd, Dy, Ho, and Er. Solid curves are the results of the DWBA calculations of the L_3 -subshell ionization cross section combined with data from the EADL database. Symbols are experimental measurements.

dependences expected from the Bote *et al.* predictive formulae. Table 11 lists the data sets we have identified.

Figure 54 shows plots of the percentage deviations of the measured total M-shell ionization cross sections from the corresponding cross sections obtained from the Bote *et al.* formulae. As in Subsections 7.1–7.3, the latter calculations were made with Eqs. (87) and (88) and the Carlson BEs,⁶⁴ as described in the Appendix. Figure 55 shows these deviations plotted as a function of U_M . While this plot is similar to Figs. 47 and 52, the deviations in Fig. 55 cluster in two groups. One of these groups has positive deviations (for U_M about 100) while the other has negative deviations (for U_M between about 10^4 and 10^5). Since the difference data in Fig. 55 are relatively sparse and the magnitudes of the differences are similar to

those in the other figures, we believe that there is no reason for suspecting a different dependence on the overvoltage ratio in Fig. 55 than in Figs. 47 and 52.

Table 11 lists the root mean square deviation RMS and mean percent deviation R from the Bote *et al.* cross sections for each data set that were calculated from Eq. (138). Average values of RMS and R , \overline{RMS} and \overline{R} , for the three elements are shown in Table 12. The values of \overline{RMS} and \overline{R} decrease with increasing Z but, since there are only three elements under consideration, we doubt that this is a valid trend. The weighted average values $\langle \overline{RMS} \rangle$ and $\langle \overline{R} \rangle$ from Eq. (139) are 23.5% and 8.2%, respectively. Not surprisingly, these values are larger than the corresponding values for K-shell and L_3 -subshell ionization cross sections due to the likely uncertainties of the larger

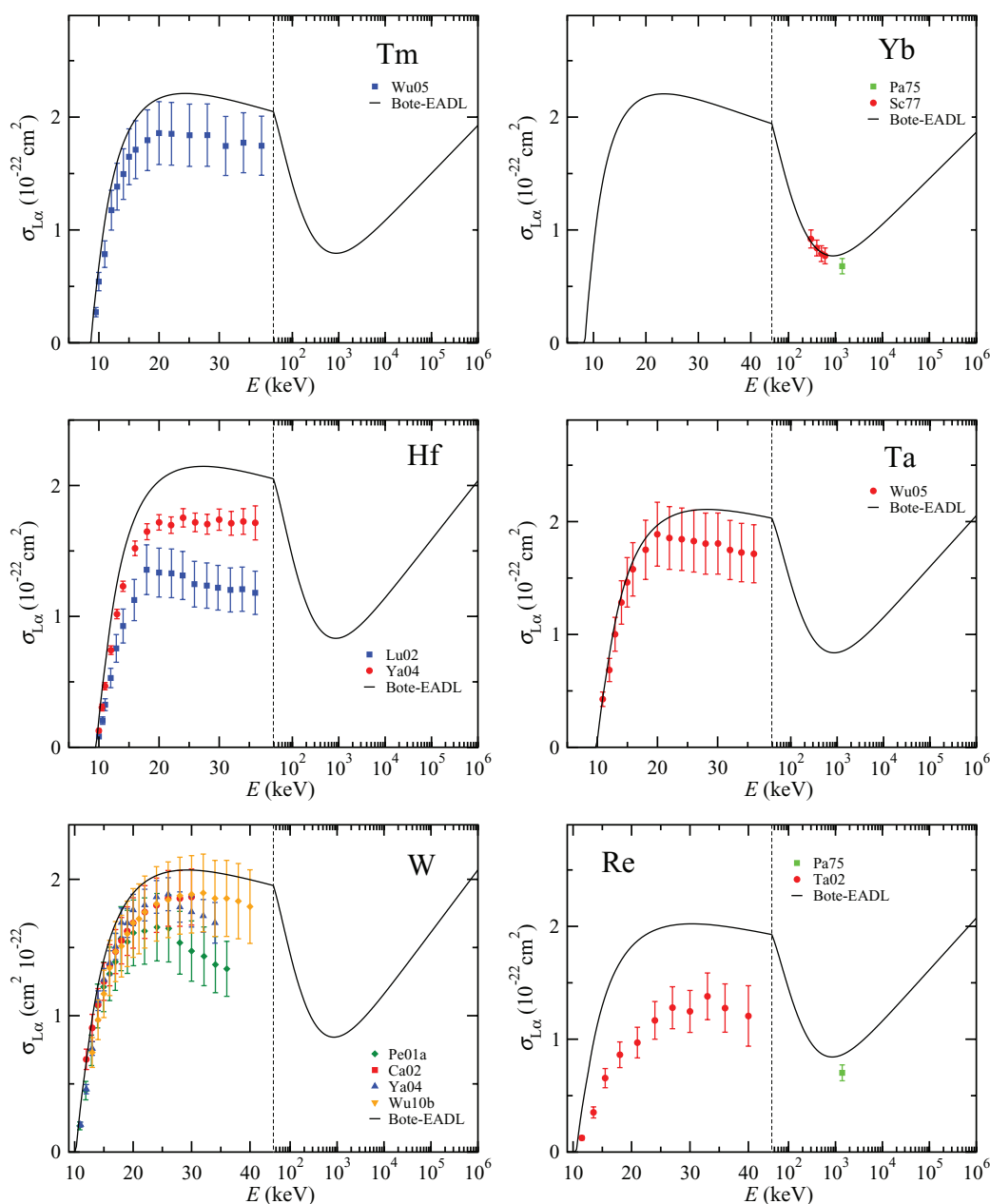


FIG. 37. (Color online) Absolute $L\alpha$ x-ray production cross sections vs. incident electron energy for Tm, Yb, Hf, Ta, W, and Re. Solid curves are the results of the DWBA calculations of the L_3 -subshell ionization cross section combined with data from the EADL database. Symbols are experimental measurements.

number of needed atomic parameters from the EADL, as discussed in Sec. 5.1.2. The Bote *et al.* predictive formulae for total M-shell ionization cross sections are thus believed to be satisfactory for at least certain high- Z elements, Au through Bi, and for overvoltage ratios from 23 to 10^5 .

7.5. $L\alpha$ x-ray production cross sections

We examined Figs. 35–37 and identified eight elements (Gd, Er, Yb, W, Pt, Au, Pb, and Bi) for which there were at least two sets of measured cross sections for production of $L\alpha$ x rays. These sets of cross sections were consistent with each other and/or with the energy dependences expected from the

Bote *et al.* formulae. Table 13 lists the data sets we have identified.

Figures 56 and 57 show plots of the percentage deviations between the measured $L\alpha$ x-ray production cross sections and the corresponding cross sections calculated from the Bote *et al.* formulae for L_3 -subshell ionization. The L_3 -subshell ionization cross sections were calculated from Eqs. (87) and (88) and the Carlson BEs,⁶⁴ as described in the Appendix, and the x-ray production cross sections were determined with fluorescence yields, radiative widths, and transition probabilities from the EADL database,¹ as described in Secs. 4.2 [Eqs. (104) and (105)] and 4.3. Figure 58 shows the percentage deviations from Figs. 56

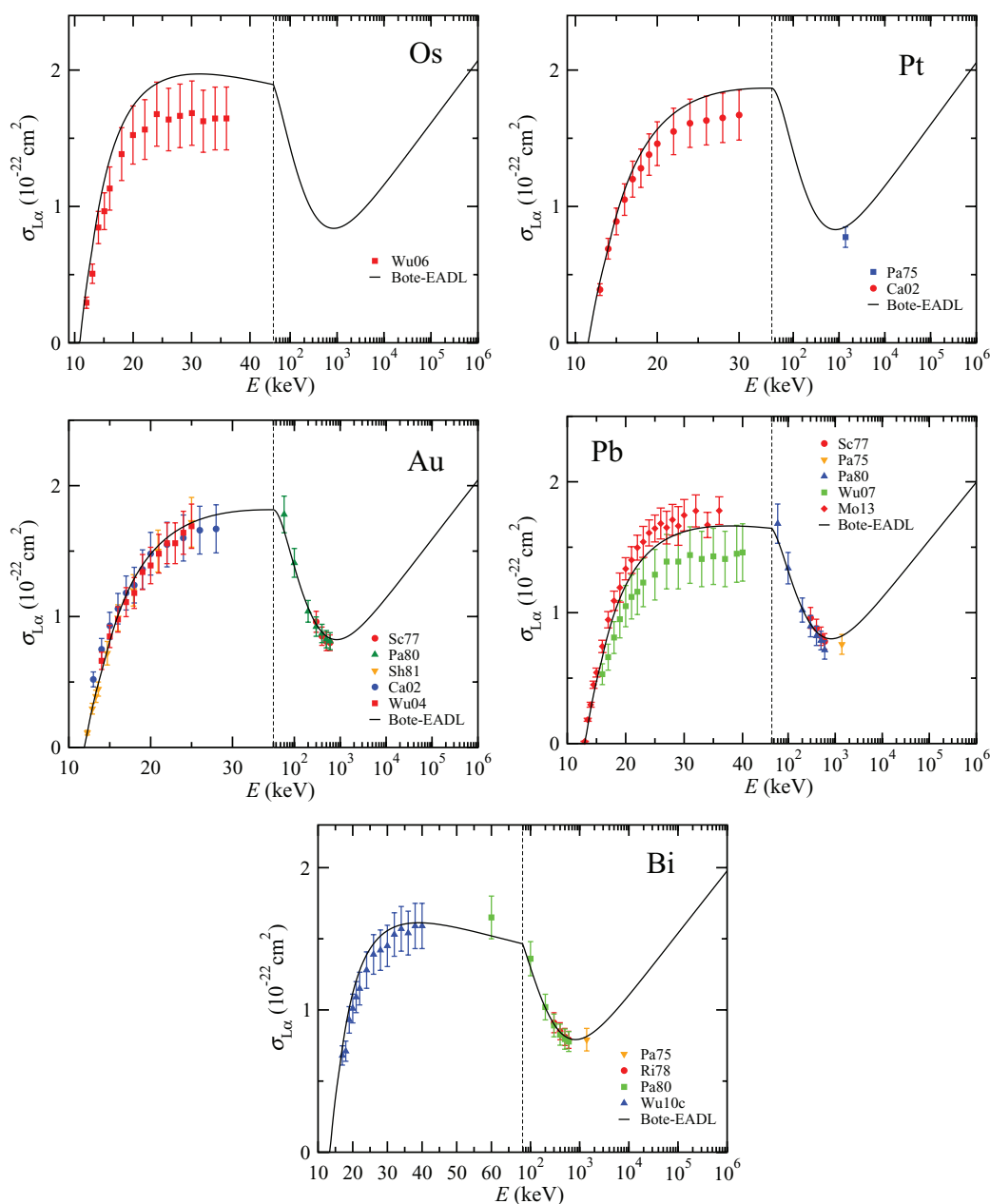


Fig. 38. (Color online) Absolute $L\alpha$ x-ray production cross sections vs. incident electron energy for Os, Pt, Au, Pb, and Bi. Solid curves are the results of the DWBA calculations of the L_3 -subshell ionization cross section combined with data from the EADL database. Symbols are experimental measurements.

and 57 as a function of U_{L_3} , the overvoltage ratio for L_3 -subshell ionization. Many of these deviations cluster about zero although there is a group of negative deviations in a cluster for values of U_{L_3} between about 1.2 and 4. There are also two relatively large deviations, one of -52.1% at $U_{L_3} = 1.24$ for Gd (Ref. 180) and the other of 54.3% at $U_{L_3} = 1.08$ for Au.¹⁶¹ We have no explanation for these latter two deviations other than they occur for relatively low values of U_{L_3} for which the ionization cross sections are relatively small. However, Campos *et al.*¹⁶¹ measured $L\alpha$ x-ray production cross sections for W and Pt at similar values of U_{L_3} (1.18 for W and 1.12 for Pt) and these cross sections had relatively small deviations from the calculated cross sections (1.8% for W and -13.5% for Pt). We conclude from

Fig. 58 that the Bote *et al.* formulae provide satisfactory values of $L\alpha$ x-ray production cross sections for values of U_{L_3} between 1.02 and 6×10^3 .

Table 13 lists the root mean square deviation RMS and mean percentage deviation R from the Bote *et al.* cross sections for each data set that were calculated with Eq. (138). These calculations included the two large deviations mentioned in the previous paragraph. Average values of RMS and R , denoted as \overline{RMS} and \overline{R} , respectively, for the group of 8 evaluated elements are displayed in Table 14.

Figure 59 shows plots of \overline{RMS} and \overline{R} as a function of Z . While there does not seem to be any substantial variation of \overline{RMS} with Z , the \overline{RMS} values appear to show a gradual decrease with increasing Z .

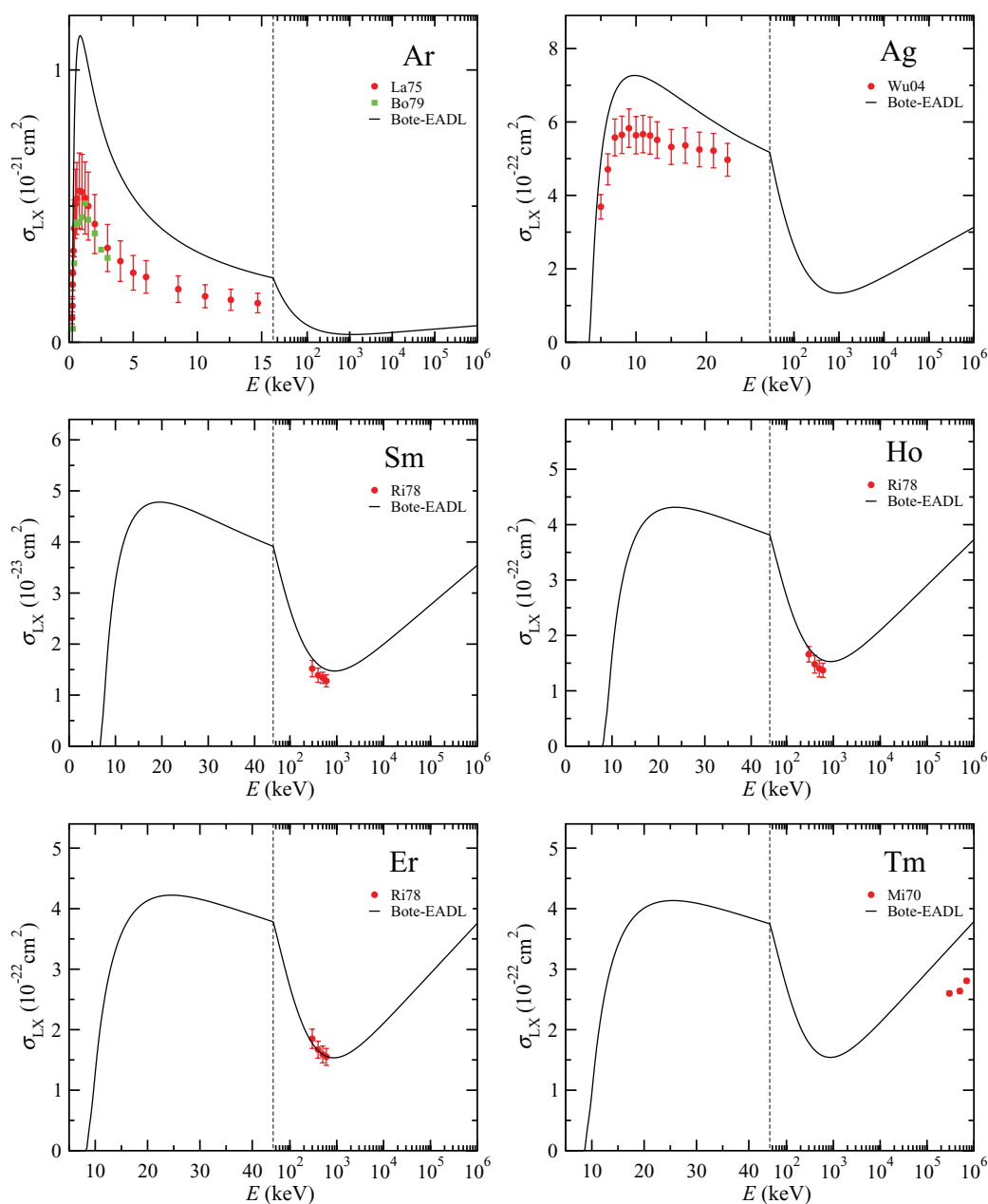


Fig. 39. (Color online) Absolute total L-shell x-ray production cross sections vs. incident electron energy for Ar, Ag, Sm, Ho, Er, and Tm. Solid curves are the results of the DWBA calculations of the total L-shell ionization cross section combined with data from the EADL database. Symbols are experimental measurements.

The weighted average values $\langle \overline{RMS} \rangle$ and $\langle \overline{R} \rangle$ from Eq. (139) were 10.6% and -7.3% , respectively. This value of $\langle \overline{RMS} \rangle$ is less than the corresponding value for L-shell ionization while the value of $\langle \overline{R} \rangle$ found here is more than double the corresponding value for L-shell ionization. We have no explanation for these changes.

7.6. Evaluation summary

We now summarize the results of our evaluation of the measured cross sections from the sets of data that were judged “superior.” These were the data sets (a minimum of three sets for the K-shell ionization cross sections and a minimum of two

sets for the other cross sections) that were judged to have satisfactory consistency with each other and with the energy dependences expected from the Bote *et al.* analytical formulae [Eqs. (87) and (88)].

Table 15 shows the values of $\langle \overline{RMS} \rangle$ and $\langle \overline{R} \rangle$ found in Secs. 7.1–7.5 for the K-, L-, and M-shell ionization cross sections as well as for the $L\alpha$ x-ray production cross sections. We also show the number of data points in the evaluation of each set of cross sections, the range of atomic numbers for the elements with superior data, and the range of overvoltage ratios for these elements.

We have the clearest results from our evaluation of the K-shell ionization cross sections. We identified 26 elements with

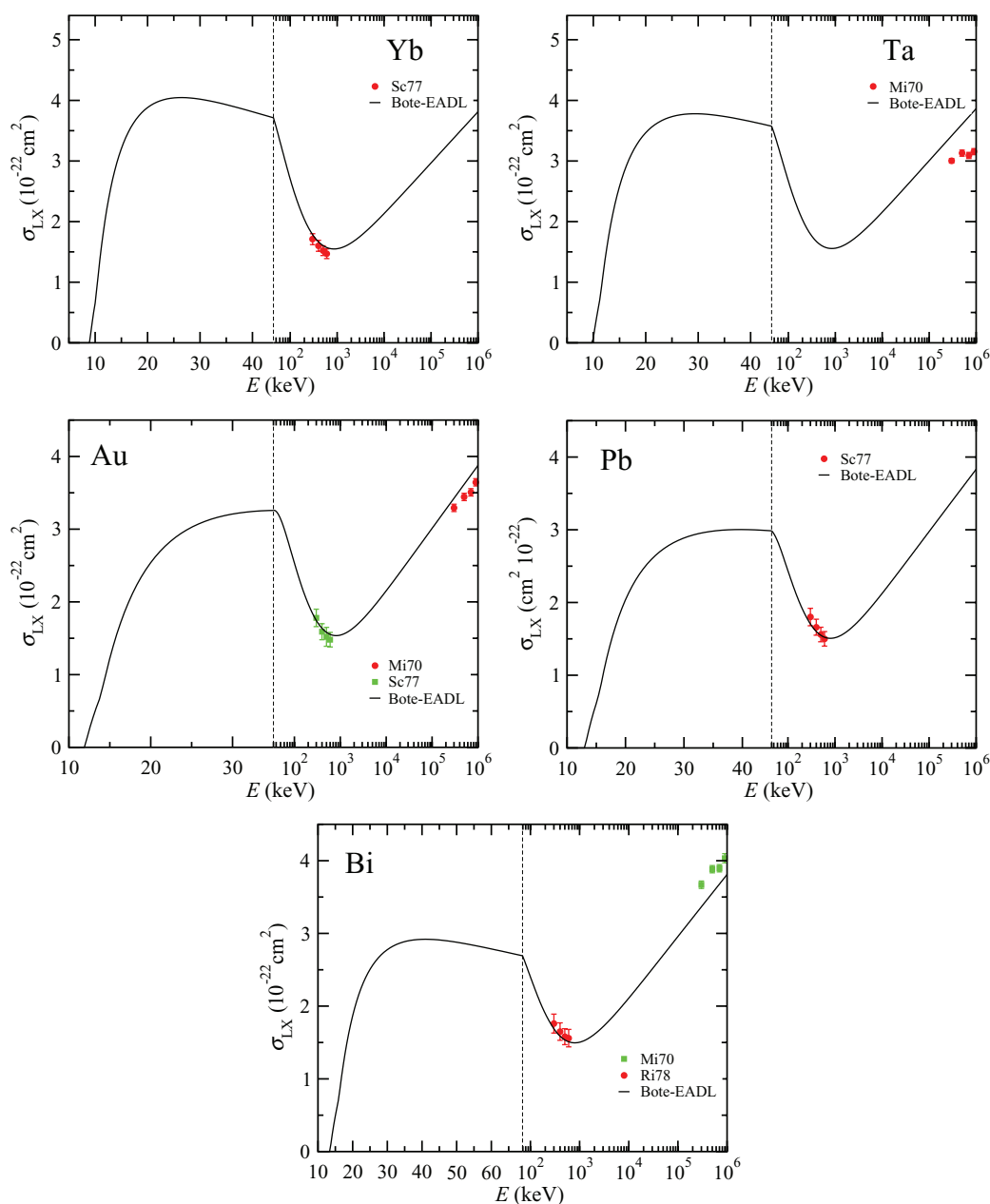


Fig. 40. (Color online) Absolute total L-shell x-ray production cross sections vs. incident electron energy for Yb, Ta, Au, Pb, and Bi. Solid curves are the results of the DWBA calculations of the total L-shell ionization cross section combined with data from the EADL database. Symbols are experimental measurements.

three of more sets of data that satisfied our evaluation criteria. For these elements, there were a total of 1022 measured cross sections. These cross sections showed satisfactory agreement with the cross sections calculated from the Bote *et al.* formulae, with an $\langle \overline{RMS} \rangle$ value of 10.3%. The individual percentage deviations between measured and calculated cross sections did not depend significantly on atomic number (between C and Bi) or overvoltage ratio (between 1.02 and 2×10^5). The measured K-shell ionization cross sections for H and He agreed with the calculated cross sections for $U_K > 16$, and we infer that the Bote *et al.* formulae should be reliable for Li, Be, and B with $U_K > 16$. The value of $\langle \overline{R} \rangle$ (-1.9%) was about 20% of the value of $\langle \overline{RMS} \rangle$, thus indicating that there

was no significant systematic offset between the calculated and measured cross sections.

As expected, there were much fewer measurements of L- and M-shell ionization cross sections than for K-shell cross sections, and it was necessary to relax our consistency requirements to two sets of measured cross sections for each element. Even so, we found only eight elements with L-shell ionization cross sections that satisfied our evaluation criteria. The individual percentage deviations between measured and calculated cross sections did not depend significantly on atomic number (between Ag and U) or overvoltage ratio (between 1.02 and 6×10^5). The measured L-shell ionization cross sections agreed satisfactorily with the cross sections calculated from the Bote *et al.* formulae, with an $\langle \overline{RMS} \rangle$

TABLE 6. Measurements of M-shell x-ray production cross sections performed up to May 2013. Information on the measured x-ray line, incident electron energy range, target used, simplified reference (as shown in Fig. 41), and the full reference is also given. The targets used were self-supporting thin films (T)

Element	Line	Energy (keV)	Target	Key	Reference
Au	$M\alpha$	2.5 to 38	T	Me08	Merlet <i>et al.</i> ¹⁷¹
Pb	$M\alpha$, $M\beta$, $M\gamma$	3 to 38	T	Mo13	Moy <i>et al.</i> ²¹⁵
Bi	$M\alpha$	2.5 to 38	T	Me08	Merlet <i>et al.</i> ¹⁷¹

value of 15.0%. We found only three elements with M-shell ionization cross sections that satisfied our evaluation criteria. The individual percentage deviations between these measured cross sections and the calculated cross sections did not depend significantly on atomic number (between Au and Bi) or over-voltage ratio (between 23 and 10^5). In the comparison of the measured M-shell ionization cross sections with the cross sections from the Bote *et al.* formulae, the $\langle RMS \rangle$ value was 23.5%. The values of $\langle \bar{R} \rangle$ for the L- and M-shell cross sections were 3.1% and 8.2%, respectively.

We identified eight elements for which two or more sets of measured $L\alpha$ x-ray production cross sections that satisfied our evaluation criteria. The individual percentage deviations between measured and calculated $L\alpha$ x-ray production cross sections did not vary significantly with atomic number (between Gd and Bi) or L_3 -subshell overvoltage ratio (between 1.02 and 6×10^3). The measured $L\alpha$ x-ray cross sections

agreed satisfactorily with the cross sections calculated from the Bote *et al.* formulae, with an $\langle RMS \rangle$ value of 10.6%, and an $\langle \bar{R} \rangle$ value of -7.3% .

We note that the $\langle \bar{R} \rangle$ values for L- and M-shell ionization cross sections and for $L\alpha$ x-ray production cross sections (-3.1% , 8.2% , and -7.3% , respectively) were appreciably larger than the value (-1.9%) found for K-shell ionization cross sections. We attribute these larger values, as well as the larger $\langle RMS \rangle$ values for L- and M-shell ionization cross sections, in part to the less stringent evaluation criteria for these cross sections and for $L\alpha$ x-ray production cross sections than for K-shell ionization cross sections. The larger $\langle \bar{R} \rangle$ values could also be due to uncertainties of the additional needed atomic data from the EADL database¹ for fluorescence yields and transition probabilities [e.g., in the use of Eqs. (104) and (105) or Eqs. (125)–(131) for obtaining L- and M-shell ionization cross sections].

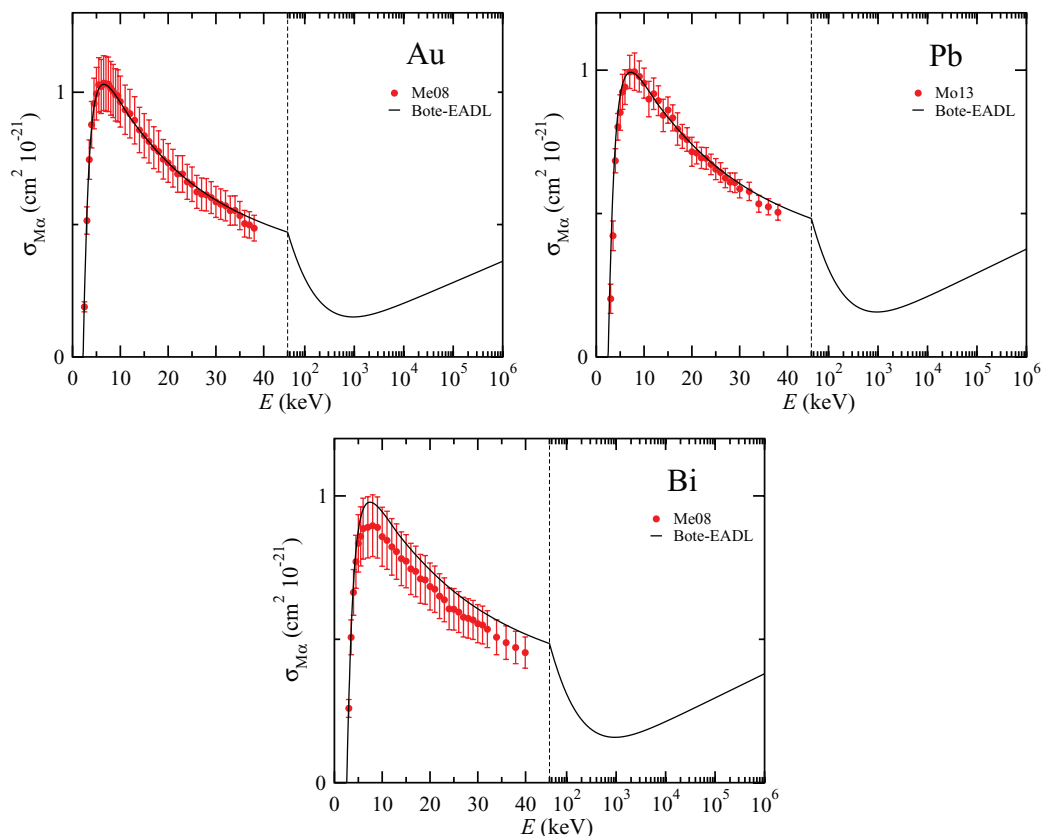


FIG. 41. (Color online) Absolute $M\alpha$ x-ray production cross sections vs. incident electron energy for Au, Pb, and Bi. Solid curves are the results of the DWBA calculations of the M_5 -subshell ionization cross sections combined with data from the EADL database. Symbols are experimental measurements.

TABLE 7. Selected sets of measured K-shell ionization cross sections that were included in the evaluation of experimental data. Also shown are the *RMS* and *R* values for each data set that were calculated from Eq. (138)

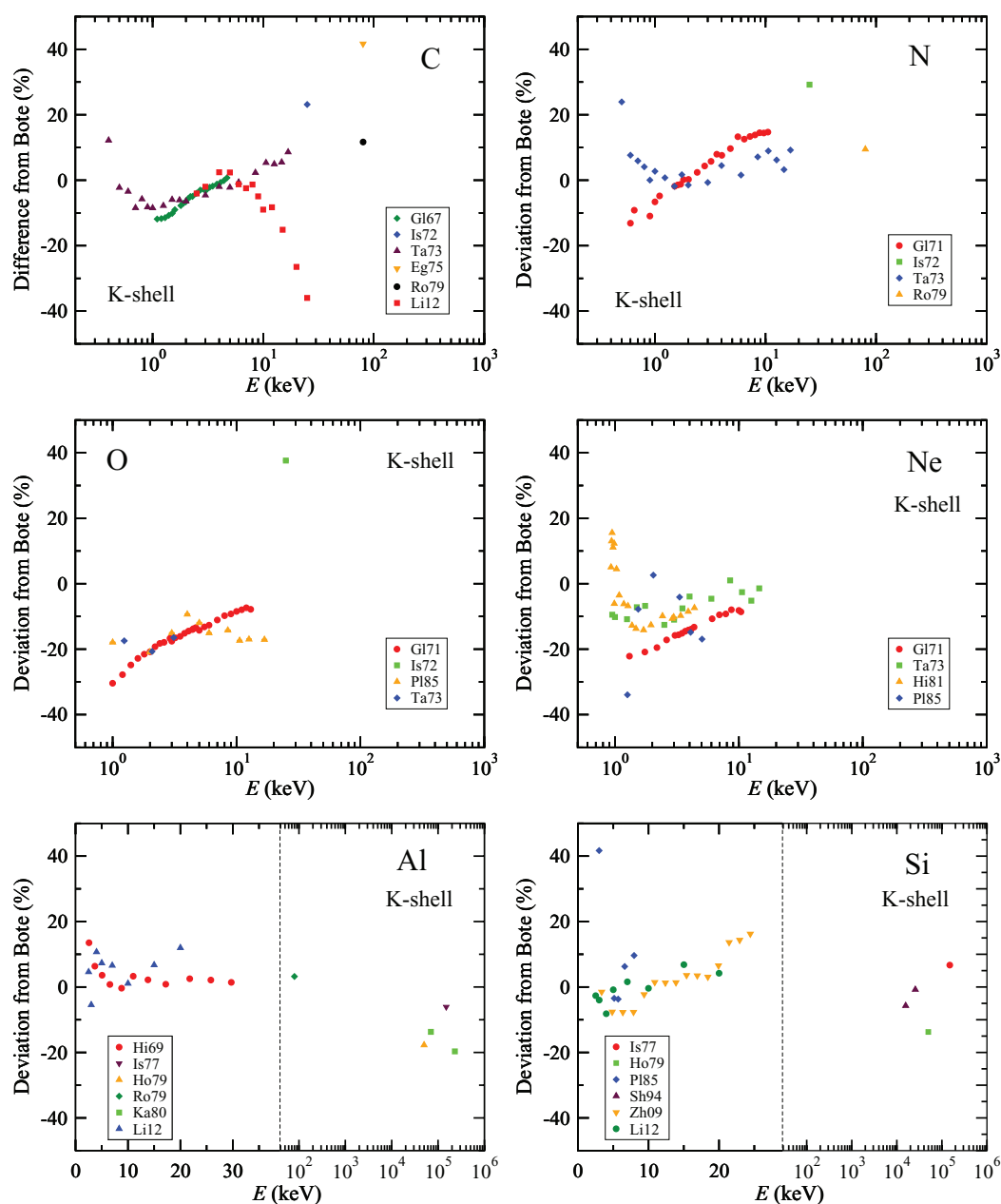
Element	Shell	Data points	Key	Reference	<i>RMS</i> (%)	<i>R</i> (%)
C	K	22	Gl67	Glupe and Mehlhorn ²²³	6.7	-5.4
C	K	1	Is72	Isaacson <i>et al.</i> ²⁶⁹	23.1	23.1
C	K	20	Ta73	Tawara <i>et al.</i> ²⁰³	6.7	-1.7
C	K	1	Eg75	Egerton ²⁷⁰	41.6	41.6
C	K	1	Ro79	Rossouw and Whelan ²⁷¹	11.7	11.7
C	K	13	Li12	Limandri <i>et al.</i> ¹⁶³	13.7	-8.2
N	K	23	Gl71	Glupe and Mehlhorn ²²⁴	9.4	3.7
N	K	1	Is72	Isaacson <i>et al.</i> ²⁶⁹	29.2	29.2
N	K	18	Ta73	Tawara <i>et al.</i> ²⁰³	7.4	4.6
N	K	1	Ro79	Rossouw and Whelan ²⁷¹	9.5	9.5
O	K	28	Gl71	Glupe and Mehlhorn ²²⁴	16.9	-15.8
O	K	1	Is72	Isaacson <i>et al.</i> ²⁶⁹	37.6	37.6
O	K	10	Ta73	Tawara <i>et al.</i> ²⁰³	15.9	-15.6
O	K	3	Pl85	Platten <i>et al.</i> ²³⁰	18.3	-18.2
Ne	K	17	Gl71	Glupe and Mehlhorn ²²⁴	14.5	-13.9
Ne	K	14	Ta73	Tawara <i>et al.</i> ²⁰³	7.6	-6.6
Ne	K	20	Pl85	Platten <i>et al.</i> ²³⁰	40.9	7.9
Ne	K	6	Hi81	Hink <i>et al.</i> ²²⁸	10.3	-3.5
Al	K	11	Hi69	Hink and Ziegler ¹¹⁷	4.9	3.3
Al	K	1	Is77	Ishii <i>et al.</i> ¹³¹	6.1	-6.1
Al	K	1	Ho79	Hoffmann <i>et al.</i> ¹³⁴	17.7	-17.7
Al	K	1	Ro79	Rossouw and Whelan ²⁷¹	3.2	3.2
Al	K	2	Ka80	Kamiya <i>et al.</i> ¹³⁶	17.0	-16.6
Al	K	8	Li12	Limandri <i>et al.</i> ¹⁶³	7.5	5.4
Si	K	21	Is77	Ishii <i>et al.</i> ¹³¹	6.7	6.7
Si	K	1	Ho79	Hoffmann <i>et al.</i> ¹³⁴	13.7	-13.7
Si	K	5	Pl85	Platten <i>et al.</i> ²³⁰	19.4	10.1
Si	K	2	Sh94	Shchagin <i>et al.</i> ²⁷²	4.1	-3.2
Si	K	15	Zh09	Zhu <i>et al.</i> ²⁰¹	7.8	2.5
Si	K	8	Li12	Limandri <i>et al.</i> ¹⁶³	4.4	-0.4
Ar	K	8	Ta73	Tawara <i>et al.</i> ²⁰³	13.4	-13.3
Ar	K	14	Ho79	Hoffmann <i>et al.</i> ¹³⁴	11.7	-10.2
Ar	K	9	Qu82	Quarles and Semaan ²⁰⁶	7.3	-3.5
Ar	K	6	Hi82	Hippler <i>et al.</i> ²⁰⁵	15.5	-13.9
Ar	K	16	Hi83	Hippler <i>et al.</i> ²⁰⁷	9.7	0.9
Ar	K	5	Pl85	Platten <i>et al.</i> ²³⁰	19.8	-19.7
Ar	K	8	Si03	Singh and Shanker ¹⁴⁶	13.5	-13.3
Ca	K	3	Is77	Ishii <i>et al.</i> ¹³¹	13.6	13.1
Ca	K	4	Ho79	Hoffmann <i>et al.</i> ¹³⁴	6.0	-6.0
Ca	K	22	Sh91	Shevelko <i>et al.</i> ¹⁴⁵	22.4	-19.7
Ca	K	16	Wu10a	Wu <i>et al.</i> ¹⁸⁴	25.1	-23.4
Ti	K	19	Je75	Jessenberg and Hink ¹²⁸	5.4	5.1
Ti	K	14	An03	An <i>et al.</i> ¹⁶⁰	12.2	1.5
Ti	K	9	Li12	Limandri <i>et al.</i> ¹⁶³	5.9	3.8
Cr	K	1	Sc72	Scholz <i>et al.</i> ¹²⁵	15.2	-15.2
Cr	K	4	Ho79	Hoffmann <i>et al.</i> ¹³⁴	2.9	-2.4
Cr	K	11	Lu96	Luo <i>et al.</i> ¹⁴⁸	11.0	-0.66
Cr	K	35	LI00	Llovet <i>et al.</i> ¹⁶⁴	3.3	2.7
Cr	K	11	An03	An <i>et al.</i> ¹⁶⁰	11.2	8.9
Mn	K	1	Fi67	Fischer and Hoffmann ¹¹⁶	8.0	-8.0
Mn	K	1	Sc72	Scholz <i>et al.</i> ¹²⁵	6.3	-6.3
Mn	K	1	Ho79	Hoffmann <i>et al.</i> ¹³⁴	9.3	-9.3
Mn	K	8	Sh80	Shima ¹³⁷	24.4	-21.9
Mn	K	11	Lu97	Luo <i>et al.</i> ¹⁴⁹	21.6	-14.2
Mn	K	10	Ta99b	Tang <i>et al.</i> ¹⁵⁶	10.7	-10.4
Mn	K	37	LI02	Llovet <i>et al.</i> ¹⁶⁵	9.3	8.6
Fe	K	1	Sc72	Scholz <i>et al.</i> ¹²⁵	2.0	-2.0
Fe	K	9	Lu97	Luo <i>et al.</i> ¹⁴⁹	10.8	-2.2
Fe	K	36	LI02	Llovet <i>et al.</i> ¹⁶⁵	7.5	-3.3
Ni	K	1	Sm45	Smick and Kirkpatrick ¹¹⁰	20.1	-20.1
Ni	K	10	Po47	Pockman <i>et al.</i> ¹¹¹	7.4	-5.6
Ni	K	10	Je75	Jessenberg and Hink ¹²⁸	14.6	14.2
Ni	K	6	Ho79	Hoffmann <i>et al.</i> ¹³⁴	8.8	1.0
Ni	K	3	Ge82	Genz <i>et al.</i> ¹⁴¹	10.0	7.6
Ni	K	8	Lu96	Luo <i>et al.</i> ¹⁴⁸	17.6	5.5

TABLE 7. Selected sets of measured K-shell ionization cross sections that were included in the evaluation of experimental data. Also shown are the RMS and R values for each data set that were calculated from Eq. (138)—Continued

Element	Shell	Data points	Key	Reference	RMS (%)	R (%)
Ni	K	35	LI00	Llovet <i>et al.</i> ¹⁶⁴	7.5	7.2
Ni	K	10	An06	An <i>et al.</i> ¹⁸¹	11.8	9.5
Cu	K	1	Fi67	Fischer and Hoffmann ¹¹⁶	1.8	1.8
Cu	K	5	Mi70	Middleman <i>et al.</i> ⁷¹	7.0	6.6
Cu	K	3	Hu72	Hubner <i>et al.</i> ¹²⁴	16.2	-16.0
Cu	K	1	Sc72	Scholz <i>et al.</i> ¹²⁵	2.5	2.5
Cu	K	1	Is77	Ishii <i>et al.</i> ¹³¹	14.6	14.6
Cu	K	4	Be78	Berenyi <i>et al.</i> ¹³³	6.2	6.1
Cu	K	1	Ho79	Hoffmann <i>et al.</i> ¹³⁴	16.4	-16.3
Cu	K	8	Sh80	Shima ¹³⁷	27.5	-19.3
Cu	K	4	Sh81	Shima <i>et al.</i> ¹⁴⁰	4.2	-4.1
Cu	K	9	An96	An <i>et al.</i> ¹⁵³	17.9	-9.2
Cu	K	8	He97	He <i>et al.</i> ¹⁵²	23.7	-14.04
Cu	K	32	LI00	Llovet <i>et al.</i> ¹⁶⁴	14.5	14.4
Cu	K	9	Zh01c	Zhou <i>et al.</i> ¹⁷⁷	5.0	0.6
Zn	K	1	Sc72	Scholz <i>et al.</i> ¹²⁵	4.5	4.5
Zn	K	1	Is77	Ishii <i>et al.</i> ¹³¹	15.7	15.7
Zn	K	10	Ta99a	Tang <i>et al.</i> ¹⁵⁵	19.1	-15.3
Zn	K	20	Wu10a	Wu <i>et al.</i> ¹⁸⁴	3.3	0.4
Ga	K	8	Zh01c	Zhou <i>et al.</i> ¹⁷⁷	5.7	3.9
Ga	K	9	Zh02	Zhou <i>et al.</i> ²⁷³	7.6	6.0
Ga	K	30	Me06	Merlet <i>et al.</i> ^{169,170}	1.4	0.9
Ge	K	4	Ho79	Hoffmann <i>et al.</i> ¹³⁴	11.9	-11.8
Ge	K	4	Sh81	Shima <i>et al.</i> ¹⁴⁰	7.5	-6.3
Ge	K	12	Ta02a	Tang <i>et al.</i> ¹⁹⁷	9.4	-6.7
Ge	K	11	Zh02	Zhou <i>et al.</i> ²⁷³	4.9	-0.4
Ge	K	32	Me04	Merlet <i>et al.</i> ¹⁶⁸	3.9	-3.2
Se	K	1	Sc72	Scholz <i>et al.</i> ¹²⁵	10.3	-10.3
Se	K	2	Is77	Ishii <i>et al.</i> ¹³¹	16.3	15.7
Se	K	4	Be78	Berenyi <i>et al.</i> ¹³³	14.4	14.3
Se	K	7	Ki81	Kiss <i>et al.</i> ¹³⁹	1.9	1.7
Se	K	10	Lu01	Luo <i>et al.</i> ¹⁶⁶	10.0	-6.3
Y	K	3	Se74	Seif <i>et al.</i> ¹²⁶	12.8	11.6
Y	K	1	Is77	Ishii <i>et al.</i> ¹³¹	8.9	-8.9
Y	K	2	Ho79	Hoffmann <i>et al.</i> ¹³⁴	6.4	-5.8
Y	K	6	Lu01	Luo <i>et al.</i> ¹⁶⁶	11.3	11.1
Pd	K	2	Be70	Berkner <i>et al.</i> ¹²⁰	14.4	13.0
Pd	K	2	Is77	Ishii <i>et al.</i> ¹³¹	3.8	1.1
Pd	K	4	Ri77	Ricz <i>et al.</i> ¹⁹⁰	26.1	26.1
Ag	K	4	Re66	Rester and Dance ¹¹⁵	17.1	17.0
Ag	K	1	Fi67	Fischer and Hoffmann ¹¹⁶	8.5	-8.5
Ag	K	1	Hu72	Hubner <i>et al.</i> ¹²⁴	13.4	-13.4
Ag	K	2	Se74	Seif <i>et al.</i> ¹²⁶	20.5	-20.3
Ag	K	3	Sc76	Schlenk <i>et al.</i> ¹³⁰	7.5	7.2
Ag	K	6	Ri77	Ricz <i>et al.</i> ¹⁹⁰	4.5	-2.9
Ag	K	4	Ho79	Hoffmann <i>et al.</i> ¹³⁴	7.9	-7.6
Ag	K	7	Ki81	Kiss <i>et al.</i> ¹³⁹	6.6	6.3
Ag	K	4	Sh81	Shima <i>et al.</i> ¹⁴⁰	8.5	-7.6
Ag	K	3	Ge82	Genz <i>et al.</i> ¹⁴¹	4.0	2.6
Ag	K	1	We87b	Westbrook and Quarles ¹⁴³	15.0	-15.0
Ag	K	10	Sc93	Schneider <i>et al.</i> ¹⁴⁷	15.1	-8.6
Ag	K	4	Zh01b	Zhou <i>et al.</i> ¹⁷⁶	10.4	-5.8
Sn	K	1	Fi67	Fischer and Hoffmann ¹¹⁶	-2.1	-2.1
Sn	K	8	Ha66	Hansen and Flammersfeld ¹¹³	6.8	-5.3
Sn	K	1	Sc72	Scholz <i>et al.</i> ¹²⁵	7.3	-7.3
Sn	K	1	Is77	Ishii <i>et al.</i> ¹³¹	14.0	-14.0
Sn	K	2	Ho79	Hoffmann <i>et al.</i> ¹³⁴	1.6	-1.5
Sb	K	1	Sc72	Scholz <i>et al.</i> ¹²⁵	6.7	-6.7
Sb	K	7	We87b	Westbrook and Quarles ¹⁴³	2.7	-2.2
Sb	K	1	Ki81	Kiss <i>et al.</i> ¹³⁹	6.8	-6.8
Au	K	8	Re66	Rester and Dance ¹¹⁵	12.5	-0.3
Au	K	2	Be70	Berkner <i>et al.</i> ¹²⁰	15.5	-15.3
Au	K	4	Mi70	Middleman <i>et al.</i> ⁷¹	4.1	-4.0
Au	K	1	Sc72	Scholz <i>et al.</i> ¹²⁵	1.2	-1.2

TABLE 7. Selected sets of measured K-shell ionization cross sections that were included in the evaluation of experimental data. Also shown are the *RMS* and *R* values for each data set that were calculated from Eq. (138)—Continued

Element	Shell	Data points	Key	Reference	<i>RMS</i> (%)	<i>R</i> (%)
Au	K	1	Is77	Ishii <i>et al.</i> ¹³¹	6.6	6.7
Au	K	4	Ho79	Hoffmann <i>et al.</i> ¹³⁴	6.2	5.8
Pb	K	1	Sc72	Scholz <i>et al.</i> ¹²⁵	5.0	-4.9
Pb	K	2	Se74	Seif <i>et al.</i> ¹²⁶	17.0	2.4
Pb	K	1	Is77	Ishii <i>et al.</i> ¹³¹	5.7	-5.7
Pb	K	1	Ho79	Hoffmann <i>et al.</i> ¹³⁴	9.8	9.8
Bi	K	2	Mi70	Middleman <i>et al.</i> ⁷¹	10.6	10.6
Bi	K	1	Sc72	Scholz <i>et al.</i> ¹²⁵	4.5	-4.5
Bi	K	1	Is77	Ishii <i>et al.</i> ¹³¹	7.4	-7.4
Bi	K	3	Ho79	Hoffmann <i>et al.</i> ¹³⁴	3.6	2.5


 FIG. 42. (Color online) Percentage deviation Δ_i of experimental values of K-shell ionization cross sections from calculated values using the Bote *et al.* formulae, as a function of electron energy for C, N, O, Ne, Al, and Si.

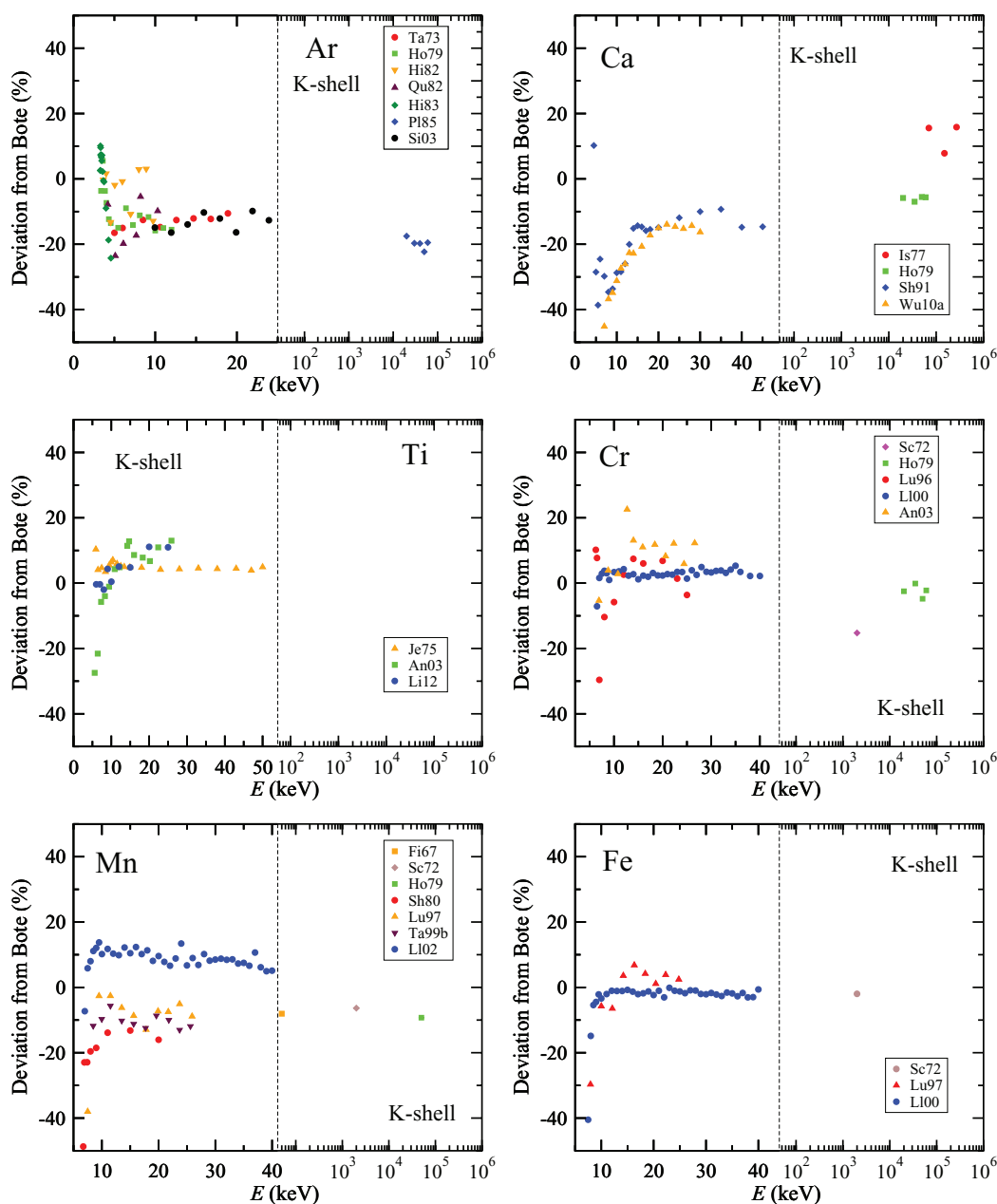


Fig. 43. (Color online) Percentage deviation Δ_i of experimental values of K-shell ionization cross sections from calculated values using the Bote *et al.* formulae, as a function of electron energy for Ar, Ca, Ti, Cr, Mn, and Fe.

For the entire sets of measurements with superior data (e.g., for K-, L-, and M-shell ionization cross sections and $L\alpha$ x-ray production cross sections), the weighted average value of $\langle \overline{RMS} \rangle$ was 10.9% and the weighted average value of $\langle \overline{R} \rangle$ was -2.5% .

We did not find any substantive differences in the plots of percentage deviations between measured and calculated ionization cross sections as a function of incident energy that were presented in this Section for monatomic gases (such as Ne and Ar), diatomic gases (such as N_2 and O_2), and numerous elemental solids over wide ranges of the incident energy. There were, however, systematic negative deviations for Ar K-shell ionization cross sections in Fig. 48 when U_K was less than 1.02 and similar negative deviations for Xe L_{3-} -subshell

ionization cross sections in Fig. 52(b) when U_{L3} was less than 1.02. Apart from these near-threshold deviations, the atomic calculations satisfactorily describe the measured cross sections for atoms, molecules, and solids.

Finally, we can make use of our sets of superior data to make an evaluation of the experimental methods utilized in the measurement of ionization and x-ray production cross sections. Table 16 shows the experimental methods given in Tables 2–5. For each measured cross section, we show the total number of data sets, the number of data sets with superior data (as judged by our evaluation criteria), and the percentage of data sets with superior data. We see that measurements of x-ray yields were utilized for most cross-section measurements. Most of these measurements were made with self-supporting

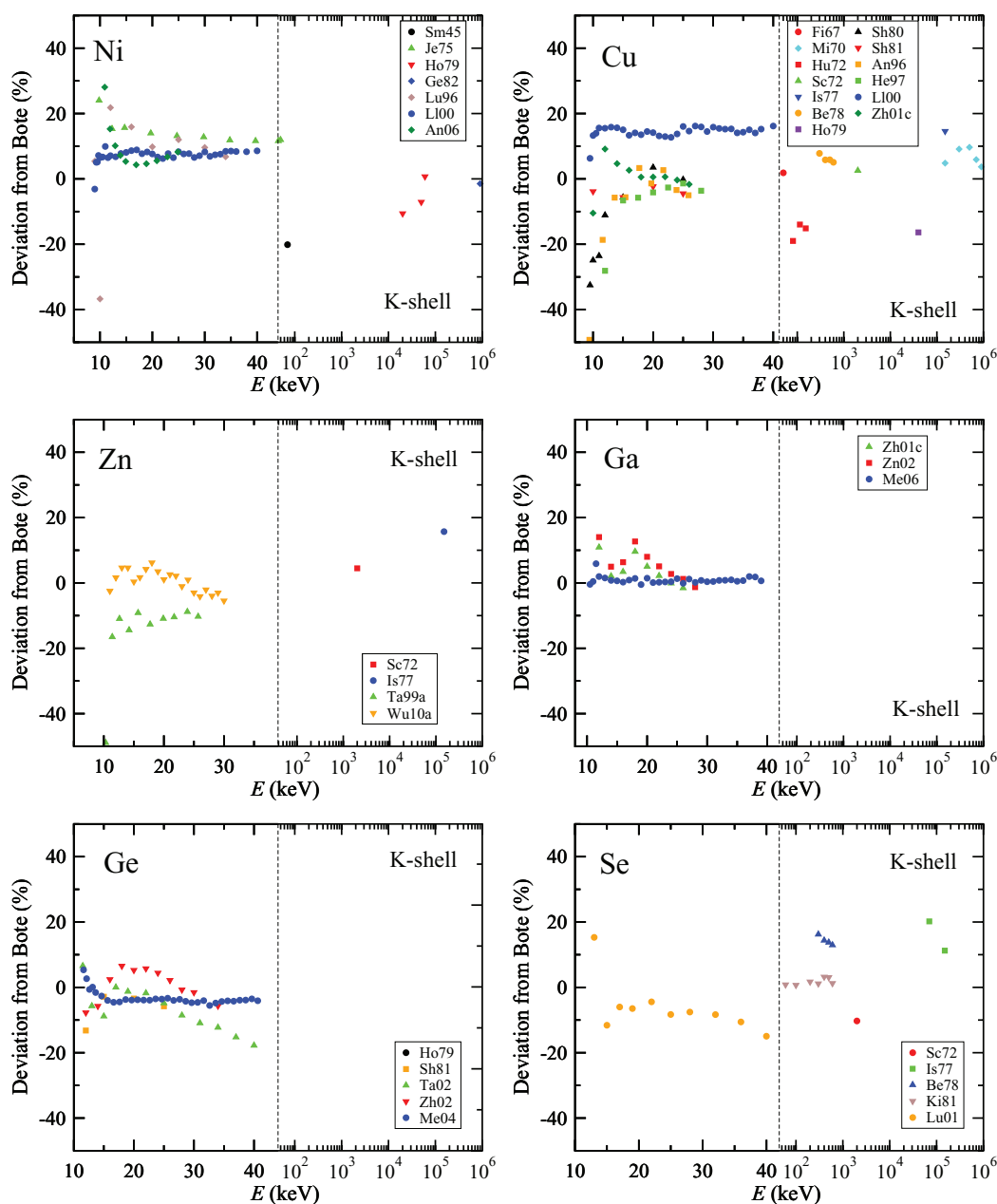


Fig. 44. (Color online) Percentage deviation Δ_i of experimental values of K-shell ionization cross sections from calculated values using the Bote *et al.* formulae, as a function of electron energy for Ni, Cu, Zn, Ga, Ge, and Se.

thin films with smaller numbers of measurements being made with thin films on substrates or with gases. Fewer measurements were made with Auger yields from gases, EELS spectra from self-supporting thin films, and x-ray yields from thick substrates.

We see from Table 16 that between 50% and 63% of the x-ray yield measurements led to superior K- and L-shell ionization cross sections and to superior $L\alpha$ x-ray production cross sections (although only 38% of the $L\alpha$ data sets for thin films on substrates led to superior data). While there were only nine sets of data with M-shell ionization cross sections, 89% of them were judged superior. Auger-yield measurements with gases led to 100% of the data sets with K-shell ionization cross sections being judged superior. Although none of the Auger-

yield data sets for gases with L- and M-shell ionization cross sections had superior data, this result was due to the scarcity of other data sets for comparisons.

While the percentages of data sets with superior data in Table 16 might be thought to be disappointing, we point out that measurements of absolute cross sections are experimentally very difficult for the reasons described in Sec. 5. We also mention that Kieffer and Dunn²⁷⁶ identified the necessary conditions to be satisfied in measurements of ionization cross sections for gases, while Powell *et al.*²⁷⁷ similarly examined the main sources of systematic uncertainty in measurements of Auger-electron intensities. The systematic uncertainties depend, of course, on the chosen measurement technique and details of the specific experiments but they can typically range

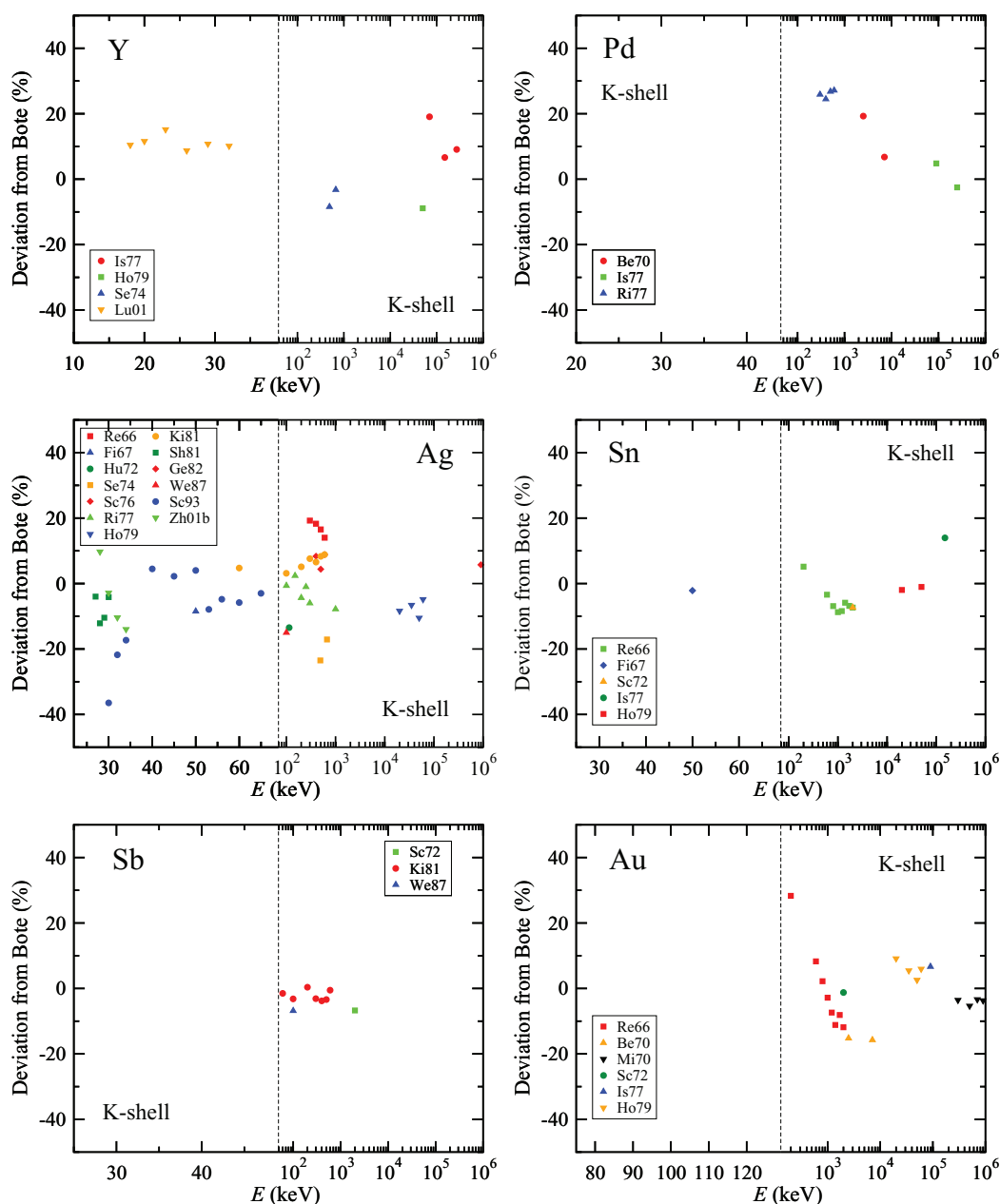


Fig. 45. (Color online) Percentage deviation Δ_i of experimental values of K-shell ionization cross sections from calculated values using the Bote *et al.* formulae as a function of electron energy for Y, Pd, Ag, Sn, Sb, and Au.

from about 10% to over 30% (Sec. 5). The derived cross sections also depend on the uncertainties (often unknown) of the needed atomic data (discussed in Sec. 4) that were obtained from the EADL.¹ We are therefore pleased with the overall values of $\langle \overline{RMS} \rangle$ (10.9%) and $\langle \overline{R} \rangle$ (−2.5%) from comparisons of measured ionization and x-ray production cross sections with the corresponding calculated cross sections, and we are also pleased that, as indicated by Table 16, many experimental groups were able to produce superior cross section data. We presume that other groups were not able to make measurements of similar quality because of oversights of possible systematic uncertainties or to inferior choices of needed parameters.

8. Evaluation of Analytical Formulae

In this section we evaluate four analytical formulae for ionization cross sections that have been widely used for practical purposes. Cross sections from these formulae are compared with those from the predictive formulae of Bote *et al.* [Eqs. (87) and (88)] that, as we have seen in Sec. 7, agree satisfactorily with measured cross sections for many elements and for a wide range of incident energies.

We will evaluate the Gryzinski formula [Eq. (83)] derived from a classical model for atomic ionization, and the empirical formula published by Casnati *et al.* [Eq. (84)], Jakoby *et al.* [Eq. (85)], and Hombourger [Eq. (86)] that were obtained from fits to measured K-shell ionization cross sections. The latter

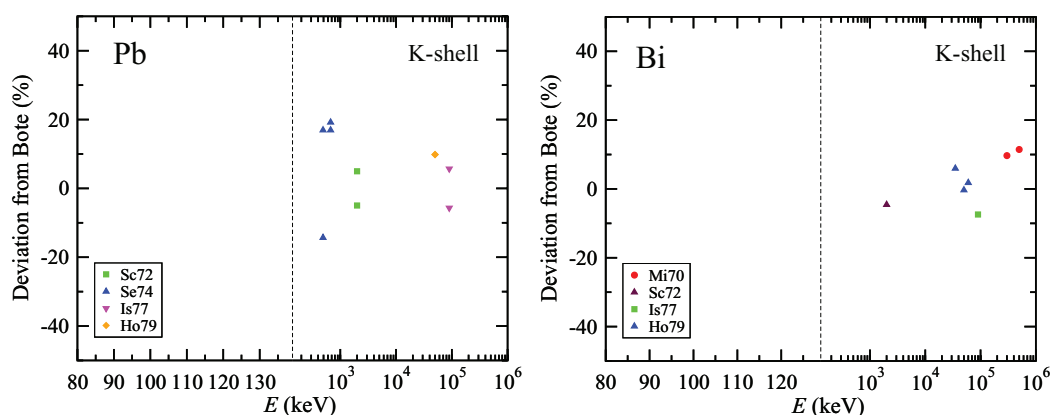


FIG. 46. (Color online) Percentage deviation Δ_i of experimental values of K-shell ionization cross sections from calculated values using the Bote *et al.* formulae, as a function of electron energy for Pb and Bi.

three formulae have frequently also been used for estimating ionization cross sections for other shells due to the lack of measured cross sections. We have previously shown comparisons of K-shell ionization cross sections from the Gryzinski, Casnati *et al.*, Jakoby *et al.*, and Hombourger formulae with the corresponding cross sections from the Bote *et al.* formulae as a function of incident electron energy for N, Si, Fe, Y, Ag, and Au in Fig. 7. Similar comparisons of L-shell ionization cross sections for Ag, Xe, Ta, and Bi and of M-shell ionization cross sections for Au and Bi were shown in Figs. 8 and 9, respectively.

We will compare K-shell, L_3 -subshell, and M_5 -subshell ionization cross sections from the selected formulae with the corresponding cross sections from the Bote *et al.* formulae [using Eqs. (87) and (88) and binding energies from the Carlson compilation⁶⁴ as described in the Appendix]. Percentage differences between the cross sections from each formula and the Bote *et al.* values have been determined for selected elements distributed throughout the Periodic Table and for incident energies from close to the ionization threshold to 1 GeV. For each element and formula, we will show values of RMS and R determined from Eq. (138).

8.1. K-shell ionization cross sections

Figure 60 shows percentage deviations between K-shell ionization cross sections from the Gryzinski, Casnati *et al.*, Jakoby *et al.*, and Hombourger formulae and the corresponding cross sections from the Bote *et al.* formulae as a function of electron energy for N, Si, Fe, Y, Ag, La, Ho, and Au. Although the percentage deviations can be relatively small (e.g., less than 10%) for some elements and energies (e.g., for Si at energies between 5 keV and 30 keV), the deviations can become much larger for other elements and wider energy ranges (e.g., for La, Ho, and Au). Table 17 lists the root mean square percentage deviation RMS and mean percentage deviation R values for each formula and the selected elements. We see similar values of RMS and R for the Casnati *et al.* and Hombourger formulae and generally larger values for the Gryzinski and Jakoby *et al.* formulae.

8.2. L_3 -subshell ionization cross sections

Figure 61 shows percentage deviations between L_3 -subshell ionization cross sections from the Gryzinski, Casnati

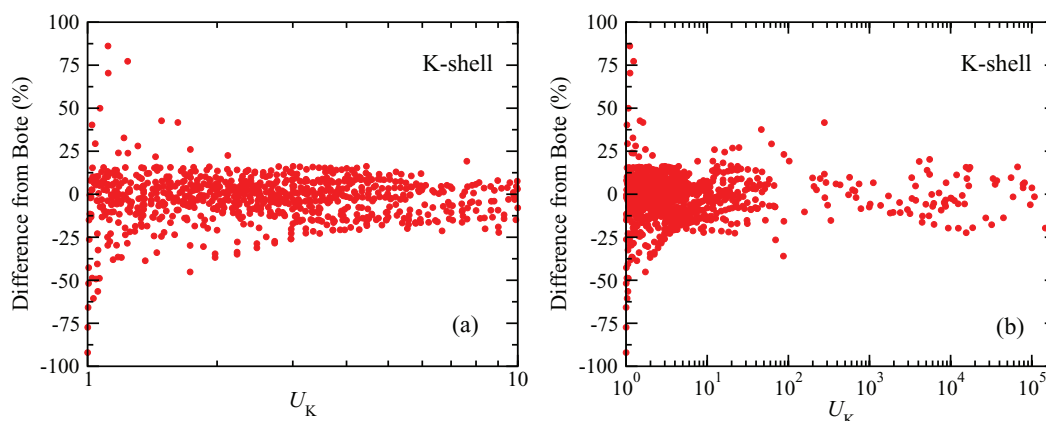


FIG. 47. (Color online) Plots of percentage deviations between measured K-shell ionization cross sections and the corresponding cross sections calculated from the Bote *et al.* predictive formulae as a function of U_K on logarithmic scales: (a) for U_K between 1 and 10, and (b) for U_K between 1 and 2×10^5 .

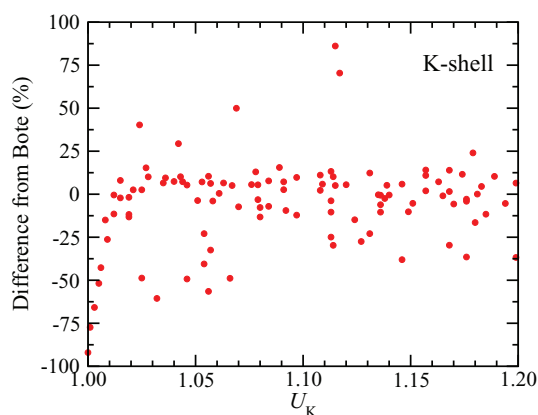


FIG. 48. (Color online) Plot of percentage deviations between measured K-shell ionization cross sections and the corresponding cross sections calculated from the Bote *et al.* predictive formulae as a function of U_K for U_K between 1.0 and 1.2.

et al., Jakoby *et al.*, and Hombourger formulae and the corresponding cross sections from the Bote *et al.* formulae for Si, Fe, Y, Ag, Xe, Gd, Ta, and Bi as a function of electron energy. While the percentage deviations can again be relatively small (<10%) for some elements, formulae, and energy ranges (e.g., Si), they are often much larger. Table 18 lists the root mean square percentage deviation RMS and mean percentage deviation R values for each formula and the selected elements.

TABLE 8. Average values of RMS and R for each selected element shown in Table 7, \overline{RMS} and \overline{R} , for K-shell ionization cross sections

Element	Shell	Data points	\overline{RMS} (%)	\overline{R} (%)
C	K	58	9.1	-3.1
N	K	43	9.1	4.8
O	K	42	17.3	-14.7
Ne	K	57	11.6	-8.3
Al	K	24	7.3	1.1
Si	K	32	8.7	2.2
Ar	K	66	12.0	-8.4
Ca	K	45	21.3	-17.6
Ti	K	42	7.7	3.6
Cr	K	62	6.2	2.5
Mn	K	69	13.1	-2.0
Fe	K	46	8.0	-3.1
Ni	K	70	10.5	7.2
Cu	K	78	14.4	1.3
Zn	K	32	8.7	-3.9
Ga	K	47	3.3	2.4
Ge	K	63	5.9	-4.0
Se	K	24	8.9	1.1
Y	K	12	10.6	6.7
Pd	K	8	17.6	16.5
Ag	K	50	10.2	-2.3
Sn	K	13	5.8	-5.2
Sb	K	9	3.5	-3.2
Au	K	20	9.0	-1.0
Pb	K	5	10.8	0.8
Bi	K	7	6.3	2.4

8.3. M_5 -subshell ionization cross sections

Figure 62 shows percentage deviations between M_5 -subshell ionization cross sections from the Gryzinski, Casnati *et al.*, Jakoby *et al.*, and Hombourger formulae and the corresponding cross sections from the Bote *et al.* formulae as a function of electron energy for Y, Ag, La, Ho, Au, and Bi. Some of the deviations are relatively small (<10%) for some elements, formulae, and energies (e.g., for Y), but the deviations are generally much larger. Table 19 lists the root mean square percentage deviation RMS and mean percentage deviation R values for each formula and the selected elements.

8.4. Evaluation summary

Table 20 shows values of $\langle \overline{RMS} \rangle$ and $\langle \overline{R} \rangle$ calculated using Eq. (139) from the values of RMS and R in Tables 17–19 for each formula. The $\langle \overline{RMS} \rangle$ and $\langle \overline{R} \rangle$ values provide measures of the degree of agreement between the ionization cross sections from each formula for each shell or subshell and the corresponding cross sections from the Bote *et al.* formulae [Eqs. (87) and (88)]. We see that the $\langle \overline{RMS} \rangle$ and the $\langle \overline{R} \rangle$ values for K-shell ionization cross sections from the Casnati *et al.* formula (12.1% and 2.3%, respectively) and Hombourger formula (11.0% and -4.0%, respectively) are similar. They are also comparable to the weighted average values of $\langle \overline{RMS} \rangle$ (10.3%) and the weighted average value of $\langle \overline{R} \rangle$ (-1.9%) found in Sec. 8.3 in the comparisons of the sets of superior K-shell ionization cross sections with cross sections calculated from the Bote *et al.* formulae. In similar comparisons of the $\langle \overline{RMS} \rangle$ and $\langle \overline{R} \rangle$ values for L_3 - and M_5 -subshell ionization, Table 20 indicates that the Casnati *et al.* and Hombourger formulae were superior to the Gryzinski and Jakoby *et al.* formulae. While the $\langle \overline{RMS} \rangle$ values for L_3 -subshell ionization from the Casnati *et al.* formula (10.6%) and Hombourger formula (12.8%) were similar to the values found for K-shell ionization, the $\langle \overline{RMS} \rangle$ for M_5 -subshell ionization (25.2% and 28.8%, respectively) were appreciably larger. The Casnati *et al.* and Hombourger formulae thus provide useful estimates of K-shell and L_3 -subshell cross sections, but the M_5 -subshell ionization cross sections from these formulae have larger uncertainties. The larger $\langle \overline{RMS} \rangle$ and $\langle \overline{R} \rangle$ values in Table 20 for the Gryzinski formula (between 31.1% and 50.4% and between -26.3% and -47.7%, respectively) and the Jakoby *et al.* formula (between 21.5% and 82.0% and between 9.3% and -64.7%, respectively) indicate that these formulae provide much poorer estimates of the K-shell, L_3 -subshell, and M_5 -subshell ionization cross sections.

9. Summary

We evaluated calculated and measured cross sections for K-shell, L-subshell, and M-subshell ionization by electron impact. We surveyed a number of theories used to calculate ionization cross sections in Sec. 2 with emphasis given to

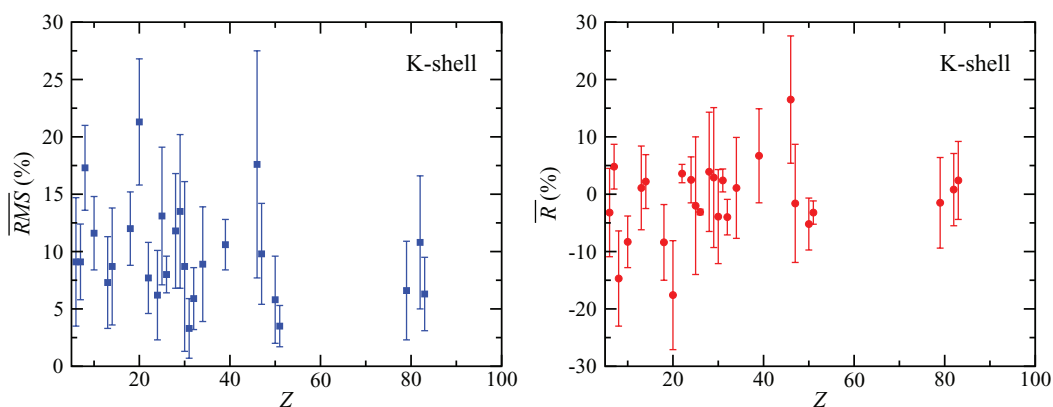


Fig. 49. (Color online) Plots of the average values of RMS and R from Table 8 for each element, \overline{RMS} and \overline{R} , as a function of Z . These parameters are measures of the degree of agreement between measured K-shell ionization cross sections and the corresponding cross sections from the Bote *et al.* predictive formulae. The error bars indicate one-standard-deviation limits.

the formulation of Bote and Salvat.³⁰ They showed that calculations could be made with the plane-wave Born approximation for overvoltages greater than 16 and with the distorted-wave Born approximation for lower overvoltages. This approach is very attractive since the calculations can be made for any neutral atom and for a wide range of incident electron energies.

Many analytical formulae have been utilized to predict inner-shell ionization cross sections, as summarized in Sec. 3. Foremost among them is the formula developed by Bethe³ in 1930 which provides ionization cross sections if the incident energy is sufficiently high. Fano plots based on the Bethe equation are a convenient means for assessing the self-consistency of calculated or measured cross sections and for determining the energy range over which the Bethe formula provides a valid description of the cross sections.^{2,69,72} Fano plots based on the calculated cross sections of Bote and Salvat clearly showed two linear regions. For overvoltages larger than about 50, the plots had the asymptotic slopes expected from the Bethe formula; for lower overvoltages, an additional linear region was found with larger slopes. Use of the Bethe formula with empirical coefficients in the latter region may be convenient but users should be aware of the limited energy ranges over which the Bethe formula will be reliable. Most other analytical formulae have been developed either for analytical convenience or from fits to available measured cross sections. We made extensive use of fits of two analytical equations, Eqs. (87) and (88), to the K-shell, L-subshell, and M-subshell ionization cross sections calculated using the Bote and Salvat approach.³⁰ Bote *et al.*³¹ determined the parameters in these equations for all atoms from hydrogen to einsteinium and for energies from threshold to 1 GeV. The Appendix gives guidance on the calculation of cross sections from these formulae.

Most measurements of inner-shell ionization cross sections are based on observations of de-excitation events, that is, of emitted x rays or Auger electrons. We outline the principles of these measurements in Sec. 4 and give more details of the experimental methods in Sec. 5. Brief mention is also made of the use of electron energy-loss spectroscopy

and crossed-beam methods for the determination of ionization cross sections.

Section 6 is a summary of K-shell, L-subshell, and M-subshell ionization cross sections and of $L\alpha$ x-ray production cross sections that were reported up to May 2013. These measured cross sections, for incident energies between the ionization threshold and 1 GeV, were compared with calculated values from the Bote *et al.* formulae; x-ray production cross sections were determined with needed relaxation data from the Evaluated Atomic Data Library.¹ Graphical comparisons are given to show the degree of consistency of measurements by different authors as well as the degree of consistency with the Bote values.

Section 7 contains a detailed evaluation of the measured and calculated cross sections presented in Sec. 6. We selected elements for which there were at least three (for K-shells) or two (for L- and M-subshells) mutually consistent sets of cross-section measurements. For these elements, we identified sets of experimental data for which the cross sections showed a satisfactory degree of consistency with each other and for which the cross sections, as a group, varied with incident electron energy in satisfactory agreement with theory. We used the calculated cross sections from Eqs. (87) and (88) that were shown in Figs. 11–41 as a guide to the expected energy dependence for each element. Use of the calculated cross sections was critical in our evaluation because we could thereby establish consistency (or otherwise) of data sets in non-overlapping energy ranges. Our selection of data sets was, of necessity, qualitative since some data sets were sparse or in non-overlapping energy ranges.

We could then make a more quantitative analysis by determining percentage deviations between measured cross sections in the selected data sets and the corresponding cross sections calculated by Bote *et al.*³¹ We examined plots of these percentage deviations as a function of overvoltage to assess whether there were any systematic trends. We then determined mean percentage deviations (\overline{R}) and root-mean-square (\overline{RMS}) percentage deviations for each element. Finally, we examined

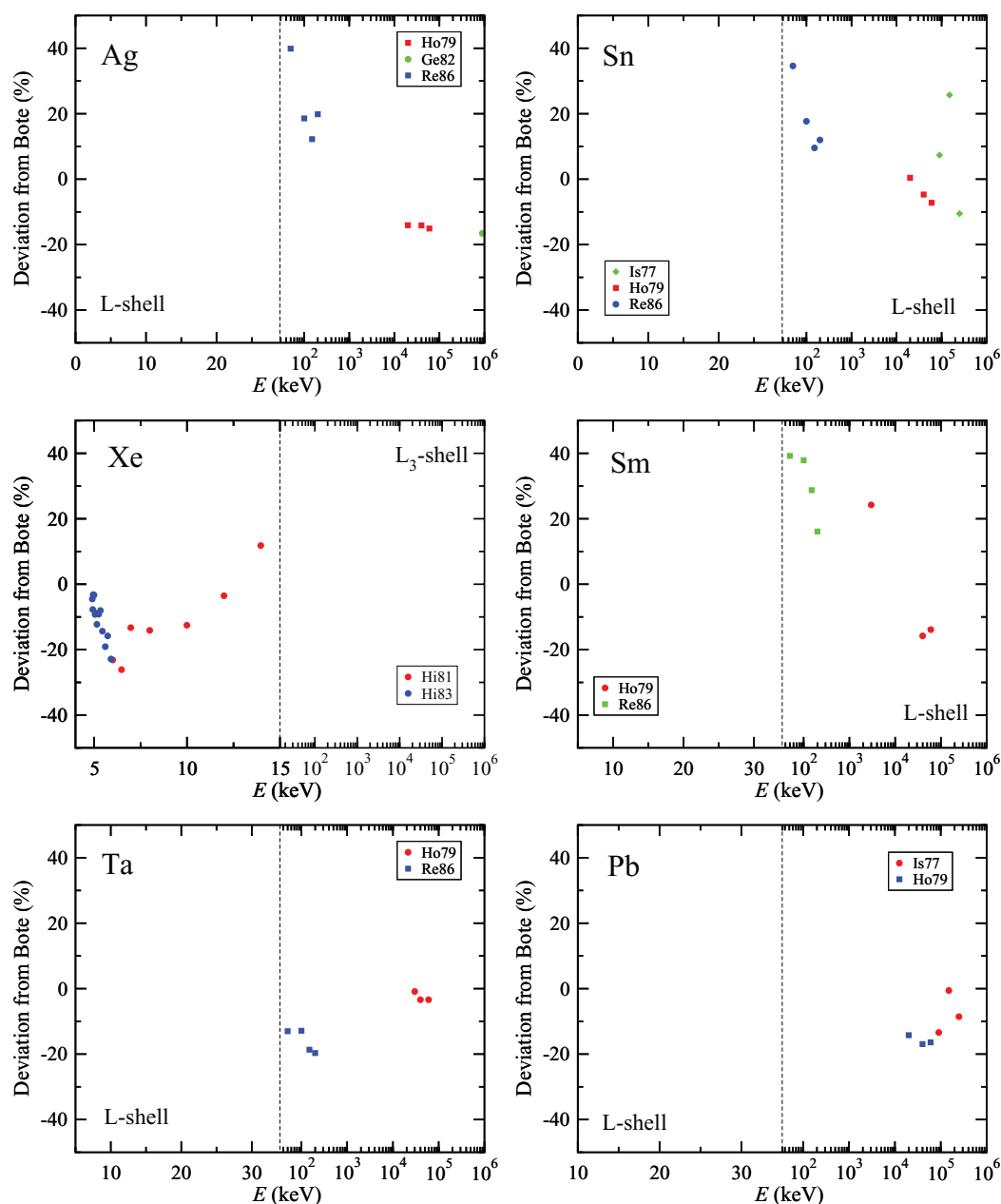


Fig. 50. (Color online) Percentage deviation Δ_i of experimental values of L_3 -subshell and total L-shell ionization cross sections from calculated values using the Bote *et al.* formulae as a function of electron energy for Ag (L), Sn (L), Xe (L_3), Sm (L), Ta (L), and Pb (L).

plots of these deviations as a function of Z to determine whether there were any systematic trends.

For K-shell ionization cross sections, we identified 26 elements with sets of measured cross sections that satisfied our selection criteria. The percentage deviations for these elements did not vary significantly with overvoltages between 1.02 and 2×10^5 , and the average values of these deviations and of the *RMS* percentage deviations did not vary significantly with atomic number from $Z = 6$ to $Z = 83$. For all of the selected elements, the average *RMS* deviation between the measured and calculated cross sections was 10.3%, while the average deviation was -1.9% . Calculated cross sections from the Bote *et al.* formulae for H and He were also found to be consistent with the measured cross sections for overvoltages

larger than 16. We therefore infer that the Bote formulae should also be valid for Li, Be, and B at similar overvoltages.

We identified seven elements for which there were two or more sets of total L-shell ionization cross-section measurements and one element (Xe) for which there were two sets of L_3 -subshell cross-section measurements that satisfied our selection criteria. The individual percentage deviations did not depend significantly on atomic number (between Ag and U) or overvoltage (between 1.02 and 6×10^5). For all of the selected elements, the average *RMS* deviation between the measured and calculated cross sections was 15.0%, while the average deviation was -3.1% .

There were only three elements with two or more sets of M-shell ionization cross sections that satisfied our evaluation

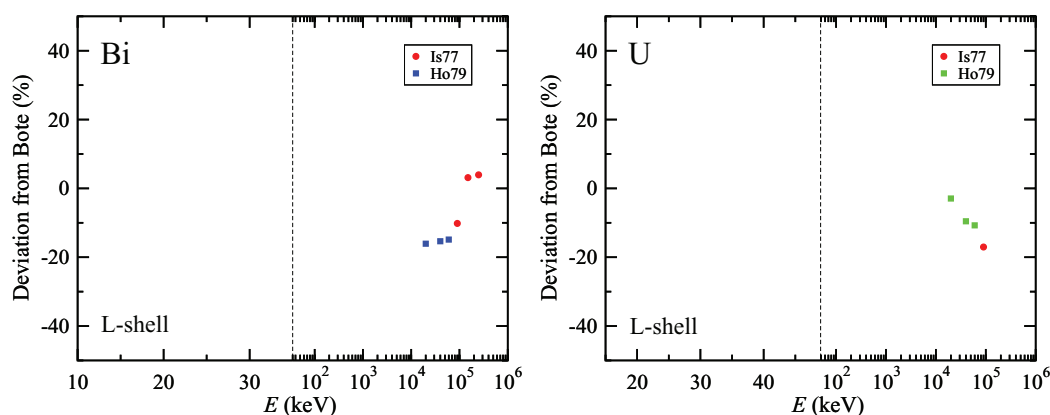


FIG. 51. (Color online) Percentage deviation Δ_i of experimental values of total L-shell ionization cross sections from calculated values using the Bote *et al.* formulae as a function of electron energy for Bi and U.

criteria. The individual percentage deviations did not depend significantly on atomic number (between Au and U) or overvoltage (between 23 and 1×10^5). For these elements, the average *RMS* deviation between the measured and calculated cross sections was 23.5%, while the average deviation was 8.2%.

We identified eight elements for which two or more sets of measured $L\alpha$ x-ray production cross sections that satisfied our evaluation criteria. The individual percentage deviations between measured and calculated $L\alpha$ x-ray production cross sections did not vary significantly with atomic number (between Gd and Bi) or L_3 -subshell overvoltage ratio (between 1.02 and 6×10^3). The average *RMS* deviation between the measured $L\alpha$ x-ray cross sections and the cross sections calculated from the Bote *et al.* formulae (and needed atomic data) was 10.6%, while the average deviation was -7.3% .

The overall average *RMS* deviation between the measured and calculated cross sections was 10.9% and the overall *R* average deviation was -2.5% . This degree of agreement between measured and calculated ionization and x-ray production cross section is believed to be very satisfactory given the uncertainties discussed in Sec. 5. It is not surprising that

there were larger deviations between measured L- and M-subshell ionization cross sections and the corresponding calculated values than for K-shell cross sections since there are additional uncertainties associated with the needed atomic data,¹ as discussed in Sec. 4.

Although we specify that the overvoltage should be greater than 1.02 for reliable use of the Bote *et al.* formulae, we add that the incident energy should also be a minimum of 50 eV larger than the threshold energy for ionization. This extra restriction is added in order to avoid effects due to post-collision interactions in free atoms or molecules and to so-called final-state or screening effects in solids.

Our sets of selected ionization and x-ray production cross sections were judged to be “superior” data. A variety of measurement methods were used to acquire these data, as indicated in Table 16. With attention to the possible sources of uncertainty identified in Sec. 5, high-quality cross-section measurements can be made with these methods.

Finally, we made comparisons of ionization cross sections from the analytical formulae of Gryzinski, Casnati *et al.*, Hombourger, and Jakoby *et al.* with those from the Bote *et al.* formulae. These comparisons were made with K-shell,

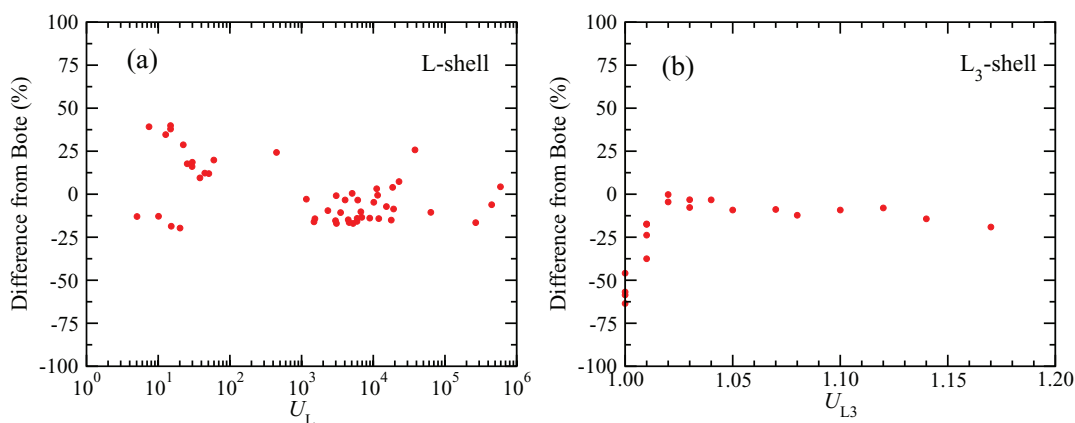


FIG. 52. (Color online) (a) Plots of percentage deviations between measured L-shell ionization cross sections and the corresponding cross sections calculated from the Bote *et al.* predictive formulae as a function of U_L on logarithmic scales. (b) Plots of percentage deviations between measured L_3 -subshell ionization cross sections^{204,207} for Xe and the corresponding cross sections calculated from the Bote *et al.* predictive formulae as a function of U_{L3} on linear scales.

TABLE 9. Selected sets of measured L-shell ionization cross sections that were included in the evaluation of experimental data. Also shown are the RMS and R values for each data set that were calculated from Eq. (138)

Element	Shell	Data points	Key	Reference	RMS (%)	R (%)
Ag	L	3	Ho79	Genz <i>et al.</i> ¹³⁴	14.4	-14.4
Ag	L	3	Ge82	Genz <i>et al.</i> ¹⁴¹	10.4	-6.1
Ag	L	4	Re86	Reusch <i>et al.</i> ¹⁴²	24.9	22.6
Sn	L	3	Is77	Ishii <i>et al.</i> ¹³¹	16.6	7.5
Sn	L	3	Re86	Reusch <i>et al.</i> ¹⁴²	5.0	-3.8
Sn	L	4	Ho79	Hoffmann <i>et al.</i> ¹³⁴	20.8	18.4
Xe	L ₃	7	Hi81	Hippler <i>et al.</i> ²⁰⁴	16.7	-11.7
Xe	L ₃	22	Hi83	Hippler <i>et al.</i> ²⁰⁷	12.1	-10.6
Sm	L	3	Ho79	Hoffmann <i>et al.</i> ¹³⁴	18.5	-1.8
Sm	L	4	Re86	Reusch <i>et al.</i> ¹⁴²	31.8	30.5
Ta	L	3	Ho79	Hoffmann <i>et al.</i> ¹³⁴	2.8	-2.5
Ta	L	4	Re86	Reusch <i>et al.</i> ¹⁴²	16.4	-16.0
Pb	L	3	Is77	Ishii <i>et al.</i> ¹³¹	9.2	-7.5
Pb	L	3	Ho79	Hoffmann <i>et al.</i> ¹³⁴	15.9	-15.8
Bi	L	3	Is77	Ishii <i>et al.</i> ¹³¹	6.5	-1.0
Bi	L	3	Ho79	Hoffmann <i>et al.</i> ¹³⁴	15.4	-15.4
U	L	1	Is77	Ishii <i>et al.</i> ¹³¹	17.0	-17.0
U	L	3	Ho79	Hoffmann <i>et al.</i> ¹³⁴	18.5	-7.7

TABLE 10. Average values of RMS and R for each selected element, \overline{RMS} and \overline{R} , from the measurements of L-subshell ionization cross sections shown in Table 9

Element	Shell	Data points	\overline{RMS} (%)	\overline{R} (%)
Ag	L	10	17.4	2.9
Sn	L	10	14.8	8.4
Xe	L ₃	20	13.6	-10.9
Sm	L	7	26.1	16.6
Ta	L	7	10.5	-10.3
Pb	L	6	15.5	-11.7
Bi	L	6	11.0	-8.2
U	L	4	10.6	-10.0

L₃-subshell, and M₅-subshell ionization cross sections for selected elements and for incident energies close to the ionization threshold to 1 GeV. We found that the Casnati *et al.* and Hombourger formulae gave cross sections for K-shell and L₃-subshell ionization that agreed satisfactorily with corresponding cross sections from the Bote *et al.* formulae; there were larger deviations, however, for the M₅-subshell cross sections. The Gryzinski and Jakoby *et al.* formulae provided much poorer estimates of ionization cross sections than the Casnati *et al.* and Hombourger formulae.

The DWBA theory described in Sec. 2 has been employed to generate an extensive database of cross sections for ionization of the K shell and the L and M subshells of all the elements from hydrogen ($Z = 1$) to einsteinium ($Z = 99$) by impact of electrons and positrons with kinetic energies up to 1 GeV. This

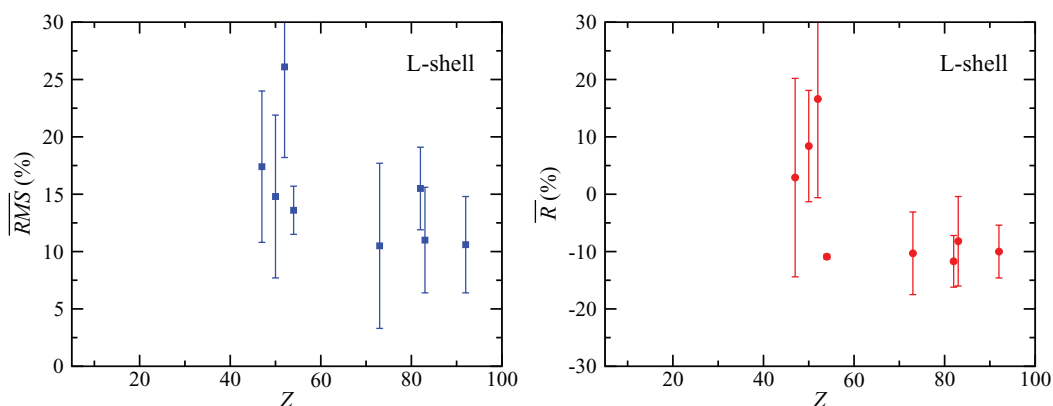


FIG. 53. (Color online) Plots of the average values of RMS and R from Table 10 for each element, \overline{RMS} and \overline{R} , as a function of Z . These parameters are measures of the degree of agreement between measured total L-shell or L₃-subshell ionization cross sections and the corresponding cross sections from the Bote *et al.* predictive formulae. The error bars indicate one-standard-deviation limits.

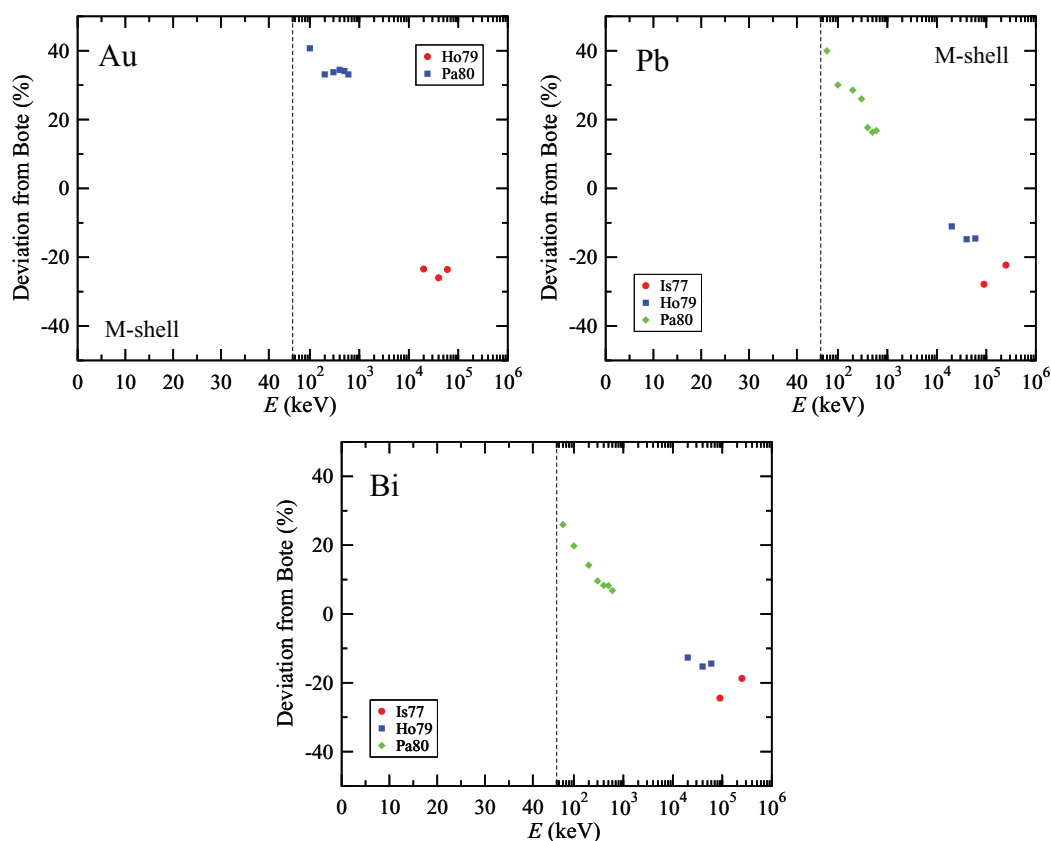


FIG. 54. (Color online) Percentage deviation Δ_i of experimental values of M-shell ionization cross sections from calculated values using the Bote *et al.* formulae, as a function of electron energy for Au, Pb, and Bi.

database is handled by a graphical interface which allows the display and the generation of tables of cross sections for ionization, and for x-ray and Auger emission. The latter are obtained by using atomic transition probabilities from the EADL (Ref. 1) as described in Sec. 4.3. This handy tool provides one of the fundamental parameters required for quantification in EPMA and AES.

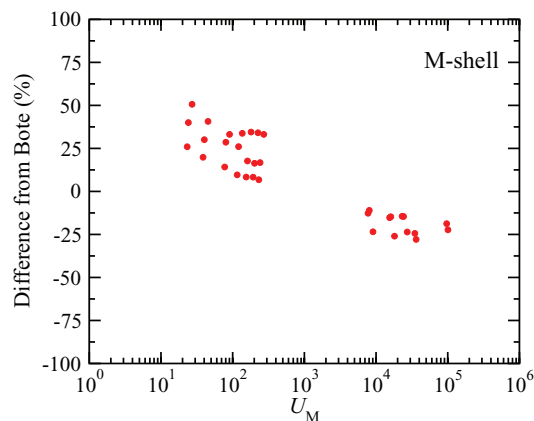


FIG. 55. (Color online) Plot of percentage deviations between measured M-shell ionization cross sections and the corresponding cross sections calculated from the Bote *et al.* predictive formulae as a function of U_M on a logarithmic scale.

Acknowledgments

We are deeply indebted to David Bote for his work in the development of the theory and computer programs, and also for preparing the numerical database. Thanks are also due to Francesc Salvat-Pujol for programming the graphical interface of the database, and to David Liljequist, José M. Fernández-Varea, and Michael Dingfelder for critically reading the manuscript. Financial support from the Spanish Ministerio de Educación y Ciencia and ERDF (Project No. FPA2009-14091-C02-01) and from AGAUR, Generalitat de Catalunya (Grant No. SGR 2009-276) is gratefully acknowledged. One of the authors (A.J.) would like to acknowledge support by the research project of the National Science Center in Poland, No. DEC-2011/01/B/ST4/00959.

Appendix: Calculations of Ionization Cross Sections from the Bote Formulae

We give guidance here on the calculation of ionization cross sections from the Bote *et al.* formulae,³¹ Eqs. (87) and (88). These cross sections depend on the overvoltage U , the ratio of the incident electron energy to the BE of the shell or subshell of interest, as well as on parameter values specific to the particular element and shell.³¹

TABLE 11. Selected sets of measured total M-shell ionization cross sections that were included in the evaluation of experimental data. Also shown are the *RMS* and *R* values for each selected data set that were calculated from Eq. (138)

Element	Shell	Data points	Key	Reference	<i>RMS</i> (%)	<i>R</i> (%)
Au	M	3	Ho79	Hoffmann <i>et al.</i> ¹³⁴	24.3	−24.3
Au	M	7	Pa80b	Pálinkás and Schlenk ²²²	37.6	−37.1
Pb	M	2	Is77	Ishii <i>et al.</i> ¹³¹	25.2	−25.1
Pb	M	3	Ho79	Hoffmann <i>et al.</i> ¹³⁴	13.6	−13.4
Pb	M	7	Pa80b	Pálinkás and Schlenk ²²²	26.3	25.0
Bi	M	2	Is77	Ishii <i>et al.</i> ¹³¹	21.7	−21.6
Bi	M	3	Ho79	Hoffmann <i>et al.</i> ¹³⁴	14.1	−14.1
Bi	M	7	Pa80b	Pálinkás and Schlenk ²²²	14.8	13.3

TABLE 12. Average values of *RMS* and *R* for each selected element, \overline{RMS} and \overline{R} , using the measurements of *M*-shell ionization cross sections shown in Table 11

Element	Shell	Data points	\overline{RMS} (%)	\overline{R} (%)
Au	M	10	33.6	18.7
Pb	M	12	22.9	7.1
Bi	M	12	15.8	0.6

The BE is usually defined as the minimum energy required to remove an electron in a particular shell or subshell of an atom or molecule to a free or unbound state. For a solid, the electron of interest is removed *to infinity*, i.e., a large distance from the solid. For atoms and molecules, BEs are conveniently measured with respect to the vacuum level (i.e., the potential at a large distance from the atom or molecule), while for solids

BEs are conveniently measured with respect to the Fermi level. In principle, it might be thought that BEs for a solid plus a work function should be the same as the corresponding BE for an atom or molecule, but this simple relationship breaks down due to a number of additional considerations.

The BE definitions given here have an important qualifier, namely that all other electrons in the atom, molecule, or solid are assumed to remain in their original states. It is well known, however, that removal of one electron from an atom, molecule, or solid will cause relaxation of other orbitals.²⁷⁸ X-ray photoelectron spectroscopy (XPS) is a common method for the determination of BEs. The act of photoionization in XPS generally causes so-called electron shake-up and shake-off in isolated atoms and molecules (i.e., excitation of a valence electron to unoccupied discrete states or to the continuum). For solids, one sees so-called satellite lines due to discrete excitations from the valence band to

TABLE 13. Selected sets of measured L-shell x-ray production cross sections included in the evaluation of experimental data. Also shown are the *RMS* and *R* values for each selected data set that were calculated from Eq. (138)

Element	Shell	Data points	Key	Reference	<i>RMS</i> (%)	<i>R</i> (%)
Gd	La	1	Pa75	Park <i>et al.</i> ¹²⁹	5.2	−5.2
Gd	La	18	Wu10	Wu <i>et al.</i> ¹⁸⁵	19.8	−17.2
Er	La	1	Pa75	Park <i>et al.</i> ¹²⁹	10.4	−10.4
Er	La	4	Ri78	Ricz ¹³²	1.8	0.1
Yb	La	1	Pa75	Park <i>et al.</i> ¹²⁹	13.5	−13.5
Yb	La	4	Sc77	Schlenk <i>et al.</i> ²¹³	1.8	0.1
W	La	14	Ca02	Campos <i>et al.</i> ¹⁶¹	10.5	−9.9
W	La	17	Ya04	Yang <i>et al.</i> ¹⁸⁹	16.7	−14.1
W	La	19	Wu10	Wu <i>et al.</i> ¹⁸⁵	13.1	−12.3
Pt	La	1	Ca02	Campos <i>et al.</i> ¹⁶¹	8.9	−12.3
Pt	La	13	Pa75	Park <i>et al.</i> ¹²⁹	8.2	−7.6
Au	La	4	Sc77	Schlenk <i>et al.</i> ²¹³	3.7	−2.6
Au	La	7	Pa80a	Pálinkás and Schlenk ¹³⁸	3.6	−0.2
Au	La	9	Sh81	Shima <i>et al.</i> ¹⁴⁰	4.4	−3.5
Au	La	12	Ca02	Campos <i>et al.</i> ¹⁶¹	18.6	−6.7
Au	La	12	Wu04	Wu <i>et al.</i> ¹⁷⁹	6.0	−1.9
Pb	La	4	Pa75	Park <i>et al.</i> ¹²⁹	3.6	1.0
Pb	La	1	Sc77	Schlenk <i>et al.</i> ²¹³	7.8	−7.8
Pb	La	7	Pa80a	Pálinkás and Schlenk ¹³⁸	5.9	−1.9
Pb	La	17	Wu07	Wu <i>et al.</i> ¹⁸³	14.7	−14.4
Bi	La	1	Pa75	Park <i>et al.</i> ¹²⁹	2.8	−2.8
Bi	La	4	Ri78	Ricz <i>et al.</i> ¹³²	1.0	−0.1
Bi	La	7	Pa80a	Pálinkás and Schlenk ¹³⁸	4.1	0.7
Bi	La	15	Wu10c	Wu <i>et al.</i> ¹⁸⁶	8.2	−6.8

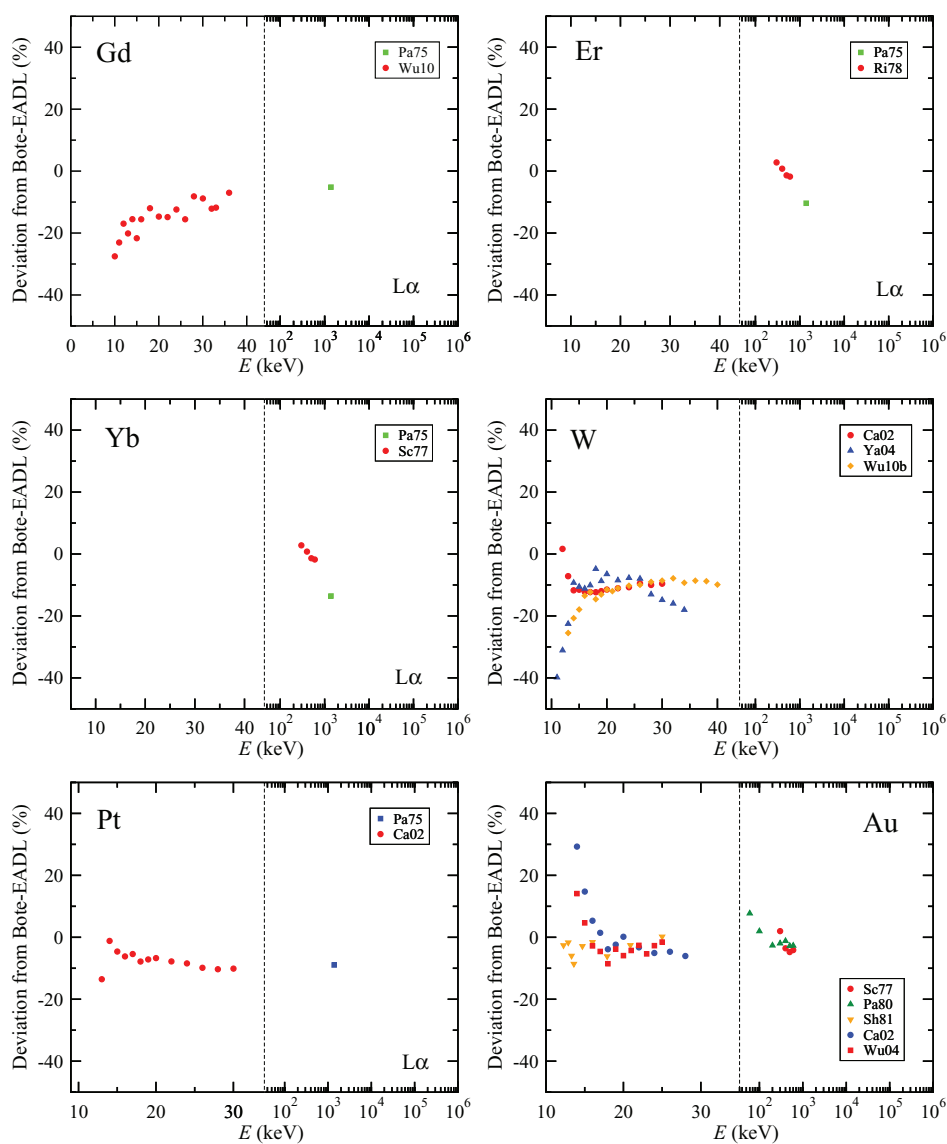


FIG. 56. (Color online) Percentage deviation Δ , of experimental values of $L\alpha$ x-ray production cross sections from calculated values using the Bote *et al.* formulae together with relaxation parameters extracted from the EADL as a function of electron energy for Gd, Er, Yb, W, Pt, and Au.

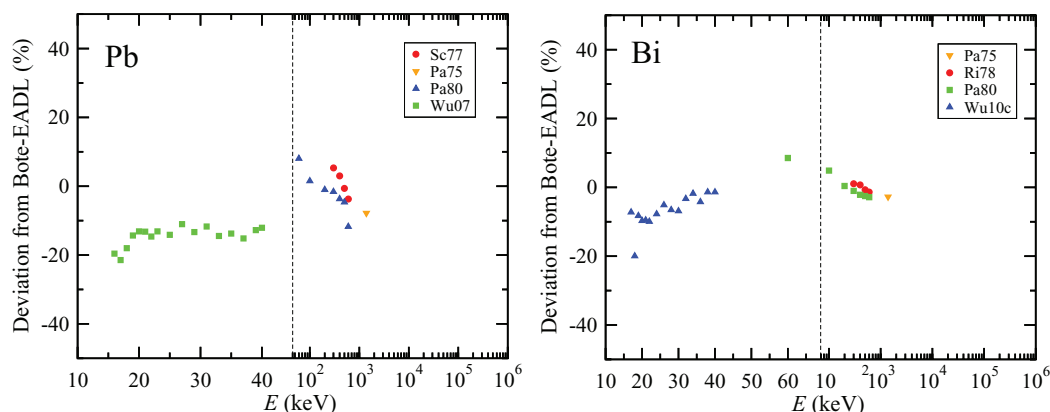


FIG. 57. (Color online) Percentage deviation Δ , of experimental values of $L\alpha$ x-ray production cross sections from calculated values using the Bote *et al.* formulae together with relaxation parameters extracted from the EADL as a function of electron energy for Pb and Bi.

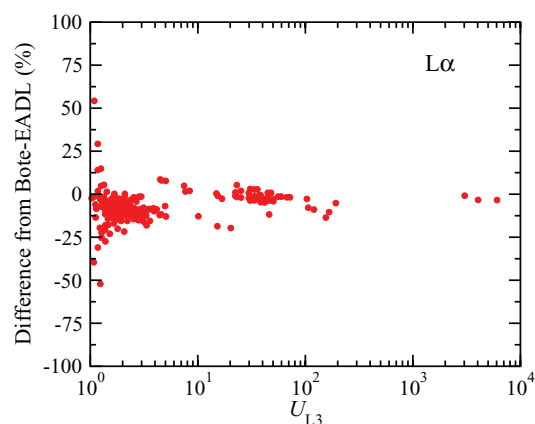


FIG. 58. (Color online) Plot of percentage deviations between measured $L\alpha$ x-ray production cross sections and the corresponding cross sections calculated from the Bote *et al.* predictive formulae for L_3 -subshell ionization together with relaxation parameters extracted from the EADL as a function of U_{L3} on a logarithmic scale.

some unfilled states or to intrinsic collective excitations (plasmons). The XPS lines of conductors also become asymmetrical due to the intrinsic excitation of electron-hole pairs. There are both “chemical shifts” of photoelectron lines for an atom in different chemical states in a molecule or solid and “surface or interface” shifts of photoelectron lines for an atom in a surface or interface atomic layer compared to its bulk. The simple one-electron picture on which the BE definitions are based breaks down for some atoms and shells. Strong many-electron effects are observed in 4s, 4p-like holes in Cd to Gd and 5s, 5p-like holes in Bi to Pu due to so-called giant Coster-Kronig fluctuations and decays.²⁷⁹

Finally, the work function of a solid is a surface property, and different crystal faces of the same solid generally have different work functions. The work functions also vary with adsorption of molecules on the surface, and with reactions such as oxidation. Work functions typically vary between 2 and 6 eV, and it is reasonable to assume an average value of 4 eV

TABLE 14. Average values of RMS and R for each selected element, \overline{RMS} and \overline{R} , using the measurements of L -shell x-ray production cross sections shown in Table 13

Element	Line	Data points	\overline{RMS} (%)	\overline{R} (%)
Gd	$L\alpha$	19	19.1	-16.6
Er	$L\alpha$	5	3.5	-1.9
Yb	$L\alpha$	5	4.8	-2.6
W	$L\alpha$	50	13.6	-12.2
Pt	$L\alpha$	14	8.2	-7.7
Au	$L\alpha$	44	8.5	0.3
Pb	$L\alpha$	29	10.8	-9.1
Bi	$L\alpha$	27	5.9	-3.7

when comparing BEs of atoms and solids; nevertheless, BE differences of up to 2 eV could occur due to work-function variations among different solids. While we have commented here on the determination of BEs by XPS, similar effects need to be considered with other methods for the determination of BEs (e.g., x-ray absorption spectroscopy and electron energy-loss spectroscopy).

We now comment on three useful compilations of BEs. The first of these is the 1967 compilation of Bearden and Burr.²⁸⁰ At least one BE for most elements was determined by XPS, and other BEs were calculated from BE differences obtained from x-ray emission and absorption spectra. Many if not most of the XPS measurements at that time had been made in instruments that did not have ultrahigh vacua. As a result, many of the “elemental” samples were probably oxidized or had other surface compounds and impurity layers. These “chemical” effects could lead to shifts or errors of several eV or more in the published BEs.

A second comprehensive table of BEs for atoms is included in a 1975 book by Carlson.⁶⁴ This compilation is based mainly on the work of Lotz²⁸¹ who lists BEs for free atoms. The latter work is based in large part on the Bearden and Burr tabulation (with work-function additions for solids to refer the BEs to the vacuum level, and some smoothing).

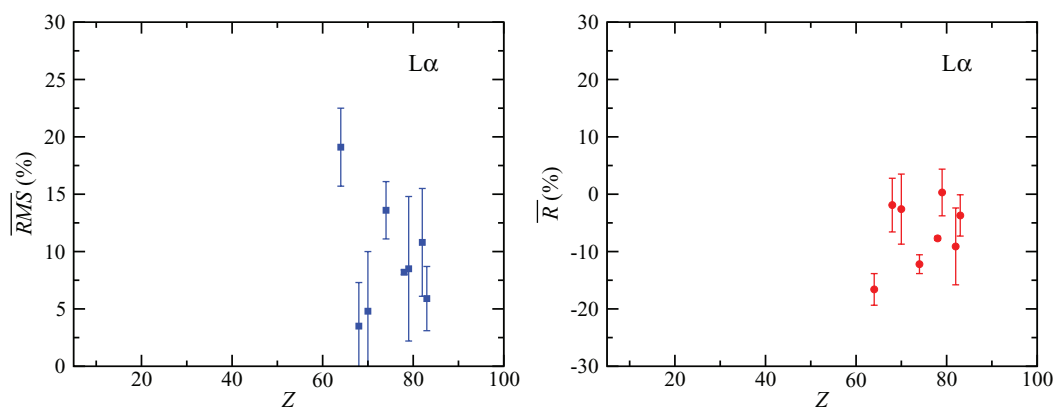


FIG. 59. (Color online) Plots of the average values of RMS and R from Table 14 for each element, \overline{RMS} and \overline{R} , as a function of Z . These parameters are measures of the degree of agreement between measured $L\alpha$ x-ray production cross sections and the corresponding cross sections from the Bote *et al.* predictive formulae. The error bars indicate one-standard-deviation limits.

TABLE 15. Summary of $\langle RMS \rangle$ and $\langle R \rangle$ values found in the evaluation of K-, L-, and M-shell ionization cross sections and of $L\alpha$ x-ray production cross sections from the selected sources with superior data. Information is also given on the number of elements in each evaluation, the total number of data points (e.g., measured cross sections considered), the range of atomic numbers, and the range of overvoltage ratios

Cross section	No. element	Data points	Z range	U range	$\langle RMS \rangle$ (%)	$\langle R \rangle$ (%)
K-shell ionization	26	1032	6 to 83	1.02 to 2×10^5	10.3	-1.8
L-shell ionization	8	70	47 to 92	1.02 to 6×10^5	15.0	-3.1
M-shell ionization	3	34	79 to 83	23 to 1×10^5	23.5	8.2
$L\alpha$ x-ray production	8	193	64 to 83	1.02 to 6×10^3	10.6	-7.3

TABLE 16. Summary of methods used for the measurement of (a) K-, (b) L-, and (c) M-shell ionization cross sections and for the measurement of (d) $L\alpha$ x-ray production cross sections, as listed in Tables 2–5, respectively. Methods include measurements of x-ray yields (X), Auger yields (A), and EELS spectra (E) with self-supporting thin films (T), thin films on substrates (TS), thick substrates (S), and gases (G). We show the number of data sets for each type of cross section, the number of data sets with superior data (as judged with our evaluation criteria), and the percentage of data sets with superior data

Cross section	X,T	X,TS	X,G	X,S	A,G	E,T
(a) K-shell ionization						
Number of data sets	151	42	16	1	9	8
Number of data sets with superior data	80	23	10	1	9	7
Percentage of superior data sets (%)	53	55	63	100	100	88
(b) L-shell ionization						
Number of data sets	32	1	4	4	8	0
Number of data sets with superior data	16	0	2	0	0	-
Percentage of superior data sets (%)	50	0	50	0	0	-
(c) M-shell ionization						
Number of data sets	9	0	0	0	1	3
Number of data sets with superior data	8	-	-	-	0	0
Percentage of superior data sets (%)	89	-	-	-	0	0
(d) $L\alpha$ x-ray production						
Number of data sets	25	24	2	0	-	-
Number of data sets with superior data	15	9	0	-	-	-
Percentage of superior data sets (%)	60	38	0	-	-	-

TABLE 17. Values of RMS and R determined using Eq. (138) with differences of K-shell ionization cross sections calculated using the formulae of Gryzinski, Casnati *et al.*, Hombourger, and Jakoby *et al.* from the cross sections obtained with the Bote *et al.* formulae for the indicated elements

Element	Shell	Gryzinski		Casnati		Hombourger		Jakoby	
		$RMS(\%)$	$R(\%)$	$RMS(\%)$	$R(\%)$	$RMS(\%)$	$R(\%)$	$RMS(\%)$	$R(\%)$
N	K	32.2	-29.3	11.0	4.8	8.9	-1.6	42.8	28.2
Si	K	36.3	-32.6	8.4	0.5	9.8	-5.7	29.4	24.2
Fe	K	33.6	-29.0	7.5	1.7	8.2	-4.5	15.2	12.6
Y	K	27.5	-21.7	9.5	4.4	7.6	-2.0	6.3	0.5
Ag	K	27.7	-21.6	11.7	3.7	9.8	-2.7	9.5	-2.9
La	K	28.0	-21.9	14.9	2.7	12.8	-3.7	13.6	-5.3
Ho	K	28.8	-22.9	18.4	1.5	15.9	-5.1	19.6	-4.8
Au	K	29.8	-24.4	22.4	-0.3	19.4	-6.9	25.8	0.6

TABLE 18. Values of RMS and R determined using Eq. (138) with differences of L_3 -subshell ionization cross sections calculated using the formulae of Gryzinski, Casnati *et al.*, Hombourger, and Jakoby *et al.* from the cross sections obtained with the Bote *et al.* formulae for the indicated elements

Element	Shell	Gryzinski		Casnati		Hombourger		Jakoby	
		$RMS(\%)$	$R(\%)$	$RMS(\%)$	$R(\%)$	$RMS(\%)$	$R(\%)$	$RMS(\%)$	$R(\%)$
Si	L_3	42.0	-38.1	11.2	-0.6	12.5	-6.9	117.3	-51.8
Fe	L_3	45.1	-42.7	16.1	-12.4	20.3	-17.8	58.9	-44.3
Y	L_3	40.3	-37.4	11.8	-7.1	15.7	-12.8	48.9	-41.0
Ag	L_3	37.2	-34.1	9.7	-3.4	12.8	-9.3	44.5	-40.0
Xe	L_3	35.1	-31.6	8.8	-0.7	11.0	-6.7	41.4	-37.3
Gd	L_3	33.2	-29.2	8.3	1.5	9.5	-4.6	37.3	-34.8
Ta	L_3	28.4	-23.5	8.9	2.8	9.5	-3.3	33.8	-32.7
Bi	L_3	27.7	-22.5	8.2	3.3	8.7	-2.9	7.9	0.5

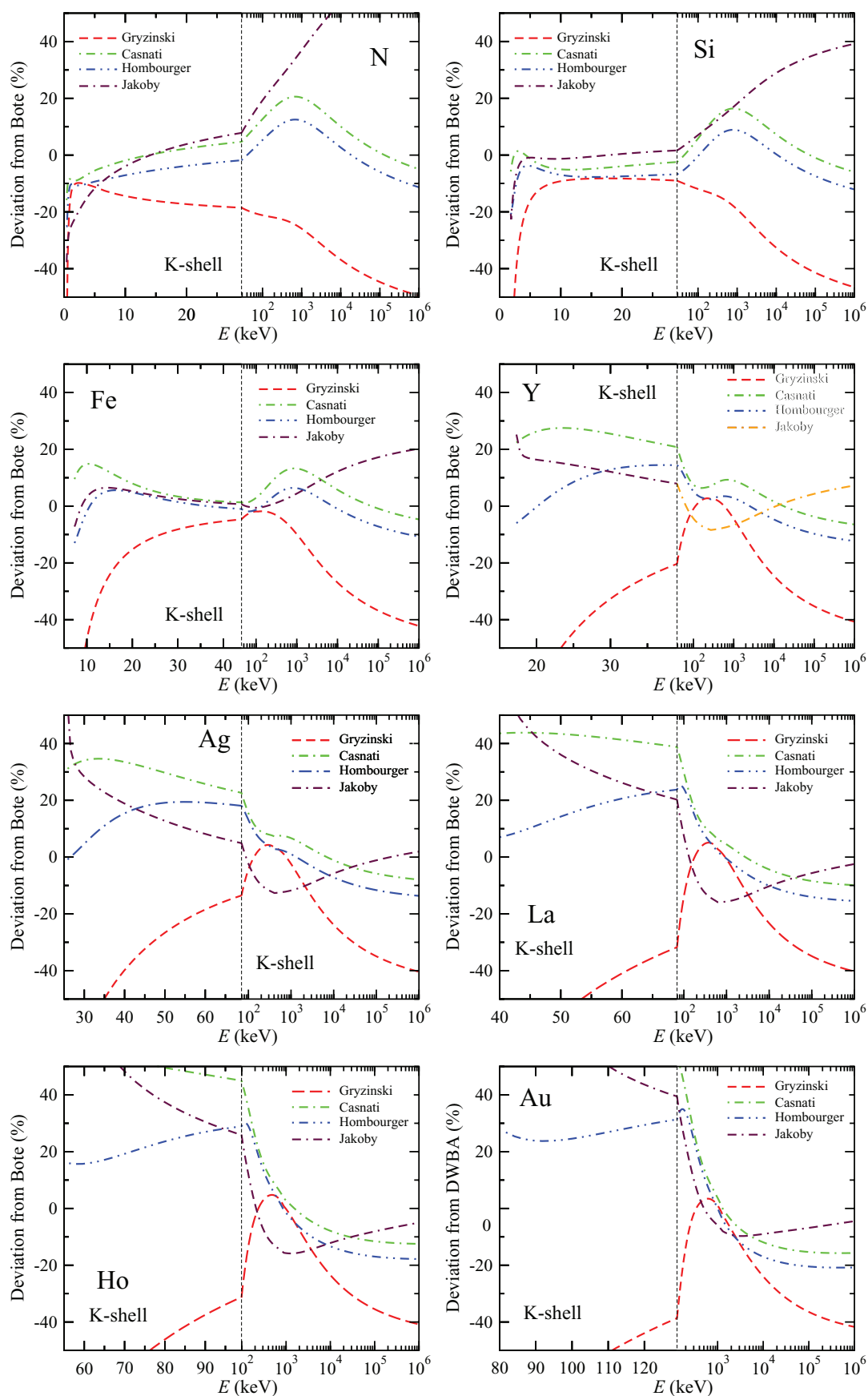


FIG. 60. (Color online) Percentage deviations Δ_i between K-shell ionization cross sections calculated using different analytical formulae (as indicated in the legends) and values calculated from the Bote *et al.* formulae as a function of electron energy for N, Si, Fe, Y, Ag, La, Ho, and Au.

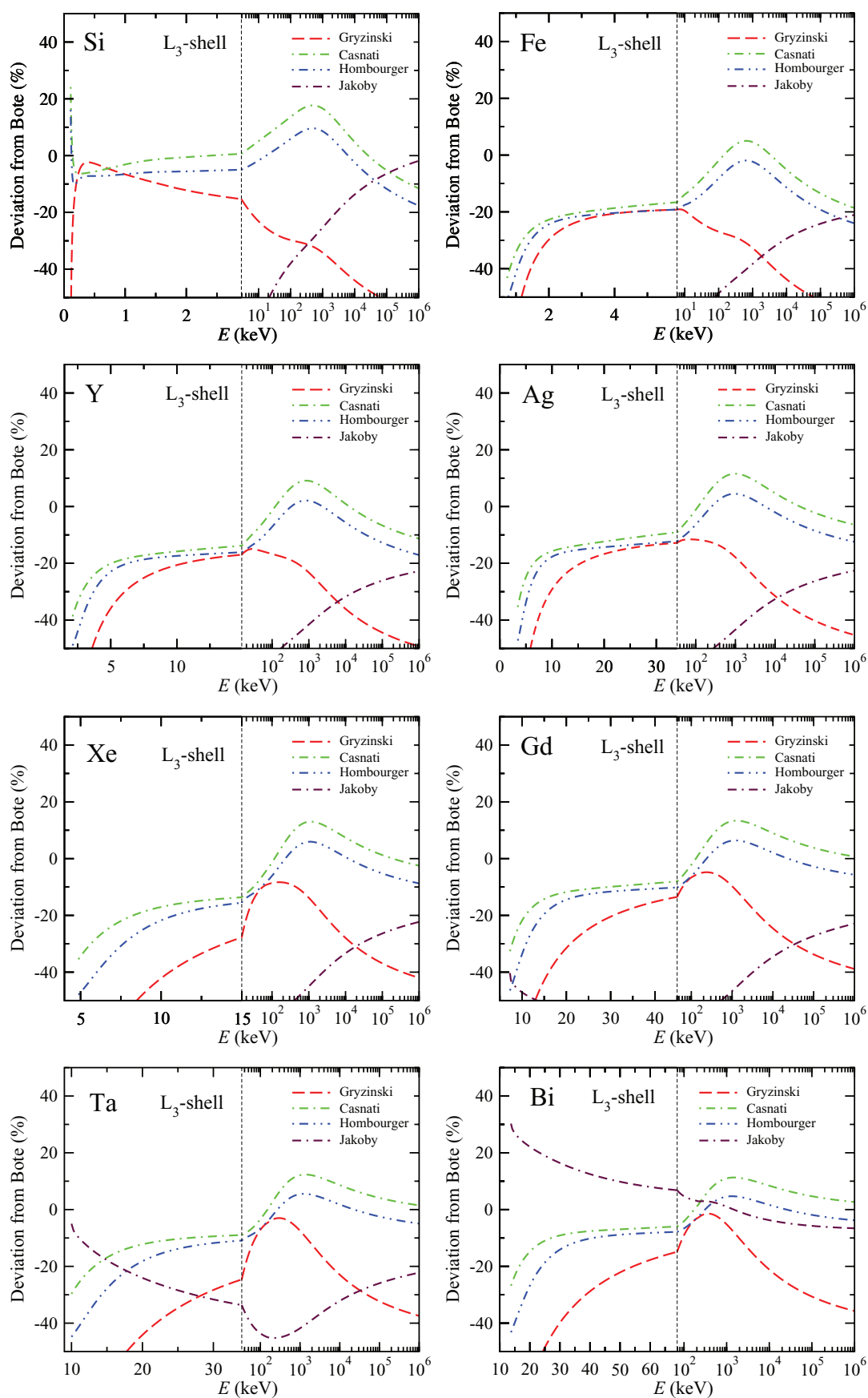


FIG. 61. (Color online) Percentage deviations Δ_i between L_3 -subshell ionization cross sections calculated using different analytical formulae (as indicated in the legends) and values calculated from the Bote *et al.* formulae as a function of electron energy for Si, Fe, Y, Ag, Xe, Gd, Ta, and Bi.

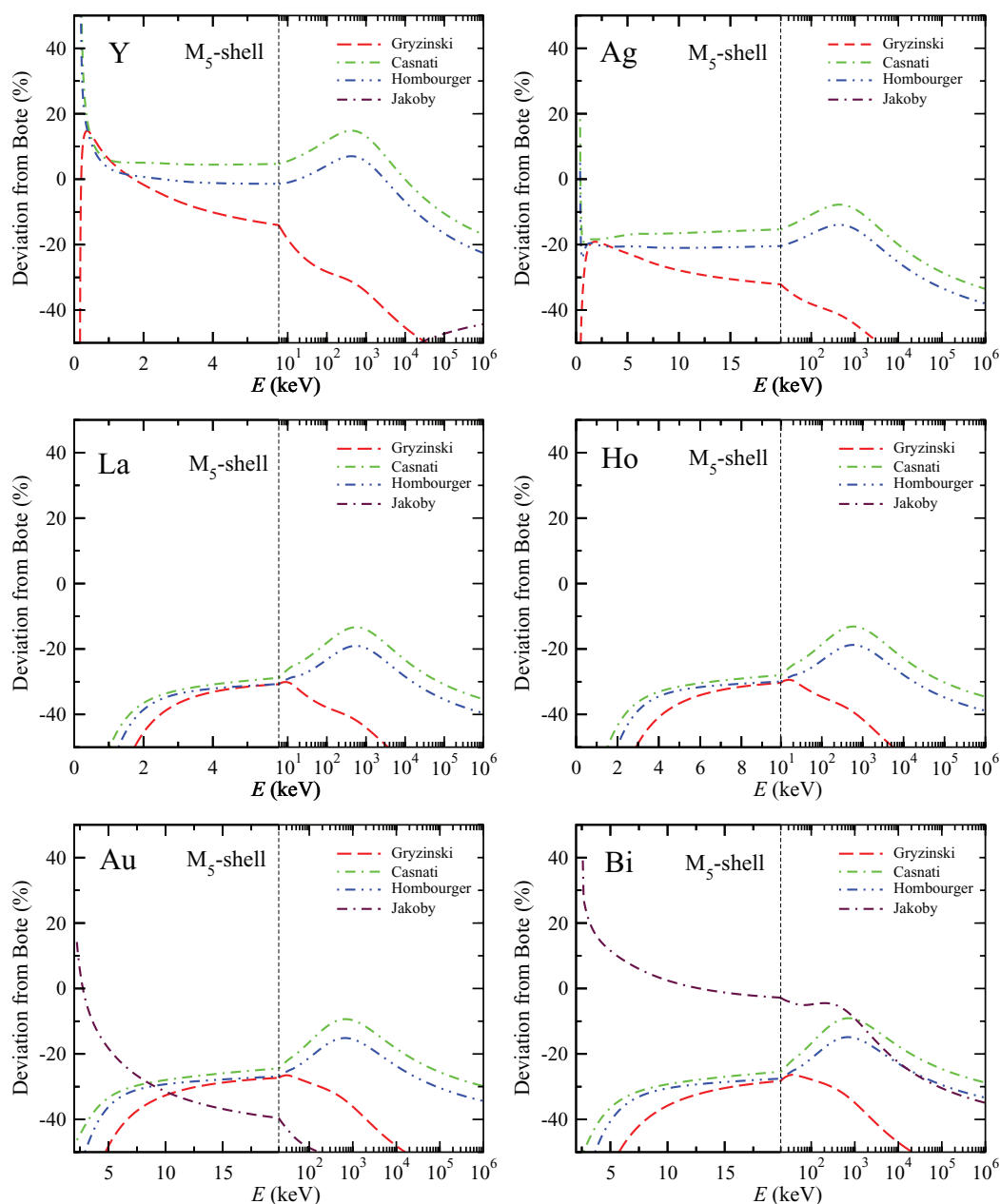


Fig. 62. (Color online) Percentage deviations Δ_i between M_5 -subshell ionization cross sections calculated using different analytical formulae (as indicated in the legends) and values calculated from the Bote *et al.* formulae as a function of electron energy for Y, Ag, La, Ho, Au, and Bi.

The third BE compilation was made by Williams.²⁸² While this compilation is not as complete as those of the other two compilations, it contains more recent BE measurements made by XPS. In addition, many (though not all) of the BEs in the Williams compilation are based on XPS measurements with samples prepared in ultrahigh vacua. We therefore expect that these BEs to be generally more reliable than those in the Bearden and Burr tabulation (and the derivative Lotz and Carlson tabulations). We also note that calibration reference data and BE-calibration procedures for XPS instruments did not become available until around the 1990s. Refined BEs for some 50 elemental solids have been published by Powell.²⁸³

Comparisons of BEs in the Carlson and Williams compilations show that a large majority of the BE differences were less than ± 3 eV. Differences of this magnitude could reasonably be expected on account of chemical shifts for some measurements (due to some early measurements probably being made on oxidized samples), uncertainties of the work-function data, or to inadequate calibrations of the BE scale for some measurements. When larger differences occur, these can be resolved in most cases by further comparisons with BEs for many atoms, molecules, and solids in the NIST XPS Database.²⁸⁴ We note, however, that most BEs in this database were measured in XPS instruments with Al $K\alpha$ x-ray sources. As a result, the BEs are typically less than about 1.4 keV.

TABLE 19. Values of RMS and R determined using Eq. (138) with differences of M_5 -subshell ionization cross sections calculated using the formulae of Gryzinski, Casnati *et al.*, Hombourger, and Jakoby *et al.* from the cross sections obtained with the Bote *et al.* formulae for the indicated elements

Element	Shell	Gryzinski		Casnati		Hombourger		Jakoby	
		$RMS(\%)$	$R(\%)$	$RMS(\%)$	$R(\%)$	$RMS(\%)$	$R(\%)$	$RMS(\%)$	$R(\%)$
Y	M_5	43.0	-36.6	16.9	-0.8	17.3	-7.0	165.0	-92.2
Ag	M_5	52.0	-49.6	24.8	-22.5	29.2	-27.3	94.5	-80.3
La	M_5	54.4	-52.7	30.0	-28.5	34.1	-33.0	75.5	-73.0
Ho	M_5	53.5	-51.8	29.5	-28.1	33.7	-32.5	69.5	-68.9
Au	M_5	50.5	-48.6	25.7	-24.2	30.0	-28.8	48.2	-46.9
Bi	M_5	50.0	-48.1	25.3	-23.8	29.7	-28.4	25.9	-20.1

TABLE 20. Summary of $\langle RMS \rangle$ and $\langle R \rangle$ values found in the evaluation of the Gryzinski, Casnati *et al.*, Hombourger, and Jakoby *et al.* formulae for K-shell, L_3 -subshell, and M_5 -subshell ionization cross sections

Shell	Gryzinski		Casnati		Hombourger		Jakoby	
	$\langle RMS \rangle(\%)$	$\langle R \rangle(\%)$						
K	31.1	-26.3	12.1	2.3	11.0	-4.0	21.5	9.3
L_3	37.0	-33.4	10.6	-2.5	12.8	-8.5	53.2	-37.4
M_5	50.4	-47.7	25.2	-20.9	28.8	-25.8	82.0	-64.7

We recommend that ionization cross sections for atoms and molecules be calculated with BEs from the Carlson compilation while similar calculations for solids should be made with BEs from the Williams tabulation. If the desired BEs are not listed in the latter tabulation, BEs from the Carlson compilation can be used (but with a reduction by the average work-function correction of 4 eV). Use can also be made of BEs for atoms, molecules, and solids in the NIST XPS Database. Small differences of BEs from the different sources (e.g., less than ~ 3 eV) will generally have negligible effects on calculated cross sections except for BEs less than about 500 eV and incident energies close to the ionization threshold (e.g. $U < 3$) where the cross sections vary rapidly with energy.

10. References

- S. T. Perkins, D. E. Cullen, M. H. Chen, J. H. Hubbell, J. Rathkopf, and J. Scofield, "Tables and graphs of atomic subshell and relaxation data derived from the LLNL Evaluated Atomic Data Library (EADL), $Z = 1-100$," Technical Report No. UCRL-ID-50400, Lawrence Livermore National Laboratory, Livermore, California, 1991.
- C. J. Powell, "Cross sections for ionization of inner-shell electrons by electrons," *Rev. Mod. Phys.* **48**, 33-47 (1976).
- H. Bethe, "Zur Theorie des Durchgangs schneller Korpuskularstrahlen durch Materie," *Ann. Phys.* **397**, 325-400 (1930).
- C. J. Powell, "Inelastic scattering electrons in solids," in *Electron Beam Interactions with Solids for Microscopy, Microanalysis and Microlithography*, edited by D. F. Kyser, H. Niedrig, D. E. Newbury, and R. Shimizu (Scanning Electron Microscopy, Inc., AMF O'Hare, 1984), pp. 19-31.
- C. J. Powell, "Inner shell ionization cross sections," in *Electron Impact Ionization*, edited by T. D. Märk and G. H. Dunn (Springer-Verlag, New York, 1985), pp. 198-231.
- C. J. Powell, "Cross sections for inelastic electron scattering in solids," *Ultramicroscopy* **28**, 24-31 (1989).
- C. J. Powell, "Inner-shell ionization cross sections," in *Microbeam Analysis*, edited by J. R. Michael and P. Ingram (San Francisco Press, San Francisco, 1990), pp. 13-20.
- D. R. Batchelor, P. Rez, D. J. Fathers, and J. A. Venables, "Auger electron spectroscopy from elemental standards. I: Theoretical calculations," *Surf. Interface Anal.* **13**, 193-201 (1988).
- S. Luo and D. C. Joy, "Calculations of x-ray ionization cross sections at low overvoltage ratios," *Microbeam Analysis - 1991*, edited by D. G. Howitt (San Francisco Press, San Francisco, 1991), pp. 67-68.
- P. Rez, "Accurate cross sections for microanalysis," *J. Res. Natl. Inst. Stand. Technol.* **107**, 487-495 (2002).
- R. Hippler, "Plane wave born calculations of K-shell ionization at low velocities," *Phys. Lett. A* **144**, 81-85 (1990).
- S. P. Khare, V. Saksena, and J. M. Wadehra, "K-shell ionization of atoms by electron and positron impact," *Phys. Rev. A* **48**, 1209-1213 (1993).
- S. P. Khare, P. Sinha, and J. M. Wadehra, " L_3 -shell ionization of xenon and gold by electron and positron impacts," *Phys. Lett. A* **184**, 204-208 (1994).
- J. H. Scofield, "K- and L-shell ionization of atoms by relativistic electrons," *Phys. Rev. A* **18**, 963-970 (1978).
- Y. K. Kim and M. E. Rudd, "Binary-encounter-dipole model for electron-impact ionization," *Phys. Rev. A* **50**, 3954-3967 (1994).
- Y. K. Kim, J. P. Santos, and F. Parente, "Extension of the binary-encounter-dipole model to relativistic incident electrons," *Phys. Rev. A* **62**, 052710 (2000).
- E. J. Williams, "Applications of the method of impact parameter in collisions," *Proc. R. Soc. London, Ser. A* **139**, 163-186 (1933).
- J. D. Jackson, *Classical Electrodynamics*, 3rd ed. (John Wiley and Sons, New York, 1975).
- H. Kolbenstvedt, "Simple theory for K-ionization by relativistic electrons," *J. Appl. Phys.* **38**, 4785-4787 (1967).
- H. Kolbenstvedt, "Asymptotic expression for K-shell ionization cross section with electrons," *J. Appl. Phys.* **46**, 2771-2773 (1975).
- S. M. Seltzer, "Cross sections for bremsstrahlung production and electron impact ionization," in *Monte Carlo Transport of Electrons and Photons*, edited by T. M. Jenkins, W. R. Nelson, and A. Rindi (Plenum, New York, 1988), p. 81.
- R. Mayol and F. Salvat, "Cross sections for K-shell ionisation by electron impact," *J. Phys. B* **23**, 2117-2130 (1990).
- M. S. Pindzola, D. L. Moores, and D. C. Griffin, "Electron-impact ionization of highly charged ions in lowest-order QED theory," *Phys. Rev. A* **40**, 4941-4946 (1989).
- S. Keller, C. T. Whelan, H. Ast, H. R. J. Walters, and R. M. Dreizler, "Relativistic distorted-wave born calculations for $(e,2e)$ processes on inner shells of heavy atoms," *Phys. Rev. A* **50**, 3865-3877 (1994).
- C. J. Fontes, D. H. Sampson, and H. L. Zhang, "Inclusion of the generalized Breit interaction in excitation of highly charged ions by electron impact," *Phys. Rev. A* **47**, 1009-1022 (1993).

- ²⁶D. H. Sampson, "Branching ratios for excitation to highly excited levels or ionization of complex ions," *Phys. Rev. A* **34**, 986–1006 (1986).
- ²⁷H. L. Zhang, D. H. Sampson, and A. K. Mohanty, "Fully relativistic and quasirelativistic distorted-wave methods for calculating collision strengths for highly charged ions," *Phys. Rev. A* **40**, 616–632 (1989).
- ²⁸S. Segui, M. Dingfelder, and F. Salvat, "Distorted-wave calculation of cross sections for inner-shell ionization by electron and positron impact," *Phys. Rev. A* **67**, 062710 (2003).
- ²⁹J. Colgan, C. J. Fontes, and H. L. Zhang, "Inner-shell electron-impact ionization of neutral atoms," *Phys. Rev. A* **73**, 062711 (2006).
- ³⁰D. Bote and F. Salvat, "Calculations of inner-shell ionization by electron impact with the distorted-wave and plane-wave Born approximations," *Phys. Rev. A* **77**, 042701 (2008).
- ³¹D. Bote, F. Salvat, A. Jablonski, and C. J. Powell, "Cross sections for ionization of K, L and M shells of atoms by impact of electrons and positrons with energies up to 1 GeV: Analytical formulas," *At. Data Nucl. Data Tables* **95**, 871–909 (2009).
- ³²D. Bote, F. Salvat, A. Jablonski, and C. J. Powell, "Erratum. Cross sections for ionization of K, L and M shells of atoms by impact of electrons and positrons with energies up to 1 GeV: Analytical formulas," *At. Data Nucl. Data Tables* **97**, 186 (2011).
- ³³J. J. Thomson, "XLII. Ionization by moving electrified particles," *Philos. Mag. Series 6* **23**, 449–457 (1912).
- ³⁴M. R. H. Rudge, "Theory of the ionization of atoms by electron impact," *Rev. Mod. Phys.* **40**, 564–590 (1968).
- ³⁵M. Gryzinski, "Classical theory of electronic and ionic inelastic collisions," *Phys. Rev.* **115**, 374–383 (1959).
- ³⁶R. C. Stabler, "Classical impulse approximation for inelastic electron-atom collisions," *Phys. Rev.* **133**, A1268–A1273 (1964).
- ³⁷L. Vriens, "Binary-encounter electron-atom collision theory," *Phys. Rev.* **141**, 88–92 (1966).
- ³⁸M. Gryzinski, "Two-particle collisions. I. General relations for collisions in the laboratory system," *Phys. Rev.* **138**, A305–A321 (1965).
- ³⁹M. Gryzinski, "Two-particle collisions. II. Coulomb collisions in the laboratory system of coordinates," *Phys. Rev.* **138**, A322–A335 (1965).
- ⁴⁰M. Gryzinski, "Classical theory of atomic collisions. I. Theory of inelastic collisions," *Phys. Rev.* **138**, A336–A358 (1965).
- ⁴¹N. F. Mott, "The collision between two electrons," *Proc. R. Soc. London, Ser. A* **126**, 259–267 (1930).
- ⁴²L. Vriens, "Electron exchange in binary encounter collision theory," *Proc. Phys. Soc.* **89**, 13–21 (1966).
- ⁴³C. Möller, "Zur Theorie des Durchgangs schneller Elektronen durch Materie," *Ann. Phys.* **14**, 531–585 (1932).
- ⁴⁴M. Guerra, F. Parente, P. Indelicato, and J. P. Santos, "Modified binary encounter Bethe model for electron-impact ionization," *Int. J. Mass Spectrom.* **313**, 1–7 (2012).
- ⁴⁵H. A. Bethe and R. Jackiw, *Intermediate Quantum Mechanics* (Westview, Boulder, CO, 1997).
- ⁴⁶M. C. Walske, "Stopping power of L-electrons," *Phys. Rev.* **101**, 940–944 (1956).
- ⁴⁷G. S. Khandelwal and E. Merzbacher, "Stopping power of M electrons," *Phys. Rev.* **144**, 349–352 (1966).
- ⁴⁸R. F. Egerton, "Electron energy-loss spectroscopy in the TEM," *Rep. Prog. Phys.* **72**, 016502 (2009).
- ⁴⁹J. F. Ziegler, "The stopping of energetic light ions in elemental matter," *J. Appl. Phys.* **85**, 1249–1272 (1999).
- ⁵⁰E. J. McGuire, "Inelastic scattering of electrons and protons by the elements He to Na," *Phys. Rev. A* **3**, 267–279 (1971).
- ⁵¹E. J. McGuire, "Electron ionization cross sections in the Born approximation," *Phys. Rev. A* **16**, 62–72 (1977).
- ⁵²S. T. Manson, "Inelastic collisions of fast charged particles with atoms: ionization of the aluminum L shell," *Phys. Rev. A* **6**, 1013–1024 (1972).
- ⁵³P. Rez, "Electron ionization cross sections for atomic subshells," *Microsc. Microanal.* **9**, 42–53 (2003).
- ⁵⁴D. H. Madison and E. Merzbacher, "Theory of charged-particle interactions," in *Atomic Inner-Shell Ionization*, Ionization and Transition Probabilities, Vol. 1, edited by B. Crasemann (Academic, New York, 1975), pp. 1–70.
- ⁵⁵V. I. Ochkur, "Ionization of the hydrogen atom by electron impact with allowance for the exchange," *Sov. Phys. JETP* **20**, 1175–1178 (1965).
- ⁵⁶H. Bethe, "Bremsformel für Elektronen relativistischer Geschwindigkeit," *Z. Phys.* **76**, 293–299 (1932).
- ⁵⁷A. Prideaux, D. H. Madison, and K. Bartschat, "Exchange distortion and postcollision interaction for intermediate-energy electron-impact ionization of argon," *Phys. Rev. A* **72**, 032702 (2005).
- ⁵⁸M. E. Rose, *Relativistic Electron Theory* (John Wiley and Sons, New York, 1961).
- ⁵⁹F. Salvat, J. M. Fernández-Varea, and W. Williamson, "Accurate numerical solution of the radial Schrödinger and Dirac wave equations," *Comput. Phys. Commun.* **90**, 151–168 (1995).
- ⁶⁰I. P. Grant, "Relativistic calculations of atomic structures," *Adv. Phys.* **19**, 747–811 (1970).
- ⁶¹R. Latter, "Atomic energy levels for the Thomas–Fermi and Thomas–Fermi–Dirac potential," *Phys. Rev.* **99**, 510–519 (1955).
- ⁶²D. A. Liberman, D. T. Cromer, and J. T. Waber, "Self-consistent-field Dirac wave functions for atoms and ions. I. Comparison with previous calculations," *Phys. Rev.* **137**, A27–A34 (1965).
- ⁶³D. Liberman, D. T. Cromer, and J. T. Waber, "Relativistic self-consistent field program for atoms and ions," *Comput. Phys. Commun.* **2**, 107–113 (1971).
- ⁶⁴T. A. Carlson, *Photoelectron and Auger Spectroscopy* (Plenum, New York, 1975).
- ⁶⁵F. Salvat and J. M. Fernández-Varea, "Overview of physical interaction models for photon and electron transport used in Monte Carlo codes," *Metrologia* **46**, S112–S138 (2009).
- ⁶⁶U. Fano, "Penetration of protons, alpha particles and mesons," *Ann. Rev. Nucl. Sci.* **13**, 1–66 (1963).
- ⁶⁷E. U. Condon, "The theory of complex spectra," *Phys. Rev.* **36**, 1121–1133 (1930).
- ⁶⁸I. P. Grant, "Relativistic self-consistent fields," *Proc. R. Soc. London, Ser. A* **262**, 555–576 (1961).
- ⁶⁹M. Inokuti, "Inelastic collisions of fast charged particles with atoms and molecules—The Bethe theory revisited," *Rev. Mod. Phys.* **43**, 297–347 (1971).
- ⁷⁰J. M. Fernández-Varea, F. Salvat, M. Dingfelder, and D. Liljequist, "A relativistic optical-data model for inelastic scattering of electrons and positrons in condensed matter," *Nucl. Instrum. Methods Phys. Res. B* **229**, 187–218 (2005).
- ⁷¹L. M. Middleman, R. L. Ford, and R. Hofstadter, "Measurement of cross sections for x-ray production by high-energy electrons," *Phys. Rev. A* **2**, 1429–1443 (1970).
- ⁷²U. Fano, "Ionizing collisions of very fast particles and the dipole strength of optical transitions," *Phys. Rev.* **95**, 1198–1200 (1954).
- ⁷³A. R. Edmonds, *Angular Momentum in Quantum Mechanics* (Princeton University Press, Princeton, NJ, 1957).
- ⁷⁴B. L. Henke, E. M. Gullikson, and J. C. Davis, "X-ray interactions: photoabsorption, scattering, transmission, and reflection at $E = 50$ –30 000 eV, $Z = 1$ –92," *At. Data Nucl. Data Tables* **54**, 181–342 (1993).
- ⁷⁵F. J. de Heer and M. Inokuti, "Total ionization cross sections," *Electron Impact Ionization*, edited by T. D. Märk and G. H. Dunn (Springer-Verlag, New York, 1985), pp. 232–276.
- ⁷⁶S. P. Khare and S. Prakash, "Electron-impact K-shell ionization of atoms," *Phys. Rev. A* **39**, 6591–6593 (1989).
- ⁷⁷F. M. de la Ripelle, "Étude sur les coefficients spécifiques d'ionisation," *J. Phys. Radium* **10**, 319–329 (1949).
- ⁷⁸C. R. Worthington and S. G. Tomlin, "The intensity of emission of characteristic x-radiation," *Proc. Phys. Soc.* **69**, 401–412 (1956).
- ⁷⁹L. H. Fong and S. G. Tomlin, "Absolute intensities of some L and M characteristic x-rays from solid targets," *Aust. J. Phys.* **23**, 17–21 (1970).
- ⁸⁰M. Green and V. E. Cosslett, "The efficiency of production of characteristic x-radiation in thick targets of a pure element," *Proc. Phys. Soc.* **78**, 1206–124 (1961).
- ⁸¹H. W. Drawin, "Zur formelmässigen Darstellung der Ionisierungsquerschnitte gegenüber Elektronenstoss," *Z. Phys.* **164**, 513–521 (1961).
- ⁸²G. A. Hutchins, "Electron probe microanalysis," *Characterization of Solid Surfaces*, edited by P. F. Kane and G. R. Larrabee (Plenum, New York, 1974), pp. 441–484.
- ⁸³W. Lotz, "Electron-impact ionization cross sections for atoms up to $Z = 108$," *Z. Phys.* **232**, 101–107 (1970).
- ⁸⁴M. R. H. Rudge and S. B. Schwartz, "The ionization of hydrogen and of hydrogenic positive ions by electron impact," *Proc. Phys. Soc.* **88**, 563–578 (1966).

- ⁸⁵M. A. Uddin, A. K. F. Haque, K. R. Karim, A. K. Basak, and F. B. Malik, "Modified Kolbenedt model for the electron impact K-shell ionization cross-sections of atoms and ions," *Eur. Phys. J. D* **37**, 361–369 (2006).
- ⁸⁶A. K. F. Haque, M. Shahjahan, M. A. Uddin, M. A. R. Patoary, A. K. Basak, B. C. Saha, and F. B. Malik, "Generalized Kolbenedt model for electron impact ionization of the K-, L- and M-shell ions," *Phys. Scr.* **81**, 045301 (2010).
- ⁸⁷B. Gstir, H. Deutsch, K. Becker, and T. D. Märk, "Calculated cross sections for the K-shell ionization of chromium, nickel, copper, scandium and vanadium using the DM formalism," *J. Phys. B* **34**, 3377–3382 (2001).
- ⁸⁸H. Deutsch, P. Scheier, K. Becker, and T. D. Märk, "Revised high energy behavior of the Deutsch-Märk (DM) formula for the calculation of electron impact ionization cross sections of atoms," *Int. J. Mass Spectrom.* **233**, 13–17 (2004).
- ⁸⁹A. K. F. Haque, M. S. I. Sarker, M. A. R. Patoary, M. Shahjahan, M. I. Hossain, M. A. Uddin, A. K. Basak, and B. C. Saha, "Modified version of revised Deutsch-Märk model for electron impact K-shell ionization cross-sections of atoms at relativistic energies," *Int. J. Quantum Chem.* **109**, 1442–1450 (2009).
- ⁹⁰C. J. Powell, "Evaluation of formulas for inner-shell ionization cross sections," in *Use of Monte Carlo Calculations in Electron Probe Microanalysis and Scanning Electron Microscopy*, NBS Special Publication 460, edited by K. F. J. Heinrich, D. E. Newbury, and H. Yakowitz (U.S. Department of Commerce, National Bureau of Standards, Gaithersburg, 1976), pp. 98–104.
- ⁹¹E. Casnati, A. Tartari, and C. Baraldi, "An empirical approach to K-shell ionisation cross section by electrons," *J. Phys. B* **15**, 155–167 (1982).
- ⁹²E. Casnati, A. Tartari, and C. Baraldi, "Corrigenda. An empirical approach to K-shell ionisation cross section by electrons," *J. Phys. B* **16**, 505 (1983).
- ⁹³M. P. Seah and I. S. Gilmore, "Quantitative AES VII. The ionization cross-section in AES," *Surf. Interface Anal.* **26**, 815–824 (1998).
- ⁹⁴A. Jablonski, F. Salvat, and C. J. Powell, "Practical formulas for inner-shell ionization cross sections by electron impact: Applications in quantitative Auger electron spectroscopy," *J. Appl. Phys.* **106**, 053706 (2009).
- ⁹⁵C. Jakoby, H. Genz, and A. Richter, "A semi-empirical formula for the total K-shell ionization cross-section by electron-impact," *J. Phys. (Paris) Colloq.* **48**, C9-487–C9-490 (1987).
- ⁹⁶C. Hombourger, "An empirical expression for K-shell ionization cross section by electron impact," *J. Phys. B* **31**, 3693–3702 (1998).
- ⁹⁷C. S. Campos, M. A. Z. Vasconcellos, J. C. Trincavelli, and S. Segui, "Analytical expression for K- and L-shell cross sections of neutral atoms near ionization threshold by electron impact," *J. Phys. B* **40**, 3835–3841 (2007).
- ⁹⁸J. H. Scofield, "Theoretical photoionization cross sections from 1 to 1500 keV," Technical Report No. UCRL-51326, Lawrence Livermore Laboratory, Livermore, California, 1973.
- ⁹⁹R. Jenkins, R. Manne, R. Robin, and C. Senemaud, "Nomenclature system for x-ray spectroscopy," *Pure Appl. Chem.* **63**, 735–746 (1991).
- ¹⁰⁰W. Bambynek, B. Crasemann, R. W. Fink, H. U. Freund, H. Mark, C. D. Swift, R. E. Price, and P. Venugopala Rao, "X-ray fluorescence yields, Auger yields and Coster-Kronig transition probabilities," *Rev. Mod. Phys.* **44**, 716–813 (1972).
- ¹⁰¹W. Bambynek, B. Crasemann, R. W. Fink, H. U. Freund, H. Mark, C. D. Swift, R. E. Price, and P. Venugopala Rao, "Erratum: X-ray fluorescence yields, Auger yields and Coster-Kronig transition probabilities," *Rev. Mod. Phys.* **46**, 853 (1974).
- ¹⁰²M. O. Krause, "Atomic radiative and radiationless yields for K and L shells," *J. Phys. Chem. Ref. Data* **8**, 307–327 (1979).
- ¹⁰³J. H. Hubbell, P. N. Trehan, N. Singh, B. Chand, D. Mehta, M. L. Garg, R. R. Garg, S. Singh, and S. Puri, "A review, bibliography, and tabulation of K, L, and higher atomic shell x-ray fluorescence yields," *J. Phys. Chem. Ref. Data* **23**, 339–364 (1994).
- ¹⁰⁴J. H. Hubbell, P. N. Trehan, N. Singh, B. Chand, D. Mehta, M. L. Garg, R. R. Garg, S. Singh, and S. Puri, "A review, bibliography, and tabulation of K, L, and higher atomic shell x-ray fluorescence yields," *J. Phys. Chem. Ref. Data* **33**, 621 (2004).
- ¹⁰⁵M. O. Krause, T. A. Carlson, and R. D. Dismukes, "Double electron ejection in the photoabsorption process," *Phys. Rev.* **170**, 37–47 (1968).
- ¹⁰⁶J. H. Scofield, "Radiative decay rates of vacancies in the K and L shells," *Phys. Rev.* **179**, 9–16 (1969).
- ¹⁰⁷J. H. Scofield, "Exchange corrections of K x-ray emission rates," *Phys. Rev. A* **9**, 1041–1049 (1974).
- ¹⁰⁸J. H. Scofield, "Relativistic Hartree-Slater values for K and L X-ray emission rates," *At. Data Nucl. Data Tables* **14**, 121–137 (1974).
- ¹⁰⁹J. C. Clark, "A measurement of the absolute probability of K-electron ionization of silver by cathode rays," *Phys. Rev.* **48**, 30–42 (1935).
- ¹¹⁰A. E. Smick and P. Kirkpatrick, "Absolute K-ionization cross section of the nickel atom under electron bombardment at 70 kV," *Phys. Rev.* **67**, 153–161 (1945).
- ¹¹¹L. T. Pockman, D. L. Webster, P. Kirkpatrick, and K. Harworth, "The probability of K ionization of nickel by electrons as a function of their energy," *Phys. Rev.* **71**, 330–338 (1947).
- ¹¹²H. Hansen, H. Weigmann, and A. Flammersfeld, "Messung des Wirkungsquerschnitts für K-Ionisierung durch Stoss niederenergetischer Negatonen und Positonen," *Nucl. Phys.* **58**, 241–253 (1964).
- ¹¹³H. Hansen and A. Flammersfeld, "Messung des Wirkungsquerschnitts für K-ionisierung durch stoss niederenergetischer Negatonen und Positonen," *Nucl. Phys.* **79**, 135–144 (1966).
- ¹¹⁴J. W. Motz and R. C. Placious, "K-ionization cross sections for relativistic electrons," *Phys. Rev.* **136**, A662–A665 (1964).
- ¹¹⁵D. H. Rester and W. E. Dance, "K-Shell ionization of Ag, Sn, and Au from electron bombardment," *Phys. Rev.* **152**, 1–3 (1966).
- ¹¹⁶B. Fischer and K. W. Hoffmann, "Die intensität der Bremsstrahlung und der charakteristischen K-Röntgenstrahlung dünner anoden," *Z. Phys.* **204**, 122–128 (1967).
- ¹¹⁷W. Hink and A. Ziegler, "Der Wirkungsquerschnitt für die Ionisierung der K-Schale von Aluminium durch Elektronenstoss," *Z. Phys.* **226**, 222–234 (1969).
- ¹¹⁸M. Green, "The angular distribution of characteristic x radiation and its origin within a solid target," *Proc. Phys. Soc.* **83**, 435–451 (1964).
- ¹¹⁹M. Green and V. E. Cosslett, "Measurements of K, L and M shell x-ray production efficiencies," *J. Phys. D: Appl. Phys.* **1**, 425–436 (1968).
- ¹²⁰K. H. Berkner, S. N. Kaplan, and R. V. Pyle, "Cross sections for K-shell ionization of Pd and Au by 2.5 and 7.1 MeV electrons," *Bull. Am. Phys. Soc.* **15**, 786 (1970).
- ¹²¹W. Hink and H. Paskche, "Der Wirkungsquerschnitt für die Ionisierung der K-Schale von Kohlenstoff durch Elektronenstoss (2–30 keV)," *Z. Phys.* **244**, 140–148 (1971).
- ¹²²S. I. Salem and L. D. Moreland, "L_{II} and L_{III} ionization cross sections in gold at very low energies," *Phys. Lett.* **37A**, 161–162 (1971).
- ¹²³D. V. Davis, V. D. Mistry, and C. A. Quarles, "Inner shell ionization of copper, silver and gold by electron bombardment," *Phys. Lett.* **38A**, 169–170 (1972).
- ¹²⁴H. Hubner, K. Ilgen, and K. W. Hoffmann, "Messung des Wirkungsquerschnitts für Ionisierung in der K-Schale durch Elektronenstoss," *Z. Phys.* **255**, 269–280 (1972).
- ¹²⁵W. Scholz, A. Li-Scholz, R. Collé, and I. L. Preiss, "K-Shell ionization cross sections for 2.04-MeV electrons," *Phys. Rev. Lett.* **29**, 761–764 (1972).
- ¹²⁶D. Berényi, S. A. H. Seif el Nasr, and G. Bibok, "Inner shell ionization cross sections for relativistic electrons," *Z. Phys.* **267**, 169–174 (1974).
- ¹²⁷A. Langenberg, F. J. de Heer, and J. van Eck, "Ar L-shell ionization by electrons and light ions: determination of x-ray emission cross sections and mean fluorescence yields for charge-state distributions," *J. Phys. B* **8**, 2079–2108 (1975).
- ¹²⁸J. Jessenberger and W. Hink, "Absolute electron impact K-ionization cross sections of titanium and nickel (<50 keV)," *Z. Phys. A* **275**, 331–337 (1975).
- ¹²⁹Y. K. Park, M. T. Smith, and W. Scholz, "Cross sections for L x-ray production and L-subshell ionization by MeV electrons," *Phys. Rev. A* **12**, 1358–1364 (1975).
- ¹³⁰B. Schlenk, D. Berenyi, S. Ricz, A. Valek, and G. Hock, "Inner-shell ionization by electrons in 300–600 keV region," *Acta Phys. Hung.* **41**, 159–163 (1976).
- ¹³¹K. Ishii, M. Kamiya, K. Sera, S. Morita, H. Tawara, M. Oyamada, and T. C. Chu, "Inner-shell ionization by ultrarelativistic electrons," *Phys. Rev. A* **15**, 906–913 (1977).
- ¹³²S. Ricz, B. Schlenk, D. Berenyi, A. Valek, G. Hock, and S. A. H. Seif el Nasr, "L x-ray production cross section for Sm, Ho, Er and Bi at several hundred keV electron impact," *J. Phys. B* **11**, 4283–4286 (1978).
- ¹³³D. Berenyi, G. Hock, S. Ricz, B. Schlenk, A. Valek, and G. Hock, "K α /K β x-ray intensity ratios and K-shell ionisation cross sections for bombardment by electrons of 300–600 keV," *J. Phys. B* **11**, 709–713 (1978).

- ¹³⁴D. H. H. Hoffmann, C. Brendel, H. Genz, W. Löw, S. Müller, and A. Richter, "Inner-shell ionization by relativistic electron impact," *Z. Phys. A* **293**, 187–201 (1979).
- ¹³⁵J. J. Bonnet, D. Hubert, F. Bonnet, M. Bonnefoy, A. Fleury, and L. Avan, "Relative line intensities in the argon L x-ray emission spectra produced by 0.3 to 3 keV electron impact," *Phys. Lett.* **70A**, 99–102 (1979).
- ¹³⁶M. Kamiya, A. Kuwako, K. Ishii, S. Morita, and M. Oyamada, "Density effect in K-shell ionization by ultrarelativistic electrons," *Phys. Rev. A* **22**, 413–420 (1980).
- ¹³⁷K. Shima, "Mn and Cu K-shell ionization cross sections by slow electron impact," *Phys. Lett.* **77A**, 237–239 (1980).
- ¹³⁸J. Pálincás and B. Schlenk, "L-Subshell ionization cross sections for Au, Pb, and Bi by 60–600 keV electron impact," *Z. Phys. A* **297**, 29–33 (1980).
- ¹³⁹K. Kiss, G. Kalman, J. Pálincás, and B. Schlenk, "Investigation of inner-shell ionization by electron-impact in the 60–600 keV energy region," *Acta Phys. Hung.* **50**, 97–102 (1981).
- ¹⁴⁰K. Shima, T. Nakagawa, K. Umetani, and T. Mikumo, "Threshold behavior of Cu-, Ge-, Ag-K-, and Au-L₃-shell ionization cross sections by electron impact," *Phys. Rev. A* **24**, 72–78 (1981).
- ¹⁴¹H. Genz, C. Brendel, P. Eschwey, U. Kuhn, W. Löw, A. Richter, P. Seserko, and R. Sauerwein, "Search for the density effect in inner-shell ionization by ultra relativistic electron impact," *Z. Phys. A* **305**, 9–19 (1982).
- ¹⁴²S. Reusch, H. Genz, W. Löw, and A. Richter, "A method to determine L-subshell ionization cross sections for medium and heavy elements," *Z. Phys. D* **3**, 379–389 (1986).
- ¹⁴³G. L. Westbrook and C. A. Quarles, "Total cross sections for ionization of the K-shell by electron bombardment," *Nucl. Instrum. Methods Phys. Res. B* **24/25**, 196–198 (1987).
- ¹⁴⁴S. C. McDonald and B. M. Spicer, "Density effect in K-shell ionization by relativistic electron impact," *Phys. Rev. A* **37**, 985–987 (1988).
- ¹⁴⁵V. P. Shevelko, A. M. Solomon, and V. S. Vukstich, "K-shell ionization of free metal atoms K, Ca, Rb, and Sr by electron impact," *Phys. Scr.* **43**, 158–161 (1991).
- ¹⁴⁶R. K. Singh and R. Shanker, "The emission of characteristic and non-characteristic x-rays from collisions of 10–22 keV electrons with argon," *J. Phys. B* **36**, 3031–3042 (2003).
- ¹⁴⁷H. Schneider, H. Tobehn, F. Ebel, and R. Hippler, "Absolute cross sections for inner shell ionization by lepton impact," *Phys. Rev. Lett.* **71**, 2707–2709 (1993).
- ¹⁴⁸Z. M. Luo, Z. An, F. Q. He, T. H. Li, X. G. Long, and X. F. Peng, "Correction of the influence of the substrate upon the measurement of K-shell ionization cross sections," *J. Phys. B* **29**, 4001–4005 (1996).
- ¹⁴⁹Z. M. Luo, Z. An, T. H. Li, L. M. Wang, Q. Zhu, and X. Y. Xia, "Measurement of K-shell ionization cross sections of Fe and Mn by electron impact," *J. Phys. B* **30**, 2681–2686 (1997).
- ¹⁵⁰F. Q. He, X. G. Long, X. F. Peng, Z. M. Luo, and Z. An, "K-shell ionization of iron by electron bombardment," *Acta Phys. Sin.* **5**, 499–504 (1996).
- ¹⁵¹F. Q. He, X. G. Long, X. F. Peng, Z. M. Luo, and Z. An, "K-shell ionization of molybdenum by electron bombardment," *Nucl. Instrum. Methods Phys. Res. B* **114**, 213–216 (1996).
- ¹⁵²F. Q. He, X. F. Peng, X. G. Long, Z. M. Luo, and Z. An, "K-shell ionization cross sections by electron bombardment at low energies," *Nucl. Instrum. Methods Phys. Res. B* **129**, 445–450 (1997).
- ¹⁵³Z. An, T. H. Li, L. M. Wang, X. Y. Xia, and Z. M. Luo, "Correction of substrate effect in the measurement of 25-keV electron-impact K-shell ionization cross sections of Cu and Co elements," *Phys. Rev. A* **54**, 3067–3069 (1996).
- ¹⁵⁴X. F. Peng, F. Q. He, X. G. Long, Z. M. Luo, and Z. An, "Cross sections for K-shell ionization of niobium by electron impact," *Phys. Rev. A* **58**, 2034–2036 (1998).
- ¹⁵⁵C. H. Tang, Z. M. Luo, Z. An, and T. H. Li, "Measurement of zinc K-shell ionization cross sections by electron impact," *Chin. Phys. Lett.* **16**, 505–507 (1999).
- ¹⁵⁶C. H. Tang, Z. An, T. H. Li, and Z. M. Luo, "Measurement of zinc and manganese K-shell ionization cross-sections by electron impact," *Nucl. Instrum. Methods Phys. Res. B* **155**, 1–5 (1999).
- ¹⁵⁷M. Liu, Z. An, C. Tang, Z. Liu, X. Peng, and X. Long, "Experimental electron-impact K-shell ionization cross sections," *At. Data Nucl. Data Tables* **76**, 213–234 (2000).
- ¹⁵⁸Z. An, C. H. Tang, C. G. Zhou, and Z. M. Luo, "Measurement of scandium and vanadium K-shell ionization cross sections by electron impact," *J. Phys. B* **33**, 3677–3684 (2000).
- ¹⁵⁹Z. An, C. H. Tang, and Z. M. Luo, "Measurement of K-shell ionization cross sections of Cr, Ni and Cu atoms by 7.5–25 keV electron impact," *Chin. Phys. Lett.* **18**, 1460–1462 (2001).
- ¹⁶⁰Z. An, M. T. Liu, Y. C. Fu, Z. M. Luo, C. H. Tang, C. M. Li, B. H. Zhang, and Y. J. Tang, "Some recent progress on the measurement of K-shell ionization cross-sections of atoms by electron impact: Application to Ti and Cr elements," *Nucl. Instrum. Methods Phys. Res. B* **207**, 268–274 (2003).
- ¹⁶¹C. S. Campos, M. A. Z. Vasconcellos, X. Llovet, and F. Salvat, "Measurements of L-shell x-ray production cross sections of W, Pt, and Au by 10–30-keV electrons," *Phys. Rev. A* **66**, 012719 (2002).
- ¹⁶²C. J. Gou, Z. W. Wu, D. L. Yang, F. Q. He, X. F. Peng, Z. An, and Z. M. Luo, "L-shell ionization cross section measurements of dysprosium and samarium by low-energy electron impact," *Chin. Phys. Lett.* **22**, 2244–2247 (2005).
- ¹⁶³S. P. Limandri, M. A. Z. Vasconcellos, R. Hinrichs, and J. Trincavelli, "Experimental determination of cross sections for K-shell ionization by electron impact for C, O, Al, Si, and Ti," *Phys. Rev. A* **86**, 042701 (2012).
- ¹⁶⁴X. Llovet, C. Merlet, and F. Salvat, "Measurements of K-shell ionization cross sections of Cr, Ni and Cu by impact of 6.5–40 keV electrons," *J. Phys. B* **33**, 3761–3772 (2000).
- ¹⁶⁵X. Llovet, C. Merlet, and F. Salvat, "Measurements of absolute cross sections for K-shell ionization of Fe and Mn by electron impact," *J. Phys. B* **35**, 973–982 (2002).
- ¹⁶⁶Z. Luo, C. Tang, Z. An, F. He, X. Peng, and X. Long, "Selenium and yttrium K-shell ionization cross-sections by electron impact," *Phys. Rev. A* **63**, 034702 (2001).
- ¹⁶⁷Z. M. Luo, Y. C. Fu, Z. An, X. F. Peng, F. Q. He, and X. G. Long, "Ionization of hafnium L-shell by electron impact," *Chin. Phys. Lett.* **19**, 1610–1612 (2002).
- ¹⁶⁸C. Merlet, X. Llovet, and F. Salvat, "Measurements of absolute K-shell ionization cross sections and L-shell x-ray production cross sections of Ge by electron impact," *Phys. Rev. A* **69**, 032708 (2004).
- ¹⁶⁹C. Merlet, X. Llovet, and J. M. Fernández-Varea, "Absolute K-shell ionization cross sections and L α and L β_1 x-ray production cross sections of Ga and As by 1.5–39-keV electrons," *Phys. Rev. A* **73**, 062719 (2006).
- ¹⁷⁰C. Merlet, X. Llovet, and J. M. Fernández-Varea, "Erratum: Absolute K-shell ionization cross sections and L α and L β_1 x-ray production cross sections of Ga and As by 1.5–39-keV electrons [Phys. Rev. A **73**, 062719 (2006)]," *Phys. Rev. A* **74**, 049901 (2006).
- ¹⁷¹C. Merlet, X. Llovet, and F. Salvat, "Near-threshold absolute M-shell x-ray production cross sections of Au and Bi by electron impact," *Phys. Rev. A* **78**, 022704 (2008).
- ¹⁷²X. F. Peng, F. Q. He, X. G. Long, Z. An, and Z. M. Luo, "L-shell ionization study of tungsten by electron impact," *Chin. Phys. Lett.* **18**, 39–41 (2001).
- ¹⁷³X. F. Peng, F. Q. He, X. G. Long, Z. An, and Z. M. Luo, "Measurement of L-shell ionization cross sections for niobium by electron impact," *Chin. Phys. Lett.* **10**, 31–34 (2001).
- ¹⁷⁴C. H. Tang, Z. M. Luo, Z. An, F. Q. He, X. F. Peng, and X. G. Long, "L-shell ionization study of indium, tin, and rhenium by low-energy electron impact," *Phys. Rev. A* **65**, 052707 (2002).
- ¹⁷⁵C. Zhou, Z. Luo, C. Tang, and Z. An, "Measurement and analysis of K-shell x-ray production cross sections of V, Cr, Mn, Fe, Co, Ni, Cu and Zn elements by electron impact," *Radiat. Phys. Chem.* **61**, 585–587 (2001).
- ¹⁷⁶C. G. Zhou, Y. C. Fu, Z. An, C. H. Tang, and Z. M. Luo, "Measurement and multiple scattering correction of K-shell ionization cross sections of silver by electron impact," *Chin. Phys. Lett.* **18**, 531–532 (2001).
- ¹⁷⁷C. G. Zhou, Z. An, and Z. M. Luo, "Measurement and correction of K-shell ionization cross sections for copper and gallium by electron impact," *Chin. Phys. Lett.* **18**, 759–760 (2001).
- ¹⁷⁸Z. W. Wu, D. L. Yang, X. B. Luo, F. Q. He, X. F. Peng, and Z. M. Luo, "L-shell x-ray production cross sections of Au and Ir atoms by electron impact near the threshold region," *Chin. Phys. Lett.* **20**, 1485–1487 (2003).
- ¹⁷⁹Y. Wu, Z. An, M. T. Liu, Y. M. Duan, C. H. Tang, and Z. M. Luo, "Measurements of L-shell x-ray production cross-sections of Au and Ag by low energy electron impact," *J. Phys. B* **37**, 4527–4537 (2004).
- ¹⁸⁰Z. W. Wu, C. J. Gou, D. L. Yang, Z. An, X. F. Peng, F. Q. He, and Z. M. Luo, "L-shell x-ray production cross sections of Ta and Tm by electron impact near the threshold region," *Chin. Phys. Lett.* **22**, 2538–2541 (2005).

- ¹⁸¹Z. An, Y. Wu, M. T. Liu, Y. M. Duan, and C. H. Tang, "Thick-target method in the measurement of inner-shell ionization cross-sections by low-energy electron impact," *Nucl. Instrum. Methods Phys. Res. B* **246**, 281–287 (2006).
- ¹⁸²Z. Wu, C. Gou, D. Yang, X. Peng, F. He, and Z. Luo, "The L-shell ionization of Ho and Os induced by electron impact," *Chin. Sci. Bull.* **51**, 1929–1933 (2006).
- ¹⁸³Y. Wu, Z. An, Y. M. Duan, M. T. Liu, and C. H. Tang, "Measurements of $L\alpha$, $L\beta$ x-ray production cross sections of Pb by 16–40 keV electron impact," *J. Phys. B* **40**, 735–742 (2007).
- ¹⁸⁴Y. Wu, Z. An, Y. M. Duan, and M. T. Liu, "Measurements of K-shell ionization cross-sections of S, Ca and Zn by 7–30 keV electron impact," *Nucl. Instrum. Methods Phys. Res. B* **268**, 2820–2824 (2010).
- ¹⁸⁵Y. Wu, Z. An, Y. M. Duan, and M. T. Liu, "Measurements of L-shell x-ray production cross-sections of Gd and W by low energy electron impact," *J. Phys. B* **43**, 135206 (2010).
- ¹⁸⁶Y. Wu, Z. An, Y. M. Duan, and M. T. Liu, "Measurements of $L\alpha$, $L\beta$ x-ray production cross sections of Bi by 17–40 keV electron impact," *Nucl. Instrum. Methods Phys. Res. B* **268**, 2473–2476 (2010).
- ¹⁸⁷Y. Wu, Z. An, Y. M. Duan, M. T. Liu, and J. Wu, "K-shell ionization cross sections of Cl and $L\alpha$, $L\beta$ X-ray production cross sections of Ba by 630-keV electron impact," *Nucl. Instrum. Methods Phys. Res. B* **269**, 117–121 (2011).
- ¹⁸⁸Y. Wu, Z. An, Y. M. Duan, M. T. Liu, and X. P. Ouyang, "K-shell ionization cross sections of K and $L\alpha$ X-ray production cross sections of I by 10–30 keV electron impact," *Can. J. Phys.* **90**, 125–130 (2012).
- ¹⁸⁹D. L. Yang, X. B. Luo, Y. C. Fu, F. Q. He, X. G. Long, X. F. Peng, and Z. M. Luo, "Ionization for Hf- and W L-shell by electron impact," *Chin. Phys.* **13**, 670–676 (2004).
- ¹⁹⁰S. Ricz, B. Schlenk, D. Berenyi, G. Hock, and A. Valek, "K-shell ionization cross sections of Pd, Ag, In and Sn for relativistic electrons," *Acta Phys. Hung.* **42**, 269–271 (1977).
- ¹⁹¹X. Llovet, C. Merlet, J. M. Fernández-Varea, and F. Salvat, "Relative Cross Sections for L- and M-Shell Ionization by Electron Impact," *Mikrochim. Acta* **132**, 163–171 (2000).
- ¹⁹²F. Salvat, J. M. Fernández-Varea, and J. Sempau, "PENELOPÉ-2011: A code System for Monte Carlo Simulation of Electron and Photon Transport," OECD/NEA Data Bank, Issy-les-Moulineaux, France, 2011. Available in PDF format from <http://www.nea.fr/lists/penelope.html>.
- ¹⁹³H. Berndt and H. J. Hunger, "Experimental determination of the M-shell ionization cross section," *Phys. Status Solidi A* **84**, K149–K152 (1984).
- ¹⁹⁴K. Murata and K. Sugiyama, "Quantitative electron microprobe analysis of ultra thin gold films on substrates," *J. Appl. Phys.* **66**, 4456–4461 (1989).
- ¹⁹⁵H. Genz, D. H. H. Hoffmann, W. Löw, and A. Richter, "L-shell ionization by relativistic electrons and energy dependence of the $L\beta/L\alpha$ branching ratio," *Phys. Lett.* **73A**, 313–315 (1979).
- ¹⁹⁶J. H. Paterson, J. N. Chapman, W. A. P. Nicholson, and J. M. Titchmarsh, "Characteristic x-ray production cross sections for standardless elemental analysis in EDX," *J. Microsc.-Oxf.* **154**, 1–17 (1989).
- ¹⁹⁷C. Tang, Z. An, Z. Luo, and M. Liu, "Measurements of germanium K-shell ionization cross sections and tin L-shell x-ray production cross sections by electron impact," *J. Appl. Phys.* **91**, 6739–6743 (2002).
- ¹⁹⁸I. Kawrakow and D. W. O. Rogers, The EGSnrc code system: Monte Carlo simulation of electron and photon transport, Report No. PIRS-701, National Research Council of Canada, Ottawa, 2001.
- ¹⁹⁹C. N. Chang, "L-subshell ionization cross section for tungsten at low energies," *Phys. Rev. A* **19**, 1930–1935 (1979).
- ²⁰⁰Z. An and Q. Hou, "Inverse problem in the thick-target method of measurements of inner-shell ionization cross sections by electron or positron impact," *Phys. Rev. A* **77**, 042702 (2008).
- ²⁰¹J. Zhu, Z. An, M. Liu, and L. Tian, "Measurements of the K-shell ionization cross sections of Si by 3–25-keV electron impact using the thick-target method," *Phys. Rev. A* **79**, 052710 (2009).
- ²⁰²L. Tian and Z. An, "Effect of surface roughness on the measurement of electron impact inner-shell ionization cross sections using thick-target method," *Nucl. Instrum. Methods Phys. Res. B* **266**, 5037–5040 (2008).
- ²⁰³H. Tawara, K. G. Harrison, and F. J. De Heer, "X-ray emission cross sections and fluorescence yields for light atoms and molecules by electron impact," *Physica* **63**, 351–367 (1973).
- ²⁰⁴R. Hippler, I. McGregor, M. Aydinol, and H. Kleinpoppen, "Ionization of xenon L-subshells by low-energy electron impact," *Phys. Rev. A* **23**, 1730–1736 (1981).
- ²⁰⁵R. Hippler, K. Saeed, I. McGregor, and H. Kleinpoppen, "Energy dependence of characteristic and bremsstrahlung cross sections of Argon induced by electron bombardment at low energies," *Z. Phys. A* **307**, 83–87 (1982).
- ²⁰⁶C. A. Quarles and M. Semaan, "Characteristic x-ray production by electron bombardment of argon, krypton, and xenon from 4 to 10 keV," *Phys. Rev. A* **26**, 3147–3151 (1982).
- ²⁰⁷R. Hippler, H. Klar, K. Saeed, I. McGregor, A. J. Duncan, and H. Kleinpoppen, "Threshold behaviour of Ar K and Xe L3 ionisation by electron impact," *J. Phys. B* **16**, L617–L621 (1983).
- ²⁰⁸L. Kissel, C. A. Quarles, and R. H. Pratt, "Shape functions for atomic-field bremsstrahlung from electrons of kinetic energy 1–500 keV on selected neutral atoms $1 \leq Z \leq 92$," *At. Data Nucl. Data Tables* **28**, 381–460 (1983).
- ²⁰⁹C. A. Quarles, "Bremsstrahlung and K X-ray production by electron bombardment of thin-film and gas targets," *Accelerator Based Atomic Physics Techniques and Applications*, edited by S. M. Shafroth and J. C. Austin (AIP, 1997), pp. 237–277.
- ²¹⁰D. D. Cohen, "Comments on several analytical techniques for L-subshell ionisation calculations," *J. Phys. B* **17**, 3913–3921 (1984).
- ²¹¹J. L. Campbell, "Fluorescence yields and Coster-Kronig probabilities for the atomic L subshells," *At. Data Nucl. Data Tables* **85**, 291–315 (2003).
- ²¹²J. L. Campbell and J. X. Wang, "Interpolated Dirac-Fock values of L-subshell x-ray emission rates including overlap and exchange effects," *Phys. Rev.* **43**, 281–291 (1989).
- ²¹³B. Schlenk, D. Berenyi, S. Ricz, A. Valek, and G. Hock, "Electron impact L-shell ionization in the bombarding energy region from 300 to 600 keV," *J. Phys. B* **10**, 1303–1308 (1977).
- ²¹⁴J. M. Fernández-Varea, S. Segui, and M. Dingfelder, " $L\alpha$, $L\beta$, and $L\gamma$ x-ray production cross sections of Hf, Ta, W, Re, Os, Au, Pb, and Bi by electron impact. Comparison of distorted-wave calculations with experiment," *Phys. Rev. A* **83**, 022702 (2011).
- ²¹⁵A. Moy, C. Merlet, X. Llovet, and O. Dugne, "Measurements of absolute L- and M-subshell x-ray production cross sections of Pb by electron impact," *J. Phys. B* **46**, 115202 (2013).
- ²¹⁶M. H. Chen and B. Crasemann, "Radiationless transitions to atomic $M_{1,2,3}$ shells: Results of relativistic theory," *Phys. Rev. A* **27**, 2989–2994 (1983).
- ²¹⁷C. P. Bhalla, "Radiative transition probabilities for vacancies in M subshells," *J. Phys. B* **3**, 916–924 (1970).
- ²¹⁸E. J. McGuire, "Atomic M-shell Coster-Kronig, Auger, and radiative rates, and fluorescence yields for Ca-Th," *Phys. Rev. A* **5**, 1043–1047 (1972).
- ²¹⁹M. H. Chen and B. Crasemann, "M x-ray emission rates in Dirac-Fock approximation," *Phys. Rev. A* **30**, 170–176 (1984).
- ²²⁰Y. Chauhan and S. Puri, " M_i ($i = 1-5$) subshell fluorescence and Coster-Kronig yields for elements with $67 \leq Z \leq 92$," *At. Data Nucl. Data Tables* **94**, 38–49 (2008).
- ²²¹S. Puri, "Relative intensities for L_i ($i = 1-3$) and M_i ($i = 1-5$) subshell x rays," *At. Data Nucl. Data Tables* **93**, 730–741 (2007).
- ²²²J. Pálinskás and B. Schlenk, "M-shell ionization cross sections for Au, Pb and Bi by 60–600 keV electron impact," *J. Phys. B* **13**, 1631–1636 (1980).
- ²²³G. Glupe and W. Mehlhorn, "A new method for measuring electron impact ionization cross sections of inner shells," *Phys. Lett. A* **25**, 274–275 (1967).
- ²²⁴G. Glupe and W. Mehlhorn, "Absolute electron impact ionization cross sections of N, O and Ne," *J. Phys. Colloq. C* **4**, 40–43 (1971).
- ²²⁵H. J. Christofzik, Master's thesis, University of Münster, Münster, 1970.
- ²²⁶G. N. Ogurtsov, "Energy distribution of electrons emitted by argon atoms under electron impact," *Zh. Eksp. Teor. Fiz.* **64**, 1149–1153 (1973).
- ²²⁷J. J. Vrakking and F. Meyer, "Electron-impact-ionization cross sections of inner shells measured by Auger-electron spectroscopy," *Phys. Rev. A* **9**, 1932–1937 (1974).
- ²²⁸W. Hink, L. Kees, H. P. Schmitt, and A. Wolf, "Near K-ionization threshold Auger electron measurements for neon under electron impact," *Inner-Shell and X-ray Physics of Atoms and Solids*, edited by D. J. Fabian, H. Kleinpoppen, and L. M. Watson (Plenum, New York, 1981), pp. 327–330.
- ²²⁹A. Yagishita, "Ionization cross sections of krypton M subshells by electron impact," *Phys. Lett. A* **87**, 30–32 (1981).
- ²³⁰H. Platten, G. Schiwietz, and G. Nolte, "Cross sections for K-shell ionization of Si and Ar by 4 keV to 10 keV electron impact," *Phys. Lett. A* **107**, 83–85 (1985).

- ²³¹H. Suzuki, T. Hirayama, and T. Takayanagi, "Giant resonances in double ionization of atomic ions," *AIP Conf. Proc.* **205**, 82–89 (1990).
- ²³²B. S. Min, Y. Yoshinari, T. Watabe, Y. Tanaka, C. Takayanagi, T. Takayanagi, K. Wakiya, and H. Suzuki, "Measurements of ionization cross sections of 4d electrons in xenon by electron impact," *J. Phys. Soc. Jpn.* **62**, 1183–1192 (1993).
- ²³³W. Hink, K. Brunner, and A. Wolf, "A 2-channel coincidence electron spectrometer with 0.7 ns time resolution," *J. Phys. E: Sci. Instrum.* **13**, 882–887 (1980).
- ²³⁴S. M. Younger, "Giant resonance effects in the electron-impact ionization of heavy atoms and ions," *Phys. Rev. A* **35**, 2841–2851 (1987).
- ²³⁵T. E. Gallon, "Estimation of backscattering effects in electron-induced Auger spectra," *J. Phys. D: Appl. Phys.* **5**, 822–832 (1972).
- ²³⁶D. M. Smith and T. E. Gallon, "Auger emission from solids - Estimation of backscattering effects and ionization cross sections," *J. Phys. D: Appl. Phys.* **7**, 151–161 (1974).
- ²³⁷M. P. Seah, "Quantification in AES and XPS," *Surface Analysis by Auger and X-ray Photoelectron Spectroscopy*, edited by D. Briggs and J. T. Grant (IM Publications and Surface Spectra Limited, Chichester, 2003), pp. 345–375.
- ²³⁸A. Jablonski and W. Hartweck, "Comments on Gallon method for determining the ionization cross section and the backscattering factor," *Surf. Sci.* **110**, L593–L598 (1981).
- ²³⁹R. L. Gerlach and A. R. DuCharme, "Total electron-impact ionization cross sections of K-shells of surface atoms," *Surf. Sci.* **32**, 329–340 (1972).
- ²⁴⁰H. J. Hunger and L. Kuchler, "Measurements of the electron backscattering coefficient for quantitative EPMA in the energy range of 4 to 40 keV," *Phys. Status Solidi A* **56**, K45–K46 (1979).
- ²⁴¹M. M. El Gomati, C. G. H. Walker, A. D. M. Assa'd, and M. Zadrzil, "Theory experiment comparison of the electron backscattering factor from solids at low electron energy (250–5,000 eV)," *Scanning* **30**, 2–15 (2008).
- ²⁴²A. Jablonski, J. Zemek, and P. Jiricek, "The backscattering factor for the Au N67VV Auger transition," *Appl. Surf. Sci.* **252**, 905–915 (2005).
- ²⁴³A. R. DuCharme and R. L. Gerlach, "Consideration of L-shell ionization cross sections in Auger Electron Spectroscopy," *J. Vac. Sci. Technol.* **10**, 188–191 (1973).
- ²⁴⁴K. Goto, K. Ishikawa, T. Koshikawa, and R. Shimizu, "Auger and secondary electrons excited by backscattered electrons - Approach to quantitative analysis," *Surf. Sci.* **47**, 477–494 (1975).
- ²⁴⁵Y. Takeichi and K. Goto, "True Auger electron spectra measured with a novel cylindrical mirror analyser (Au, Ag and Cu)," *Surf. Interface Anal.* **25**, 17–24 (1997).
- ²⁴⁶S. Ichimura and R. Shimizu, "Backscattering corrections for quantitative Auger analysis. I. Monte Carlo calculations of backscattering factors for standard materials," *Surf. Sci.* **112**, 386–408 (1981).
- ²⁴⁷D. R. Batchelor, H. E. Bishop, and J. A. Venables, "Auger electron spectroscopy from elemental standards. II. Peak height and area," *Surf. Interface Anal.* **14**, 700–708 (1989).
- ²⁴⁸T. Sato, Y. Nagasawa, T. Sekine, Y. Sakai, and A. D. Buonaquisti, "Conversion of Auger sensitivities at one primary excitation energy to those at another," *Surf. Interface Anal.* **14**, 787–793 (1989).
- ²⁴⁹G. Love, M. G. Cox, and V. D. Scott, "Surface ionization function $\phi(\theta)$ derived using a Monte Carlo method," *J. Phys. D: Appl. Phys.* **11**, 23–31 (1978).
- ²⁵⁰M. P. Seah and I. S. Gilmore, "High resolution digital Auger database of true spectra for Auger electron spectroscopy intensities," *J. Vac. Sci. Technol.* **14**, 1401–1407 (1996).
- ²⁵¹H. W. Drawin, "Zur spektroskopischen Temperatur und Dichtemessung von Plasmen bei Abwesenheit thermodynamischen Gleichgewichtes," *Z. Phys.* **172**, 429–452 (1963).
- ²⁵²R. F. Egerton, *Electron Energy Loss Spectroscopy in the Electron Microscope* (Plenum, New York, 1996).
- ²⁵³R. L. Gerlach and A. R. DuCharme, "Differential cross sections for K-shell ionization of surface atoms by electron impact," *Phys. Rev. Lett.* **27**, 290–293 (1971).
- ²⁵⁴R. L. Gerlach and A. R. DuCharme, "Backscattering cross sections for ionization of surface-atom K shells by electron impact," *Phys. Rev. A* **6**, 1892–1901 (1972).
- ²⁵⁵R. L. Gerlach and A. R. DuCharme, "L-shell ionization threshold structure from Auger-electron spectra," *Jpn. J. Appl. Phys.* **2**, 675–678 (1974).
- ²⁵⁶E. H. S. Burhop, "The inner shell ionization of atoms by electron impact," *Proc. Cambridge Philos. Soc.* **36**, 43–52 (1940).
- ²⁵⁷W. L. Fite and R. T. Brackmann, "Collisions of electrons with hydrogen atoms. I. Ionization," *Phys. Rev.* **112**, 1141–1151 (1958).
- ²⁵⁸E. Rothe, L. L. Marino, R. H. Neynaber, and S. M. Trujillo, "Electron impact ionization of atomic hydrogen and atomic oxygen," *Phys. Rev. A* **125**, 582–583 (1962).
- ²⁵⁹M. B. Shah, D. S. Elliot, and H. B. Gilbody, "Pulsed crossed-beam study of the ionisation of atomic hydrogen by electron impact," *J. Phys. B* **20**, 3501–3514 (1987).
- ²⁶⁰T. W. Shyn, "Doubly differential cross sections of secondary electrons ejected from atomic hydrogen by electron impact," *Phys. Rev. A* **45**, 2951–2956 (1992).
- ²⁶¹D. Rapp and P. Englander-Golden, "Total cross sections for ionization and attachment in gases by electron impact. I. Positive ionization," *J. Chem. Phys.* **43**, 1464–1479 (1965).
- ²⁶²J. Schutzen B. L. Schram, H. R. Moustafa and F. J. De Heer, "Ionization cross sections for electrons (100–600 eV) in noble and diatomic gases," *Physica* **32**, 734–740 (1966).
- ²⁶³K. Stephan, H. Helm, and T. D. Mark, "Mass-spectrometric determination of partial electron-impact ionization cross-sections of He, Ne, Ar and Kr from threshold up to 180-eV," *J. Chem. Phys.* **73**, 3763–3778 (1980).
- ²⁶⁴R. G. Montague, M. F. A. Harrison, and A. C. H. Smith, "A measurement of the cross section for ionisation of helium by electron impact using a fast crossed beam technique," *J. Phys. B* **17**, 3295–3310 (1984).
- ²⁶⁵R. C. Wetzel, F. A. Baiocchi, T. R. Hayes, and R. S. Freund, "Absolute cross-sections for electron-impact ionization of the rare-gas atoms by the fast-neutral-beam method," *Phys. Rev. A* **35**, 559–577 (1987).
- ²⁶⁶M. B. Shah, D. S. Elliot, P. McCallion, and H. B. Gilbody, "Single and double ionisation of helium by electron impact," *J. Phys. B* **21**, 2751–2761 (1988).
- ²⁶⁷R. Rejoub, B. G. Lindsay, and R. F. Stebbings, "Determination of the absolute partial and total cross sections for electron-impact ionization of the rare gases," *Phys. Rev. A* **65**, 042713 (2002).
- ²⁶⁸C. Colliex and B. Jouffrey, "Inelastic-scattering of electrons in a solid by excitation of deep atomic levels. I. Energy-loss spectra," *Philos. Mag.* **25**, 491–511 (1972).
- ²⁶⁹M. Isaacson, "Interaction of 25 keV electrons with nucleai-acid bases, adenine, thymine, and uracil. II. Inner-shell excitation and inelastic scattering cross sections," *J. Chem. Phys.* **56**, 1813–1818 (1972).
- ²⁷⁰R. F. Egerton, "Inelastic scattering of 80 keV electrons in amorphous carbon," *Philos. Mag.* **31**, 199–215 (1975).
- ²⁷¹C. J. Rossouw and M. J. Whelan, "The K-shell cross-section for 80 kV electrons in single-crystal graphite and AlN," *J. Phys. B* **12**, 797–807 (1979).
- ²⁷²A. V. Shchagin, V. I. Pristupa, and N. A. Khizhnyak, "K-shell ionization cross section of Si atoms by relativistic electrons," *Nucl. Instrum. Methods Phys. Res. B* **84**, 9–13 (1994).
- ²⁷³C. Zhou, Z. An, and Z. Luo, "Measurement of K-shell production cross sections for Ga, Ge and Zr elements by electron impact," *J. Phys. B* **35**, 841 (2002).
- ²⁷⁴G. H. Wannier, "The threshold law for single ionization of atoms or ions by electrons," *Phys. Rev.* **90**, 817–825 (1953).
- ²⁷⁵D. Gräf and W. Hink, "Measurements on PCI and threshold law in K-shell ionisation of Ar by electron impact," *J. Phys. B* **18**, L803–L808 (1985).
- ²⁷⁶L. J. Kieffer and G. H. Dunn, "Electron impact ionization cross-section data for atoms, atomic ions, and diatomic molecules. I. Experimental data," *Rev. Mod. Phys.* **64**, 032713 (1996).
- ²⁷⁷C. J. Powell, R. J. Stein, P. B. Needham, Jr., and T. J. Driscoll, "Attenuation lengths of low-energy electrons in solids derived from the yield of proton-excited Auger electrons: beryllium and aluminum," *Phys. Rev. B* **16**, 1370–1379 (1977).
- ²⁷⁸S. Huefner, *Photoelectron Spectroscopy: Principles and Applications* (Springer-Verlag, Berlin, 1995).
- ²⁷⁹G. Wendin, *Breakdown of the One-Electron Pictures in Photoelectron Spectra, Structure and Bonding*, Vol. 45 (Springer-Verlag, Berlin, 1981).

- ²⁸⁰J. A. Bearden and A. F. Burr, "Reevaluation of x-ray atomic energy levels," *Rev. Mod. Phys.* **39**, 125–142 (1967).
- ²⁸¹W. Lotz, "Electron binding energies in free atoms," *J. Opt. Soc. Am.* **60**, 206–210 (1970).
- ²⁸²G. P. Williams, "Electron binding energies of the elements," in *CRC Handbook of Chemistry and Physics*, edited by W. M. Haynes and D. R. Lide, 91st ed. (CRC, Boca Raton, 2011), Section 10, pp. 221–226.
- ²⁸³C. J. Powell, "Recommended Auger parameters for 42 elemental solids," *J. Electron Spectrosc. Relat. Phenom.* **185**, 1–3 (2012).
- ²⁸⁴A. Naumkin, A. Kraut-Vass, S. W. Gaarenstroom, and C. J. Powell, "NIST X-ray Photoelectron Spectroscopy Database, NIST Standard Reference Database 20, Version 4.1," Technical Report, National Institute of Standards and Technology, Gaithersburg, MD, 2012, available at <http://srdata.nist.gov/xps>.